Université de Technologie de Troyes

Light, Nanomaterials, Nanotechnologies (L2N)

Spécialité: Matériaux, Mécanique, Optique, Nanotechnologie

In cotutelle with

Eberhard Karls Universität Tübingen

Institute for Applied Physics

Spécialité: Physics

Thesis presented for obtention of the Title Ph.D. in Physics
Fang DAI

Investigation of LSPR and Raman sensing sensitivities of circular metal-insulator-metal (MIM) cavity arrays

Jury

NORDIN Felidj	Professeur des Universités	Examinateur
BELLESSA Joel	Professeur des Universités	Rapporteur
LIENAU Christoph	Professor	Rapporteur
MEIXNER Alfred J.	Professor	Examinateur
ADAM Pierre-Michel	Professeur des Universités	Directeur de thèse
FLEISCHER Monika	Professor	Directrice de thèse

Investigation of LSPR and Raman sensing sensitivities of circular metal-insulator-metal (MIM) cavity arrays

Dissertation

der Mathematisch-Naturwissenschaftlichen Fakultät

der Eberhard Karls Universität Tübingen

zur Erlangung des Grades eines

Doktors der Naturwissenschaften

(Dr. rer. nat.)

vorgelegt von

Fang DAI

aus Xiantao / China

Tübingen

2019

Gedruckt mit Genehmigung der Mathematisch-Naturwissenschaftlichen Fakultät der Eberhard Karls Universität Tübingen.

Tag der mündlichen Qualifikation:	03.07.2019
Dekan:	Prof. Dr. Wolfgang Rosenstiel
1. Berichterstatter:	Prof. Dr. Christoph LIENAU
2. Berichterstatter:	Prof. Dr. Joël BELLESSA

Acknowledgements

Doing my Ph.D. thesis has been an important and great journey to me in many senses. There have been many nice persons around to support and accompany me, to make this journey as inspiring and interesting as it can ever be.

I would like to express my sincere gratitude to my supervisors, Prof. Pierre-Michel Adam and Prof. Monika Fleischer, for the time and energy they have devoted to help me finish my thesis. Both of them have always been very attentive and encouraging when discussing physics with me. And inspired by their ways of doing research and their attitudes towards science, it has always been super easy for me to find the fun and fulfilment in doing my thesis. Besides, I appreciate very much the one-of-a-kind experience they have offered me to immerse in both French and German working environment and cultures throughout my thesis period.

Besides my supervisors, I wish to thank my Jury committee, Prof. Christoph Lienau, Prof. Joel Bellessa, Prof. Alfred J. Meixner and Prof. Nordin Felidj. Thanks for their encouragement, constructive comments and inspiring questions.

I would like to thank Dr. Andreas Horrer, who helped me to get familiar with the necessary techniques and methods when I just started. I appreciate the detailed discussions through these years. My sincere thanks also goes to Dr. Sergei Kostcheev, Dr. Anna Rumyantseva, Dr. Jeremie Beal, Dr. Anne-Laure Baudrion-Beal, Dr. Regis Deturche and Dr. Hind Kadiri in University of Technology of Troyes and Dr. Ronny Löffler, Dr. Eva Lohmann, Dr. Simon Dickreuter, Florian Laible, Prof. Katharina Broch, Christoph Dreser and Annika Bräuer in University of Tuebingen. I would like to thank them for introducing various of different equipments and techniques to me.

I would like to thank Chinese Scholarship Council for financing my thesis for four years. Also thanks goes to my supervisors for their efforts to find financial support for me for the last six months, so that I was able to be more focused on my thesis.

I want to thank my friends for their support and accompany during this period: Shijie, Andi, Yi, Feifei, Liyuan, Nan, Xi, Junze, Feng, Jiyong, Yongjian, Yangcan, Siyao, Hang, Ziwei, Loic, Dalia, Rita, Yann, Thomas...You have added bright colors and highlight moments in my memory.

Last but not least, I wish to thank my loving parents and brother for their spiritual support during all the time.

Abstract

Surface plasmonic resonances provide well-defined absorption and scattering peaks in the far-field spectra together with strongly enhanced electromagnetic near-fields, which make plasmonic structures promising candidates for bio-sensors and plasmonically assisted spectroscopy. Since the discovery of plasmonic resonances, a lot of efforts have gone into the application of plasmonic sensors and plasmonically assisted spectroscopy in the field of clinical diagnosis, food security, or environment monitoring. In this thesis, we investigated the performance of vertical metal-insulator-metal (MIM) structures as a refractive index (RI) sensor and SERS substrate. However, the appealing strongly enhanced near-field is localized inside the dielectric spacer and not accessible to the surrounding medium and Raman molecules. In order to address this problem, this thesis is aiming at achieving a better understanding of the fundamentals of vertical MIM structures, exposing the 'hot spots' of cavity plasmon modes, investigating the RI sensing capabilities of MIM cavities and improving the surface-enhanced Raman spectroscopy (SERS) performance of MIM cavities.

Disc-on-film structures with different geometrical parameters and different spacer configurations were systematically studied by experiments and simulations. A circular Fabry-Pérot (FP) cavity model was applied to describe the cavity plasmon modes in MIM cavities. The cavity plasmon modes (TEMmn) were divided into edge cavity modes (TEM1n) and surface cavity modes (TEMm1), which show different optical variation with wet etching, RI sensing performance and SERS enhancement factors. The dependency of cavity plasmon modes as a function of periodicity, cavity radius and cavity height was studied. The reasons for different line shapes of far-field optical spectra were revealed.

The influence of varying spacers on the locations of 'hot spots' and resonance wavelengths was systematically studied. The 'hot spots' of cavity plasmon modes were exposed by wet etching.

The RI sensitivities of MIM structures were thoroughly studied including different types of plasmonic modes, sensing based on spectral shifts or intensity changes, and bulk/molecular RI sensing configurations. The sensitivities of cavity plasmon modes and surface plasmon polariton (SPP) modes were tuned by creating Rabi-analog splitting.

Notable SERS enhancement factors (EFs) have been achieved by underetching. EF peaks attributed to different orders of cavity plasmon modes were observed in both experiments and simulations. Good qualitative agreement has been found between the experimental and simulated results. A SERS performance comparison was made between the disc-on-film substrate and vertical disc dimers: similar dependency of effective SERS EF as a function of cavity radius was found for the two SERS substrates.

Keywords:

Plasmons, nanoparticles, Fabry-Pérot interferometers, optical properties, Raman effect, surface enhanced, sensing

Résumé

Les résonances plasmoniques de surface fournissent une absorption nette et un pic de diffusion dans les spectres de champ lointain et, associées à un champ proche électromagnétique fortement amplifié, font des structures plasmoniques des candidats prometteurs pour les capteurs biologiques et la spectroscopie assistée par plasmonique. Depuis la découverte des résonances plasmoniques, de nombreux efforts ont été consacrés à l'application de capteurs plasmoniques et à la spectroscopie assistée par plasmonique dans les domaines du diagnostic clinique, de la sécurité alimentaire ou de la surveillance de l'environnement. Dans cette thèse, nous avons étudié les performances des structures verticales métal-isolant-métal (MIM) en tant que capteurs d'indice de réfraction (RI) et substrats Raman effet augmenté en surface (SERS). Cependant, le champ proche fortement exalté est localisé à l'intérieur de l'espaceur diélectrique et n'est pas accessible au milieu environnant ni aux molécules Raman. Afin de résoudre ce problème, cette thèse vise à mieux comprendre les principes fondamentaux des structures MIM verticales, à exposer les "points chauds" des modes de plasmon de cavité, à étudier les capacités de détection RI des cavités MIM et à améliorer les performances SERS de MIM cavités.

Les structures en disques sur films avec différents paramètres géométriques et différentes configurations d'espaceurs ont été étudiées de manière systématique par des expériences et des simulations. Les modèles circulaires de cavité FP ont été appliqués pour décrire les modes de plasmon dans les cavités MIM. Les modes de plasmon de la cavité ont été divisés en modes de cavité de bord et modes de cavité de surface, qui montrent différentes variations optiques avec la gravure humide, les performances de détection RI et les facteurs d'amélioration SERS. La dépendance des modes de plasmon de la cavité en fonction de la périodicité, du rayon de la cavité et de sa hauteur a été étudiée. L'origine des différentes raies présentes dans les spectres optiques en champ lointain a été révélée.

L'influence de différents espaceurs sur la localisation des «points chauds» et des longueurs d'onde de résonance a été étudiée. Les «points chauds» des modes de plasmon dans la cavité ont été révélés par gravure humide.

Les sensibilités RI des structures MIM ont été minutieusement étudiées, notamment différents types de modes plasmoniques, différents types de modulations de détection et différents types de configuration de détection RI. La sensibilité des modes plasmon de la cavité et des modes polaritons de plasmons de surface (SPP) a été ajustée en créant l'analogue d'un dédoublement Rabi.

Des facteur d'amélioration (EF) SERS notables ont été atteints en sous-gravant. Des pics EF attribuables à différents ordres de modes de plasmon dans la cavité ont été observés à la fois dans les expériences et les simulations. Un bon accord qualitatif a été trouvé entre les résultats expérimentaux et simulés. Une comparaison de performance SERS a été faite entre le dimère de disque sur film et les dimères de disque verticaux: une dépendance similaire du SERS EF effectif en fonction du rayon de la cavité a été trouvée pour les deux substrats SERS.

Mots-clés : Plasmons, nanoparticules, Fabry-Pérot, Interféromètres de, propriétés optiques, Raman, effet augmenté en surface, détecteurs

Zusammenfassung

Die Resonanzen von Oberflächenplasmonen (LSPR von engl. localized surface plasmon resonance) in metallischen Nanostrukturen liefern genau definierte Absorptions- und Streuungspeaks in deren optischen Fernfeldspektren. Zusammen mit dem damit einhergehenden stark verstärkten elektromagnetischen Nahfeld macht dies plasmonische Strukturen zu vielversprechenden Kandidaten für Biosensoren und plasmonisch unterstützte Spektroskopie. Seit der Entdeckung plasmonischer Resonanzen sind viele Anstrengungen unternommen worden, um solche Sensoren und die plasmonisch unterstützte Spektroskopie zur Anwendung im Bereich der klinischen Diagnose, der Lebensmittelsicherheit oder der Umgebungsüberwachung zu bringen. In dieser Arbeit haben wir die Leistungsfähigkeit von vertikalen Metall-Isolator-Metall (MIM)- Strukturen als Brechungsindex (RI von engl. refractive index) -Sensoren und als Substrate für oberflächenverstärkte Raman-Streuung (SERS von engl. surface enhanced Raman scattering) untersucht. Das verstärkte Nahfeld der MIM-Struktur ist jedoch innerhalb der nur wenige Nanometer dicken Isolatorschicht lokalisiert und für das umgebende Medium und die nachzuweisenden Raman-Moleküle nicht frei zugänglich. Um dieses Problem zu lösen, zielt die vorliegende Arbeit zum einen darauf ab, die Grundlagen der vertikalen MIM-Strukturen besser zu verstehen und zum anderen darauf, die Bereiche mit besonders starkem Nahfeld (engl. hotspots) der Resonatormoden freizulegen. Weiterhin wird die Sensitivität der MIM-Strukturen auf RI-Änderungen bestimmt und untersucht, wie die SERS-Leistung verbessert werden kann.

Bei den MIM-Strukturen handelt es sich um Goldscheibchen, welche sich, durch eine Siliziumdioxidschicht getrennt, auf einem dünnen Goldfilm befinden. Diese Disc-on-Film-Strukturen mit unterschiedlichen geometrischen Parametern und unterschiedlichen Abstandhalter-Konfigurationen wurden systematisch durch Experimente und Simulationen untersucht. Ein Modell für kreisförmige Fabry-Pérot(FP)-Kavitäten wurde angewendet, um die Resonatormoden in MIM-Kavitäten zu beschreiben. Die Resonatormoden wurden in Rand-Moden und Oberflächen-Moden unterteilt, deren Resonanzen sich bei Veränderung der Isolatorschicht, bei der RI-Sensitivität und bei den SERS-Verstärkungsfaktoren unterschiedlich verhalten. Die Abhängigkeit der Resonatormoden von der Periodizität, dem Resonator-Radius und der Höhe des Kavität wurde untersucht. Der Grund für unterschiedliche Linienformen der optischen Fernfeldspektren wurde aufgezeigt.

Der Einfluss verschiedener Geometrien der isolierenden Abstandhalter-Schicht auf die Position der "Hot Spots" und die Resonanzwellenlängen wurde systematisch untersucht. Im Experiment wurden die "Hot Spots" der Resonatormoden durch Nassätzen des Spacermaterials freigelegt.

Die RI-Sensitivitäten der MIM-Strukturen wurden durch Simulation und Experiment untersucht. Es wurden verschiedene Arten plasmonischer Moden, die in den Strukturen auftreten, verglichen. Im Experiment wurden dabei verschiedene Sensormodulationen und –konfigurationen verwendet. Die Sensitivität der Resonatormoden und der Oberflächenplasmon-Moden konnte durch Kopplung und daraus resultierendes Rabi-Splitting eingestellt werden.

Es wurden bemerkenswerte SERS-Verstärkungsfaktoren in den Strukturen, in welchen

durch Unterätzen der Spacer freigelegt wurde, erreicht. Maxima des Verstärkungsfaktors, die auf unterschiedliche Ordnungen von Resonatormoden zurückgeführt werden konnten, wurden sowohl im Experiment als auch in der Simulation beobachtet. Es wurde eine gute qualitative Übereinstimmung zwischen den experimentellen und simulierten Ergebnissen gefunden. Ein SERS-Leistungsvergleich wurde zwischen Disc-on-Film-Substraten und vertikalen Disc-Dimeren durchgeführt: Eine ähnliche Abhängigkeit des effektiven SERS EF als Funktion des Radius wurde für die beiden SERS-Substrate gefunden.

Stichwörter : Plasmonen, Nanopartikel, Fabry-Pérot-Resonator, optische Eigenschaften, oberflächeverstärkte Raman-Streuung, Brechungsindexsensor

General introduction

Plasmonic resonances, which are associated with the collective oscillations of the electron gas in noble metal nanostructures, show well-defined absorption and scattering peaks together with strongly enhanced electromagnetic near-fields. On one hand, the resonance conditions of the plasmonic modes make both the resonance positions and the intensities of far-field spectra very sensitive to the refractive index change of the surrounding medium, allowing biomedical sensors to be created based on such nanostructures. On the other hand, the strongly enhanced near-field provides an appealing platform for plasmonically assisted spectroscopy, for instances surface enhanced Raman spectroscopy (SERS), surface enhanced fluorescence (SEF), surface enhanced infrared absorption spectroscopy and etc. Hence, since the discovery of plasmonic resonances, a lot of efforts have gone into the application of plasmonic sensors and plasmonically assisted spectroscopy in the field of clinical diagnosis, food security, or environment monitoring. In this thesis, I investigated the performance of vertical metal-insulator-metal (MIM) structures as a refractive index (RI) sensor and SERS substrate. This thesis is organized as follows.

In **Chapter 1**, the state of the art is given for the plasmonic RI sensors and SERS subsrates, as well as the recent study on vertical MIM structures. It has been pointed out that the RI sensitivities and SERS enhancement factors have been significantly restricted due to the fact that the 'hot spots' of cavity plasmon modes reside inside the insulator layer, and are therefore not accessible to the detecting medium and Raman molecules. In order to address this problem, the objectives of this thesis are to achieve a better understanding of the fundamentals of vertical MIM structures, to expose the 'hot spots' of cavity plasmon modes, to study the RI sensing capabilities of MIM cavities, and to improve the SERS performance of MIM cavities, which are the main topics of **Chapter 4**, **Chapter 5**, **Chapter 6** and **Chapter 7**, respectively.

In **Chapter 2**, the basic theory about surface plasmon polaritons (SPPs), localized surface plasmonic resonances (LSPRs) and the different kinds of coupling regimes between them are presented. In the last section, recent progress in applying Fabry-Pérot (FP) models in the radio frequency regime to describe the standing-wave plasmonic resonances in 1D, 2D and 3D plasmonic resonators is presented.

In **Chapter 3**, the fabrication and characterization methods that have been used in this thesis are shown. Firstly, the fabrication processes of disc-on-film substrates and vertical disc dimer substrates are presented. Then the methods for geometrical characterization: scanning electron microscope (SEM) and focused ion beam (FIB) cross-sectioning are presented. They are followed by the introduction of the optical characterization set-ups including extinction, reflection, scattering and Raman measurements. Finally the simulation cell in Comsol Multiphysics for the investigated vertical MIM structures is shown.

In **Chapter 4**, the cavity plasmon modes (TEMmn) in MIM structures are described by a model for a circular FP cavity with perfect electronic conductor (PEC) reflectors. The resonance wavelengths are found to appear at the intersection of the eigenvalues of a circular FP cavity with the dispersion of gap surface plasmons in corresponding infinite MIM waveguides. Most importantly, two sets of cavity plasmon modes are

identified: edge cavity plasmon modes (TEMm1) with modal lobes distributed along the circumferences of circular cavities, and surface cavity plasmon modes (TEM1n) with modal lobes along the diameters of cavity modes. The different field distribution characteristics of edge modes and surface modes lead to very different performances in optical variation when exposing the 'hot spots', the RI sensitivities and SERS performance, which are studied in **Chapter 5**, **Chapter 6** and **Chapter 7**, respectively. Then it is shown that the plasmonic modes in disc-on-substrate samples can be described as well by the circular FP model. A comparison of the properties, including bandwidth, resonance wavelength and field intensity, of cavity plasmon modes in MIM cavities and Au discs is presented. The resonance characteristics of cavity plasmon modes in MIM cavity arrays as a function of periodicity, cavity radius and cavity height are investigated. Strong coupling with Rabi-analog splitting has been observed, and the energy exchange and the physical properties of hybridized modes have been studied. The Fano-shaped extinction spectra have been revealed to result from the Fano hybridization between the narrow Lorentz shaped cavity plasmon modes and the transmitted broad incidence continuum.

In **Chapter 5**, the importance and possibility to expose the 'hot spots' of cavity plasmon modes are studied. Firstly, the resonance characteristics of cavity plasmon modes are investigated in three MIM cavities with different spacer configurations by simulations. On one hand, it is concluded that for open FP cavities, field maxima always appear at the edges of FP cavities however the spacer configuration varies. On the other hand, the resonance position is significantly influenced when the variation of the spacer configuration induces RI changes in the modal lobes of cavity plasmon modes, while it exhibits no resonance spectral shift when the RI in the modal nodes is modified. Then the experimental results for underetching are presented: the cavity plasmon modes blue-shift as the SiO_2 disc spacer gets reduced by wet etching. For the surface modes, more modal energy resides in the central modal lobes rather than in the edge lobes, therefore edge modes TEM11 and TEM31 show higher sensitivity than surface modes TEM12 and TEM13. It is observed as well in experiments and the simulations, that the higher order surface plasmon mode TEM13 shows a smaller spectral shift compared to the lower order TEM12 mode, due to less near-field energy residing at the edge lobes of the TEM13 mode compared to the TEM12 mode.

In **Chapter 6**, the RI sensing capabilities of MIM cavities are studied. The Lorentz shaped reflection spectra are well suited for RI sensing based on spectral shifts, while the Fano-shaped extinction spectra show excellent sensitivity as an intensity-modulated sensor. It is concluded that the edge cavity modes show better sensitivities than surface cavity modes, and the lower order surface plasmon modes show better sensitivities than those of the higher order surface modes, due to the near-field distribution characteristics. Then the RI sensing capabilities of MIM structures with a SiO_2 disc spacer (MIM(II)) are investigated in the bulk sensing configuration for MIM arrays with varying Au disc sizes and varying periodicity. The resolution of sensors, the sensitivities of the LSPR modes as spectral shift modulated and intensity modulated sensors, the sensitivities of the SPP mode and the sensitivities of cavity plasmon modes TEMmn are discussed experimentally. Moreover, the possibility to tune the RI sensitivities of cavity plasmon modes and SPP modes by mode hybridization was confirmed by simulations and experiments. Finally, the sensitivities of MIM cavities have been studied by simulation in molecular sensing configurations: the cavity plasmonic modes show more

promising performance compared to SPP modes, due to the difference in near-field intensity inside the sensing volume.

In **Chapter 7**, the SERS EF of MIM cavities with varying cavity radius and periodicity, with and without underetch are studied by experiments and simulations, taking the SERS signal from 5 nm island films as a reference. For the MIM structures with an unetched SiO_2 disc spacer, comparable SERS EFs to those of the 5 nm island films were achieved with the Raman molecule 4-mercaptobenzoic acid (4-MBA). The EFs are plotted as a function of cavity radius, and two EF peaks attributed to the first two order cavity modes (TEM11 and TEM12) are identified. Good qualitative agreement has been found between the experimental and simulated EFs variation as a function of cavity radius. It is observed in both experiments and simulations, that notable SERS EF improvement has been achieved after wet etching even without any efforts to optimize the etching process, and the cavity radius which gives rise to the highest EFs attributed to TEM11 and TEM12 modes, shifts to a bigger cavity radius after wet etching. Good qualitative agreement has been found for the SERS performance variation before and after etching as well. The SERS performance of vertical disc dimers with varying geometrical parameters has been investigated and compared to that of disc-on-film substrates by experiments and simulations, with the Raman molecule trans-1,2-bis (4-pyridyl)-ethylene (BPE). Similar dependency of the effective SERS EF as a function of cavity radius was found for the two SERS substrates.

Contents

Chapter 1

Introduction

1.1 State of the art

There are two kinds of surface plasmons: localized surface plasmon polaritons (LSPPs) and surface plasmon polaritons (SPPs), depending on either light being coupled into non-propagating surface plasmonic modes in nanostructures or propagating surface plasmons at extended metal/dielectric interfaces. Details about these plasmonic modes will be described in Chapter 2. The collective oscillation of the free electron gas in the metal according to the local electric field with respect to the fixed ionic cores, which is inherent to the excitations of LSPPs and SPPs, results in a well confined and enhanced electromagnetic (EM) field. Due to the mechanism of this plasmon oscillation, both the resonant position and the intensity of plasmonic modes are very sensitive to a change of the surrounding medium, as well as the size and shape of the nanostructures [1–4]. These properties allow for biomedical sensors and plasmon-enhanced Raman sensors to be created based on such nanostructures. Hence, since the discovery of LSPPs and SPPs, a lot of efforts have gone into the application of plasmonic sensors in clinical diagnosis, food security, or environment monitoring. The objective of this section is to provide an overview over the state of the art with respect to the refractive index plasmonic sensor and surface enhanced Raman scattering sensor, which are relevant to this thesis.

1.1.1 Refractive index plasmonic sensors

1.1.1.1 Performance considerations of plasmonic sensors

Refractive index plasmonic sensors are one of the simplest and most straightforward applications of plasmonic nanostructures. The refractive index sensitivity of plasmonic sensors is a common standard to evaluate the sensing performance, and it is defined by the resonance wavelength shift per refractive index unit (nm/RIU),

$$Sensitivity = \frac{d\lambda_{resonance}}{dn_d} \tag{1.1}$$

where $\lambda_{resonance}$ is the resonance wavelength of the nanoparticle and n_d represents the refractive index of the surrounding medium.

Besides the refractive index sensitivity, resolution is another key performance characteristic for the evaluation of the sensing capability. It is defined by the smallest refractive index change that can be discerned by the plasmonic sensor, and is affected by the signal/noise ratio and the line width of the plasmonic mode.

The figure of merit (FoM) which takes into consideration both sensitivity and resolution of plasmonic sensors, is defined by the refractive sensitivity divided by the FWHM (full width at half maximum) of plasmonic modes

$$FoM = \frac{Sensitivity}{FWHM} = \frac{d\lambda_{resonance}/dn_d}{FWHM} \tag{1.2}$$

where the FWHM characterises the linewidth of the plamonic modes.

The FoM has been suggested to be a more general standard to evaluate the global sensing performance of a plasmonic sensor [5–8]. For instance, nanoparticles with bigger sizes usually tend to show higher refractive index sensitivities due to stronger near field and extinction efficiency [6]. However, that does not mean, that bigger nanoparticles are always better sensing structures than smaller particles. Figure 1.1 shows the simulated extinction spectra for Au disc arrays with a periodicity of 350 nm, while the diameters of the Au discs vary from 80 nm to 320 nm. The extinction of Au disc arrays increases as a function of increasing disc diameter. Whereas, the line width of the dipolar plasmonic modes also increases dramatically with increasing diameter due to the radiation retardation and the multipolar plasmonic modes excitation. As a result, the FoM and thereby the sensing resolution will decrease as a function of increasing disc diameter, attributed to the expanding of the line width.

Sensors possessing high sensitivity and FoM have been developed based on many kinds
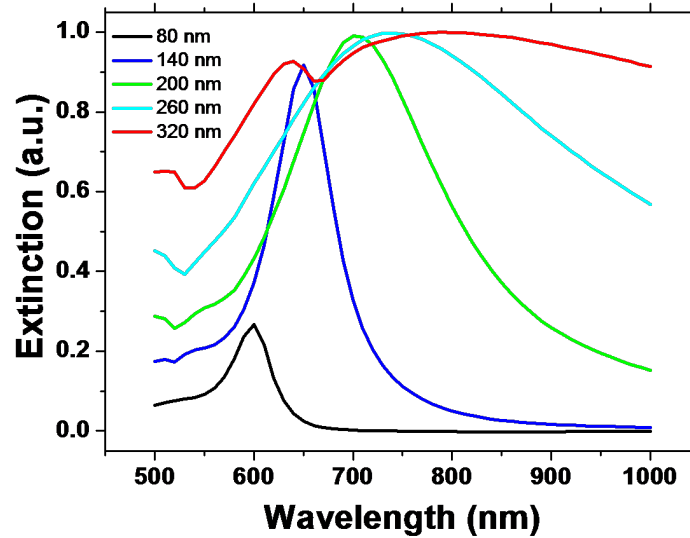
Figure 1.1: Simulation of extinction spectra for disc arrays with different diameters

of plasmonic structures [9–11]. A variety of nanostructure substrates, which can support either LSPPs or SPPs, have been widely investigated as refractive index sensors. In the following sections, a state of the art for SPP refractive index (RI) sensors and LSPP RI sensors is presented.

1.1.1.2   SPP sensors

The first SPP biosensor was presented in 1983 by Liedberg [12]. SPP biosensors have become a popular research subject since then. Till today, SPP sensing has become a well established method in immuno-assay biosensing, DNA hybridization biosensing, label free biosensing and others [5]. SPP sensor products with excellent performance have been available commercially [13, 14].

SPP sensors can be characterized in three categories based on the different excitation mechanisms of the plasmon polaritons : prism based SPP sensors, grating based SPP sensors and waveguide coupled SPP sensors. The excitation of SPPs demands that the wave vector mismatch between the illumination light and plasmonic wave on the propagating direction be overcome. The basics of these methods are shown in the following. A more detailed treatment can be found in the next chapter.

* **Prism based SPP sensor**

Using a prism to excite surface plasmon polaritons on the surface of a metal film

is the most straight-forward and most popular method. The first SPP sensor ever proposed [12] is based on this coupling method.
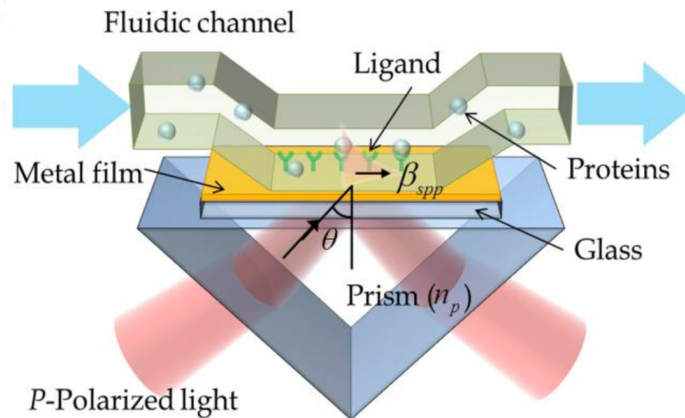
Figure 1.2: Schematic of a SPP sensor based on prism coupling [15]

Figure 1.2 shows a schematic for a biochemical SPP sensor based on the so-called Kretschmann configuration. It consists of a glass prism with a metallic thin film evaporated on its surface. The light is coupled into plasmon waves on one side of the thin metal film, when the film is illuminated through the prism with high refractive index from its backside. A microfludic channel is combined with the compact SPP sensing unit to provide a precise control and manipulation of fluids. The metal surface is functionalized with recognition molecules, such as antibodies, single strand DNA etc. Another important advantage of a SPP sensor based on a prism is that it can be easily combined with any type of sensing modulation where the resonance wavelength shift, or resonance angle or intensity is measured. A detection of RI changes of 5×10^{-6} RIU [16] and the detection of short oligonucleotides (23-mers) at concentrations as low as 100 pM [17] by intensity modulations have been shown. RI resolutions of 5×10^{-7}, 2×10^{-7}, 5.5×10^{-8} were reported for resonant angle modulated [18], resonant wavelength shift modulated [19] and phase modulated SPP sensors [20], respectively.

* **Grating based SPP sensor**

In the grating coupled configuration, the wave vector of the illumination light is increased by diffraction of a grating (m·2π/P), where P is the grating constant and m is the diffraction order. The grating can be fabricated directly on the metal film by lithographic methods. Grating coupled systems are not as widely used as prism coupling, however, they are more compatible to mass production and it is easier to miniaturize the size of the sensing unit. This makes grating-couplers an attractive approach for the fabrication of low-cost and compact SPP sensing structures [21].
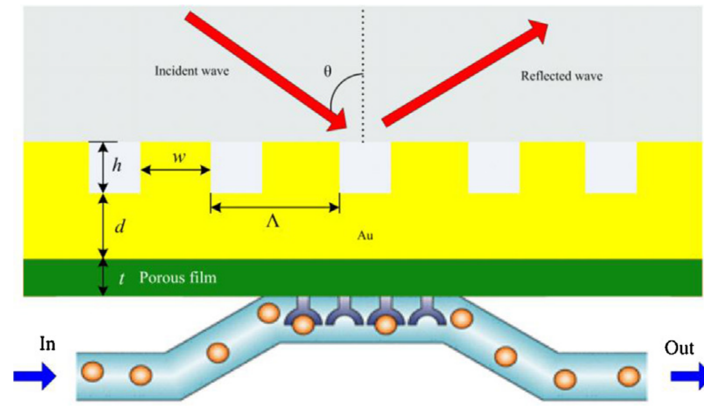
Figure 1.3: Schematics of a SPP sensor based on grating coupling [21]

Figure 1.3 shows a schematic diagram of a SPP biosensor based on grating excitation. In this method, the metallic film has one smooth surface while the other surface is tailored into a metallic grating. As mentioned above, the smooth side of the thin metal film is treated with recognition molecules to achieve high selectivity and combined with a microfludic channel. When light is incident on the metallic grating, it will obtain a diffraction momentum, and the wave vector of free light is increased to match that of the plasmonic waves. In this biomedical sensor, both wavelength and angular sensitivity were studied, and the detection sensitivities are estimated to be 700 nm/RIU and 509°/RIU in wavelength and angle sensing modulation [21].

* **Waveguide coupled SPP sensor**

In the waveguide coupling configuration, the coupling mechanism is similar to prism coupling. In this case, the metallic film is in direct contact with a photonic waveguide. The wave vector matching condition is fulfilled by total internal reflection of guided modes at the waveguide/metallic film interfaces. Among all the waveguide coupled SPP biosensors, sensing schemes combined with planar waveguides and optical fibers are the most popular and widely used. With the prism being replaced by a waveguide, SPP sensors can be fabricated to be more compact, user-friendly and readily integrated with any commercialized optical elements.

Figure 1.4 (a) shows the schematics for two of the most studied SPP sensors based on optical fibers. The upper structure in Figure 1.4 (a) is fabricated by deposition of a metal layer onto the waist of a biconical tapered multimode fiber. Although this tapered optical fiber showed high sensing sensitivity, the tapered fiber waist is very small, making this sensor configuration not robust and difficult to fabricate. Alternatively, the lower configuration in Figure 1.4 (a) is proposed. One side of an optical fiber is polished to expose the core, followed by the deposition of a uniform
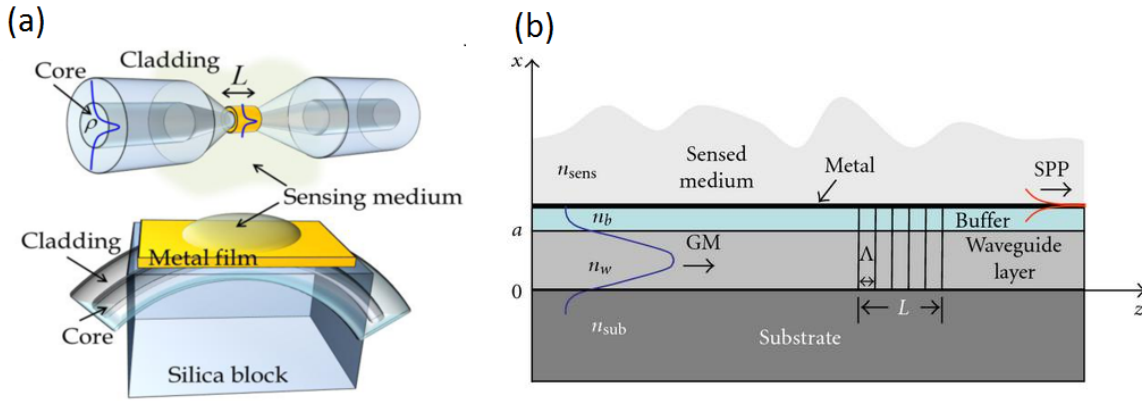
Figure 1.4: SPP biochemical sensors based on waveguide coupling. (a) SPP sensor based on planar waveguide coupling [22]. (b) Side-polished polariton fiber sensor [15].

metal film on the fiber waist. The strong evanescent wave of the optical modes will excite SPP waves on the gold surface, which can examine the surrounding medium. A theoretical sensitivity of 2300 nm/RIU has been estimated [23].

Figure 1.4 (b) presents a planar waveguide coupled SPP biosensor with a long period grating (LPG) imprinted in the waveguide layer [22]. The imprinted (LPG) grating SPP sensor shows higher sensitivity than a short period grating (SPG) SPP sensor. LPG is applied as a method to address the low sensitivity issue for a Bragg grating SPP sensor, in which the detected signal is a hybrid SPP mode, mainly the guided mode and slightly weighted by the excited surface plasmon polaritons. With the presence of a long period grating, the guided wave will excite a SPP wave propagating in the same direction. The transmitted guided mode through the grating is then applied in the sensing interrogation process. This waveguide coupled SPP sensor is modulated by the resonant wavelength shift according to the RI change in the surrounding material and a sensitivity of 1100 nm/RIU is estimated.

1.1.1.3   LSPR sensors

The dependence of the LSP resonance (LSPR) wavelength as a function of the dielectric constant of the surrounding medium, can be analytically studied using the frequency-dependent dielectric permittivity from the Drude model of metals $\Re(\varepsilon_m) = 1 - \frac{\omega_p^2}{\omega^2 + \gamma^2}$ and the resonance condition for a nanosphere $\Re(\varepsilon_m) = -2\varepsilon_d$, where ε_m, ε_d are the dielectric constants for metal and dielectric surrounding, ω_p means the plasma frequency and γ means the damping parameter of the bulk metal.

Converting from dielectric constant to refractive index, we get a condition for the

resonance wavelength [11]

$$\lambda_{resonance} = \lambda_p \sqrt{2n_d^2 + 1} \tag{1.3}$$

where λ_p is the wavelength corresponding to the bulk plasma frequency. From equation 1.3, one can easily draw the conclusion that the localized plasmon resonance position red shifts as the surrounding refractive index increases.

* **Colloid based LSPR sensors** Without any demands for sophisticated nano-fabrication equipments and the expertise to operate them, colloid nanostructures are the simplest and most accessible in the laboratory. They can be fabricated with different shapes, sizes and materials, using a variety of well-developed chemical synthesis methods, as shown in figure 1.5 [24, 25]. Many works have been
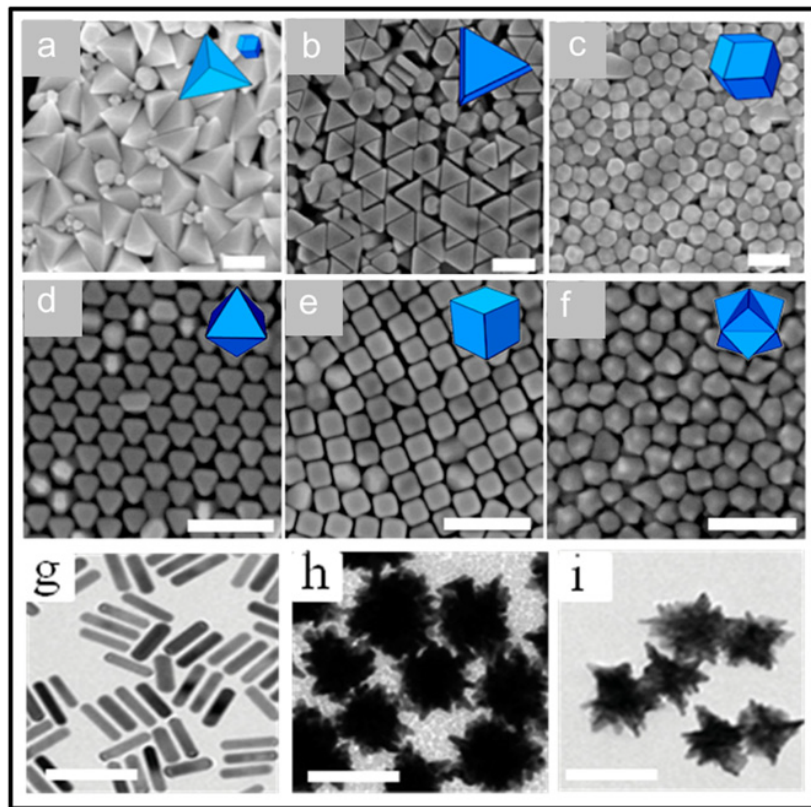
Figure 1.5: (a)-(i) Transmission electron microscopy (TEM) images of nanostructures with different geometries. Scale bars: 200nm. [24]

dedicated to applying different colloids for plasmonic sensors and to study the factors affecting their RI sensitivities.

In Ref. [6], the sensitivities of spherical particles with radii of 40 nm, 30 nm and 15 nm were investigated. The LSPR sensor is fabricated by depositing colloids on a glass chip, which is then integrated with a microfluidic chamber. Sensitivities of 49.1 nm/RIU, 57.8 nm/RIU and 90.0 nm/RIU were achieved for 15 nm, 30 nm

and 40 nm nanoparticles, respectively. This shows that the bulk RI sensitivity of LSPR sensors increases with the size of the used nanoparticles.

The influence of the aspect ratio, meaning the ratio of the length to the width of a nanorod, on the RI sensitivity is also studied by many groups [25, 26]. It was demonstrated that for nanorods with fixed radius, the RI sensitivity increases from 157 to 497 nm/RIU, when the aspect ratio increases from 1.0 to 3.4. As before, for nanorods with fixed aspect ratio while varying sizes, the nanorods with bigger sizes show higher sensitivity.

It has also been shown that the shape of nanostructures plays a dramatic role for the RI sensitivity [27]. For nanostructures with the same volume but different shapes, single silver nanotriangles were proved to have a much higher sensitivity than spheres [28]. In [11], Mayer et al. summarized the refractive index sensitivities of different gold and silver nanostructures, such as spheres, core/shell structures, rods, stars, pyramids, bipyramids, cubes etc. It is a general rule that nanostructures with more sharp edges and sharp tips, such as nano triangles and nano pyramids, show especially high RI sensitivities and the sensitivity increases with increasing resonance wavelength. A sensitivity as high as 801 nm/RIU was achieved with nanorice, a bipyramid structure with two sharp tips [11].

* **LSPR sensor based on patterned structure** In chemical synthesis, the desired nanostructures are always accompanied with by-products of undesired shapes and sizes. And even though the colloids are treated with stabilizing agents, aggregation between nanoparticles cannot be completely prevented. As a result, the ultra high sensitivity of LSPR sensors based on colloids is at the expense of homogeneity and reproducibility. Apart from colloids, another class of LSPR substrate is fabricated on glass or silicon substrates by patterning techniques such as electron beam lithography [29, 30], focused ion beam milling [31] and nanosphere lithography [32, 33], or nanoimprint lithography [34]. The advantages are a high controllability of the shape and order of the structures and therefore their plasmonic properties.
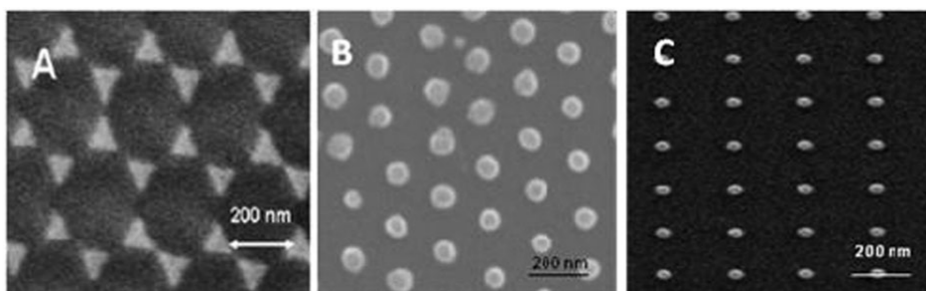
Figure 1.6: SEM images of different nanostructures fabricated by patterning techniques [35]

1.1.1.4 MIM sensors

In this section, plasmonic sensors based on metal-insulator-metal (MIM) structures are presented. Significant improvement in patterned nano fabrication methods and nanoparticle synthesis technology have made it possible to deliberately design the sizes and shapes of simple nanostructures and readily manipulate the precise location and distances to each other [15]. When metallic nanostructures are closely spaced, with a gap of a few nanometers, the near-fields of surface plasmonic modes from different nanostructures can strongly interact with each other. As a result, a huge electromagnetic (EM) field is confined in the gap, which is also referred to as 'hot spot'. The idea
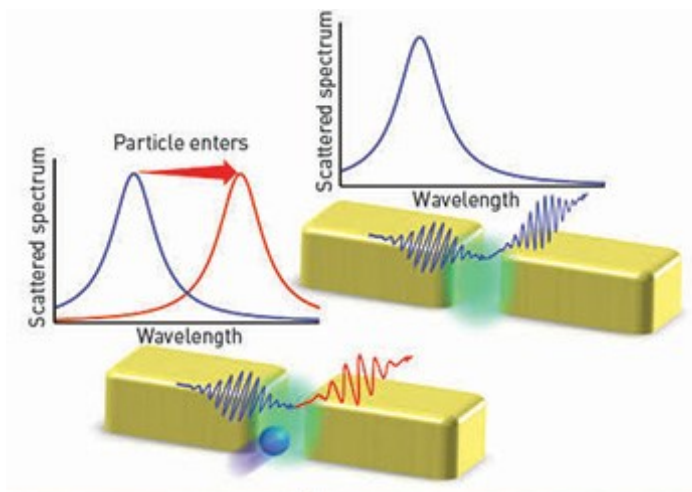
Figure 1.7: Schematic of the principle of RI sensing using a MIM structure [36]

of using a coupled nanostructure for refractive index sensing is shown in Figure 1.7. When the refractive index in the plasmonic 'hot spots' is modified, a notable red-shift will be detected in the optical spectra.

The resonance wavelength and field intensity of the gap mode is strongly dependent on the gap distance. Strong field intensity and confinement was observed for distances smaller than 50 nm [37]. The confined EM field of the gap mode gets stronger as a function of decreasing spacing distance. Whereas, a bigger gap distance is more appealing for the accessibility of detecting molecules in the gap. The fabrication resolution also sets a limit to the smallest gap possible with precise control and high reproducibility. Figure 1.8 shows ordered MIM nanostructures with controllable small separations fabricated by different methods that have been used for LSPR sensing. Figure 1.8 (a) shows a schematic of a plasmonic gas sensor [38]. The structure was fabricated by a dual exposure method with high resolution electron beam lithography. It is demonstrated that the plasmonic resonance of the gold triangle can not be changed by hydrogen and a single palladium disc only shows noisy and unstructured spectra under different hydrogen pressure. However, the MIM sensor, consisting of a
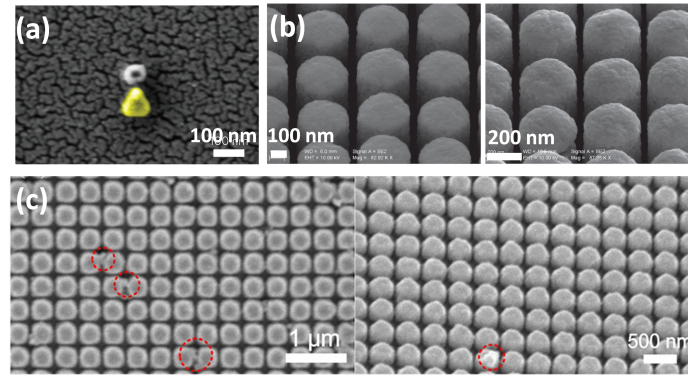
Figure 1.8: Ordered MIM structures with small separations fabricated by (a) dual exposure [38]; (b) E-beam lithography and electroplating [39]; (c) interference lithography followed by ion beam milling [40]

palladium disc and gold triangle, shows a 5 nm red shift for a 1% concentration change of hydrogen, and a 9 nm red shift for a 2% concentration change.

The SEM images in Figure 1.8 (b) show ultra tall gold nanopillars which had a height of 2 μm, and gaps of 60 nm and 30 nm, respectively. When the sample is illuminated by normal incident light, different orders of longitudinal localized surface modes will be excited along the nanopillar sidewall, featuring standing wave characteristics [39]. As the nanopillars are closely spaced, strong coupling will take place between the longitudinal LSPR modes excited on adjacent nanopillars, resulting in strong 'hot spots' localized in the gap. A sensitivity of 970 nm/RIU was achieved with a nanopillar array with a height of 2.62 μm, gaps of 117 nm and a period of 400 nm.

Figure 1.8 (c) shows ordered MIM silver structures obtained by interference lithography and ion beam milling [40]. Compared to other pattering methods, this fabrication method has the advantage of fast and large scale fabrication, and the profiles can be easily tuned by varying the exposure condition and milling condition. In 1.8 (c), the average gap distance is approximately 10 nm. This structure has not been investigated as a plasmonic sensor yet. However, with the strong 'hot spot' in the ultrasmall gap and the Fano-shaped absorption spectra [40], this structure possesses the key advantages for LSPR sensors.

1.1.2   Surface enhanced Raman scattering sensor

Raman scattering is an inelastic scattering process, which delivers spectra with features that are specific to the investigated molecule. The Raman interaction leads to two possible outcomes: the material absorbs energy and the scattered photon has a lower energy than the absorbed photon, this outcome is termed Stokes Raman scattering.

The other outcome is that the material loses energy and the emitted photon has a higher energy than that of the absorbed photon, this process is called anti-Stokes Raman scattering. Raman spectroscopy has been widely rated as a very powerful analytical method for chemical and biomedical applications thanks to many advantages [1, 4].

* **'Fingerprint signature' of molecules** : Very well defined Raman peaks show unique chemical and structural information about the detected molecules, providing ultrahigh detecting selectivity. The sample preparation, in the case of complicated detecting environments, is significantly simplified because the analytes can be accurately identified among a complex environment.

* **No interference from water** : Whereas water acts as a poor solvent for infrared absorption study, water shows no pronounced Raman signal, making water an ideal solvent for Raman sensing.

* **High sensitivity** : Single molecule sensitivity has been achieved with enhanced Raman measurements.

* **High spatial resolution** : The spatial resolution is mainly determined by the laser wavelength and the microscopic objective being used. The theoretical diffraction limited spatial resolution is defined by $0.61\lambda/NA$, where λ is the laser wavelength and NA is the numerical aperture of the objective. Tip enhanced Raman can provide even higher spatial resolution by a well defined metal tip with a small radius [41].

Despite all the advantages stated above, the intensity of Raman scattering however is very low compared to the intensity of elastic scattering [4]. Only a small fraction of the scattered photons, approximately 1 in 10 million, contributes to the Raman signal in the spectrum [42]. Therefore, many attempts for enhancing the signal have been pursued. A very common way is to make use of the strong near fields in the vicinity of plasmonic nanoparticles, know as surface enhanced Raman scattering (SERS).

1.1.2.1 Enhancement factor of SERS substrate

The enhancement factor (EF) is the most crucial aspect of a SERS substrate. It is widely accepted that there are two enhancing mechanisms contributing to the enhancement factor: Electromagnetic enhancement and chemical enhancement. The EM enhancement mechanism is believed to be the dominant enhancing effect, because it contributes to the EF by amplifying local fields in plasmonic nanostructures, with typical enhancement factors lying between 10^4 and 10^8 [4]. Whereas, the chemical enhancement yields a significantly smaller enhancement from 10 to 100, through introducing

charge transfer between the plasmonic nanostructures and the adsorbed nanostructures [9, 43].
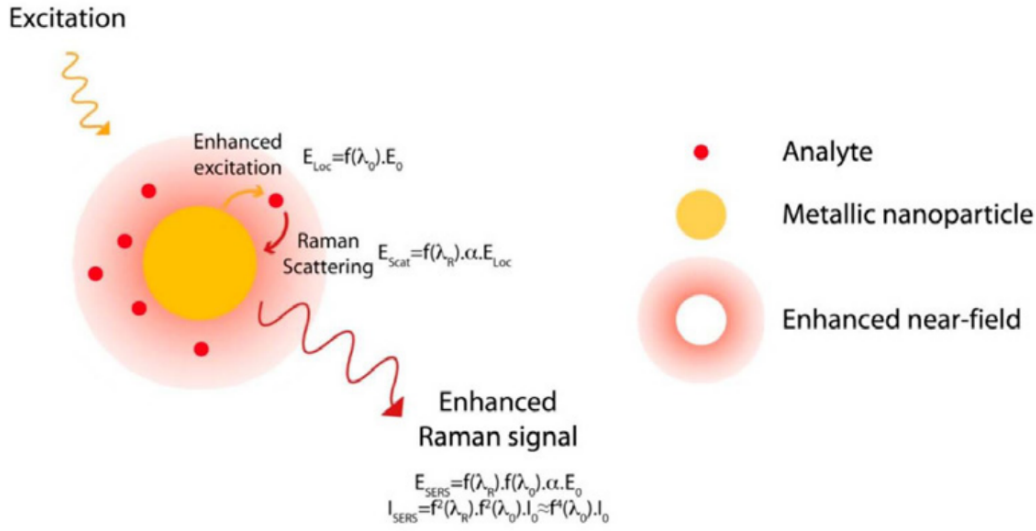
Figure 1.9: Schematic of the EM enhancement mechanism [44]

EM enhancement includes the enhancement of the excitation field and the enhancement of the Raman scattering cross-section [4, 8, 45], as shown in Figure 1.9. The strong near field of a plasmonic resonance at the vicinity of a metal surface, initially enhances the excitation electric field, with an enhancement of $\tilde{E}_{Loc}(\omega_L) = E_{Loc}(\omega_L)/E_{Inc}(\omega_L)$. This is subsequently followed by the enhancement of the Raman scattering, with an enhancement of $\tilde{E}_{Loc}(\omega_R) = E_{Loc}(\omega_R)/E_{Inc}(\omega_R)$. Thus, the SERS enhancement factor can be calculated as

$$
\begin{aligned}
EF &= |\frac{E_{Loc}(\omega_L)}{E_{Inc}(\omega_L)}|^2 \times |\frac{E_{Loc}(\omega_R)}{E_{Inc}(\omega_R)}|^2 \\
&= |\tilde{E}_{Loc}(\omega_L)|^2 \times |\tilde{E}_{Loc}(\omega_R)|^2
\end{aligned}
\tag{1.4}
$$

Where, $E_{Loc}(\omega_L)$ and $E_{Loc}(\omega_R)$ represent the enhanced local electric field strength at the laser wavelength and the Raman scattering wavelength, respectively, while $E_{Inc}(\omega_L)$ and $E_{Inc}(\omega_R)$ mean the incident E field strength at the laser and the Raman wavelength. $\tilde{E}_{Loc}(\omega_L)$ and $\tilde{E}_{Loc}(\omega_R)$ are the enhancement of the excitation and emission field, respectively. Owing to the fact that Stokes shifts are usually small compared to the band width of plasmonic modes, one can make a simple estimation of the SERS EF by assuming that the enhancement of the radiative Stokes field is the same as the enhancement of the exciting field [42]. Thus EFs of $|\tilde{E}|^4$ can be derived from formula 1.4.

$$
EF \approx |\tilde{E}_{Loc}|^4
\tag{1.5}
$$

Where $\tilde{E}_{Loc}$ is the local field enhancement of the field of incidence at the Raman active

site.

1.1.2.2   SERS sensing

The emerging nanofabrication techniques and synthesis methods, together with a better understanding of the signal enhancement mechanism [46, 47], have fuelled the research on plasmonically enhanced spectroscopy, such as SERS [48–53], surface-enhanced infrared absorption spectroscopy (SEIRAS) [54–56], surface enhanced fluorescence (SEF) [57, 58] and tip enhanced Raman scattering (TERS) [59, 60]. Various plasmonic structures have been studied for SERS enhancement capabilities.

* **Single molecule Surface Enhanced Raman Spectroscopy (SMSERS)** : SERS substrates with EFs high enough to detect single molecules have been developed [61–64]. Lim et al. functionalized DNA molecules on Au nanoparticles to create well defined nano bridge nanogaps, as shown in Figure 1.10. The engineered nanogap between the Au core and the Au shell can be occupied by quantifiable Raman molecules. A linear dependence of the SERS signal intensity on the molecule concentration has been found, with a limit of detection down to 10 fM concentration. Single particle Raman mapping analysis manifested that most of the Au nanoparticle aggregations show EFs between 1×10^8 and 1.5×10^9, which is enough for single molecule studies [62]. Despite the ultra high sensitivity these SMSERS substrates can provide, their fabrication requires sophisticated biochemistry functionalization of the gold nanostructures, as well the Raman dyes. These substrates can be a powerful tool for molecular study, however, not a proper tool for sensing and monitoring as it demands the analyte to be modified by DNA strands first.

* **Metallic islands** : Thin films of nobel metals, with a thickness of ~ 5 nm, have been proved to be an easily fabricated SERS substrate with excellent EFs [65, 66]. A thermally evaporated ~ 5 nm metallic film is not a continuous film, but consists of island-like structures which are separated by nanogaps. There are works focused on investigating the enhancement mechanism of these metallic island films [65, 67, 68]. It is believed that 'hot spots' can be excited in the nanogaps between nano islands, and these 'hot spots' feature stronger local near fields when the neighbouring islands are nearly touching, allowing for maximum near field coupling. Figure 1.11 (a) and (b) show the simulated field distribution, local field enhancement and a $|\tilde{E}_{Loc}|^4$ approximation SERS EF for a semicontinuous Ag island film. The enhancement of such a film varies significantly from spots to spots, even though an EF of 3×10^6 can be achieved locally. To address this
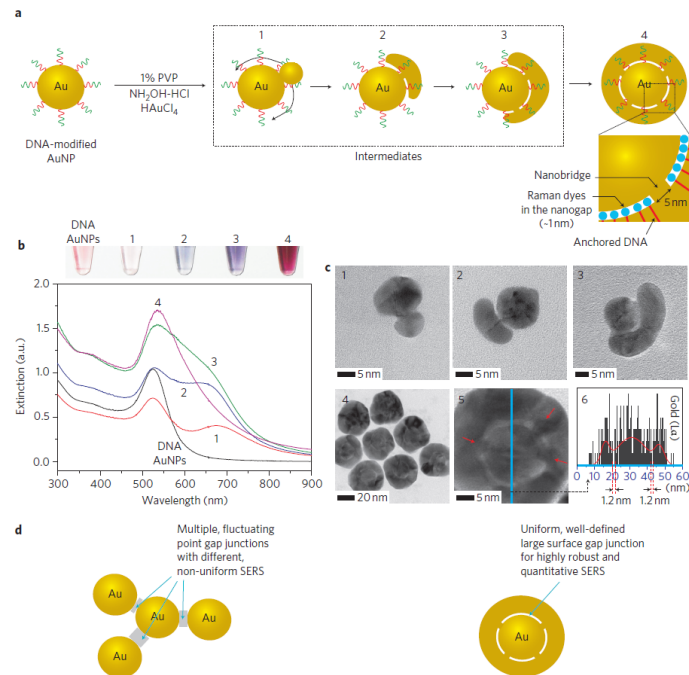
Figure 1.10: Surface DNA-mediated synthesis and characterization of DNA-anchored nanobridged nanogap particles, adapted from [62]
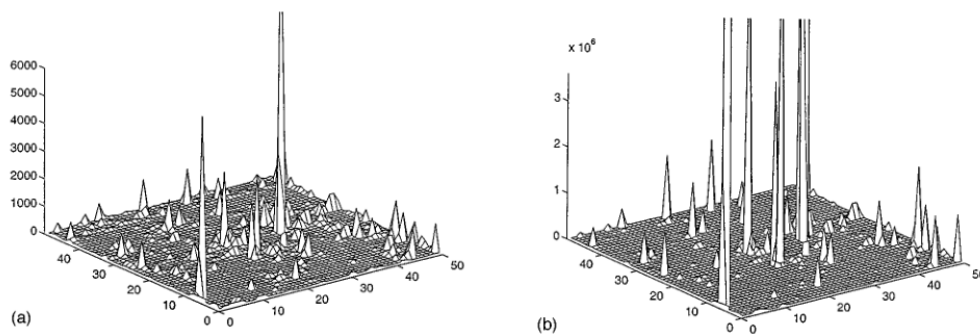
Figure 1.11: The electric field intensities on a silver semicontinuous film at the percolation threshold, for the wavelength 0.5 μm; (a) $I_2(r) = |E(r)|^2$ and (b)$I_4(r) = |E(r)|^4$, adapted from [67]

issue, some groups have applied thermal annealing to these island film structures [69, 70]. After annealing, the islands of the film become spherical and grow in height, which allows for a comparatively sharper LSPR peak and more uniform EF. However, the enhancement factors of metallic island films vary from film to film depending on the quality of the glass substrate, glass pretreatment, film deposition rate, deposition temperature, deposition geometry, and postdeposition annealing [71]. Despite the impressive average EFs of metallic island films, the high EF cannot be effectively reproduced on a nanometric scale.

* **Lithographically fabricated SERS substrate** : Lithographically fabricated nanostructures are good candidates to be applied as SERS substrates, in terms of reproducibility of the signal and tunability. Optical responses of lithographic substrates can be readily tuned by the nanostructure size, shape and array period, over the whole range of the vis-NIR spectral window to detect molecular analytes [72]. Dependences of SERS EFs of EBL samples, on the structure sizes, edge
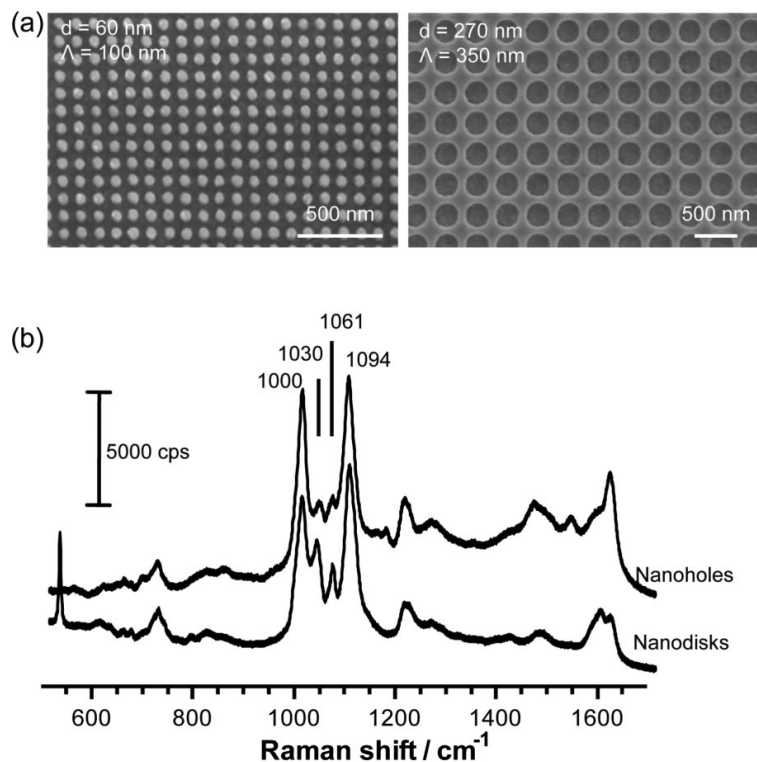
Figure 1.12: (a) SEM images of nanodisc array and nanohole array fabricated by EBL; (b) SERS spectra for 4-mercaptopyridine (4-MP) adsorbed on the nanodisc and nanohole arrays [73]

to edge distances, shapes and array periods have been studied [73–75]. Yu et al. studied the SERS EF of nanodisc arrays and nanohole arrays with different geometrical parameters. The nanohole array with a diameter of 370 nm, a grating constant of 500 nm and a hole depth of 550 nm, shows the highest EF of 4.2×10^5,

which is two orders of magnitude higher than the highest EF of 1.3×10^3 obtained with nanodisc arrays. Figure 1.12 shows similar SERS signal obtained from nanodisc and nanohole arrays. The gold nanoholes have a diameter of 270 nm and an edge to edge distance of 80 nm, while the discs have a diameter of 40 nm and an edge to edge distance of 60 nm [73].

* **Film on nanoparticles (FON)** : SERS substrates such as gold disc arrays and nano holes on gold film, fabricated by EBL, have been investigated for their Raman enhancement capability [73]. For substrates fabricated by the sophisticated EBL technique, reproducibility and stability of the SERS EF is less of a problem. While EBL is a sophisticated and time-consuming technique, the EF of an EBL substrate is usually not comparable to that of a metallic islands film. As a compromise for reproducible SERS signal and high EF, films on nanoparticles (FON) have been widely investigated as SERS substrates [76, 77]. Figure 1.13 shows
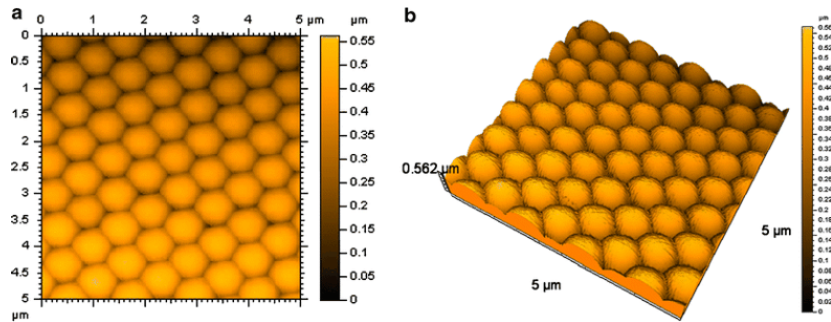
Figure 1.13: The (a) 2D and (b) 3D AFM images of an AgFON structure fabricated by using polystyrene nanospheres with a diameter of 820 nm, adapted from [77]

the images of an AgFON fabricated by depositing a 120 nm thick silver film on the top of drop-coated polystyrene nanospheres. Lin et al. studied the SERS EF of AgFONs as a function of the nanosphere size, and an optimal enhancement factor of 4.3×10^6 was obtained.

1.1.3   Vertical MIM structure based applications

In the last sections, an overview over the state of the art for plasmonic based RI sensors and SERS substrates has been presented. MIM structures show great potential in these plasmonic applications due to stronger field confinement and enhancement compared to monomer plasmonic structures. The strong near field interaction of plasmonic modes in MIM structures, results in strong modification of the emission properties. In coupled MIM structures, many advantageous phenomena such as Fano-shaped resonances, plasmonic induced transparency, super absorbers and other material properties

of metamaterials occur [78]. Vertical MIM structures have been widely investigated because it is comparatively easy to fabricate them in the laboratory.

Vertical MIM structures have been exploited in applications such as color plasmonic pixels [79–81], photovoltaics [82–84], narrow-band perfect absorbers [85], enhancing the spontaneous emission rate of quantum dots (QD) [86], enhanced infrared absorption [87] and others. Among all the other applications, plasmonic sensing [88–93] and surface enhanced physics including SERS [94, 95], are two of the hottest topics.
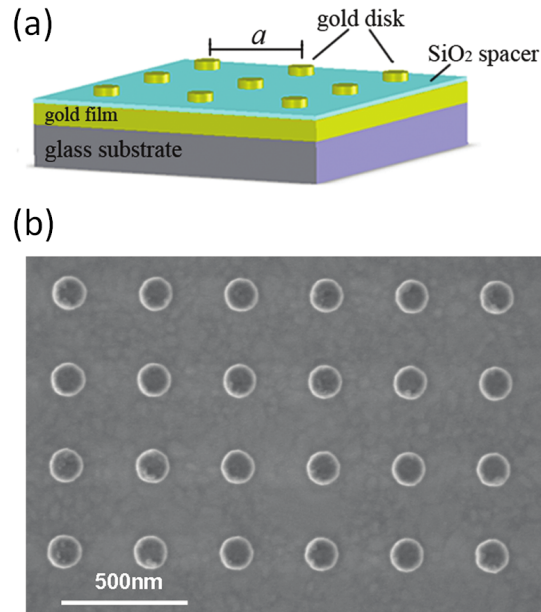
Figure 1.14: (a) Schematic and (b) SEM image of disc array on film used as SERS substrate [94]

In Ref. [91], the coupling of LSPR and SPP modes in ordered nanoparticle arrays on gold film MIM structures was studied. They consist of an array of nanostructures which is prepared on top of a gold film separated by a dielectric spacer. A localized mode with hot spots on the top was applied for RI sensing. A sensitivity of 192 nm/RIU and a FoM of 3.76 was achieved for the discs on film MIM structure with disc diameters of 170 nm. In Ref. [90], a vertical MIM structure, consisting of a Au discs stack separated by an insulator disc with the same diameter, was studied. Three plasmonic modes were identified through extinction spectra: a symmetric mode, an antisymmetric mode and a surface lattice mode. The symmetric mode shows a field distribution similar to the case of single discs with a strong EM field at the bottom edges. The antisymmetric mode features 'hot spots' located in the dielectric spacer and just outside the spacer. The surface lattice mode was observed at the grating orders. Sensing capabilities were investigated for different plasmonic modes in the cases of bulk RI sensing and molecule sensing. RI sensitivities of 326 nm/RIU and 248 nm/RIU were achieved for the antisymmetric LSPR mode and surface lattice resonance mode, with

FoMs of 8.6 and 4, respectively, in a bulk sensing situation. On the contrary, in the case of molecular sensing, the antisymmetric LSPR mode showed better performance than the SLR, and a limit of detection of 6 nmol/L was obtained for testosterone-antibody sensing.

In other works, Chu et al. used the same vertical MIM structure, see Figure 1.14, as in our study [91]. In this study double resonances were used, which were created by coupling of SPP modes with localized cavity modes, to enhance the excitation and emission of Raman scattering at the same time. The SERS EF of the vertical MIM structure was two orders of magnitude higher than that of a gold disc array on a glass substrate. Furthermore, the MIM structures with optimal grating periods provide a significantly larger SERS EF than MIM structures with non-optimal periods, even if the structures are more dense.
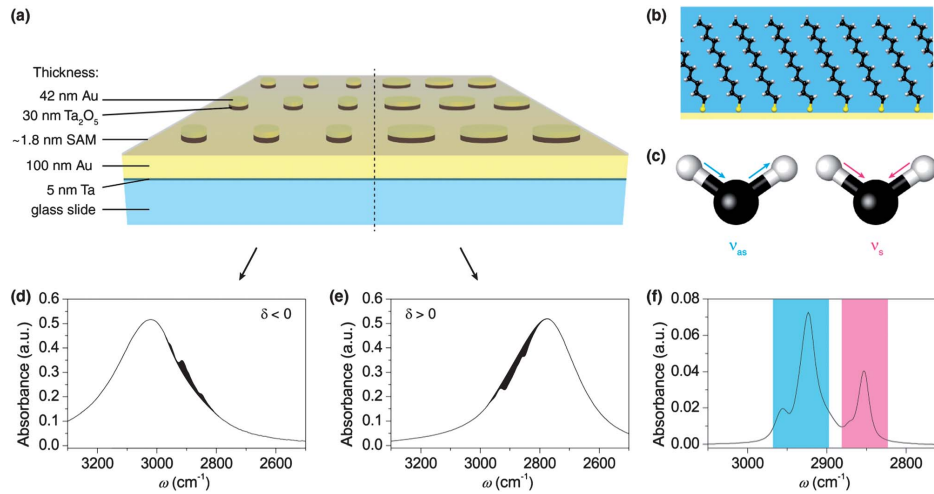
Figure 1.15: Vertical MIM structures used for enhanced infrared absorption [87]

A MIM structure as in Figure 1.15 has been applied by Srajer et al. for enhanced infrared absorption [87]. Instead of a continuous insulator film spacer, they sandwiched an insulator disc in between patterned metallic nanostructures and film. The insulator disc has the same size as the gold disc arrays. It has been demonstrated in experiments that the MIM structure enhanced the absorption signal of the molecules by a factor of $\sim 2.2 \times 10^6$, while preserving the characteristic molecular absorption line shape well.

1.1.4   Exposing the 'hot spot' in vertical MIM structures

It is easy to imagine that when the thickness of the insulator spacer layer is less than 10 nm, the electromagnetic field is well confined and enhanced, in the cylindrical dielectric cavity sandwiched between the gold nanodisc and the gold film. In the works mentioned above, either a thin continuous dielectric film [91, 94] or an insulator disc with the same

size as the gold nanoparticles [87, 90] were evaporated as a spacer layer. This however means, that only a very small fraction of the enhanced field of the cavity modes is accessible to the surrounding environment, since most of the 'hot spot' is occupied by the dielectric spacer. By making this part of the near field accessible to detecting molecules or a changing surrounding medium, the performance of this ordered MIM substrate as plasmonic RI sensors, SERS substrates and other applications based on enhanced EM fields, can be considerably improved.
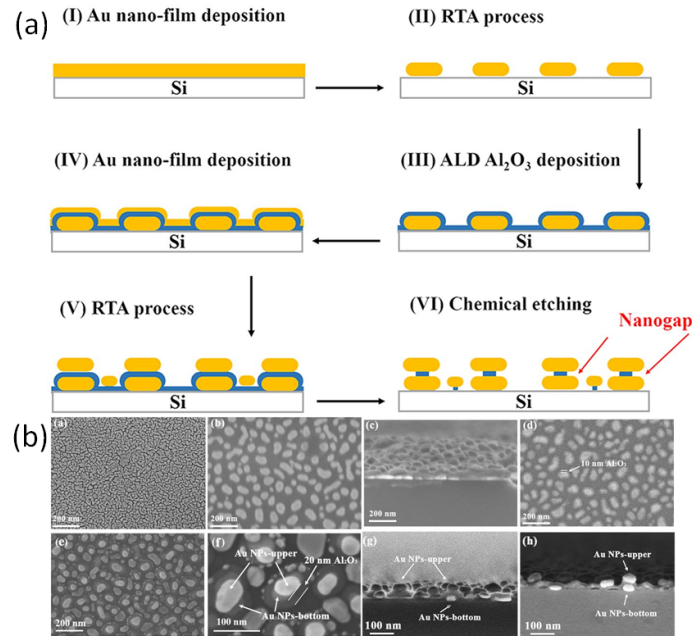
Figure 1.16: (a) One example for a fabrication process of a vertical MIM structure with exposed 'hot spots'; (b) SEM images of the fabricated structures in (a) [95]

Cao et al. developed a vertical MIM structure which consists of two gold nanoparticles separated by a sacrificial Al_2O_3 layer, with exposed 'hot spots' obtained by chemical etching [95]. As shown in Figure 1.16, the MIM structures were fabricated by rapid thermal annealing (RTA) of a thin Au film to obtain the first layer of gold nanoparticles, then a layer of Al_2O_3 layer was deposited by ALD to define the gap distances between Au nanoparticles. Then another thin layer of Au film was deposited by magnetron sputtering, followed by RTA to create the second layer of gold nanoparticles. Finally, 5% KOH was used to etch the sacrificial Al_2O_3 layer. A SERS EF over 10^7 for methylene blue was achieved in experiments. Furthermore, it was demonstrated that Au NPs/nanogap/Au NPs structures showed higher EFs with smaller gap distances. Finite-difference time-domain simulation (FDTD) results show that most of the enhanced EM field is localized inside the nanogap, and that the MIM structures provide a stronger EM field enhancement with smaller gap distances.

In [93], Manoj et al. developed a MIM structure with exposed 'hot spots', based on

the same structure configuration as in Ref [91, 94]. The MIM structure consists of a smooth gold film with a thickness of 30 nm, a sputtered SiO_2 layer with a thickness of 5 nm, and Au disc arrays with a thickness of 30 nm and diameters varying from 90 nm to 110 nm. To expose the hot spots of the plasmonic cavity modes, inductively coupled plasma (ICP) etching with CF_4 and O_2 gases was used to selectively etch the SiO_2 insulator layer.
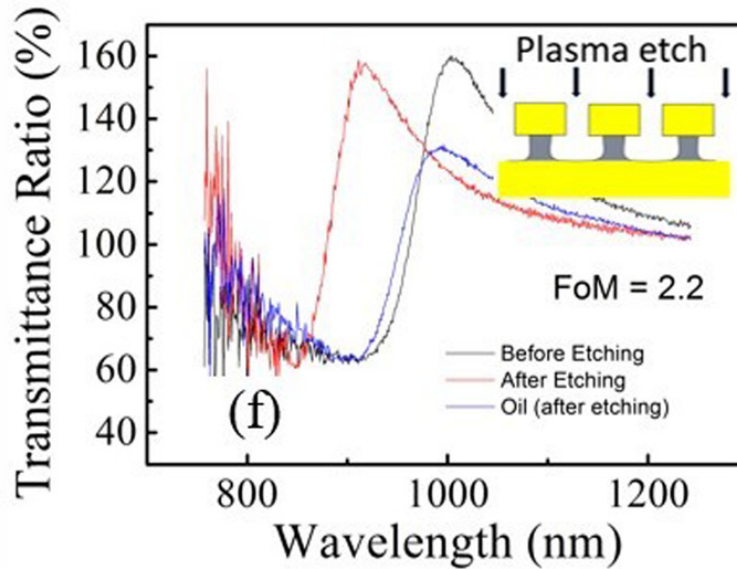
Figure 1.17: Vertical MIM structure with exposed 'hot spot' used for RI sensing [93]

The etched structures were applied in LSPR sensing, as shown in Figure 1.17. The plasmonic resonance blue shifted as the dielectric insulator layer got selectively etched. A FoM of 2.2 was achieved in sensing experiments with oil, this FoM is well improved compared to the FoM of 0.9 for vertical MIM structures without etching and of 0.6 for nanodisks on a glass substrate [93]. In this work, an interpretation of the Fano-shaped transmittance spectra was also presented. In agreement with [91], they believe the Fano shape arises from coupling of the narrow spectral plasmonic resonance to the continuum of the white light transmitted through the substrate.

1.2   Our Objectives

In the last sections, the research background of this thesis has been presented. From the state of the art, it comes with no surprise that MIM structures in general provide better performance in RI sensing and enhancing Raman signal than monomer nanostructures under the same conditions. Then applications based on vertical MIM structures, which are relatively easy to fabricate in the lab, were briefly reviewed. Driven by the intention

of improving the sensing capability, the necessity of exposing the hot spot in vertical MIM structures was concluded, followed by an introduction of recent works on this subject.

Although high sensitivity and SERS EFs have been achieved by vertical MIM structures with exposed 'hot spots', there are still some improvements to be made. In Ref. [95], the Au NPs were created by thermal annealing of a thin layer of Au film, giving little control over the generation of MIM structures. This can be seen in the SEM images in Figure 1.16. The high SERS EF is at the expense of reproducibility. In Ref. [93], the selective etching of the insulator started from a continuous SiO_2 film, which can be replaced by insulator discs, so that the undercut in the MIM structures can be introduced more effectively. As it is not easy to monitor how the geometry of the insulator layer is changing with the etching time, it is necessary to study the role of the insulator layer in the plasmonic properties of cavity MIM structures. Furthermore, as the 'hot spots' of cavity plasmon modes are exposed, it is a exciting topic to study their capability in SERS.

Our objective is to develop a plasmonic substrate which contains arrays and is reproducible, while providing strongly enhanced near fields and narrow linewidths of the plasmonic modes for well-performing plasmonic sensing applications. Different plasmonic modes, such as grating induced SPPs, LSPR modes at gold nanoparticles, and cavity modes in the insulator cavity will be identified in experiments and simulations. The influence of each building element of the MIM structure on the plasmonic properties, especially the geometry of the insulator layer, will be studied. A better understanding of the fundamental physics in cavity MIM structures will guide the way to an optimized sample geometry. An undercut will be created by wet etching of the spacer layer. The potential of this undercut MIM structure in RI sensing and SERS will be investigated.

1.2.1 Reproducible and accessible 'hot spot'

Many efforts have been dedicated to fabricate and profit from the 'hot spots' of lateral MIM structures [37, 39, 40]. The coupling strength of plasmonic modes strongly depends on the gap distance. The field confinement and enhancement increases dramatically as the gap distance decreases. For lateral MIM structures arrays, as shown in Figure 1.18, gaps are most commonly created by e-beam lithography (EBL), which means that gaps narrower than 10 nm are of poor reproducibility, limited by the resolution of the EBL technique. In contrast in the case of vertical MIM structures, the precise control of a gap down to a few nanometers is better controllable, because the
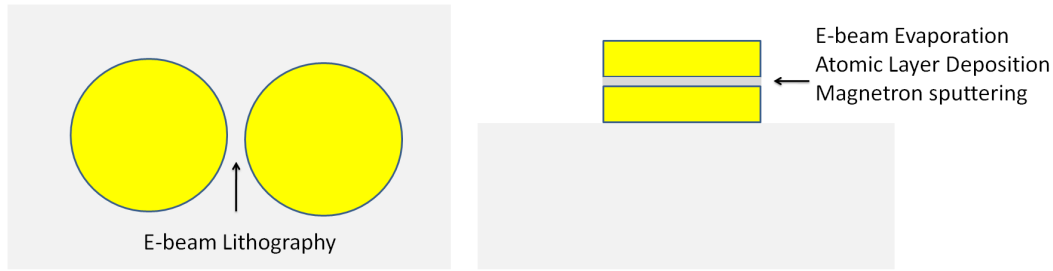
Figure 1.18: Schematic of lateral (left) dimer and vertical (right) dimer

gap in a vertical MIM structure is defined by thin layer deposition techniques, such as thermal/E-beam evaporation, sputtering or atomic layer deposition, as shown for a vertical dimer in Figure 1.18. A sub-nanometer gap can be achieved when an insulator layer with a thickness of less than a nanometer is sandwiched between two metal nanostructures by atomic layer deposition [96, 97]. Besides, reproducible realization of gaps larger than 5 nm can be achieved with sufficient thickness control by established techniques like evaporation and sputtering.

Apart from the advantage in gap control and reproducibility, vertical MIM structures are also a better configuration for fabricating heterodimers. Heterodimers are a way to gain more tunability of the plasmonic resonance by using different metals for two nanostructures. In the case of lateral heterodimers, a dual exposure method is usually used, which demands for high precision of alignment, sophisticated equipment and operation expertise. Whereas, vertical MIM structures can be easily achieved by using a different deposition source.

Finally, vertical MIM structures can exhibit larger mode volumes in the gap (a field map will be shown in chapter 4) than lateral MIMs, such as bowties. In addition, the spatial overlap of different plasmonic resonances can be high, which enables a Raman molecule residing at that location, to be enhanced simultaneously at the excitation and emission wavelengths of Raman scattering [94].

The ordered 'hot spots' in vertical MIM structures will be exposed to the sensing environment after well controlled wet etching in this thesis. The refractive index change in the 'hot spot' will dramatically change the resonant condition of the cavity plasmon modes, leading to strong resonance position shifts. This is shown in chapter 5. In the case of SERS applications, Raman molecules immobilized in the 'hot spot' of vertical MIM structures, will scatter a notably enhanced Raman signal according to formula 1.4. This will be shown in chapter 5 and chapter 7.

1.2.2   Fundamental physics in vertical MIM structures

In a vertical MIM structure, for instance, gold disc arrays on gold film separated by a thin insulator layer, a rich set of plasmonic modes of different natures can be excited. These include localized surface plasmon resonances (LSPRs) from gold nanoparticles, surface lattice modes arising from the far field interaction of the plasmonic radiation among neighboring nanoparticles, and surface plasmon polaritons (SPPs) on the two sides of the gold film excited by the gold disc arrays.

By varying the geometrical parameters or building materials of the MIM structures, the plasmonic modes can be tuned and interfere with each other, resulting in shifted resonance positions, Fano-shaped extinction profiles and further enhanced near field. Optimal MIM plasmonic applications can be designed in accordance to different illumination conditions and molecules to detect, based on a better understanding of how these different modes couple and hybridize with each other.

Amongst all the excited modes in MIM structures, cavity plasmon modes are the most interesting ones with highly confined and enhanced localized fields, sandwiched between gold nanostructures. It is necessary to systematically study these modes and their dependency on the dimensions of the MIM structures. This topic will be systematically studied in chapter 4.

Due to the fact that we want to introduce an undercut in the insulator layer and expose the 'hot spots' of the MIM structures, it is crucial to know how the near field would be modified when the insulator dimension is reduced.

1.2.3   Improvement of LSPR sensor performance

According to equation 1.2, the RI sensing capacity can be improved by reducing the linewidth or by increasing the RI sensitivity of plasmonic modes. As has already been stated previously and will be demonstrated in detail in this thesis, high RI sensitivity can be expected when a strongly enhanced local field is subject to the refractive index change of the surrounding media. Moreover, MIM structures provide a very uncomplicated way to be able obtain very narrow linewidths by confining plasmonic modes in a Fabry-Pérot (FP) cavity in the spacer.

Figure 1.19 shows the simulated extinction and reflection spectra for Au nanodisc arrays on a glass substrate and on a gold film separated by a SiO_2 insulator disc, the Au disc radius and insulator SiO_2 spacer radius are 40 nm for both sample configurations. The extinction spectra are evaluated taking the transmission through the Au film as
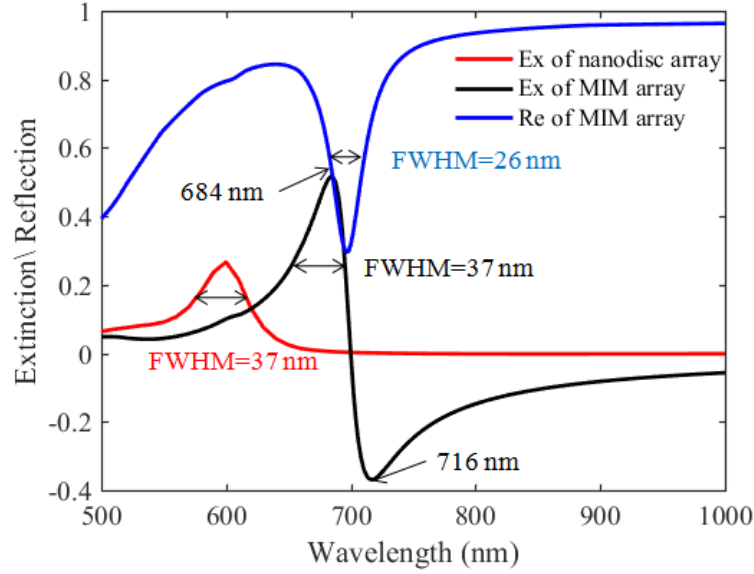
Figure 1.19: Simulated extinction and reflection spectra for Au nanodisc arrays on glass substrate and on gold film, separated by a SiO$_2$ insulator disc with a thickness of 10 nm, the disc radius is 40 nm in both cases. The extinction of the MIM structure is evaluated taking the transmission through a gold film as reference. The Fano shape and negative extinction will be explained in detail in section 4.6.

a reference. (That is why the negative extinction appears in extinction spectra, which will be explained in section 4.6.). The extinction of Au nanodisc arrays, red curve in Figure 1.19, shows an extinction peak with a line width of 37 nm and an extinction intensity of around 0.28, while in the case of the MIM structure, the extinction spectrum (black curve in Figure 1.19) provides a Fano line shape with a line width of 37 nm (estimated from the positive extinction part) and an extinction maximum of 0.52. The reflection spectrum (blue curve in Figure 1.19) shows a dip with a FWHM of 26 nm and a reflection loss of 0.71. The RI sensing resolution will be improved both by the narrower line width, and the higher signal/noise ratio obtained in the MIM structure compared to nanostructures on glass as well. Besides, instead of a Lorentz line shaped extinction as in the disc array on glass, the extinction spectrum for MIM structures shows a Fano line shape, with a steep decrease between 684 nm and 716 nm, and the extinction efficiency changes from 0.52 to -0.39. This feature of the Fano line shape can be advantageous for designing a highly sensitive intensity-modulated RI sensor by evaluating the intensity at a certain wavelength [98].

Another very important advantage of a MIM structure as RI sensing element is that its plasmonic modes can still show very narrow line widths even for large discs. Figure 1.20 shows the simulated diffuse reflection spectra (reflection from all reflected angles is collected instead of only one specific angle as in the case of specular reflection) for disc arrays on glass (red curve) and on thin Au film (blue curve). The disc diameter is 320

nm in both cases. For Au disc arrays on glass, the dipolar plasmonic mode is hardly
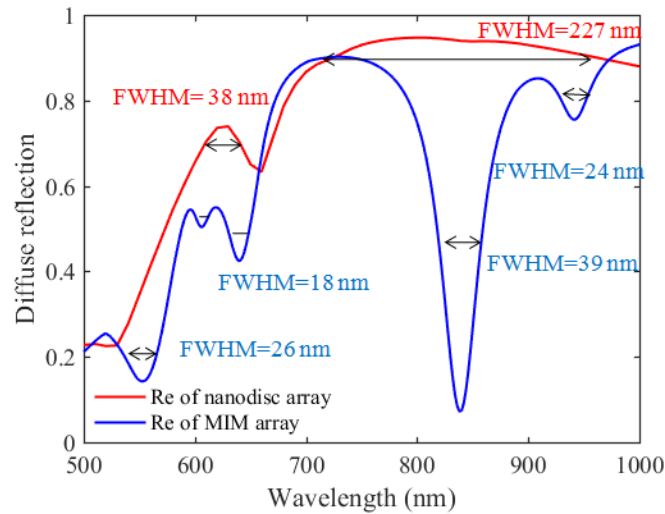
Figure 1.20: Simulated diffuse reflection spectra for Au nanodisc arrays on glass substrate, and on gold film separated by a SiO$_2$ insulator disc with a thickness of 10 nm, disc radius is 160 nm in both cases.

discernible due to multi mode excitations and retardation effects, with a FWHM of 227 nm. In the MIM structure, the plasmonic modes manifest themselves in reflection dips. In the reflection spectra for MIM structures, a series of well defined and distinct cavity plasmon modes can be found at 640 nm, 838 nm and 940 nm, with a line width of 18 nm, 39 nm and 24 nm, respectively, which show great improvement compared to 227 nm in Au disc arrays on glass.

The detailed study on the RI sensitivity of vertical MIM cavities will be presented in chapter 6. To conclude, MIM structures can improve the RI sensing capability in four ways :

- Higher sensitivity based on stronger near field [93].

- Narrower line width for better sensing resolution.

- More pronounced extinction bands and reflection dips provide higher signal/noise ratio for better sensing resolution.

- The Fano profile shows great potential for intensity modulated RI sensors.

1.2.4   Increasing the EF of SERS substrates

According to equation 1.5, the EF of SERS is proportional to the fourth power of the enhancement of the local near field strength. To engineer a nanostructure configuration

with the ability to provide stronger local field enhancement, is the most straightforward way to fabricate a SERS substrate with high EF. In Figure 1.21, the simulated modulus
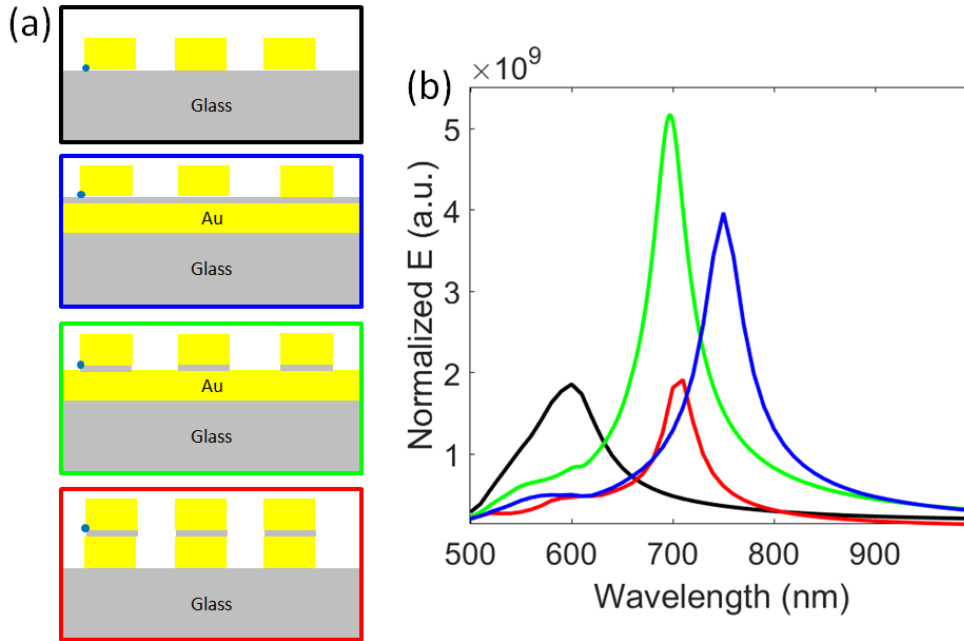
Figure 1.21: Simulated near-field intensity for different structure configurations.

of the E field ($|E| = \sqrt{E_x^2 + E_y^2 + E_z^2}$) is shown for different structures, excited under the same conditions. In Figure 1.21 (a), the dimensions for the Au discs and insulator thicknesses are fixed. The height of the Au discs and Au films are 50 nm, the spacer layer is 10 nm SiO_2. The curves in different colors in Figure 1.21 (b) represent the E-field strengths of the structure in a frame of the same color as in Figure 1.21 (a). The modulus of the E field is evaluated at the lower edge of the gold discs in each configuration, as indicated in Figure 1.21 (a) by the blue spots. In Figure 1.21 (b), it is clear that the local fields of the MIM structures show a higher field enhancement than the nanodisc arrays on glass. In the case of vertical disc stacks, the plasmonic resonance wavelength is red shifted compared to nanodisc arrays, and only a slightly higher local field enhancement at the resonance wavelength is found. The Au nanoparticles on film MIM structures show stronger enhancement than nanoparticle on nanoparticle structures. In the case of Au nanodiscs on Au film with SiO_2 disc spacer, the enhanced near field is 3 times the near field strength of nanodiscs on glass. The details of how the different structure configurations modify the optical response of the plasmonic structures, will be discussed in Chapter 4. Yet, we can expect better SERS capability from the MIM structures than from nanodiscs on glass substrates. Even better performance can be anticipated from the vertical MIM structures when the hot spot in the dielectric spacer gets exposed to the detecting environment by etching. Details will be presented in Chapter 7.

Chapter 2

Basic theory

2.1 Fundamental plasmons

2.1.1 Dielectric function from Drude model

In the Drude model, when light is incident on metal nanostructures, the free conduction electrons will oscillate with the time-dependent electromagnetic (EM) field. These oscillations are damped by collisions with the metal ion lattice. The interaction between electromagnetic waves and metal nanostructures can be described in the classic framework based on Maxwell's equations [1, 2]. For the collective oscillation of the conduction electrons, there is a characteristic frequency ω_p, known as the plasma frequency of the electron gas.

$$\omega_p^2 = \frac{ne^2}{\epsilon_0 m_{eff}} \tag{2.1}$$

Here n refers to the density of electrons, m_{eff} means the effective mass, e is the charge of an electron and ϵ_0 is the permittivity of free space. The plasma frequency is an indicator of how fast the electron gas can respond to an incident EM wave.

By considering the motion of an electron gas in a bulk metal under the influence of a harmonic time dependent EM field, one can derive the dielectric function of the free electron gas [1, 2], as :

$$\epsilon(\omega) = 1 - \frac{\omega_p^2}{\omega^2 + i\gamma\omega} \tag{2.2}$$

Here γ is the damping, which in the Drude model stands for the collision frequency. It equals the reciprocal of the relaxation time of the free electron gas. The complex dielectric function $\epsilon(\omega)$ can be written as $\epsilon(\omega) = \epsilon_1(\omega) + i\epsilon_2(\omega)$, where $\epsilon_1(\omega)$ and $\epsilon_2(\omega)$ are the real and imaginary part of the metal dielectric function, respectively.

The dielectric constant is an indicator whether the electrons can oscillate at the given frequency of light.

For incident light with a frequency $\omega > \omega_p$, the metal will lose its metallic character, the real part of ϵ will be positive and the metal will become transparent. In this case, the conduction electrons will not oscillate and the light will simply be transmitted or absorbed through other mechanisms like interband transitions.

For incident light with a frequency $\omega < \omega_p$, but very close to ω_p, $\omega/\gamma \gg 1$, the collision damping will be negligible and ϵ will be predominantly real.

For incident light with a frequency $\gamma \leqslant \omega \leqslant \omega_p$, the free conduction electrons will oscillate with the EM field of the incident light, but 180° out of phase due to the charge of the electron. And the majority of light will be reflected.

For incident light with very low frequency, where $\omega \ll \gamma$, it is $\epsilon_2 \gg \epsilon_1$. In this region, metals are mainly absorbing.

In an ideal free-electron model, according to 2.2, when $\omega \gg \omega_p$, we get $\epsilon \to 1$. Whereas in a real metal, there is a residual polarization due to the positive background of the ion cores. This effect can be described by a dielectric constant ϵ_∞. The revised dielectric function for a real metal in the Drude model can be written as

$$\epsilon(\omega) = \epsilon_\infty - \frac{\omega_p^2}{\omega^2 + i\gamma\omega} \tag{2.3}$$

In this thesis, both in experiments and simulations, gold is the metal investigated for its plasmonic properties. Thus, the Drude model of Au will be briefly introduced here. The optical constants results obtained by Johnson and Christy are commonly used as shown in Figure 2.1. Figure 2.1 shows the real and imaginary parts of the refractive index for Au from [99]. The relative permittivities of Au from Johnson and Christy experimental data in the visible-NIR domain of wavelengths can be fitted with the dielectric function from equation 2.3 [1].

The fitting parameters for the Drude model of Au are

$$\begin{aligned} \epsilon_\infty &= 9.5 \\ \hbar\omega_p &= 8.95 eV \\ \hbar\gamma &= 0.065 eV \end{aligned} \tag{2.4}$$

where $\hbar$ is the reduced Planck constant.

The fitting parameters to the Johnson and Christy results in 2.1 are used in chapter 4 for the calculation of grating induced surface plasmon polaritons and for the calculation
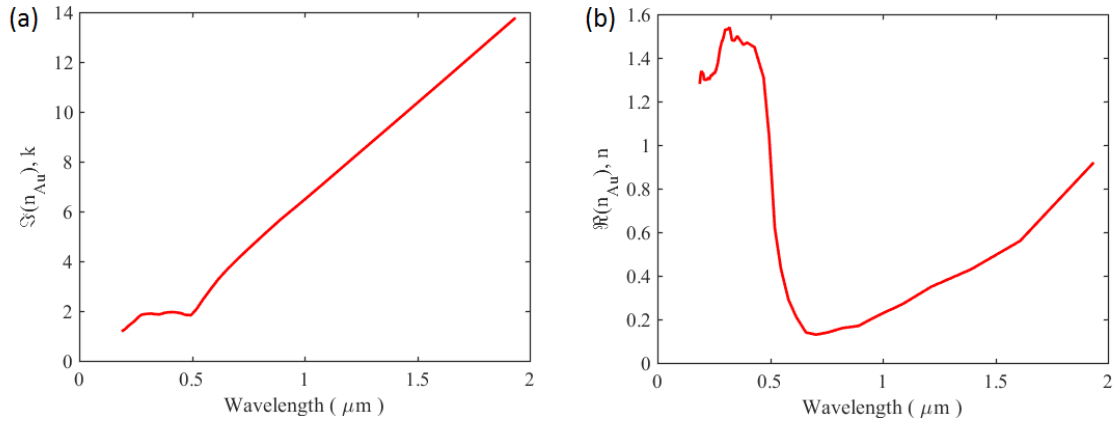
Figure 2.1: Complex index of refraction of Au ($n_{Au} = n + ik$) calculated from experimental results by Johnson and Christy [99]

of the resonance positions of cavity plasmon modes. In simulations shown in this thesis, which are based on Comsol Multiphysics, the optical constants from Johnson and Christy are used.

2.1.2 Surface plasmon polariton (SPP)

As mentioned in section 1.1.1.2, under proper illumination configurations, surface plasmon polaritons can be excited on the interfaces of a thin metal film. When light is incident on a thin film, the oscillation of the electron gas can only exist on the surface, resulting in propagating charge waves, known as surface plasmon polaritons. As shown in [1, 2], by applying Helmholtz equations on the metal and dielectric side, making use of the continuity condition for the normal component of the electric field and the tangential component of the magnetic field at the metal/dielectric interface, one can arrive at the dispersion relation of SPPs, excited at the interface.

$$k_{spp} = \frac{\omega}{c} \sqrt{\frac{\epsilon_m \epsilon_d}{\epsilon_m + \epsilon_d}} \tag{2.5}$$

Here ϵ_m and ϵ_d mean the dielectric permittivity for metal and dielectric, respectively. The equation sets k_{spp}, the wave vector of the plasmon wave, in relation to the frequency of the incident light ω. The blue curve in Figure 2.2 shows the dispersive curve for the SPP excited on the metal/air interface. The wave vector of the SPP wave is always larger than that of the incident light, given by $k = \frac{\omega}{c}$, shown in Figure 2.2 (blue curve is at the right side of black curve). This wave vector mismatch has to be overcome in order to excite SPPs on the metal/dielectric interface. The classic ways to add extra momentum to the incident light is by prism coupling, grating coupling or waveguide coupling. There are SPP sensors developed based on these different configurations, as
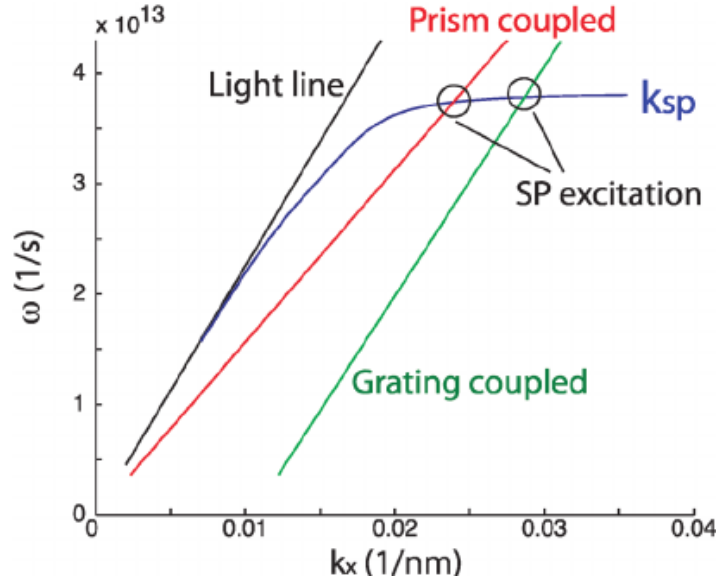
Figure 2.2: The dispersive curve of SPP excited on gold surface [100]

presented in section 1.1.1.2. In Figure 2.2, the red and green curve demonstrate the extra momentum provided by prism coupling and grating coupling, respectively.

The grating coupled SPP will be briefly introduced here due to the fact that grating induced SPPs are inevitable in ordered nanoparticle arrays on a film MIM system. When light is incident on a grating coupler, the momentum of the light can be changed by diffraction, depending on the diffraction order. The momentum of the diffracted light by a two-dimensional square grating can be described as [1, 5, 10]

$$k_d = \frac{2\pi}{\lambda} n_d \sin\theta + \frac{2\pi}{P}\sqrt{i^2 + j^2} \tag{2.6}$$

Where λ, θ represent the wavelength and the incident angle of the free space light, P stands for the grating constant and n_d is the refractive index of the dielectric material surrounding the grating, i and j are the diffraction orders on the two periodic axes, $i, j = 0, \pm 1, \pm 2 \cdots$. On the right side of equation 2.6, the first component is the propagating constant of the incident light along the metal/dielectric interface, while the second component is the grating induced momentum.

The resonance condition of grating induced SPPs $k_d = k_{spp}$ can thus be given by combining equation 2.5 and equation 2.6:

$$\frac{2\pi}{\lambda} n_d \sin\theta + \frac{2\pi}{P}\sqrt{i^2 + j^2} = \frac{\omega}{c}\sqrt{\frac{\epsilon_m \epsilon_d}{\epsilon_m + \epsilon_d}} \tag{2.7}$$

For normal incidence, where $\theta = 0$, the resonance position λ_{spp} of SPPs can be deduced

from equation 2.7, as:

$$\lambda_{spp} = \frac{P}{\sqrt{i^2 + j^2}} \sqrt{\frac{\epsilon_m \epsilon_d}{\epsilon_m + \epsilon_d}} \tag{2.8}$$

2.1.3   Localized surface plasmon resonance (LSPR)

When light interacts with particles much smaller than the incident wavelength, localized surface plasmon resonances will be excited. LSPRs are non-propagating oscillations of conduction electrons coupled to the EM field of incident light. The polarizability α introduced by incident light in a small sphere qualified for electrostatic approximation, can be written as

$$\alpha = 4\pi a^3 \frac{\epsilon_m - \epsilon_d}{\epsilon_m + 2\epsilon_d} \tag{2.9}$$

Where a is the radius of the sphere and $a \ll \lambda$, details can be found in [1]. The resonance condition of the dipolar surface plasmon of the metal nanoparticle can be deduced from equation 2.9:

$$\Re[\epsilon_m(\omega)] = -2\epsilon_d \tag{2.10}$$

In practice, this dipole plasmon resonance condition provides a reasonable good approximation for spherical particles smaller than 100 nm illuminated within the visible-NIR regime. For nanoparticles with larger size beyond the electrostatic scope, there will be energy shifts due to retardation effects, occurance of higher order resonances and radiation damping which results in a significantly broadened dipole plasmon resonance.

2.2   Coupling between surface plasmons

The resonance position of a single nanoparticle is determined by the details of nanoparticle sizes and shapes, as well as the dielectric function of the particle material and of the surrounding dielectric. For an ensemble of nanoparticles, the polarizability of each individual nanoparticle will be influenced through far field or near field interaction with its neighbouring particles, resulting in shifting of the resonance position, modified line shape and bandwidth of the plasmon modes in the extinction/reflection spectra [101–105].

In principle, there are two different kinds of plasmon coupling with respect to the magnitude of particle distances. One coupling type is near field coupling and it happens when the nanoparticles are closely separated, typically when the spacing distance is

smaller than the dimensions of the nanoparticles. The plasmon near field, which extends beyond the physical dimensions of the particle, can then spatially overlap with that of its neighbour. So here the plasmons are directly influenced by the plasmonic near field of the neighbour particle. For larger particle separations beyond the regime of near field coupling, far field coupling dominates. It is mediated by the scattered light of the nanoparticles. In this case, the sizes of the nanostructures are much smaller than the spacing distance and the wavelength, so that the scattered field is of dipolar character and the particles are justified to be treated as point dipoles. The resonant plasmons of the individual particles can couple with each other through the dipolar field interactions which interfere to form collective radiation [101].

2.2.1   Far field plasmon coupling

The periodicity dependency of the plasmonic resonance wavelength, linewidth and amplitude in spatially ordered structures has been extensively investigated [101, 102, 106]. In Ref. [101, 107], arrays of nanoparticles in the pattern of a two-dimensional (2D) square grating were studied. It is manifested that particularly strong far field plasmon coupling happens when the scattered light fields, corresponding to a certain grating order, change from evanescent to radiative. This critical grating constant is termed P_c. Only normal incidence is considered here, if not stated otherwise. When the grating constant $P \geqslant P_c$, the light field is radiating. The transition from the radiating regime to the evanescent regime happens when the array periodicity decreases to the order of the wavelength of the LSPR of individual particles. Then the radiating LSPR modes diffract in-plane, creating modes propagating through the structures, evanescently bound to the grating plane [101, 102]. This phenomenon is also widely referred to as surface lattice resonance, featuring collective resonances of the ensemble of the particles due to the coupling between the diffractive orders of the arrays and the LSPR of the individual elements.

In Ref. [101], substrates consist of a square 2D grating of Au-nanoparticles with heights of 14 nm and diameters of 150 nm on an indium-tin-oxide (ITO) coated quartz substrate. Varying periodicity was studied. Figure 2.3 (a) shows the extinction spectra of the same particle arrays. The spectra were normalized to a constant particle density for better comparison. It can be found from the extinction spectra that both the plasmon decay time and resonance wavelength varies with changing grating periodicity. In Figure 2.3 (b), there is the decay time and resonance position evaluated and extracted from extinction spectra in Figure 2.3 (a). The plasmon decay time for particle arrays with grating periodicities ranging from $P = 350$ nm to $P = 850$ nm is shown. The decay time is obtained by femto second (fs)-resolved measurements and it strongly depends
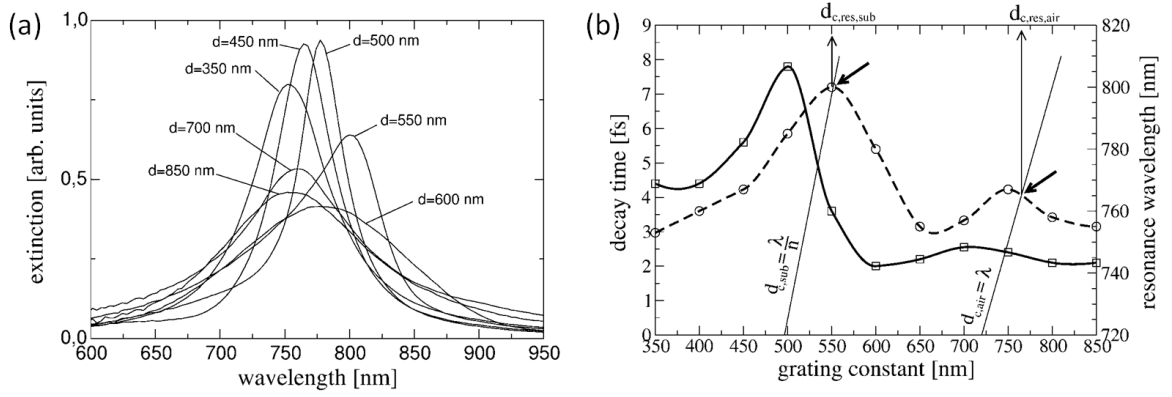
Figure 2.3: (a) Extinction spectra for particle arrays with different periodicity; (b) Plasmon decay time and resonance wavelength versus periodicity [101]

on the grating constant. This means the linewidth of collective plasmon resonances can be readily modified through far-field plasmonic coupling. P_c can be identified by plotting the lines $P_{c,sub} = \lambda/n$ and $P_{c,air} = \lambda$. The critical periodicity is indicated by the intersections of these lines with the experimental curve $\lambda_{res}(P)$, $P_{c,sub} = 550$ nm and $P_{c,air} = 765$ nm for radiation in substrate and air, respectively.

As can be seen in Figure 2.3 (b), the intersection values show good agreement with the red shifted maxima of the resonance wavelengths. The red shift of the resonance position, which happens when $P \to P_c$, can be explained by the fact that the scattered optical fields in the plane of the grating become almost in-phase with the scattered light from neighbouring particles. The energy required to excite the surface plasmon decreases (fields add constructively, weakening the inner restoring force in each particle [105]), causing the red shift of the resonance position.

Another conclusion from Figure 2.3 (b) is that the decay time of the LSPR mode is longer in the evanescent regime $P \leqslant P_c$ than in the radiating regime $P \geqslant P_c$. For $P \geqslant P_c$, the field of the first grating order is radiating in the substrate. The dramatically enhanced plasmonic oscillation damping results from the strongly enhanced radiation damping. In the regime $P \leqslant P_c$, more of the excitation couples into the array elements, which reduces scattering and reflection, resulting in a longer life time. This enhancement of the residence time of the incident optical energy within the array may provide advantages for applications which depend on the utilization of absorbed radiation rather than simply locally enhanced field intensities, such as light harvesting and photocatalysis [101, 102].

In summary, far field plasmon coupling has a pronounced influence on the plasmon line shape, both in terms of resonance wavelength as well as band width, due to the modification of the polarizability of the individual particles by the scattered fields of their neighbours. The red shift of the maxima occurs as a result of an in-phase addition

of the maxima from the neighbours when the grating period is $P = P_c$. The varying band width is due to a significant dependence of the plasmon decay time on the grating constant via its influence on the amount of radiative damping [1].

2.2.2   Far- to near-field effects on plasmon coupling

In the last section, we discussed about the plasmon coupling when the particle separation is about the order of the wavelength of the incident light. As we know, the penetration depth of SPPs in the dielectric is $\sim$ 100-200 nm, and the LSPR decay length is $\sim$ 10-30 nm. When the particle separation is smaller than the penetration depth, there will be a spatial overlap of the near-fields, thus near field coupling happens. It is also of great interest to study the behaviour of plasmonic coupling at an intermediate regime, where the transition of far-field to near-field coupling occurs.

In Ref. [105], the optical properties of ordered 2D arrays of Au nanoparticles with a diameter of 50 nm are investigated by experiments and simulations. The periodicity in X-direction, termed x, is fixed to 80 nm, while the periodicity in Y-direction, termed y, varies from 60 nm to 300 nm, ranging from the near-field coupling regime to the far-field coupling regime.
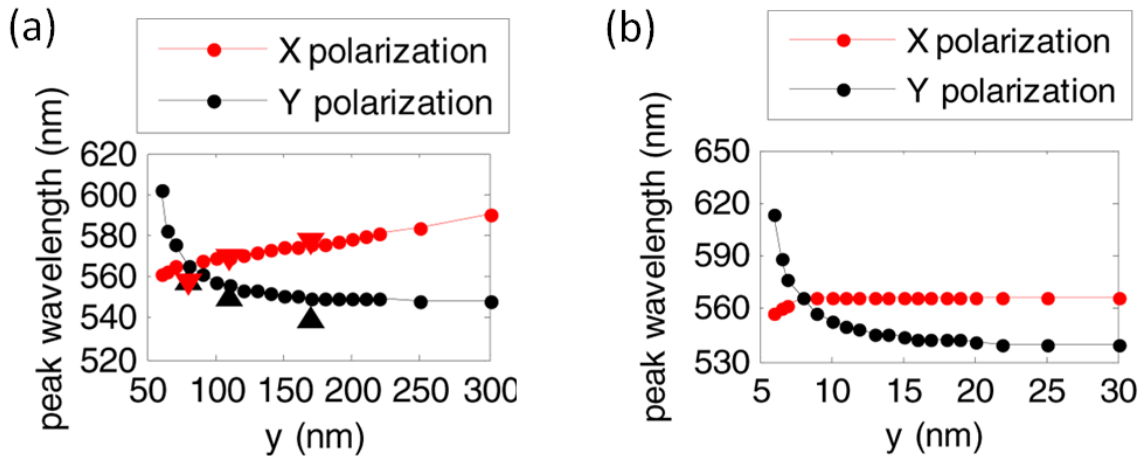
Figure 2.4: Characteristics of the plasmon band of (a) 50 nm particle and (b) 5 nm particle arrays as a function of the periodicity y at X- and Y-polarization [105].

Figure 2.4 (a) shows the evolution of the calculated plasmon band characteristics with the periodicity in Y-direction. In order to highlight the contribution of the phase retardation and the far-field radiation to the plasmon coupling, simulations were also performed for Au particle arrays with a disc diameter of 5 nm, where the phase retardation and scattering effect can be neglected [105]. Figure 2.4 (b) shows the plasmon

band characteristics for the small particle arrays. As can be seen in Figure 2.4, for both 50 nm and 5 nm Au particle arrays, the SPR peak wavelength shows a slightly different variation as a function of periodicity y, at both polarizations. As all arrays have the same periodicity x, the variations of band characteristics can be ascribed to the variation of the coupling between the particle chains.

For 5 nm particle arrays, the absorption dominates [9], and plasmon coupling mainly occurs in the near field. This explains why in Figure 2.4 (b), in the case of large periods (from 20 nm to 30 nm), there is nearly no variation of the plasmon band characteristics, at both polarizations. Numerical calculations based on the discrete dipole approximation (DDA) show, that the phase of the induced near field between two particle chains (periodicity x is fixed) is larger than 90° in X-polarization, which leads to destructive interference. Thus a slight blue-shift of the resonance wavelength with decreasing y is observed at X-polarization. On the other hand, an induced phase of less than 90° in Y-polarization, results in constructive interference and a red-shift of the resonance peak. The red-shift in Y-polarization is more notable than the blue-shift in X-polarization, because the near field dominates at the direction parallel to the induced dipole axis, so the plasmon coupling strength between particle chains is more significant in Y-polarization than that of X-polarization. More details can be found in Ref. [105]. For the particles with a diameter of 50 nm, the scattering cross section
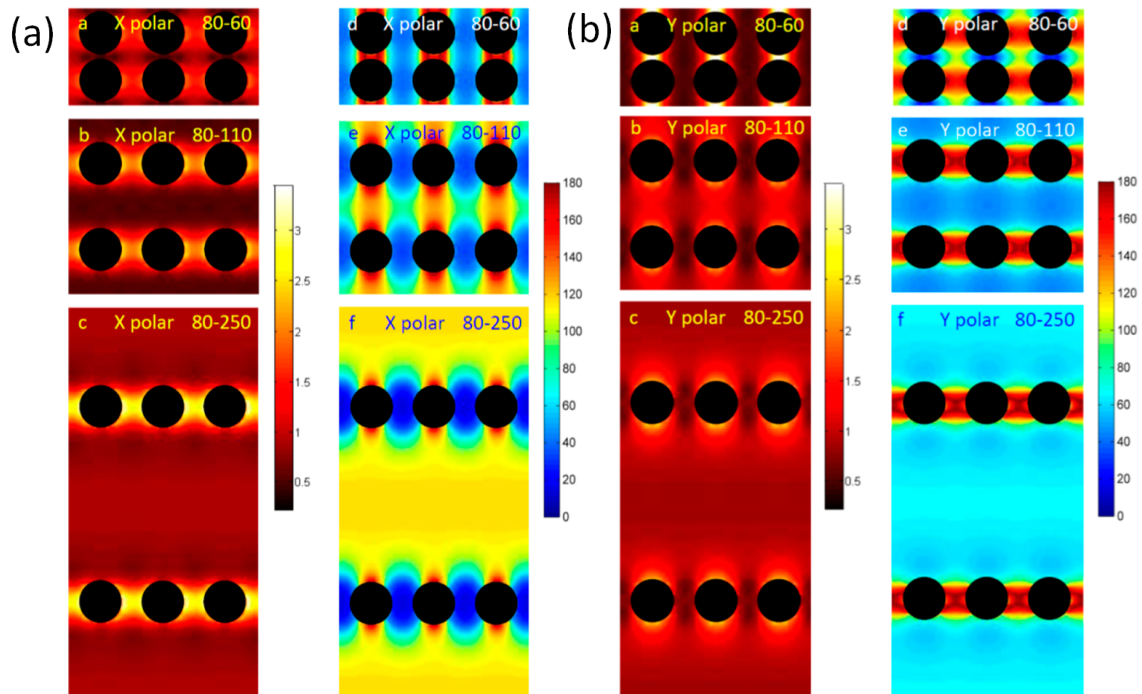
Figure 2.5: Distribution of the field amplitude enhancement and the field phase in X-polarization (a) and Y-polarization (b), adapted from Ref. [105]

induced by the collective oscillation is larger than the absorption cross section. In 50 nm

particle arrays, both near field and far field coupling need to be considered. Figure 2.5 shows the field enhancement and phase distributions in three particle arrays (labelled by periodicity x-y) in X-polarization (a) and Y-polarization (b). For X polarization and large periodicity y, the coupling between two particle chains is mainly through the far field coupling mechanism, as presented in section 2.2.1. From the phase distribution in the second and fourth columns of Figure 2.5, induced phases of bigger than 90° and less than 90° were found in the Y-direction (coupling direction of particle chains), at X-polarization and Y-polarization, respectively. This results in the blue-shift and red-shift of the resonance position with decreasing y, at X- and Y-polarization, as in Figure 2.4 (a).

For large periods, the far-field radiation dominates in the Y-direction, perpendicular to the applied field for X-polarization, while the far-field radiation is very weak in Y-direction for Y-polarization, which can be observed in the phase map. This explains, why the magnitude of the blue-shift in X-polarization is larger than that of the red-shift in Y-polarization, when y is decreased from 300 nm to 200 nm. The near field coupling works more efficiently at smaller periods of y, at Y-polarization, resulting in a more significant red-shift in Y-polarization than blue-shift in X-polarization (from $y = 200$ nm to 60 nm). This can be seen in 2.4 (a). The same phenomenon of the resonance position showing an initial blue-shift, then the red-shift with decreasing periodicity has also been reported in square arrays [108].

2.2.3   Near-field plasmon coupling

The last section made clear that the coupling strength for near-field coupling is much stronger than for far-field coupling, with a distance dependence of d^{-3} [1]. The theory of the near-field coupling mechanism, the distance and polarization dependence of the coupling strength has been investigated thoroughly e.g. in hollow metallic structures [109–111], homo- and hetero- dimers [112–115], trimers [114], particle chains [116], and thin metallic films [117, 118]. In this section, different kinds of near-field coupling will be presented according to the different nature of the coupling plasmonic modes.

2.2.3.1   Coupling between LSPR and LSPR

A model which has analogies to coupling electronic orbitals in molecules, has been adapted to describe the plasmons in composite metallic nanostructures. The plasmon modes supported by individual parts of these composite structures, with a spectral and spatial near-field overlap, can hybridize with each other. The plasmon hybridization
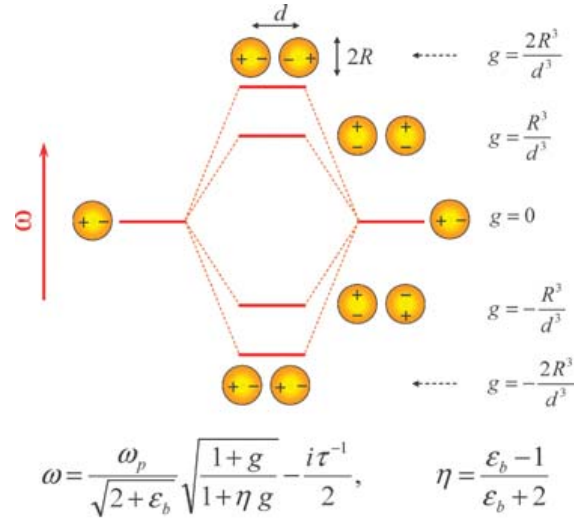
Figure 2.6: Plasmon hybridization in a spherical particle dimer [111]

scheme for a particle dimer which falls into the non-retarded regime, is a characteristic example as shown in Figure 2.6 [111].

The dipole plasmons supported by individual spherical particles are 3-fold degenerate. These three dipole modes in each particle are hybridized in the dimer, and the composite structure will exhibit new resonances, as seen in Figure 2.6. The splitting between corresponding symmetric and anti-symmetric modes is governed by the coupling strength which decreases upon increasing separation distance. Two of the hybridized plasmon modes feature a charge distribution parallel to the dimer axis, with a symmetric mode at low energy and an anti-symmetric mode at high energy. The symmetric mode shows a net dipole moment and couples best to external light, governing the far-field optical properties of the dimer. Two sets of degenerate modes have dipoles oriented perpendicular to the dimer axis. All these new modes of this interacting system are derived from the eigenfrequencies of two-particle DDA calculations [111]. The mode frequencies can be determined by the formula quoted at the bottom, with values of g shown in the insets of Figure 2.6.

Another interesting aspect about LSPR and LSPR coupling is that the 'hot spots' of the nanoostructures will also be modified. For a monomer metallic disc on a substrate, the 'hot spots' are mainly localized below the disc, inside the substrate, while in the case of a disc dimer (or disc chains) on the substrate, strong 'hot spots' have been observed in the nano-sized gaps [116, 119]. When strong near-field coupling happens between LSPRs, the field localization in the gap is caused by the suppression of scattering into the far-field via excitation of plasmon modes in the particles along the dimer (or chain) axis. In Ref. [116], it is shown in experiments and simulations that the scattering is significantly suppressed for closely spaced particles, and the fields are localized at

interparticle sites instead. Composite structures which enable the near field coupling between LSPRs can therefore support 'hot spots' in the interparticle junction, thus they serve as an excellent platform for surface enhanced applications.

For large neighbouring particles with small distances, calculations including retardation are needed, while the plasmon hybridization scheme is still the same. The modes of the single nanoparticles will split into two new plasmon resonances which are characterized by the symmetry of charge oscillations [104, 120]. Apart from this classic plasmon orbital hybridization scheme, a Hamiltonian model has been built to explain the anti-crossing phenomena of the resonance position and band linewidth of hybridized modes [120, 121].

2.2.3.2   Coupling between SPP and SPP

In a multilayer system with alternating metallic and dielectric thin films, SPPs can be excited on each metal/dielectric interface. Coupling between SPPs occurs, when the separation between interfaces is comparable to or smaller than the penetration depth of SPP modes. There are two typical structure configurations for the study of coupled SPPs: An insulator/metal/insulator (IMI) structure and a metal/insulator/metal (MIM) structure. For the sake of simplicity, here the interesting special case, where the sub- and the superstrates (insulator in the case of IMI or metal in the case of MIM) show the same dielectric response, is considered. By applying the requirements of continuity of the electric and the magnetic field at both interfaces, the dispersion relation of the supported SPPs in the coupled system can be described as [1]

$$tanh(k_1 a) = -\frac{k_2 \epsilon_1}{k_1 \epsilon_2} \tag{2.11}$$

$$tanh(k_1 a) = -\frac{k_1 \epsilon_2}{k_2 \epsilon_1} \tag{2.12}$$

Where ϵ_1, k_1 are the dielectric constant and the wave number of the EM wave, which is associated with the sandwiched material, while ϵ_2, k_2 are those of the sub- and superstrates. Equation 2.11 describes modes of odd vector parity ($E_x(z)$ is odd), and equation 2.12 describes modes of even vector parity ($E_x(z)$ is an even function). In IMI structures, the confinement of odd SPP modes to the metal film decreases drastically as the mode evolves into a plane wave supported by the homogeneous dielectric environment. So the odd SPP modes in IMI waveguides are also called long-ranging SPPs. They have a longer attenuation length along the direction of propagation than that of SPPs. The confinement of even SPP modes increases with decreasing metal film thickness.

In MIM structures, the fundamental odd SPP modes are of great interest in energy confinement because they show no cut-off for vanishing core dielectric layer. When the dielectric film is thin enough, large wave vectors of the odd SPP modes and thus small penetration depths into the metallic layers can be obtained. Therefore, the localization effects for such MIM structures can also be realized for excitations even in the infrared [1].

If the dielectric constants of sub- and superstrates are different, prohibiting phase-matching between the coupling SPP modes, the SPP coupling between two different metal/dielectric interfaces varies significantly .

2.2.3.3 Coupling between LSPR and SPP

The interactions between localized and propagating surface plasmons have been investigated, as well as applications based on 'hot spots' generated by this coupling [122–129]. Many different models have been built to describe the coupling phenomena between LSPR and SPP. In Ref. [122], ordered Au disc arrays on Au film MIM systems were studied. An anti-crossing behaviour of the LSPR and SPP resonance positions is observed in reflection spectra, in both experiments and simulations. In Figure 2.7 (a), the
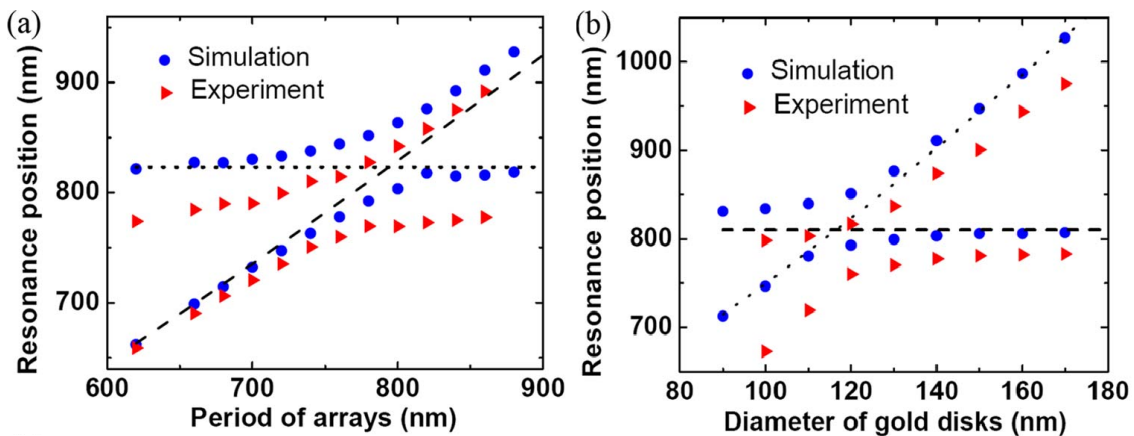
Figure 2.7: Ant-crossing behaviours of LSPR and SPP resonances (a) as a function of grating period and (b) as a function of the diameter of gold discs, adapted from [122]

calculated and experimental SPP resonance positions and LSPR resonance positions are shown as blue dots and red triangles, respectively, as a function of the period while the size of the Au discs is kept constant (diameter 120 nm and thickness 40 nm). The dotted line represents the LSPR resonance of an isolated Au disc on a Au film and the dashed line indicates the SPP resonance position calculated from equation 2.8. An anti-crossing behaviour can be seen when the LSPR resonance of the isolated disc on film and SPP are approximately equal to each other, at the period of 790 nm. Similar

anti-crossing behaviour was also observed when the periodicity is kept constant and the LSPR resonance is tuned by the size of the discs, as shown in Figure 2.7 (b). Strong coupling between LSPR and SPP resonances was indicated by the repulsive behaviour.

2.3   Coupling between plasmonic and optical cavity

In the last section, different coupling scenarios between different plasmonic modes were presented. In this section, the mechanism of coupling between plasmonic modes and a Fabry-Pérot (FP) cavity will be discussed. In plasmonic cavity structures, the metal/dielectric interfaces can act as reflective mirrors to squeeze and confine electromagnetic energy in the nanocavities. The coupling between the plasmonic modes and the discrete and sharp cavity modes, gives rise to plasmonic cavity modes which show strong standing wave characteristics. Plasmonic cavity modes have advantageous properties like strong field enhancement and confinement originating from their plasmonic resonance origin, and very narrow and distinct resonance line shapes from their cavity modes origin. These advantageous properties make plamonic cavity structures a very promising substrate for surface enhanced phenomena and refractive index sensing. The plasmonic cavity modes have attracted extensive research interest in understanding the resonance properties [130–134], and applications of plasmonic colors [79–81, 135], plasmonic lasers [136, 137], plasmonic absorbers [138], slow plasmons [139–141], etc. Field distributions inside plasmonic cavities have been found to be very similar to those of FP antenna resonators in the radio and microwave regime. The well-established dielectric FP cavity models have been adapted to explain the plasmonic modes in various plasmonic resonators as presented below.

2.3.1   1D plasmonic cavity

One-dimensional plasmonic cavity structures are the simplest structures which allow plasmonic modes to interact with FP cavity modes. The Fabry-Pérot (FP) model has been applied to understand the plamonic resonances in nanowire antennas [142], nanorod antennas [143], 1D MIM waveguides [139, 140], etc.

Dorfmüller et al. studied Au nanowires with a width of 40 nm and length varying from 40 to 1630 nm with scanning near-field optical microscopy (SNOM), as shown in Figure 2.8. The near field images of the samples, shown in Figure 2.8(d), were measured with an excitation polarization parallel to the wire axis. The near field strength varies notably from wire to wire. For the nanowire with a length of 40 nm, the near field map
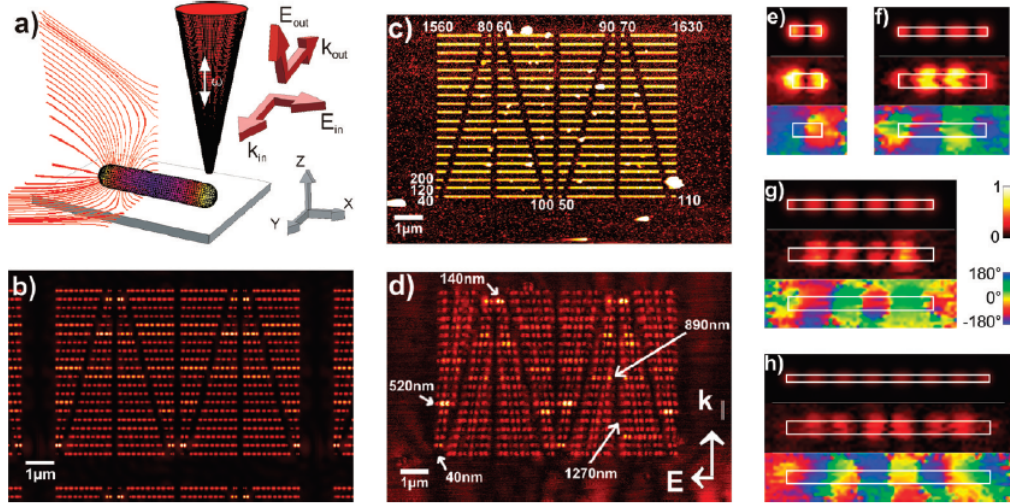
Figure 2.8: (a) Scheme of SNOM measuring setup. (b) Simulated z-component of the electric field 24 nm above the nanowires shown in (c). (c) Topography of the Au nanowires. (d) Simultaneously obtained, baseline-corrected near-field optical amplitude image for an excitation wavelength of $\lambda = 492$ nm. (e)-(h) Simulated magnitude, measured magnitude and phase for the 140, 520, 890 and 1270 nm long wires [142].

(see Figure 2.8(e)) featured two amplitude lobes, indicating the characterization of a dipolar mode. This indication is furthermore confirmed by the optical phase image which showed a phase difference of 180° between the two lobes. Higher order resonances were observed for longer nanowires. Good agreement has been found between the simulated and measured near field distribution (see Figure 2.8(e)-(h)). Similar observations have appeared in many works [139, 140, 143–145], an intuitive and clear interpretation of these plasmonic properties has been given by regarding the nanowires as 1D plasmonic FP resonators. Guided surface polaritons supported by the nanowire, travel along the wire with a wave vector of k_{spp} and obtain a phase shift ϕ upon reflection at the terminations. When various nanowires with different wire lengths were studied with a fixed laser wavelength, the mth order resonance wire length is given by [142]

$$2k_{spp}L(m) + 2\phi = 2\pi m \qquad (2.13)$$

In the case, when the wire length of the nanowire is fixed, the resonance wavelengths for various orders of plasmonic modes are given by [139, 140, 143] :

$$\frac{2\pi}{\lambda_{spp}}L + \phi = \pi m \qquad (2.14)$$

The phase shift ϕ upon reflection has been widely noticed due to the failure in considering the nanowire as a simple optical antenna. For instances, Söndergaard et al. found that half-wavelength metal nanostrip resonators possess a length of only one-third of the wavelength of the supported surface polaritons [140]. Schider et al. found that

the eigen frequencies for plasmonic modes follow a dispersive curve similar to that of a metal/dielectric interface, but with smaller frequencies (when the resonance wavelength λ_{spp} was determined by the length of the nanowire L as $L = j\lambda_{spp}/2$, where j denotes the order of plasmonic resonance [145]). These phenomena result from the fact that the reflection coefficients at the metal/dielectric terminations are complex and as a result, a phase shift is introduced upon reflection.

To promote the rational design of plasmonic structures with desired resonance characteristics, it is crucial to understand the relation between the design parameters and resonance conditions. Thus, it is important to precisely take into account the phase shifts upon reflections at the metal/interface terminations of plasmonic resonators. Many have demonstrated theoretically or experimentally, that the phase shift ϕ is dependent on cavity parameters and order of the modes [139, 140, 142].

2.3.2   3D plasmonic cavity

Plasmonic modes have been studied in 3D plasmonic resonators where the plasmonic waveguide modes are confined and interact with the cavity modes of a 3D FP cavity. The field distributions of plasmonic modes demonstrate strong standing wave characteristics, and are very similar to those of the cavity modes in a 3D dielectric antenna. So the resonance condition in a 3D dielectric cavity has been adapted to determine the resonance condition of a 3D plasmonic resonator [80, 81, 146–148]. In a cylindrical 3D dielectric cavity, the resonance wavelength for TMmnp (a tranverse magnetic mode, m,n,p denote the radial, angular and longitudinal modal index) is given by [149, 150]

$$\lambda_{TM_{mnp}} = \frac{2\pi\sqrt{\epsilon_d}}{\sqrt{(\frac{\chi`_{mn}}{R})^2 + (\frac{p\pi}{h})^2}} \tag{2.15}$$

Here, ϵ_d represents the effective refractive index in the dielectric region. $\chi`_{mn}$ represents the nth root of the derivative of the mth Bessel function of the first kind. As in a plasmonic cylindrical resonator, the EM field of plasmonic modes penetrates into the metallic layers and beyond the radius of the metallic disc, thus the radius and height of the cylindrical cavity resonator are $R + \Delta R$ and $h + 2\Delta h$, respectively. Under the same model as for the dielectric cavity, the plasmonic cavity modes of different orders of TM_{mnp} can be given by

$$\lambda_{TM_{mnp}} = \frac{2\pi\sqrt{\epsilon_d}}{\sqrt{(\frac{\chi`_{mn}}{R+\Delta R})^2 + (\frac{p\pi}{h+2\Delta h})^2}} \tag{2.16}$$

Equation 2.16 is adapted from Ref. [137]. Yu et al studied the fundamental TM and TE cavity mode in a 3D cylindrical plamonic resonator, in order to investigate the possibility of applying plasmonic resonators for nanolasers.
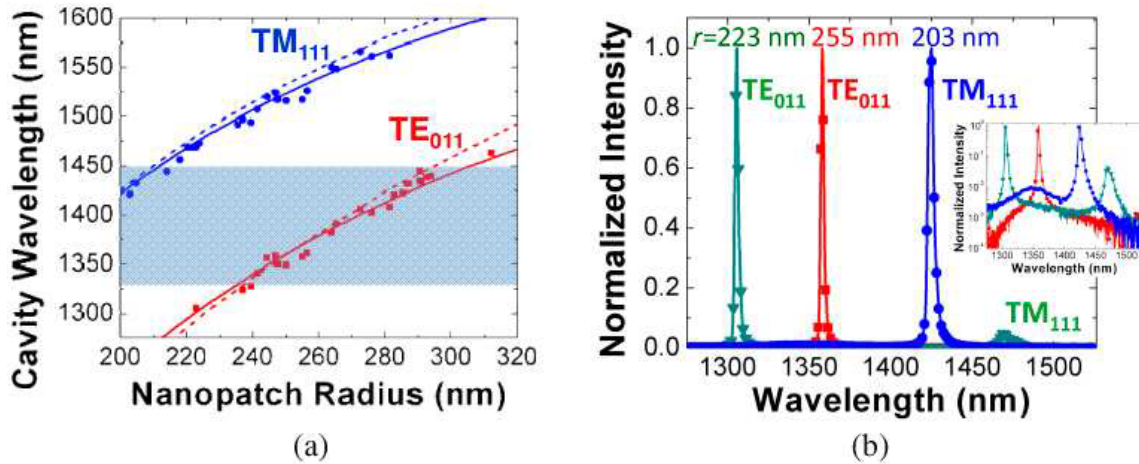
Figure 2.9: (a) Spectral properties and (b) laser emission spectra for different nanopatch sizes of the nanopatch laser [137]

In Figure 2.9 (a), Yu et al. showed the measured resonance wavelength evolution of plasmonic cavities with various radii. The measurements showed good agreement with the numerical calculations based on equation 2.16 (solid line) and numerical simulations based on the finite-different time-domain (FDTD) method (dashed line). The penetration depth in equation 2.16 was adjusted to Δh_{TM111}=13 nm and Δh_{TE011}=8 nm, to obtain the best fit with the measurements. However, the penetration of the field in the dielectric region ΔR was not considered. Single mode lasing with > 20 dB single mode suppression was observed for most cavities as in Figure 2.9 (b). It is demonstrated that the cavity loss (including plasmonic absorption) can be easily compensated by the strongly enhanced EM field at the laser gain region. Fan et al. investigated dynamic color-tuning reflectors based on surface enhanced plasmons of 3D nanoatennas. The studied 3D nanoantennas consist of two 2D cavities defined by two different cavity arms. The excitation conditions of two different cavity modes can be readily tuned by adjusting the incidence angle, allowing for dynamic and fine tuning of plasmonic colors [80, 81].

2.3.3   2D plasmonic cavity

2.3.3.1   Rectangular plasmonic cavity

In Ref. [151] Miyazaki et al. showed the Fabry-Pérot resonance of plasmonic polaritons in a rectangular nanocavity. They demonstrated controlled squeezing of free space light

into nanometer-sized optical cavities, where the light is perpendicularly confined in a few-nanometer-thick SiO_2 film sandwiched between Au claddings. It is shown in the field distribution that the near field of these modes exhibits Fabry-Pérot resonance characteristics in the longitudinal direction. In Figure 2.10(a), a rectangular MIM
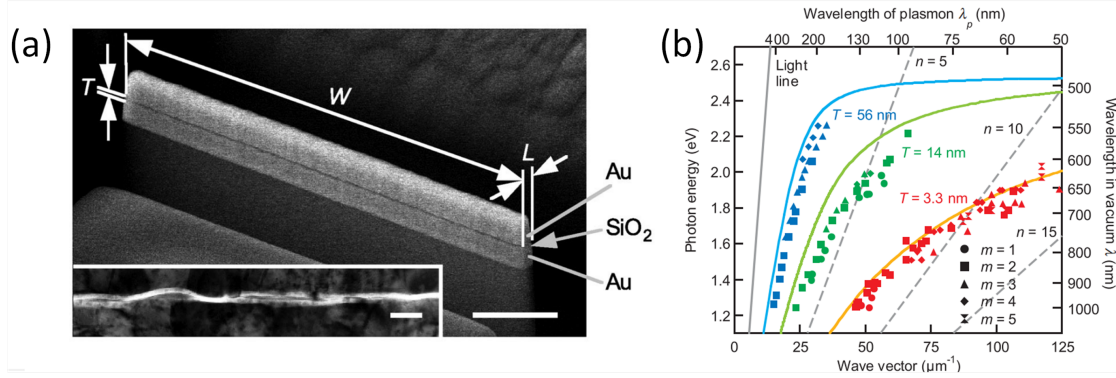
Figure 2.10: (a) SEM image of a rectangular plasmonic cavity. Scale bar, 20 nm; (b) Experimentally obtained dispersion relations (color). Solid curves: Analytical dispersion of MIM waveguides. [151]

cavity with gap defined by thin film deposition is shown. The thickness for the Au cladding layers is 150 nm. Rectangular cavities with varying thickness of SiO_2 film and varying cavity length were studied. According to the resonance condition of a FP cavity, a resonance occurs whenever the phase accumulated on a single round trip amounts to 2π. For the mth cavity resonance modes in a cavity with a length of L, the corresponding wave vector of the plasmon polaritons can be expressed as

$$k_{spp} = 2\pi/\lambda_p = m\pi/L \tag{2.17}$$

Here, k_{spp} and λ_p mean the wavevector and resonance wavelength of the plasmon polaritons in the cavity. L is the length of the cavity resonator.

Thus, the dispersion relation of plasmonic cavity modes can be determined through measurements. The reflection dip positions as a function of wave vector in different cavities are shown in Figure 2.10(b). It can be observed, that the resonances of various orders of plasmonic resonators with various length L, form single dispersive curves unique to each gap thickness T of the cavity. Moreover, a fairly good agreement was found between the experimentally determined cavity modes dispersion curves and the analytical dispersive curves for infinite MIM waveguides (solid curves in Figure 2.10(b)). It is also noted, that macroscopic electromagnetics is applicable to a 2D cavity, as far as far-field responses are discussed. Nanometric slits can be considered as media with a large refractive index n which is unattainable by bulk materials. In Figure 2.10(b), there is a small difference between the experimentally determined dispersion relation and the dispersion curve for an infinite MIM waveguide. This is because the reflection

coefficient at the metal/dielectric interface is a complex value (same as stated for 1D plasmonic cavities). Thus, an additional phase term acts like an increase of the cavity length. The additional phase is dependent on the order of the modes, the thickness of the dielectric spacer and the length of the cavities.

When the polarization is perpendicular to the nanoslit resonator, the resonance condition can be given by [138, 152] :

$$d\frac{2\pi}{\lambda}n_{spp} = m\pi - \phi \tag{2.18}$$

Here, d means the width of the nanoslit resonator, n_{spp} means the refractive index of the supported waveguide SPP in the nanoslit, m represents the cavity mode order and ϕ is the phase acquired upon reflection at the cavity terminations.

2.3.3.2 Circular plasmonic cavity

When the height of a 3D cylindrical plasmonic cavity in section 2.3.2 is far smaller than λ_p, the wavelength of the plasmon, there is no oscillation behavior of plasmonic modes along the axis of the cylindrical resonator. It becomes a 2D circular plasmonic cavity. The resonance condition can be modified based on equation 2.16, when the modal index p = 0.

$$\lambda_{TM_{mn}} = \frac{2\pi\sqrt{\epsilon_d}}{\sqrt{(\frac{\chi'_{mn}}{R+\Delta R})^2}} = 2\pi\sqrt{\epsilon_d}\frac{R+\Delta R}{\chi'_{mn}} \tag{2.19}$$

Minkowski et al. studied the plamonic cavity modes in a silver/SiO$_2$/silver multilayer system by simulations [133]. The analytical model for a FP dielectric cavity in cylindrical coordinates was used to describe the electrical field in this plasmonic resonator. The Neumann boundary condition ($\partial E/\partial\rho = 0$) can be then used to determine the resonance condition for plasmonic cavity modes. The resonance condition was given by :

$$k_{gsp}(R + d) = \chi'_{mn} \tag{2.20}$$

Here, k_{gsp} is the wave number of the MIM waveguide supported surface polaritons, d represents the thickness of the SiO$_2$ layer. This resonance condition is in accordance with equation 2.19 when $d = \Delta R$.

The resonant condition equation 2.20 was verified by comparing it with the simulated resonance frequency of the plasmonic cavity modes, as shown in Figure 2.11. The black solid curve is the dispersive relation of surface polaritons supported by the silver/SiO$_2$/silver waveguide. The evolution of the resonance frequency of the
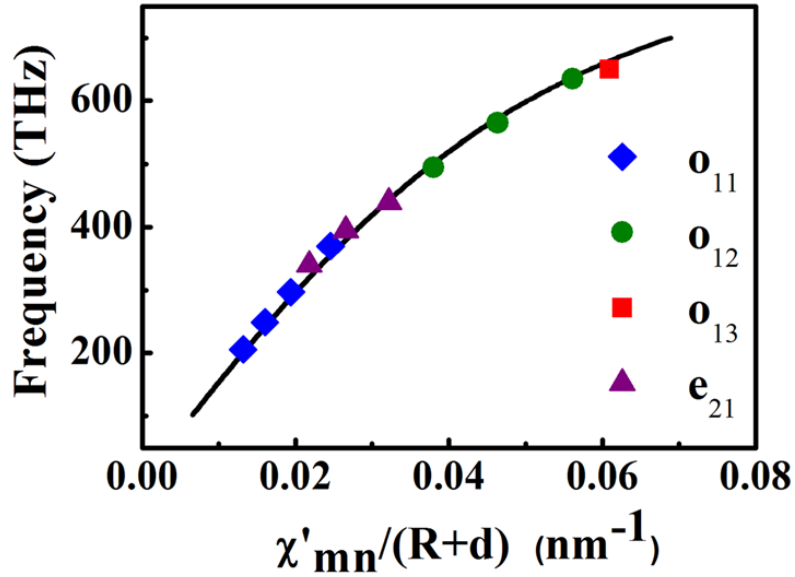
Figure 2.11: Cavity resonant frequency of various orders of plasmonic cavity modes versus $\chi'_{mn}/(R+d)$ for different silver disc sizes [151]

plasmonic cavity modes agrees well with the dispersion of waveguide plasmons. This indicates that the FP cavity model works well in plasmonic resonators as well.

Minkowski et al. considered the extension of the EM field beyond the geometrical dimensions of a MIM cavity by taking R+d as the resonant radius in equation 2.20. This correction is the same as the additional ϕ in equation 2.13, 2.14 and 2.18. The phase jump obtained upon reflection at the metallic/dielectric terminations can be regarded like an increased resonance radius. Filter et al. built an analytical approach to describe the resonance properties of optical antennas consisting of vertical disc stacks [130]. In this 2D circular system, the resonances are also explained by the FP resonator model. Predictions were compared to rigorous simulations and show excellent agreement.

2.4   Conclusion

In this chapter, the basic physics theories behind plasmonic structures were presented. The Drude model which describes the dielectric function of metals was discussed with respect to ideal and real metals. The excitation mechanisms of SPPs and LSPRs were introduced. The second section discussed about plasmonic modes coupling with each other in the far-field coupling regime, intermediate regime and near-field regime. In the third section, plasmonic modes interacting with different FP cavities were presented. FP cavity models have been successfully applied to describe the field distribution and resonance condition of plasmonic cavity modes. In MIM structures many different plasmonic modes can be excited and interact with each other through different principles.

Theories presented in this chapter will help to understand the complicated plasmonic behaviours in these composite plasmonic systems.

Chapter 3

Fabrication and characterization

As presented in Chapter 1, there are many different kinds of substrates with nanostructures that can support plasmonic modes, which feature strong confinement and high enhancement of electromagnetic fields. For the disordered substrates such as colloids and metallic nano islands film, despite the fact that they can provide ultra high EFs of the localized electromagnetic field, these substrates are subject to problems of low reproducibility and poor tunability at the nanometric scale. With the help of the EBL technique, we are provided with the ability to tailor nanostructures as we want and pattern them as designed. With the geometric dimensions and locations of nanostructures being controllable and reproducible, surface plasmonic modes can be readily tuned by varying the parameters with high precision. All the vertical MIM structures in this thesis are fabricated by EBL. The nature of different plasmonic modes is investigated both experimentally with optical characterizations and theoretically with numerical analysis and simulations.

3.1 Fabrication of vertical MIM cavities

Patterning techniques are demanded in order to fabricate ordered structures, for instances, the EBL technique or FIB milling. Fabrication processes of the three different vertical MIM structures which we investigated in this thesis are more or less similar, with EBL to obtain the desired patterns in resist and then transfer of the patterns to the actual structure through deposition.

In order to compare the modes in three different kinds of vertical MIM structures, structures with the same diameters and spacing distances were fabricated, meaning similar pattern files with only modified exposure doses were used. For all vertical

systems, the gap distance can be easily controlled through governing the thickness of the evaporated dielectric material. For the purpose of simplicity, in this fabrication section, we show fabrication processes of three different kinds of MIM structures with gap distances of 10 nm: disc MIM cavity arrays (with three different spacer configurations) and vertical disc dimer arrays.

3.1.1 Disc-on-film cavity arrays
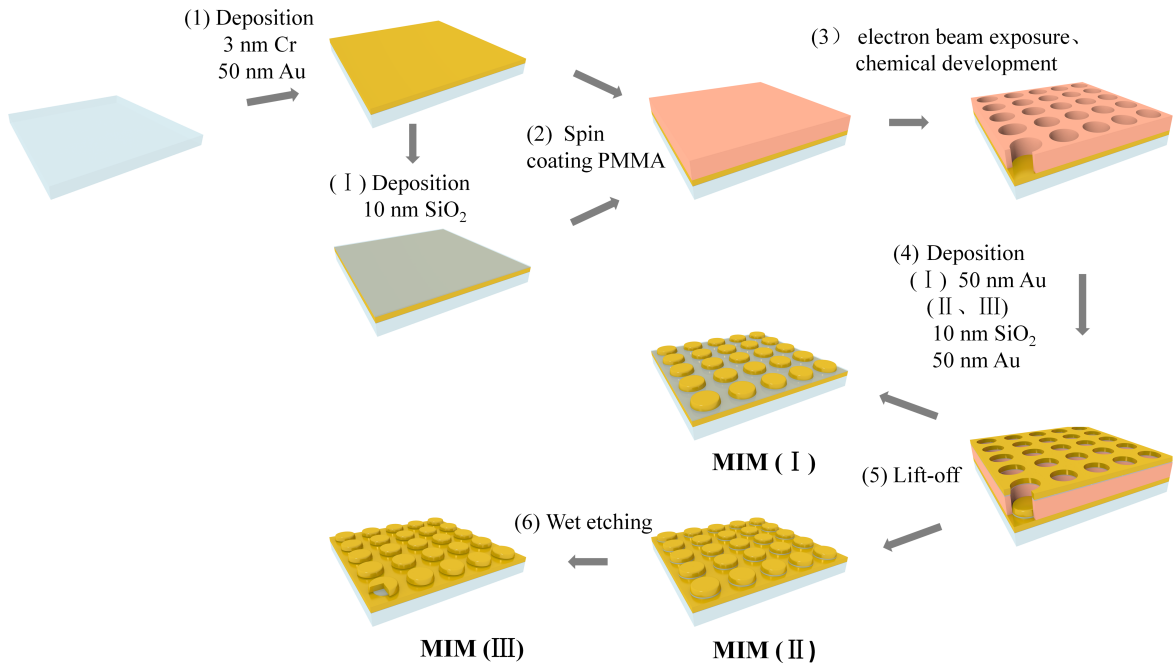
Figure 3.1: Schematic description of the fabrication of vertical MIM structures: with a SiO$_2$ film spacer layer (I), SiO$_2$ disc spacer where R$_{SiO_2}$ = R$_{Au}$ (II), and disc spacer with a diameter smaller than that of the Au discs, R$_{SiO_2}$<R$_{Au}$ (III).

The fabrication process of arrays of disc-on-film MIM cavities, consisting of gold discs on gold film separated by a dielectric insulator, is quite straightforward. As shown in Figure 3.1, the fabrication flow starts from cleaning substrates, the first deposition, spin coating, E-beam lithography, then second deposition, followed by lift-off. In this thesis, three kinds of disc-on-film structures, named as MIM(I)-(III) will be investigated. The only difference among MIM(I)-(III) is the different insulator configuration: a continuous SiO$_2$ film insulator for MIM(I), SiO$_2$ disc insulator with the same size as the Au disc R$_{Au}$=R$_{SiO_2}$ for MIM(II), and SiO$_2$ disc insulator with a smaller size than that of the Au disc R$_{SiO_2}$ < R_{Au} for MIM(III). The details for fabricating a disc MIM cavity array with SiO$_2$ film spacer, shown in Figure 3.1 as MIM(I) are as follows:

* **Cleaning substrates:** Glass substrates were first cleaned in sodium hydroxide aqueous solution in ultrasonic bath for 5 min and then the same volume of 35%

hydrogen peroxide was added to further eliminate the organic contaminants on the substrates, still in the ultrasonic bath for 5 min. Glass substrates were then rinsed with distilled water and immersed in clean distilled water and placed in an ultrasonic bath for 5 min. Cleaned glass substrates were dried by nitrogen gun.

* **First deposition:** Due to the poor adhesion of thermally evaporated gold to glass substrates, an adhesion layer between the substrate and gold film is necessary. Some use chemical agents to introduce active groups on the glass substrate such that the adhesion between gold film and glass substrate can be promoted. Another possibility is to evaporate a thin layer of Cr, Ti or TiO_x before the evaporation of gold. For our samples, we evaporated 3 nm of Cr as an adhesion layer. There are two kinds of evaporation: thermal evaporation and e-beam evaporation, depending on whether the target material gets heated by ohmic heating from a boat or electron bombardment of a crucible. In our experiments, the deposition was performed using the evaporator PLASSYS MEB400. In this evaporator, there are two boats for thermal evaporation and six crucibles for E-beam evaporation with auto control to select the active targeting material without opening the evaporation chamber. Usually, the noble metals are evaporated by thermal evaporation, dielectric materials and metals with high melting temperatures are evaporated with e-beam evaporation.

  The evaporation chamber was pumped till the pressure inside the vacuum chamber was $\sim 4\times 10^{-6}$ Torr. Then 3 nm Cr layer were evaporated by e-beam evaporation with a rate of 0.3 nm/s, followed by evaporation of 50 nm Au film by thermal evaporation at an evaporating rate of 0.3 nm/s, and then insulator layers sandwiched in MIM cavities were obtained by evaporating 10 nm of SiO_2 using e-beam evaporation at a rate of 0.03 nm/s.

* **Spin coating:** Polymethylmethacrylate (PMMA) is the most commonly used EBL resist. The recipe introduced here is designed for obtaining a PMMA layer with a thickness of 160 nm. 2.5 wt.% PMMA in MIBK (Methyl isobutyl ketone) solution was used. In order to obtain high quality PMMA thin films on the substrate, a two-step spin coating method was applied. A low spinning speed of 2600 rpm was applied for 6 s to spread the resist all over the substrate and roughly achieve the designed film thickness, then a high spinning speed of 5000 rpm for 60 s was used to spin off the corner beads and obtain a resist layer with the desired thickness. After spin coating the PMMA layer, the substrates are postbaked inside an oven at 150 ° C to evaporate the remaining solvent and to enhance adhesion of PMMA to the substrate as well.

* **E-beam Lithography:** Patterns with circular discs are designed, with dif-

ferent radii and different spacing distances. During an EBL process, a pattern generator and a beam blanker will control the fields of exposure and expose only the structured area with the desired exposure dose. It is crucial to align well the electron beam before the exposure is started, in order to get the desired structure features on the nanoscale. When PMMA is subjected to electron exposure, the PMMA chains break and lead to a higher solubility in MIBK. After electron beam exposure, the substrate was then immersed in a developer, consisting of MIBK (Methyl isobutyl ketone)/IPA (Isopropanol) 1:3, for 1 min 15 s, then was rinsed by IPA and dried by nitrogen gun. PMMA molecules that were exposed will dissolve in the developer and be washed away. Therefore, the development step will yield the designed pattern, and a dark-field microscope can be used to easily check if the e-beam lithography worked out due to the grating effect of ordered holes in PMMA.

* **Second deposition:** A second evaporation is necessary in order to obtain the second metal layer to form the MIM cavity. So in this step, 50 nm of gold were deposited by thermal evaporation at the rate of 0.3 nm/s.

* **Lift-off:** After the second deposition, the substrate was immersed in acetone for 1 h. The acetone attacks the PMMA resist and dissolves the PMMA resist layer over time. As a result, the superstrate including unexposed PMMA and deposited gold by the second evaporation could be gently flushed away from the substrate with a pipette. The lift-off process yields the plasmonic structure consisting of ordered MIM cavities.

3.1.1.1   Dark-field image of disc MIM cavity arrays
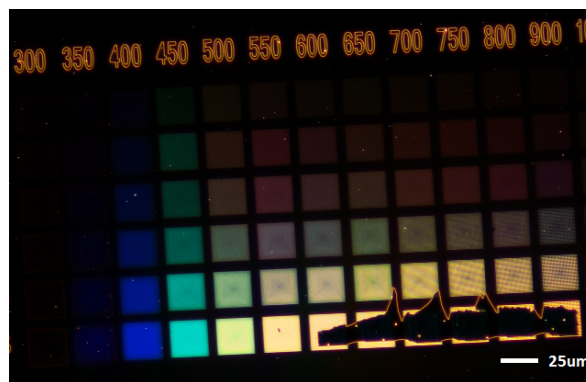
Figure 3.2: Dark field image of arrays of MIM cavities with increasing cavity radius from first row to fourth row and increasing grating constants from left column to right column. The MIM cavity consists of Au disc arrays on gold film separated here by Al_2O_3 film spacer.

A look at the nanostructures under the dark-field microscope can give a preliminary idea whether the fabrication is successful. Thanks to grating effects of the disc arrays, the nanostructures are quite bright and readily to locate. Any defect on the micrometer scale or contaminants on the nanostructure areas can be easily identified. Apart from MIM cavities with SiO_2 spacer layer, MIM cavities with Al_2O_3 insulator layer were also fabricated. Figure 3.2 shows the dark field image of MIM cavities with evaporated Al_2O_3 as an insulator layer. Different arrays of MIM cavities manifest themselves in different colors due to different plasmonic modes excitation and grating effects, resulting from different cavity radii and different grating constants. A wide range of colors from blue to red can be generated by tuning the dimensions of MIM cavities. Many works have been focused on the plasmonic color generation based on MIM structures.

3.1.1.2   SEM images of disc MIM cavity arrays

In Figure 3.1, besides the disc MIM(I) with film spacer, the fabrication steps for disc MIM(II) and disc MIM(III) are also shown. Disc MIM (II) can be obtained by simply moving the evaporation of 10 nm SiO_2 from the first evaporation (labelled as step (1)) to the second evaporation (labelled as step (4)). MIM (III) can be fabricated by wet etching MIM(II) with diluted hydrofluoric (HF) acid, details will be presented in chapter 5. These three structures were studied in chapter 5, for their different plasmonic responses and performance as applications for plasmon-assisted spectroscopy and sensing.

The geometry and dimension of the fabricated sample is crucial for numerical analysis of plasmonic modes, and also provides guidance for building the simulation cell in Comsol. However, the resolution of the optical microscope is limited by the optical diffraction limit, and nanostructures at the scale of a few tens of nanometers are beyond the imaging capability of a regular optical microscope. Scanning electron microscopy (SEM) is much more sophisticated and it is the proper method to investigate the geometrical shape and dimensions of nanostructures.

The as-fabricated MIM structures were characterized by SEM, in order to achieve a good correspondence between the simulated structures and the real fabricated structures. The radii of the gold discs and the grating constants of the disc arrays can be measured from the SEM image in top view, as shown in Figure 3.3. SEM images of a MIM(II) with a disc radius of 130 nm and a grating constant varying from 335 nm to 720 nm are shown in the first row of Figure 3.3. The second row in Figure 3.3 shows arrays of disc MIM cavities with fixed period of 530 nm and varying radii of 35 nm, 62 nm, 100 nm, 130 nm and 162 nm. The third row shows monomers of MIM cavities with different radius.
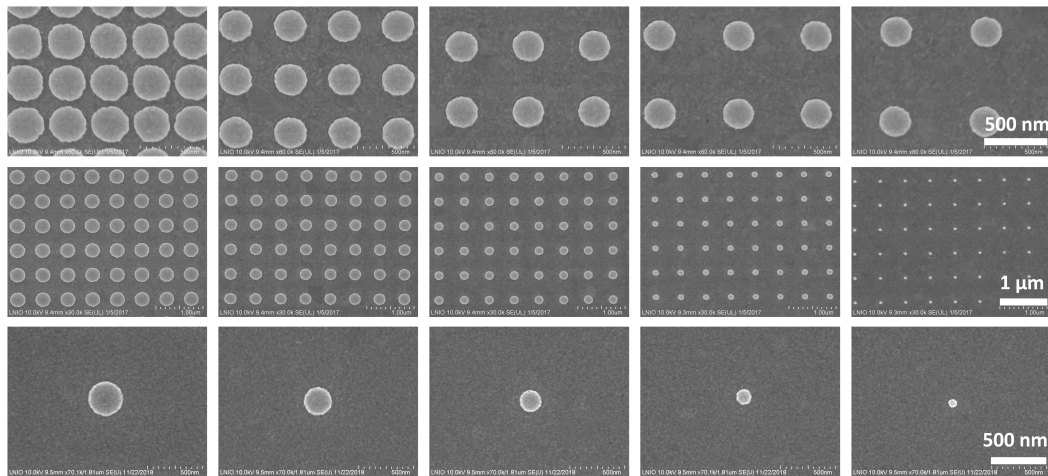
Figure 3.3: SEM images of disc MIM cavities with SiO$_2$ disc spacer. The first row presents arrays of MIM cavities with a radius around 130 nm and periods ranging from 335 nm, to 440 nm, 530 nm, 620 nm and 720 nm. The second row presents arrays of MIM cavities with a period of 530 nm and the radius varies from 162 nm, 130 nm, 100 nm, 62 nm to 35 nm. Monomer MIM cavities with radii around 169 nm, 132 nm, 103 nm, 70 nm, 35 nm are shown in the third row. Images in the same row share the same scale bar that is given in the last image of each row.
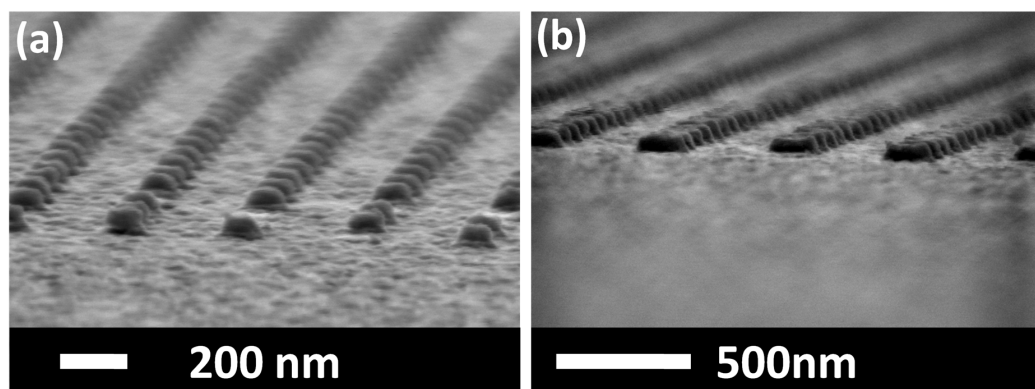
Figure 3.4: Scanning electron microscopy (SEM) images of MIM(II) structures tilted by an angle of 70°. Array of MIM cavities with a radius of 62 nm (a) and 100 nm (b), grating constant of 440 nm.

Figure 3.4 shows a side view under a tilting angle of 70°, indicating slanted side walls of the Au discs and rounded top edges, which are typical for structures fabricated by EBL and deposition. The measurement of the dimensions was always conducted as the last step of characterization, because carbonization while imaging with electron beam is inevitable, and that might influence the optical signal.

3.1.2   Vertical dimers

Investigation of localized surface plasmon resonances (LSPR) interacting with a propagating surface plasmon resonance (PSPR) supported by a gold film is possible through studying the two structures presented above, while vertical dimers provide the possibility for the study of LSPRs interacting with LSPRs. Thanks to the popular 'hot spots' excited in the gap between two laterally displaced discs, lateral dimers have been intensively studied during the last decades. Aside from the strong field enhancement and potential application for the obvious overlap of different cavity modes, vertical dimers show advantages over lateral dimers from a fabrication point of view. First of all, gaps in lateral dimers are defined by e-beam lithography, that means the gap distances below 10 nm are limited in terms of reproducibility and precise control. While gaps are created by evaporation in the vertical dimer case, this thin film technique can easily create layers thinner than 10 nm with high reproducibility and specified thickness. It is even possible to obtain sub-nano gaps with atomic layer deposition (ALD) to investigate quantum plasmonics. Second, heterodimers are the easiest way to obtain more tunability. Lateral heterodimers require high accuracy overlay e-beam lithography which means expensive equipments and experienced expertise. On the contrary, in the case of vertical dimers, only evaporation of different materials is needed.

Fabrication of vertical dimers is easier and less time consuming than nanostructures on a gold film MIM system. There are two typical ways to fabricate vertical dimers: the etch mask transfer method and the lift-off method.

3.1.2.1   Etch mask transfer method

To fabricate vertical dimers using the etch mask transfer method, firstly, 3 nm of Cr, 40 nm of gold, 10 nm of dielectric material and a second layer of 40 nm of gold were subsequently deposited on cleaned glass substrates. Then PMMA was spin coated on the substrates with the same parameters as showed earlier, followed by standard E-beam lithography. After development, instead of building materials such as a gold layer or insulator layer, a sacrificial layer of Al_2O_3 was evaporated to be the milling

mask for the later milling process. Argon ions will etch away unprotected gold. The sacrificial Al_2O_3 mask is subject to the attack of argon ions as well and being etched thinner with a much smaller rate compared to the milling rate of gold. Al_2O_3 was removed by chemical etching with ma-D 331 (developer) subsequently after milling.

3.1.2.2 Lift-off method

Bottom up fabrication of vertical dimers is very similar to the fabrication processes stated above. First, glass substrates were cleaned and PMMA was spin coated onto the glass surface. Different from the samples prepared above, there is no conducting layer on the glass substrate, as a result the electrons will accumulate on the substrate and display strong charging effects. There are different methods to circumvent this charging problem and do e-beam lithography on non-conductive substrates. One method is to deposit a layer of Indium Tin Oxide (ITO) on the glass substrate to introduce conductivity. Another method is to deposit either a thin aluminium layer or conductive polymer on the PMMA covered substrates. For the vertical dimers fabricated here we mainly used conductive polymer (PEDOT:PSS) to get rid of charging problems considering that spin coating a thin layer of conductive polymer is more time-effective compared to evaporating aluminium using a evaporation machine where a good vacuum is demanded. A layer of conductive polymer was spin coated on substrates with the same parameters used for PMMA. The conductive polymer is aggressive to PMMA and can attack the resist layer, so the time when condutive polymer was in contact with PMMA is restricted in order to make well defined and reproducible nanostructures.

Electron beam lithography was then performed, followed by washing away the conductive polymer with deionized water and then development of PMMA. For the deposition, 3 nm of Cr, 40 nm of gold, 10 nm of dielectric material (either SiO_2 or Al_2O_3) and another 40 nm of gold were deposited in sequence. Lift-off then revealed the vertical dimers. Figure 3.5 shows SEM images of vertical dimers.

3.2 Determination of geometrical parameters by FIB

The thickness of the insulator spacer sandwiched in MIM cavities was crucial for numerical analysis of the plasmonic responses of cavity MIM structures, because the confinement of the near-field inside the cavity scales with d^{-3}, where d is the thickness of the insulator layer [1]. Ellipsometry was also used to determine the thickness of the SiO_2 film spacer layer. However, MIM cavity structures are too complicated with too many variables to be determined: the thicknesses of the gold film t_{Au} and SiO_2
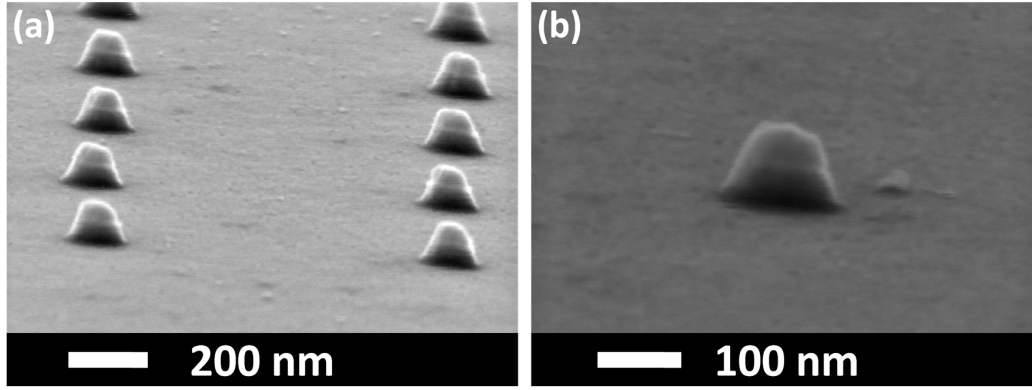
Figure 3.5: SEM images of MIM dimers at a tilting angle of 45°.

layer t_{SiO_2}, the optical constants of evaporated gold and SiO_2. On the other hand, a cross-section obtained by focused ion beam milling is a straight-forward way to check the thickness of the thin dielectric layer, and the other geometrical information such as the slanted angle of the slanted side walls and the curvatures for the round edges of the gold disc can be obtained from the cross-section as well.

A helium ion microscope (HIM) was our first choice to obtain cross sections of MIM cavities due to its high milling resolution, which allows us to cut any selected MIM cavity. However without a sacrificial superstrate, the redeposition of milled gold leads to strong deformation of the milled structure. So in this thesis, we finally used a focused gallium ion microscope (GIM) to accomplish the cross section, even though the milling resolution (~ 50 nm) is much lower compared to HIM.

Figure 3.6 shows the SEM images of the same array of MIM cavities after each step. To achieve a clear cut, the structures were covered with a platinum sacrificial layer first and subsequently cut with a focused gallium ion beam. The deposition of a platinum layer is crucial for two reasons: to get rid of the deformation of MIM structures from redeposition and to compensate for the low cutting resolution, in order to get a clear cross section image at the region of MIM cavities. Figure 3.6 (a),(c-f) were obtained by electron beam imaging at a tilted angle of 52°, and Figure 3.6 (b) was achieved with FIB imaging from the top. (Methylcyclopentadienyl)trimethyl platinum vapour was introduced as precursor gas to deposit the platinum layer. The FIB induced deposition is much more efficient than electron beam induced deposition (EBID) due to the much higher energy of the gallium ion beam. However, there is a risk that the ion beam would destroy the gold MIM cavities while depositing platinum. So we applied EBID to firstly achieve a platinum layer of ~ 300 nm, as shown in Figure 3.6 (a), to protect the MIM cavities from the ion beam. Then FIB induced deposition was performed to obtain efficiently a thick platinum layer of ~ 800 nm, as in Figure 3.6 (b). In Figure 3.6 (c), a preliminary cross section cut was performed parallel to the edges of MIM cavities
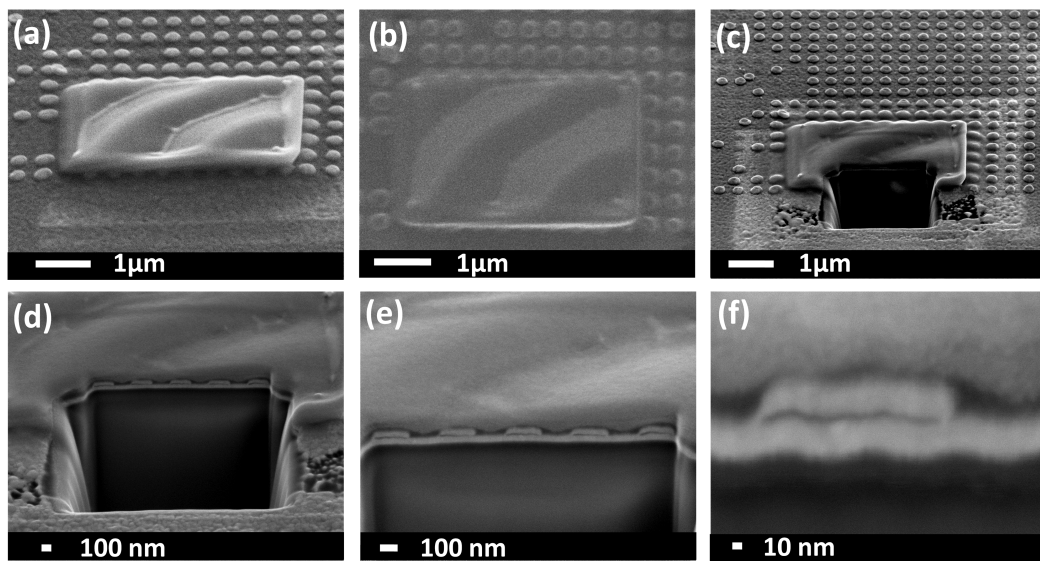
Figure 3.6: SEM images (a), (c-f) at a tilting angle of 52° and FIB image (b) from top view of MIM cavities after each step in order to achieve a cross section by GIM. (a) ~ 300 nm of platinum were deposited by electron beam induced deposition (EBID) at an area of 4 $\mu m \times 4\mu m$. (b) ~ 800 nm of platinum were deposited by FIB (ion-beam) induced deposition at the same area as in (a). (c) A preliminary cross-section cut of 3 $\mu m \times 2\mu m$ was performed at the edge of certain MIM cavities. (d) Cross sections with fine steps were performed in order to obtain a cross-section at the center of MIM cavities. (e) A series of fine polishes of the cross section were performed in order to have a clean cross section. (f) A zoomed in cross section image of a MIM cavity. (Acknowledgement to Dr. Ronny Löffler for kind collaboration)

at a certain row in the array. The MIM cavities outside of the platinum layer can serve as a reference. This is followed by a series of cross section cuts with small steps to get close to the center of the selected MIM cavities, as shown in Figure 3.6 (d). In Figure 3.6 (e), the structures were tilted for - 2° relative to the focused ion beam, a series of very fine polishes of the cross section were performed in order to clean the cross section and get rid of contaminants from redeposition. Figure 3.6 (f) shows a zoomed in image of a MIM cavity. The cross section of the gold film, the discs and the spacer can be clearly seen in Figure 3.6 (e-f). The cross section images obtained by FIB cutting will give us a guidance to design the simulation cell, which is presented in section 3.4, in order to have a better correspondence between experimental and simulated structure. I would like to thank Dr. Ronny Löffler for his help and contribution in this FIB cross sectioning experiment.

3.3   Optical characterization

The optical properties of plasmonic nanostructures can be characterized by many methods in the far-field and near-field. In the far-field regime, the reflection, extinction (or transmission) and scattering of nanostructures can be investigated. These far-field characterizing methods are easy to perform and can provide us with preliminary information about the plasmonic resonance wavelength, intensity and damping. The near-field properties of plasmonic structures can be studied by scanning near-field optical microscope (SNOM) or by near-field enhanced physics phenomena. These optical characterizations not only help to understand the dependency of plasmonic structures on the geometry parameters, but also open up the possibility for applications such as plasmonic sensing in the far-field regime and SERS and others in the near-field regime.

3.3.1   Extinction measurements

Extinction spectroscopy is the most accessible method in the laboratory to obtain information about plasmonic resonances. Optical extinction spectra are usually achieved by measuring the percentage of light transmitted through a plasmonic sample as a function of the wavelength/frequency of the incident light. The explicit expression for extinction is

$$Extinction = 1 - Transmission = Absorption + Scattering \qquad (3.1)$$

The schematic for the layout of an extinction (or transmission) setup is shown in Figure

3.7. The white light source is collimated and then illuminated on the structures from the normal angle. The transmitted light is then gathered by a collecting objective and then focused through a lens, and passed into the spectrometer. In our experiments, the numerical aperture for the collecting objective is 0.9. The light source is a laser driven lamp (ENERGETIQ EQ-99 LDLS) which provides a stable spectral range from 200 nm to 1100 nm.
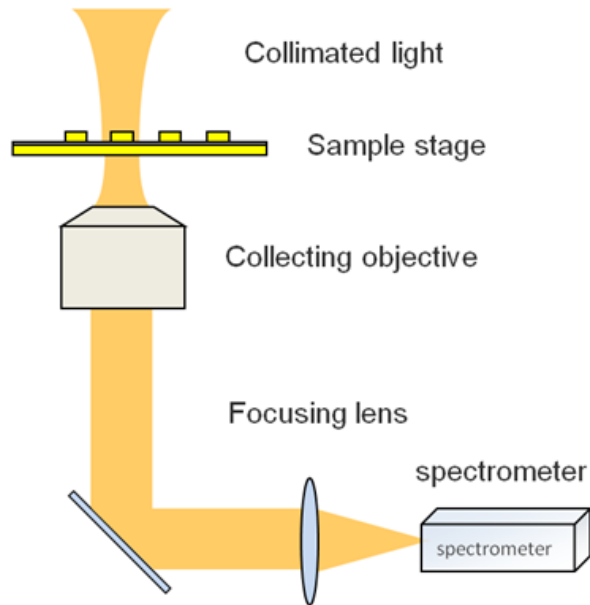
Figure 3.7: Schematic of the layout of an extinction measurement.

$$Extinction = \frac{T_{film} - T_{MIM}}{T_{film} - I_{dark}} \tag{3.2}$$

In this thesis, both in experiments and simulations, the extinction was evaluated as in equation 3.2. T_{film} represents the transmission through only the Au film, which is also widely referred to as reference. T_{MIM} represents the transmission through the MIM cavities array, I_{dark} means the intensity of the intrinsic dark signal of the spectroscopy. In the extinction spectra presented in this thesis, the disc arrays on gold film MIM cavities sometimes show negative extinction. This is due to the fact that the transmitted incident radiation gets Fano modulated by the narrow cavity plasmon modes, which will be demonstrated in detail in section 4.6.

3.3.2   Reflection measurements

A reflection set-up is another way to obtain information about the plasmonic resonance. The plasmonic nanostructure can act as an optical antenna to convert incident

light into evanescent fields bound at the metal/dielectric interface, meanwhile, the excited plasmons can as well re-radiate their energy into the far-field as scattering. The schematic of the layout for reflection measurements is usually very similar to the one for extinction, except the collecting part is at the same side as the illuminating part, and the incident light is usually focused with an objective. Figure 3.8 shows two con-
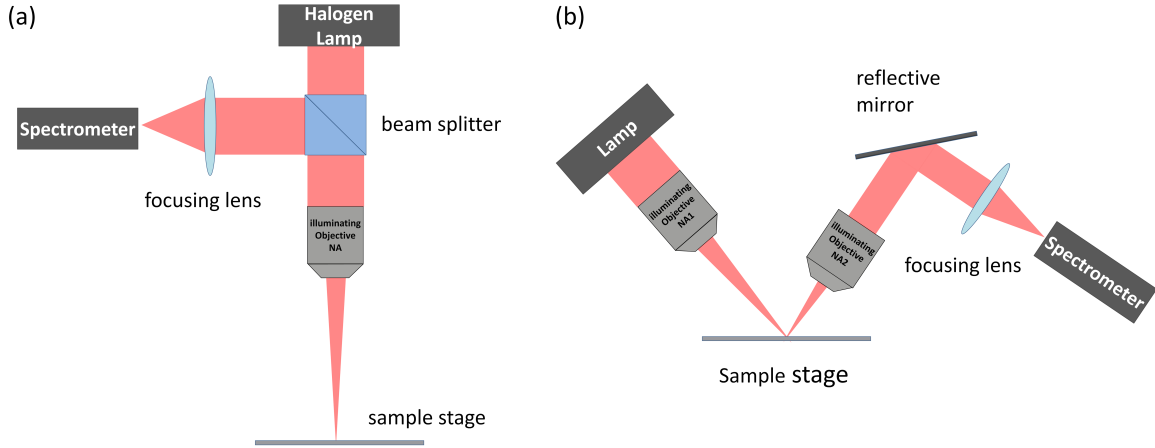
Figure 3.8: Schematic of the layout of reflection measurements. (a) Reflection set-up with normal incidence; (b) Reflection set-up with tilted incidence

figurations for reflection measurements with different illuminating angles: (a) normal incidence and (b) tilted illumination. In our experiment, reflection is measured using configuration (b) with an illuminating angle of 18.5°. The reflection measurement setup is combined with the extinction setup stated above, sharing the same white light source and the collecting part. The numerical aperture of the collecting objective is 0.42. And the same light source as in Figure 3.7 is used.

$$Reflection = \frac{R_{MIM} - I_{dark}}{I_{lamp} - I_{dark}} \tag{3.3}$$

The measured and simulated reflection spectra were evaluated as in equation 3.3, where I_{lamp} is the lamp intensity, R_{MIM} means the reflection on an array of MIM cavities and on gold film, respectively. The I_{lamp} is recorded in experiments by using a Teflon plate to reflect the lamp light.

3.3.3 Scattering measurements

In many cases, the positions of far-field extinction/reflection peaks and dips do not correspond to the near-field resonance position, resulting from the radiation damping and far-field interaction with the incident radiation [103, 153–155]. Scattering measurements are more straightforward to obtain the plasmonic resonance characteristics

compared to extinction and reflection, due to the fact that the transmitted/reflected continuum is blocked and any optical signal recorded is purely contributed by the decay of plasmons into photons. There are generally three types of dark-field micro-
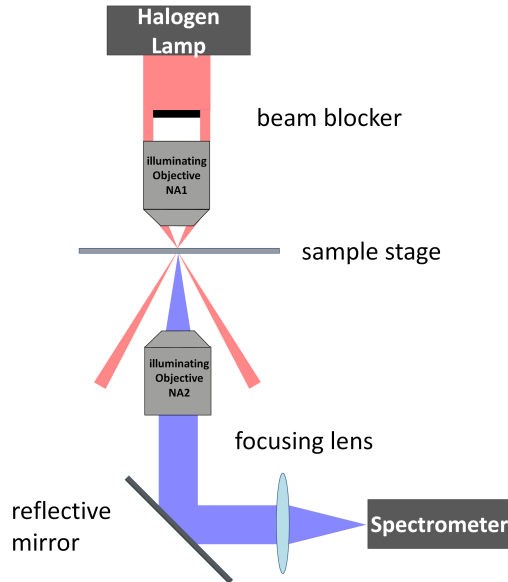
Figure 3.9: Schematic of the layout of transmission scattering measurements

scope based on different configurations: transmission dark-field microscope, reflection dark-field microscope and total internal reflection dark-field microscope.

In this thesis, the dark-field microscope in Figure 3.9 was used to investigate the cavity modes in MIM cavities of different cavity radius and different periodicity. Configuration details for the dark-field microscopy are as follows:

The numerical aperture (N.A.) of the condenser lens is 0.85-0.95, corresponding to illumination angles of 58° - 72°, and the N.A. of the collecting objective is 0.7. The light source is a Halogen lamp.

The scattering spectra were evaluated as in equation 3.4:

$$Scattering = \frac{S_{MIM} - I_{dark}}{I_{lamp} - I_{dark}} \qquad (3.4)$$

where S_{MIM} means the scattering from a MIM structure. Due to the near-field distribution of different plasmonic modes, the excitation efficiency of different plasmonic modes varies with different illuminating angles. For instances, the LSPR mode with strongly localized near-field on the top of the gold disc will dominate the scattering spectra when the incident angle is small, while the cavity plasmon modes will dominate at almost grazing incidence. The details will be presented in chapter 4.

3.3.4   Raman spectroscopy

A Raman spectrometer LabRAM HR800 from HORIBA Jobin Yvon (L2N, UTT) was used to record the SERS signal in our experiments. This Raman microspectrometer is based on a confocal optical microscope. A schematic of the layout of this confocal Raman microspectrometer is as shown in Figure 3.10
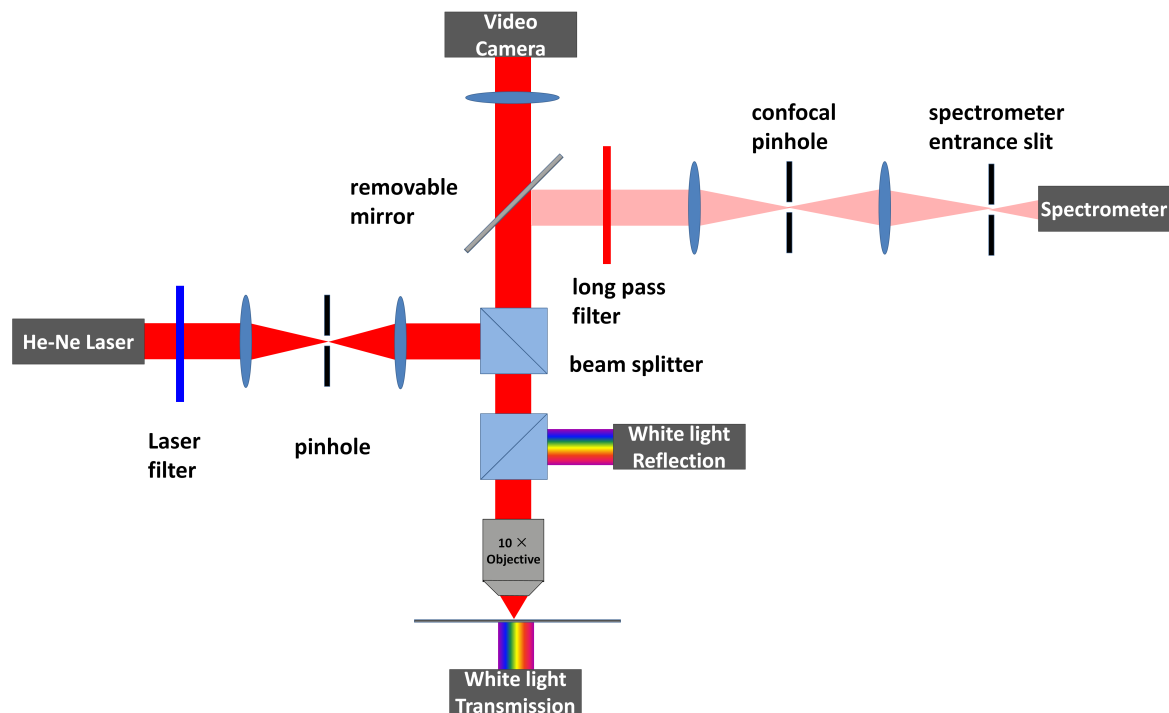
Figure 3.10: Schematic of the layout of a confocal Raman microspectrometer.

A pinhole is placed in front of the spectrometer at the image plane of the input pinhole, so that the signal from outside of the focal plain will not be collected and a better resolution can be achieved. The laser used for excitation is a built-in He-Ne laser, with the output wavelength of 632.8 nm and output power of 8.3 mW. There are a set of neutral filters to decrease the laser power by 2, 4, 10, 100, 1000 and 10000 times. The scattering signal is collected in backscattering configuration. The elastic Rayleigh scattering is blocked by two edge filters. The collected SERS signal is input through a diffraction grating and then to a nitrogen cooled CCD. There are three diffraction gratings with different grating constants to be chosen from, 300, 600 and 1800 lines/mm. Different gratings applied in the Raman measurements lead to a different resolution and spectral range of the SERS spectra. The confocal pinhole can be tuned between 0-1000 µm.

The sample stage is controlled by piezo motors, which enables the stage to move in plane with fine steps. Together with the advantage of the confocal Raman spectroscope, a three-dimensional material can be reconstructed based on a series of optical sections.

Before measuring the Raman signal of our substrate, it is very important to turn on the laser for at least 15 min until the laser power is stable. Then it is crucial to calibrate the Raman spectrometer so that the Raman shift is reliable in the measurements. The calibration of the Raman system is realized by measuring the very intense Raman band of a silicon substrate at 520.7 cm^{-1} and the laser wavelength at 632.8 nm. The acquisition time can be set accordingly. Each spectrum can be set to be averaged over a certain amount of measurements.

If not stated otherwise, all the SERS signal throughout this thesis is recorded under the measuring configuration : the confocal hole is set to 1000 μm, the entrance slit is set to 200 μm, the 600 lines/mm diffraction grating and 10× objective are used. The main SERS measurements will be presented in chapter 7.

3.4 Simulation methods

Coupled plasmonic structures give very complicated plasmonic responses. In order to understand the physics that lies behind the sensing and near-field enhancing capability, it is important to gain insight into the nature of the modes. On the other hand, if the simulations are proven to be in good agreement with experiments, we can also use the simulation as a more efficient way to optimize the geometry of MIM cavities according to different situations. In this thesis, simulations were performed using Comsol Multiphysics, which is based on the finite element method (FEM). FEM is one of the most popular EM solvers, and it is suitable for analysis of antenna performance and geometry at the subwavelength scale. Simulations were performed for MIM structures with different geometries, in order to investigate their influences on the field distribution and the resonance wavelength of plasmonic modes.

Figure 3.11(a) shows the simulation cell for the arrays of MIM(II), for a disc base radius (R_{Au}) of 130 nm. The geometrical parameters were determined by characterization techniques in section 3 in order to achieve a good resemblance between experiments and simulations. The side wall of the Au disc was designed to show a 75° slope instead of vertical side walls, as in Figure 3.11(b), while the SiO$_2$ disc shows a slope of 45°. As has been presented in section 3, the slanted side walls and rounded corners are inevitable for substrates fabricated by EBL and evaporation. According to our experiences, the evaporation rate plays an important role in determining the slanted degree of the side walls. The big evaporation rate difference between Au and SiO$_2$ leads to the different slanted angles. The top edge was rounded with a curvature of a circle with a radius of 5 nm. The thickness of the Au film (t_{film}) and height of the Au disc (t_{disc}) are t_{Au} = 50 nm, fixed for all the structures in this work. The refractive index of the glass
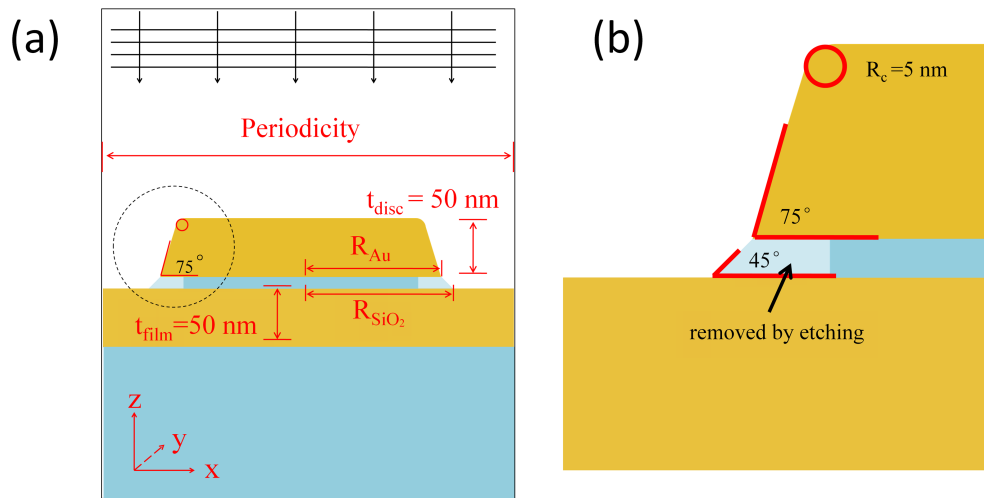
Figure 3.11: Schematic of simulation unit for MIM(II) in Comsol Multiphysics. (a) The simulation cell of dimension P×P is shown. The periodic boundary conditions are applied at the four faces of the simulation cell to simulate square arrays of MIM structures. The incident field is a plain wave under normal incidence, and it is linearly polarized along the y direction. Based on the SEM and FIB images, the side wall of the Au disc is designed to show a 75° slope as in Figure 3.11(b), while the SiO_2 disc shows a slope of 45° due to smaller evaporation rate. The thickness of the gold film t_{film} and the height of the Au disc t_{disc} are both t_{Au}= 50 nm. The cavity height (t_{SiO_2}), radius of the MIM cavity (R_{Au}) and periodicity (P) can be varied in fine steps, in order to investigate the evolution of plasmonic resonance as a function of geometrical parameters.

substrate and the SiO_2 insulator layer is set to a constant value of 1.5 over the calculated spectral range. The refractive index of Au is adapted from Johnson and Christy [99]. The incident source is a linearly polarized plane wave under normal incidence. Periodic boundary conditions were applied at the four faces of the simulation cell to simulate square arrays of MIM structures.

The cavity height (t_{SiO_2}), radius of the MIM cavity (R_{Au}) and periodicity (P) can be varied in fine steps, in order to investigate the evolution of the plasmonic resonances as a function of geometrical parameters. Similar parameters are used for the simulations of MIM(I)-(III), only with different insulators sandwiched between Au discs and Au film, such that the influence of the insulator configurations on the location of 'hot spots' and the resonance wavelength can be studied, which will be presented in Chapter 5 and 7. For the simulation of MIM(III), the radius of the SiO_2 discs spacer (R_{SiO_2}) is designed to be half the diameter of the Au discs (R_{Au}), if not stated otherwise.

3.5   Conclusion

In this chapter, the methods and techniques which were used in this thesis were presented. First of all, the fabrication processes for different MIM systems including Au disc on film and vertical disc dimers, were demonstrated. The EBL technique was applied to define the pattern, including the disc radius and periods, and then evaporation was used to transfer the pattern from the resist to the MIM structures. Gap distances of $\sim$ 10 nm can be easily achieved with well-established evaporation techniques with high accuracy and reproducibility. Different optical methods have been introduced to study the plasmonic properties of the as-fabricated MIM structures.

The far-field characteristics of plamonic modes can be studied by extinction, reflection and scattering methods. These far-field characterization methods can show different characteristics of plasmonic resonances due to different excitation and measuring configurations, thus these methods in combination provide a more systematic study of the plasmonic modes in MIM cavities. This will be the main topic of chapter 4. Raman spectroscopy is a powerful analytical tool which is based on the near-field characteristics of plasmonic resonances. Through Raman measurements, the near-field intensity as a function of MIM cavity radius, and different insulator geometries can be demonstrated without a SNOM.

In composite nanostructures such as gold discs on gold film separated by an insulator layer, many plasmonic modes of different natures can be excited and identified from optical measurements. In order to understand the far-field and near-field properties of

different plamonic modes, simulations were performed to provide an insight into the different resonance characteristics of different plasmonic modes. SEM and FIB were conducted to obtain the geometrical parameters of the fabricated MIM cavities, and provide a guidance for the designing of the simulation cell.

Chapter 4

Cavity plasmon modes in MIM cavities

In a coupled system like a vertical MIM structure, many different kinds of plasmonic modes can be excited with proper illumination configurations. The surface plasmonic resonance wavelengths are strongly dependent on the geometrical parameters of the nanostructures and the excitation conditions. For instance, the grating introduced SPP modes can be excited both on the substrate/metal and the insulator/metal interfaces, and the resonant wavelength λ_{SPP} can be tuned by changing the grating constant, illumination angle and substrate refractive index.

In Ref. [91], the LSPR modes appearing at $\sim$ 520 nm to 550 nm for different gold disc radius and periods have been studied. This LSPR mode with 'hot spots' on the top of the gold disc arises from the hybridization of a dipolar mode and quadrupolar mode [156]. The surface plasmon polaritons at a metal/dielectric interface induced by a square grating have been thoroughly studied as well. The resonance of the SPP can be determined by [1, 157]

$$\lambda_{res} = \frac{P}{\sqrt{i^2 + j^2}} \sqrt{\frac{\epsilon_m \epsilon_d}{\epsilon_m + \epsilon_d}} \tag{4.1}$$

where ϵ_d and $\epsilon_m(\lambda)$ are the dielectric constants of the dielectric and metal, P represents the periodicity of the square grating, and i and j are the integers implying the orders of SPP resonance.

The surface lattice modes, resulting from the far-field interaction of nanostructures in an array, have been studied in square gratings as well. This SLR mode is also referred as Rayleigh and Wood anomalies, usually associated with diffraction from a metallic

grating [3, 158]. The resonance position of the SLR can be predicted by

$$\lambda_{slr} = \frac{P}{\sqrt{i^2 + j^2}} \sqrt{\epsilon_d} \tag{4.2}$$

In this chapter, the cavity plasmon modes of MIM cavities will be the main object of study. The cavity plasmon modes in MIM cavity arrays will be studied by different optical measurements. Figure 4.1 shows the measured reflection spectra for MIM(I)
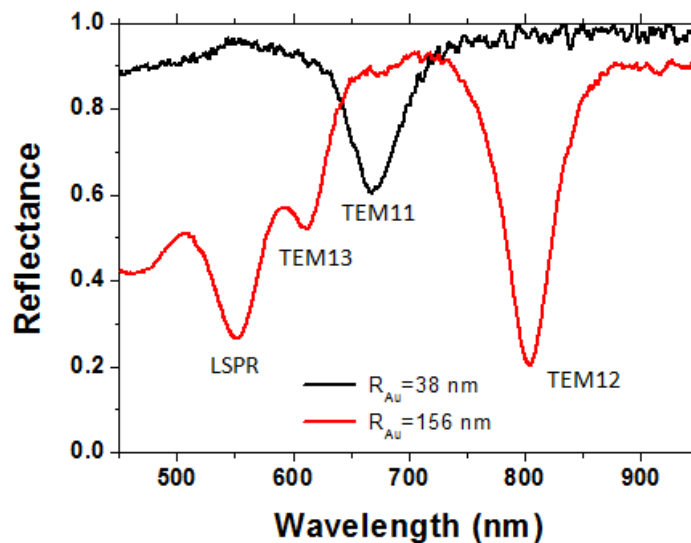
Figure 4.1: Measured reflectance of MIM(I) cavity arrays with R_{Au}=38 nm (black curve) and R_{Au}=155 nm (red curve), the periodicity is P=440 nm, and the cavity height is t_{SiO_2}=15 nm. The nature of different modes are labelled accordingly and the rule of nomenclature will be presented in the following section.

cavities with a cavity radius of 38 nm (black curve) and 155 nm (red curve), respectively. The periodicity and cavity height are kept the same as: P=440 nm and t_{SiO_2}=15 nm. For smaller MIM cavity, the spectra is simple with only one pronounced plasmonic mode, which is similar to the dipolar mode for Au disc nanostructures. For MIM cavity array with R_{Au}=155 nm, there are a sequence of well-defined plasmonic modes with surprisingly narrow bandwidth for such a large nanostructure. More reflection measurements and detailed interpretation will be given in section 4.4. In order to understand the fundamental physics in this coupled system, FEM simulation with Comsol Multiphysics is performed. The simulation can as well provide a guidance for the design of optimal samples according to different application situations in the future work. For simplicity, the cavity plasmon modes were studied in disc MIM(I) systems where the cavity plasmon modes are distributed in a homogeneous insulator (continuous SiO_2 film), if not stated otherwise.

4.1 Cavity plasmon modes in circular MIM cavity

4.1.1 Field description of cavity plasmon modes

In section 2.3, the theory about cavity plasmon modes in 1D, 2D and 3D plasmonic nanocavities has been presented. The cavity plasmon modes arise from the interference of counter-propagating SPPs, which are reflected at the edges of plasmonic cavities. In vertical MIM structures, the cavity plasmon modes arise from the interferences of outgoing and incoming gap surface plasmons which get reflected at the edges of MIM cavities. In the scope of this thesis, the cavity height (t_{SiO_2}) is a few tens of nanometers maximum, $t_{SiO_2} \ll \lambda_{gsp}$. There will be no longitudinal mode excited along the cylindrical cavity axis. Thus, the MIM cavity studied in this thesis can be seen as a 2D circular cavity.
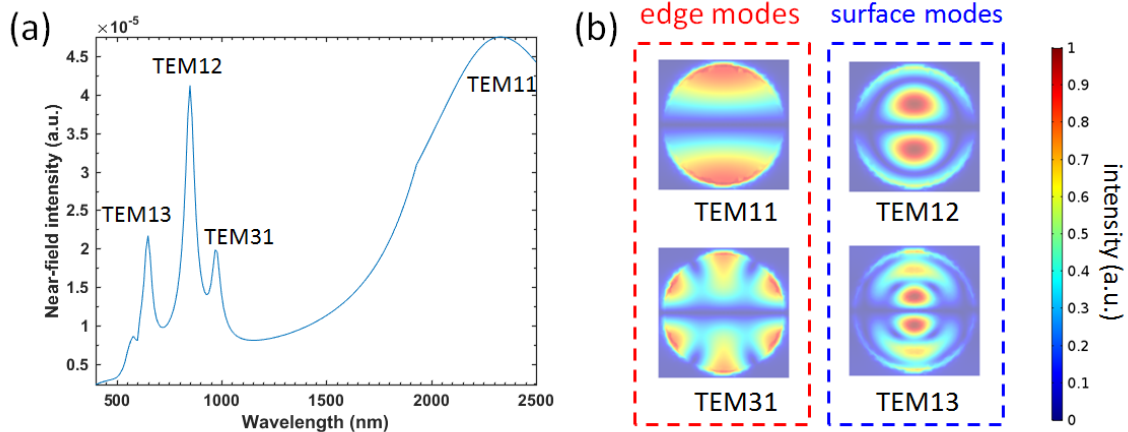
Figure 4.2: (a) Simulated near-field resonance spectrum for a MIM(I) structure with a cavity radius of R_{Au}=160 nm, a cavity height of t_{SiO_2}=10 nm, a periodicity of P=350 nm. The near-field intensity is integrated on the bottom surface of the Au disc. The cavity plasmon modes are labelled in the spectra and corresponding field maps at the resonance wavelengths are shown in the right panel (b). Two sets of cavity plasmon modes are distinguished: edge modes and surface modes.

Figure 4.2 shows the near-field resonance spectrum which was obtained by Comsol simulations for a disc MIM(I) structure with a cavity radius of R_{Au}= 160 nm, a cavity height of t_{SiO_2}=10 nm, a periodicity of P=350 nm. The near-field was integrated at the bottom of the gold disc. The cavity plasmon modes are labelled by TEMmn, where m and n are the angular and radial mode index denoting the numbers of full-wave patterns along the circumferences and the diameters of the MIM cavity, respectively. The near-field maps at each resonance wavelength are shown in the right panel of Figure 4.2. The field maps show very clear standing wave characteristics and resemble those in a dielectric FP cavity.

The theory of the cylindrical dielectric FP cavity is well established [150]. In Ref. [90], it is presented that the cavity modes have asymmetric charge distributions on the two Au/insulator interfaces. So the electric field inside the cavity is primarily perpendicular to the metal film, and the electric component $E_z(\rho, \phi, z)$ dominates. Therefore the cavity plasmon modes are TM modes. The field distribution in a circular cavity confined by parallel plates made of a perfect electric conductor (PEC) and a perfect magnetic conductor (PMC) has been described by the first-order Cohn model [133, 137, 149, 159]. Relating to the field distribution in a dielectric FP cavity, the E_z field components of TM modes in a MIM cavity can be written as a product of three functions in cylindrical coordinates as: [133, 159]

$$E_z(\rho, \phi, z) = P(\rho)F(\phi)Z(z) \quad = J_m(k_{gsp}\rho)(\cos m\phi + \varphi)[Ae^{k_z z} + Be^{-k_z z}] \qquad (4.3)$$

where k$_{gsp}$ means the wave vector of the propagating gap modes in the MIM cavity, and m is an integer to indicate the mth Bessel function J$_m$. ik$_z$ is the wave vector of the gap surface plasmon which is a evanescent wave. $P(\rho)$, $F(\phi)$ and $Z(z)$ are the field function along the radial, azimuthal and vertical direction. $\varphi = 0$ or $\pi/2$ represents degenerate cavity modes rotated by $\pi/2m$. The other field components can be obtained by simple differentiation based on Maxwell's equations, detailed expressions can be found in [159]. For PEC cavity reflectors, E$_z = 0$ and $\hat{n} \times E_s = 0$ is required on the PEC cylindrical surface [159, 160]. Thus the Neumann boundary condition: $\partial E/\partial \rho = 0$, needs to be satisfied on the PEC surface. It can be expressed as [133, 137, 149, 159]:

$$\partial E/\partial \rho \mid_{\rho=R_{Au}+\Delta R} = J'_m(k_{gsp}\rho) \mid_{\rho=R_{Au}+\Delta R} = 0 \qquad (4.4)$$

where J$_m$' is the derivative function of the mth Bessel function. R_{Au} is the radius of the gold disc and ΔR is induced by the phase shift upon reflection at the disc edge, so $R_{Au} + \Delta R$ is the resonance radius of the circular FP cavity. By combining the field distribution in equation 4.3 and the boundary condition equation 4.4, the resonance condition of a cavity plasmon TEMmn mode can be expressed as [133, 137, 149, 159]

$$k_{gsp}(R_{Au} + \Delta R) = \chi'_{mn} \qquad (4.5)$$

where χ'_{mn} is the nth root of the derivative function of the mth Bessel function. The TEMmn modes represent cavity plasmon modes with m full-wave patterns along the circumference, and n full-wave patterns along the diameter, respectively. The values of χ'_{mn} for the TEMmn modes are listed in Table 4.1. The TEM0n modes are not discussed in this thesis because they are not excited in our system with linear polarization and normal incidence.

Table 4.1: Values of χ'_{mn} for TEMmn modes of a circular cavity

m	χ'_{m1}	χ'_{m2}	χ'_{m3}
0	3.8317	7.0156	10.1735
1	1.8412	5.3314	8.5363
2	3.0542	6.7061	9.9695
3	4.2012	8.0152	11.3459

4.1.2 Edge modes and surface modes

In Figure 4.2(a), two sets of modes are excited. On one hand, there are TEMm1 modes with modal lobes along the circumference of a circular cavity (analog to whispering gallery modes in acoustic cavities), such as TEM11 and TEM31 mode as in Figure 4.2(b), which are referred to as edge cavity modes. The TEMm1 mode when m is an even integer are dark modes with an net dipole moment of 0, so they do not show in optical spectra. This is why TEM21 is missing in Figure 4.2(a). On the other hand, there are the TEM1n modes referred to as surface cavity modes, including TEM11, TEM12 and TEM13 mode. These surface cavity modes possess modal lobes along the diameter of the cavity, with most of the near-field energy residing in the central modal lobes rather than the edge lobes, which can be observed in Figure 4.2(b). The different field distribution characteristics of edge modes and surface modes determine their very different response upon decreasing the insulator radius R_{SiO_2}, RI sensing capabilities and SERS EF, which will be discussed in detail in chapter 5, chapter 6 and chapter 7, respectively.

The lowest order cavity mode TEM11 appears at an infrared (IR) wavelength of 2330 nm. In the case of edge cavity modes, the higher order modes shift to a shorter wavelength with increasing χ'_{mn}. TEM11 and TEM31 modes appear at 2330 nm and 970 nm, while χ'_{11}, χ'_{31} equal to 1.8412, 4.2012, respectively. In the case of surface cavity plasmon modes, the resonance wavelength shifts from 2330 nm, 850 nm to 650 nm for TEM11, TEM12 and TEM13 modes, respectively, while the values of χ'_{11}, χ'_{12}, χ'_{13} are 1.8412, 5.3314, 8.5363. This observation agrees well with the prediction of equation 4.5.

In Table 4.2, the χ'_{mn} are presented for each TEMmn mode, then the corresponding k_{gsp} are calculated based on the resonance condition equation 4.5, while assuming $\Delta R = t_{SiO_2} = 10$ nm which can be estimated from the field map in Figure 4.4(b). In Figure 4.4(b), it can be observed that most of the near-field of the cavity plasmon modes is inside the MIM cavity defined by the two Au/SiO_2 interfaces and the edge of the Au disc. Nevertheless, part of the near-fields is distributed beyond the physical radius of the Au disc and lies a bit outside of the physical cavity (ΔR), which is

Table 4.2: The k_{gsp} and resonance wavelength λ_0, and resonance frequency ν_0 of cavity plasmon modes TEMmn in Figure 4.2.

TEMmn	TEM11	TEM12	TEM13	TEM31
χ'_{mn}	1.8412	5.3314	8.5363	4.2012
$k_{gsp} = \frac{\chi'_{mn}}{160+10}$ (nm^{-1})	0.0108	0.0314	0.0502	0.0247
λ_0 (nm)	2330	850	650	970
ν_0 (THz)	129	309	353	462

referred to as a fringe field later. We note that ΔR can be considered as induced by the phase shift upon reflection at the MIM cavity edge, and it is a complicated variable depending on many parameters. Here for simplicity, we assume $\Delta R = t_{SiO_2}$ based on the estimation from the fringe field in Figure 4.4(b). More details about ΔR will be presented in section 4.4.2. The resonance wavelengths λ_0 are read from the simulation results in Figure 4.2 for each TEMmn mode and then the resonance frequencies ν_0 are calculated according to $\nu_0 = c/\lambda_0$, where c presents the speed of light in vacuum.

4.1.3   Dispersion of infinite MIM waveguide and cavity modes

The dispersion of an infinite MIM waveguide with a core (dielectric layer) thickness of t_d and cladding (Au layer) thickness of t_m can be described by: [133, 161]

$$\frac{k_m \epsilon_d}{k_d \epsilon_m} = \frac{-1 + \sqrt{e^{-2t_d k_d} + e^{-2t_m k_m} + e^{-2t_d k_d - 2t_m k_m}}}{1 + \sqrt{e^{-2t_d k_d} + e^{-2t_m k_m} + e^{-2t_d k_d - 2t_m k_m}}},$$
$$k_{m(d)} = \sqrt{k_{gsp}^2 - \epsilon_{m(d)}\omega^2/c^2} \tag{4.6}$$

where $t_d = t_{SiO_2}$ and $t_m = t_{Au}$.

Figure 4.3 shows the dispersion curves for infinite MIM waveguides with different core thicknesses t_{SiO_2}, which is indicated by the colorbar. The author will come back to this figure in section 4.2.2 and section 4.5.

The eigen frequencies of a FP cavity with a resonance radius of $R+\Delta R$ can be expressed as:

$$k_{gsp} = \frac{\chi'_{mn}}{R_{Au} + \Delta R} \tag{4.7}$$

In Figure 4.4(a), the discrete eigenvalues of a circular FP cavity with a resonance radius of $R_{Au} + t_{SiO_2}$ are shown by black dotted lines which are calculated based on equation 4.7. The dispersion curve of a MIM waveguide with a core thickness of t_{SiO_2} and a cladding thickness of t_{Au} are shown by the solid black curve which is calculated based on
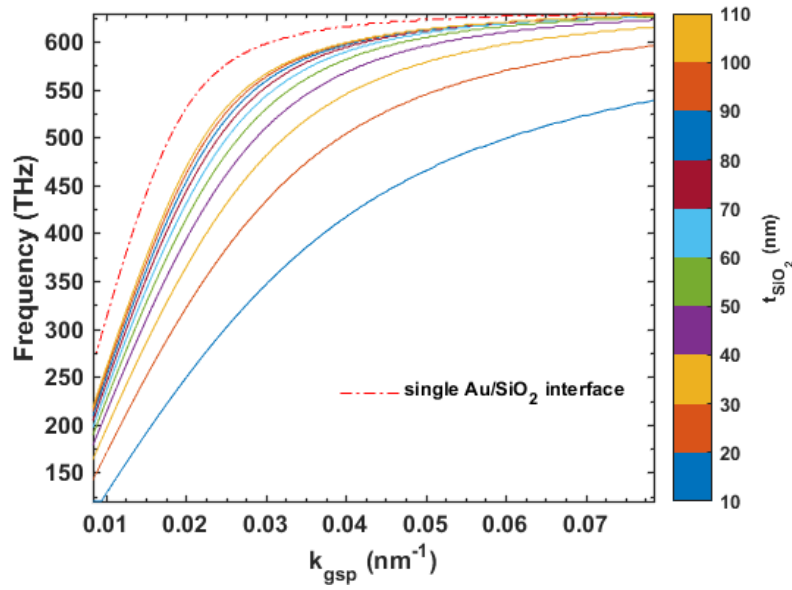
Figure 4.3: Dispersion curves calculated based on equation 4.6 for infinite MIM waveguides with different core thicknesses t_{SiO_2} ranging from 10 nm to 100 nm, which is indicated by the colorbar. The dispersion curve of SPP mode on an infinite single Au/SiO_2 interface is calculated according to equation 2.5.
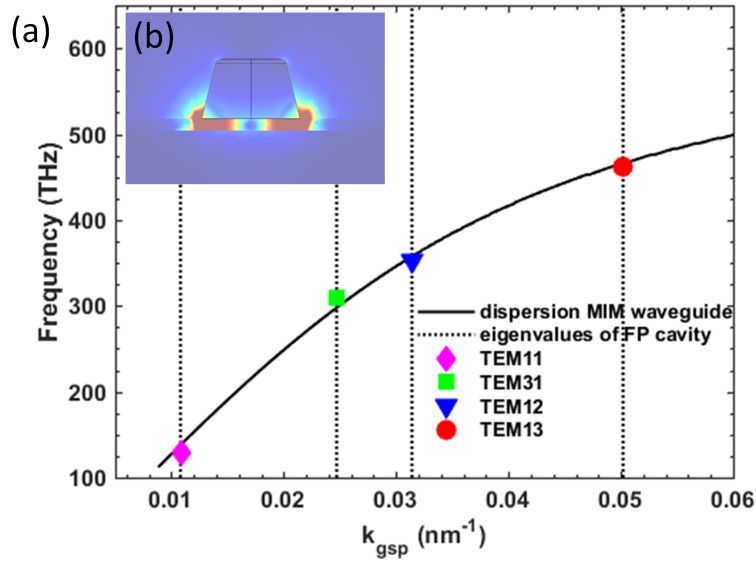
Figure 4.4: (a) The black curve is the dispersive curve of an infinite MIM waveguide with the same t_{SiO_2} and t_{Au} as those of the MIM cavities, the dispersion is calculated based on equation 4.6; the dotted black lines present the discrete eigenvalues of the circular FP cavity with a resonance radius of $R_{Au} + t_{SiO_2}$, which are calculated based on equation 4.7. The markers of magenta, green, blue and red mark the resonance position of TEM11, TEM31, TEM12 and TEM13 in the dispersion map, respectively. It can be observed that the cavity plasmon modes always appear at the intersection of the dispersion of the MIM waveguide and the eigenvalues of the FP cavity. (b) Cross-section field map of the TEM11 mode.

equation 4.6. The markers of magenta, green, blue and red mark the resonance position of TEM11, TEM31, TEM12 and TEM13 in the dispersion map, respectively, based on the corresponding values in Table 4.2. It can be observed that the cavity plasmon modes always appear at the intersections of the dispersion of the MIM waveguide and the eigenvalues of the FP cavity. Thus, it is evident that the cavity plasmon modes in a MIM cavity arise from the continuous gap surface plasmon modes of the MIM waveguides that get selected by the discrete FP cavity modes.

4.2   Comparison of TEMmn modes in MIM cavity and disc arrays

In section 1.2, we showed that the cavity plasmon modes are better candidates for plasmon-assisted sensing and spectroscopy compared to LSPR modes in gold nanodiscs, due to their higher field enhancement and narrower bandwidth. These advantageous properties of cavity plasmon modes are a product of their plasmonic and FP cavity origin. However, the standing-wave characteristics are not unique to MIM cavities, the LSPR modes in metal nanodisc arrays show similar standing-wave characteristics [162]. This means the LSPR modes in a metal nanodisc can be described using the model of a FP resonator as well. In this section, we compare the cavity plasmon modes in a MIM cavity array and in a gold disc array from the aspects of field distribution, resonance bandwidth, resonance wavelength, and field intensity.

4.2.1   Cavity plasmon modes in disc arrays

Figure 4.5 shows the extinction spectra for a gold disc array with a radius of 160 nm and a periodicity of 350 nm on top of a glass (black curve) and ITO substrate (red curve). The thickness of ITO is 50 nm. Three plasmonic modes can be identified from the extinction maxima: TEM11, TEM31 and TEM12. The near-field maps for each plasmonic resonance are presented under each extinction peak, showing standing wave characteristics and similar modal patterns to those in Figure 4.2. For a gold disc with a radius of 160 nm, the size of the disc is comparable to the wavelength of SPP modes propagating on a Au/SiO_2 interface, so that a sequence of different orders of standing wave modes appear in the visible/near-IR spectra, as in Figure 4.2. The gold disc array on normal glass substrate (black curve) shows the same profile as the one on ITO, but with less pronounced higher order modes and shorter resonance wavelengths due to the smaller refractive index. Our field maps of TEMmn modes in gold disc arrays are in
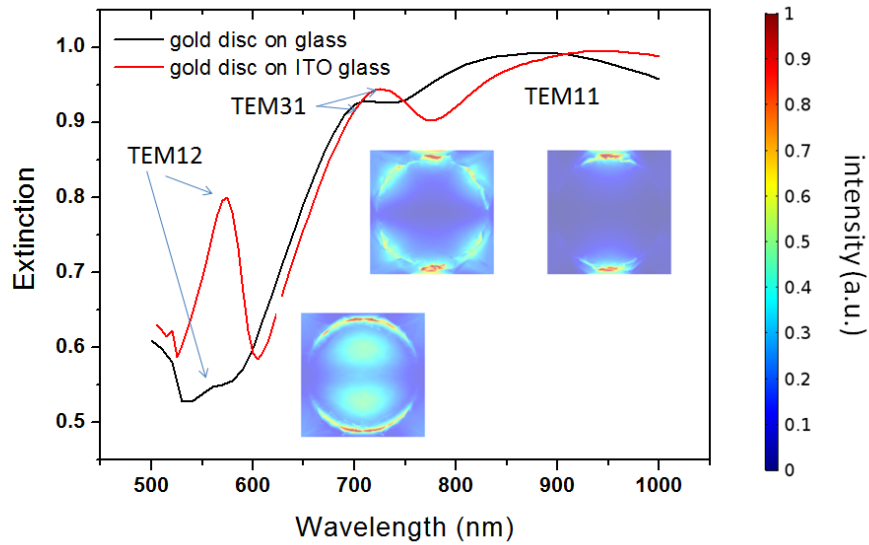
Figure 4.5: Simulated extinction spectra for gold disc array with a radius of 160 nm on top of the Indium Tin Oxide (ITO) glass substrate (red curve) and standard glass substrate (black curve). The ITO glass is covered by 50 nm of ITO film. P =350 nm. The near field maps are shown next to each plasmonic resonance.

accordance with the field maps obtained by investigating large silver nanodiscs with electron energy loss spectroscopy (EELS) [162].

We conclude that similar to a disc MIM cavity, gold discs function as a 2D circular FP resonator as well. There are two main reasons why the cavity plasmon modes in gold disc structures and MIM cavities exhibit different properties. The most important one is due to different plasmonic damping mechanisms. The strong radiation damping of plasmonic modes on gold disc structures leads to a wide bandwidth of the modes. For small gold discs, only the fundamental TEM11 mode appears in the investigated range. For large gold discs, more higher order plasmonic modes are excited. However, because of the wide bandwidth of each plasmonic mode, their far-field spectra overlap which makes them hard to distinguish. As a result, no distinct plasmonic mode can be identified in a far-field optical spectrum, as can be seen in Figure 4.5. On the contrary, gap surface plasmons (GSP) in MIM cavities are slow plasmons with bigger effective refractive index (details will be explained in the following section 4.2.2) and have a much longer lifetime (most of the energy is confined in the cavity rather than decaying into photons). Therefore, in MIM cavities, the plasmonic damping mostly arising from non-radiative damping, leads to narrow resonance bandwidths. As a result, the cavity plasmon modes manifest themselves as disctinct bands with narrower bandwidth in the far-field spectra. The difference in the origin of damping leads to different bandwidths of each plasmonic mode in the far-field. This is the reason why the TEMmn modes

still show well-defined reflection dips and extinction peaks in the case of a MIM cavity with big R_{Au}, while no pronounced peaks can be identified for large gold discs on a glass substrate.

4.2.2 Resonance bandwidth

In Figure 4.6, the simulated reflection spectra for the TEM11 mode for a gold disc on top of a glass substrate (red curve) and 50 nm gold film (MIM(I), black curve) are presented. The cavity height is 10 nm in MIM(I) and the disc radius R_{Au} is 40 nm in both cases. It can be noticed that the TEM11 mode is a reflection dip in the case of the MIM cavity array, while it is a reflection peak in the case of the gold disc array.
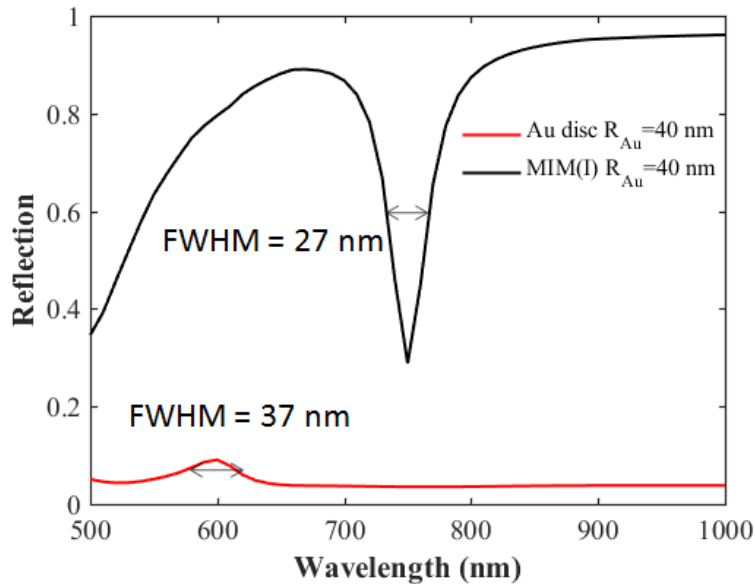
Figure 4.6: Simulated reflection spectra for the TEM11 mode for a gold disc on top of a glass substrate (red curve) and a 50 nm gold film (black curve), respectively. The radius of the gold disc is 40 nm in both cases.

In Figure 4.3, the dispersion relations of SPP modes propagating on an infinite Au/SiO_2 interface (red curve) and GSPs in a $Au/SiO_2/Au$ waveguide with different gap distance t_{SiO_2} ranging from 10 nm to 100 nm are plotted, based on the dispersion equation 4.6. As the standing-wave arises from the interference of incoming and outgoing surface plasmonic waves, the dispersion relation of the TEMmn modes in gold discs follow the dispersion of SPP waves on a single gold/SiO_2 interface. The TEMmn modes in the MIM cavity follow the dispersion of gap surface plasmons (GSP) of corresponding MIM waveguides. The resonance wavelengths of the TEM11 mode are 600 nm (500 THz) and 750 nm (400 THz) in gold disc array and MIM cavity array, respectively, which correspond to a wave vector of 0.018 nm^{-1} ($\lambda_{spp} = 349$ nm) and 0.03721 nm^{-1}

(λ_{gsp} = 169 nm) by relating to the single interface and t_{SiO_2}=10 nm curves in Figure 4.3. The effective refractive index of a plasmon wave can be calculated by $n_{eff} = \lambda_0/\lambda_{sp}$. The effective refractive indices of the TEM11 modes are ~1.72 and ~4.44 in gold discs and MIM(I), respectively. According to the Fresnel Equation for reflection ($Re = |\frac{n_{eff}-n_{d,eff}}{n_{eff}+n_{d,eff}}|$, where n_{eff} is the effective refractive index of surface plasmons and $n_{d,eff}$ is the effective refractive index of the dielectric environment outside of the MIM cavity), the gap surface plasmon wave in the MIM(I) cavity gets reflected at the cavity edge with a much higher reflection efficiency, compared to that in a gold disc. Therefore, the scattering of the TEMmn mode in the MIM cavity is reduced due to most of the gap surface plasmons being confined inside the cavity by the high reflection efficiency. However, in the case of a gold disc, the scattering process prevails over the absorption process due to part of the surface plasmon polaritons decaying into photons at the edge of the gold disc. As a result, a reflection dip appears at the resonance wavelength of the TEMmn modes attributed to the strong confinement in the MIM cavity, while a reflection peak appears in the case of the gold disc due to radiation in the backscattering configuration.

In Figure 4.6, the resonance bandwidths of the TEM11 mode are 27 nm and 37 nm in the MIM cavity and gold disc array, respectively. In the last section, we explained the difference in bandwidth from the origin of damping. The difference in bandwidth can be understood by the lifetime of the surface plasmons as well. The GSP waves in MIM structures, also referred to as slow plasmons, have higher propagating effective refractive indices ($n_{eff} = \lambda_0/\lambda_{sp} = c\frac{\partial k_{gsp}}{\partial \omega}$ in Figure 4.3). The higher effective indices result in higher reflectance upon reflection. That means the MIM cavities have better field confinement, and possess a higher cavity quality than a gold disc, leading to longer lifetimes of TEMmn modes in a MIM cavity compared to those in a gold disc.

4.2.3   Resonance wavelength

Besides the difference in plasmonic resonance bandwidth, the difference in resonance wavelengths of TEMmn modes in gold discs and MIM cavities is another reason why the sequences of standing-wave modes usually are not seen in far-field spectra of gold disc arrays.

The resonance wavelengths of the higher order cavity modes in gold discs on glass substrate are in the blue/UV range, which is around the wavelength of the interband transition in gold. ITO possesses a higher refractive index, thus red shifts the resonance of the TEM12 mode from 540 nm to 570 nm in Figure 4.5. When gold discs are on top of the gold film, the presence of the gold film red shifts more higher order modes into

the measuring range of a standard visible/near-IR spectrometer, as in Figure 4.2. This red-shift of the resonance wavelength in the disc MIM(I) cavity can be understood by the mirror effect of the gold film [124, 163, 164]. The disc hybridizes with its image in the gold film mirror, resulting in a bonding mode resonating at a longer wavelength. This mirror effect is reflected in Figure 4.6, the TEM11 mode is shifted from 600 nm to 750 nm by the presence of the gold film.

The red shift of the cavity modes in a MIM structure compared to a gold disc can be explained by the dispersion curves in Figure 4.3 as well. When two gold/SiO$_2$ interfaces are placed at small separations, SPP modes excited on each interface will interact with each other, resulting in a bonding mode and anti-bonding mode. In this thesis only the bonding gap mode is considered because the anti-bonding mode is a dark mode under our illumination configuration. The gold disc on glass can be considered as MIM structures with gap distance $t_{SiO_2} \rightarrow \infty$. As the gap distance decreases from infinity to 10 nm, the coupling strength increases drastically and the GSP polaritons are strongly red shifted.

4.2.4   Near-field intensity and confinement

Figure 4.7(a) presents the field intensity integrated over the bottom of a gold disc in disc MIM(I) and gold disc arrays with the same disc sizes and periodicity. The field intensity for the TEM12 and TEM11 mode in the MIM(I) cavity is 4.5 and 3 times stronger than that in the disc array when $R_{Au} = 160$ nm and $R_{Au} = 40$ nm, respectively. In Figure 4.7(b), the field maps at cross-sections for the cavity modes TEM11 are shown for a gold disc and MIM cavity. In the case of the gold disc, the decay length of the LSPR mode perpendicular to the Au/dielectric interface in the dielectric medium is around tens of nanometers. The improvement of confinement of the MIM cavity in the perpendicular direction is clear because the gap distance is much smaller than the decay length of the surface plasmons in the perpendicular direction. In the radial direction, we know the resonance cavity radius is $R_{Au} + \Delta R$, as demonstrated in equation 4.5, where ΔR is introduced by the phase shift upon reflection at the edge of the Au disc. The penetration depth ΔR is analogue to the penetration depth at the Bragg grating reflectors in a fiber acoustic resonator, where the penetration depth ΔR is proportional to Re^{-1} (Re represents the reflection coefficient) [165]. The higher effective refractive index of the TEMmn mode in a MIM cavity, resulting in higher reflective coefficients in the MIM structure, leads to a smaller ΔR. Therefore, a MIM cavity provides better confinement in the radial direction as well, compared to a gold disc as can be observed in Figure 4.7(b).
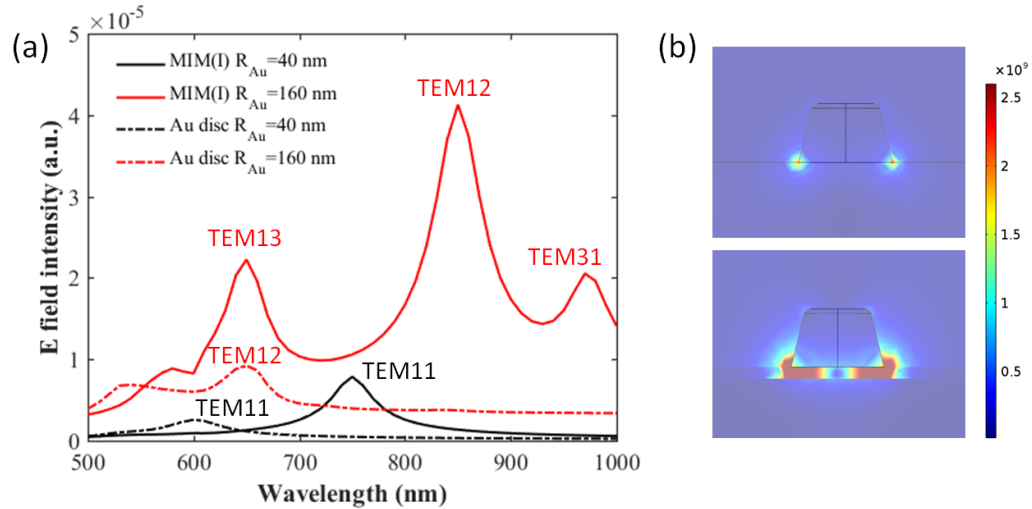
Figure 4.7: (a) Simulated near-field intensity integrated over the bottom of a gold disc for a disc MIM(I) cavity (solid curves) and gold disc arrays (dotted curves). The periodicity is P=350 nm and cavity height t_{SiO_2}=10 nm. The radius of the gold discs is R_{Au}=40 nm (black curves) and R_{Au}=160 nm (red curves). (b) Field distribution of cavity mode TEM11 at cross-sections in a gold disc (top) and MIM cavity (bottom), R_{Au}=40 nm

So in MIM cavities, the spatial extent of the plasmon energy is perpendicularly decreased by gold claddings and radially confined by the highly reflective circular cavity edges. The plasmonic energy is squeezed inside a cavity with very low volume, down to $(\lambda/10)^3$ in a disc MIM cavity, resulting in higher field intensity of the TEMmn modes. These advantages of high cavity Q factor and small mode volume V make MIM cavities very promising candidates for the investigating of the Purcell effect, where the Purcell enhancement $F_p \sim \frac{Q}{V}$.

4.2.5 Conclusion

When the disc size is comparable to the wavelength of plasmon polaritons (SPP in the gold disc and GSP in the MIM structure), the classical optics are still applicable in these FP cavities. The TEMmn modes can be excited on metal disc structures as well, the bottom surface of the metal disc functioning as a circular FP cavity. For small gold discs which justify the quasi-static approximation, only the TEM11 mode appears in the visible/near-IR regime. For big gold discs, higher order modes can be excited. However, the short lifetime of surface plasmons at the single metal/dielectric interface leads to a wide bandwidth of the resonances in far-field spectra. As a result, a sequence of different orders of cavity modes has not been spotted in optical experiments. The cavity plasmon modes in big metal discs are, however, distinct in spectra obtained by EELS where the bandwidth mostly depends on the non-radiative damping of surface

plasmons [162].

The presence of a gold film red shifts the cavity modes in gold disc samples to a longer wavelength. More importantly, the radiation damping at the edge of the cavity is drastically reduced by enhancing the reflection efficiency. The quality factor of a circular FP cavity is improved, thus the lifetime of TEMmn modes in a MIM cavity is longer than that in a gold disc. The longer lifetime of GSPs leads to small radiation damping and a narrower bandwidth of the TEMmn mode in the far-field spectra. As a result, on the contrary to gold discs, cavity plasmon modes in MIM cavities can be easily distinguished in far-field spectra. Due to the facts that the cavity plasmonic modes show narrow bandwidths and small mode volumes, MIM cavities are suitable candidates for the investigation of plasmon-exciton coupling in both the weak (Purcell effect) and strong (Rabi-analog splitting) regime.

4.3   Periodicity dependency

4.3.1   Independency on periodicity

In Figure 4.8(a), simulated near-field spectra integrated at the bottom of discs in MIM(I) with different periodicities P= 350 nm (black curve), P= 450 nm (blue curve), P= 550 nm (green curve), and P= 650 nm (red curve) are presented, respectively. Apart from the periodicity, all the other parameters are fixed: R_{Au} = 160 nm, t_{SiO_2} = 10 nm.

The resonance position of the plasmonic modes as a function of varying periodicity is presented in Figure 4.8(b). For a cavity array with P= 650 nm, strong coupling behaviour is observed between TEM13 mode and air/gold interface SPP, and TEM31 mode and glass/gold interface SPP as well. The strong coupling will be presented in section 4.3.2, and is not shown in Figure 4.8(b). The TEM11 mode strongly depends on the grating constants, and shifts from 2330 nm, to 2130 nm, to 2090 nm, then to 2080 nm for P = 350 nm, 450 nm, 550 nm and 650 nm, respectively. On the other hand, the resonance wavelengths of cavity mode TEM31, TEM12 and TEM13 are hardly modified by the varying periodicity, appearing at 970 nm, 850 nm and 650 nm, respectively. Table 4.3 can be obtained by relating to the dispersion curve in Figure 4.3.

In Table 4.3, λ_0 and ν_0 represent the resonance wavelength and frequency in free space of the cavity plasmon modes, k_{gsp}, λ_{gsp} and n_{gsp} represent the wave number (obtained from Figure 4.3), wavelength ($\lambda_{gsp} = \frac{2\pi}{k_{gsp}}$) and effective refractive index ($n_{gsp} = \frac{\lambda_0}{\lambda_{gsp}}$)
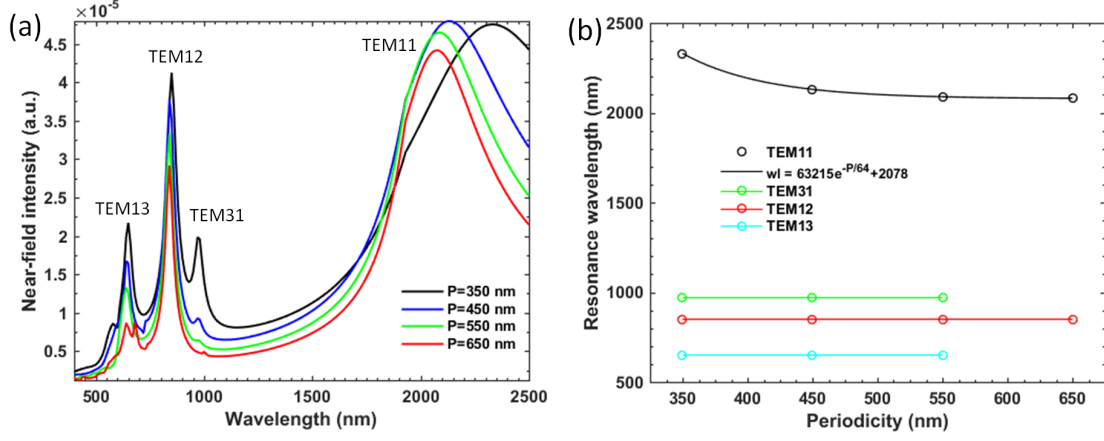
Figure 4.8: (a) Simulated near-field resonance spectra of disc MIM(I) with R_{Au}=160 nm and cavity height t_{SiO_2}=10 nm, and varying grating constants of P= 350 nm (black curve), P= 450 nm (blue curve), P= 550 nm (green curve), P= 650 nm (red curve); (b) The resonance wavelengths of different cavity orders TEMmn as a function of periodicity. The black curve is an exponential function wl=$(63215e^{-P/64\ nm} + 2078)$ nm.

of the gap surface plasmons. For the TEM11 mode the GSP wavelength is $\lambda_{gsp} = 621$ nm, while the edge-to-edge distance between discs is 30 nm when P = 350 nm. Besides, the comparatively smaller n_{gsp} of 3.75 indicates lower reflection efficiency and less confinement in radial direction, such that the near-fields of TEM11 modes in neighbouring MIM cavities would overlap, resulting in near-field coupling. As a result, the TEM11 mode is notably influenced at the small periodicity range P= 350 nm. However, as it can be seen in the black curve in Figure 4.8(b), the TEM11 mode gets less sensitive to the periodicity variation as the periodicity increases, due to the decoupling of the overlapping fringe fields of neighbouring TEM11 modes. It has been proved that the red-shift in resonance wavelength due to near-field coupling between two nanoparticles scales with an exponential decay of the particle separation [133, 166]. In Figure 4.8(b), the red shift of the resonance wavelength for the TEM11 mode as a function of periodicity can be fitted very well by wl =$(63215e^{-P/64\ nm} + 2078)$ nm.

Table 4.3: The optical parameters of cavity plasmon modes TEMmn in Figure 4.8.

TEMmn	λ_0 (nm)	ν_0 (THz)	k_{gsp} (nm^{-1})	λ_{gsp} (nm)	n_{gsp}
TEM11(P=350 nm)	2330	129	0.01012	621	3.75
TEM11(P=450 nm)	2130	140.7	0.01103	569.4	3.74
TEM11(P=550 nm)	2090	143.4	0.01123	559.2	3.74
TEM11(P=650 nm)	2080	144.1	0.01129	556.2	3.74
TEM31	970	309	0.02584	243	3.99
TEM12	850	353	0.03083	204	4.17
TEM13	650	461	0.04897	128	5.08

In the case of cavity modes TEM31, TEM12 and TEM13, the wavelength of the GSP λ_{gsp} is shorter than that of the TEM11 mode. Besides, the effective refractive indices n_{gsp} are bigger than for TEM11, leading to better confinement for the higher order TEMmn modes. As a result, the near-fields of TEM31, TEM12 and TEM13 of two neighbouring cavities are decoupled when P$\geqslant$350 nm. This explains why the higher order cavity modes exhibit no variation as a function of periodicity in Figure 4.8(b). We can conclude that, in general, cavity modes in MIM cavities are much more insensitive to the periodicity compared to those in gold disc arrays. Figure 2.3(b) demonstrates that the resonance wavelengths of plasmonic modes in gold discs shift drastically with varying periodicity between 350 nm and 850 nm [101]. We attribute the difference in periodicity dependence to the bounding nature of TEMmn modes in MIM cavities and the radiative nature of those in gold discs, respectively. The MIM cavity confined the plasmonic energy tightly inside the cavity: near-field coupling is decreased by the small energy fringe beyond R_{Au} (smaller ΔR), while far-field coupling is reduced because cavity modes in MIM cavities are less radiative.

For the investigated MIM cavities with R_{Au} <160 nm, the corresponding cavity modes will be excited at shorter wavelengths than those in Table 4.3, which means bigger wave number (k_{gsp}) and shorter GSP wavelength (λ_{gsp}). According to the dispersive curve (t_{SiO_2}=10 nm) in Figure 4.3, a shorter resonance wavelength leads to a bigger effective refractive index (n_{gsp}) of the GSP wave, thus resulting in a better quality factor. Therefore, in a MIM cavity with a cavity height of $t_{SiO_2} \sim 10$ nm, the cavity plasmon modes in the visible/near-IR region are independent of periodicity variation when P$\geqslant$ 350 nm.
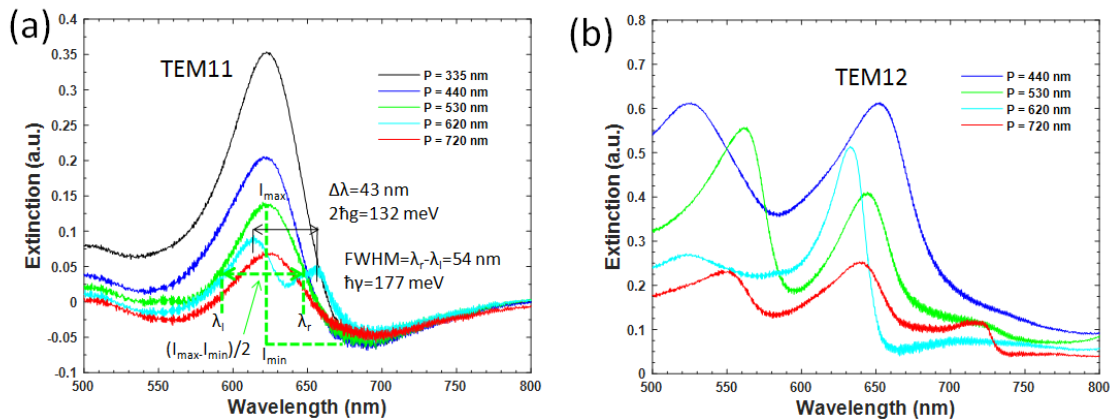
Figure 4.9: Measured extinction spectra for MIM cavity array (a) R_{Au}=38±2 nm and (b) 115±3 nm. The periodicity varies from 335 nm to 720 nm. The cavity height t_{SiO_2} = 12 nm. In Figure(a), the splitting energy is estimated for the double-peak structure at P=620 nm. The FWHM and linewidth are estimated as well, details will be presented in section 4.3.2

In Figure 4.9, the measured extinction spectra of fabricated MIM(I) cavity arrays are shown for (a) R_{Au}=38±2 nm, (b) 115±3 nm. For cavities with a radius around 38 nm (Figure 4.9(a)), the TEM11 mode dominates in the visible/near-IR regime, while the extinction spectra show no dependency on the periodicity, except when the narrow cavity mode overlaps with an SPP mode ($R_{Au} \simeq 40$ nm, P = 620 nm). In Figure 4.9(b), the TEM11 mode is shifted out of range for $R_{Au} \simeq 115$ nm, while the TEM12 mode appears at around 650 nm and dominates in the visible/near-IR range. The independence of the TEM12 mode to the periodicity can be observed as well except when P = 620 nm, where the coupling between SPP modes and cavity modes occurs. Details about strong coupling between SPP modes and TEMmn modes will be presented in the following section.

4.3.2 Strong coupling between cavity modes and SPPs

In the previous section, we presented that the periodicity does not affect the cavity modes by near-field coupling between neighbouring MIM cavities. The influence of far-field coupling between neighbouring MIM cavities is limited as well because the TEMmn modes are less radiative than LSPR modes. However, the periodicity influences significantly the resonance characteristics of cavity plasmon modes by strong coupling between SPP modes and cavity plasmon modes, which can be seen in the red curve in Figure 4.8, and Figure 4.9(a) and (b) with P=620 nm, where the Rabi-analogue splitting can be observed.

The concept of Rabi splitting originates from atomic physics and refers to strong coupling where the coupling strength exceeds the dissipation rates of the system and therefore the energy exchanges coherently between an atom and a cavity photon. Thus, Rabi splitting is an important signature of strong coupling. Recently, interest in the quantization of plasmons has extended the investigation of Rabi splitting into the emerging areas of plasmon-exciton, plasmon-cavity and plasmon-plasmon coupling systems [167–171]. The couping regime of two modes interacting with each other can be distinguished on the basis of the relationship between coupling strength g and γ_A and γ_B which are the inverse of the lifetimes of the excited states of emitters, photon in a cavity, or plasmon polaritons in nanostructures. The coupling occurs in the weak regime if g< γ_A, γ_B is met, while the condition g> γ_A, γ_B implies strong coupling. In order to resolve the characteristic of double-peak structure observed in Rabi-splitting, it is demanded that the splitting energy be larger than the transmission linewidth of each peak of the coupled system, which leads to a stricter condition for observing strong coupling $2g > (\gamma_A + \gamma_B)/2$ [172]. Different strong-coupling conditions have been given as well depending on different coupling systems. For instances, in Ref. [173], 2g> κ_{pl} is

given, where κ_{pl} is the FWHM of the plasmon branch; and in Ref. [174], the condition that the energy splitting needs to be larger than the sum of the line widths is given. The rule of thumb to justify the observation of strong coupling is widely accepted as $2g > (\gamma_A + \gamma_B)/2$ [167, 172, 175, 176]. In this section, this condition will be applied to verify the strong coupling between the SPP mode and the cavity mode.

The resonance wavelengths of grating induced SPP modes on the air/gold interface and glass/gold interface in a disc-on-film system are plotted in Figure 4.10 based on equation 4.1. The mode $SPP_{air/Au}(i,j)$ means the SPP mode excited on the air/Au interface with grating orders of i and j along the x and y direction, respectively, while y is the polarization direction as well, likewise for the SPP modes $SPP_{glass/Au}(i,j)$ excited on the interface of the glass/Au interface.
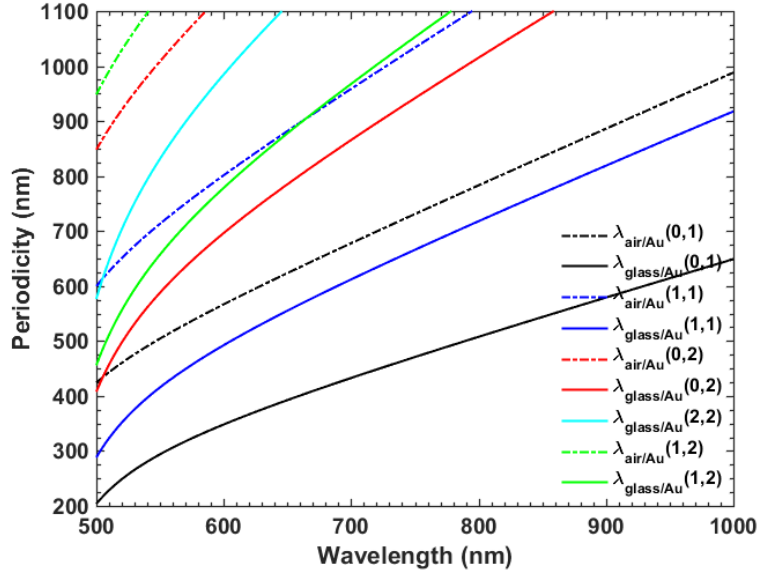
Figure 4.10: The resonance wavelength of SPP modes excited on the air/gold interface and glass/gold interface based on equation 4.1. $\lambda_{air/Au}$(i,j) and $\lambda_{glass/Au}$(i,j) represent different orders of SPP modes on the air/gold and glass/gold interface, respectively.

The calculated SPP resonance wavelengths $\lambda_{air/Au}(0,1)$ and $\lambda_{glass/Au}(0,1)$ are 674 nm and 1002 nm for P = 650 nm, respectively, as can be obtained in Figure 4.10. Meanwhile, the cavity plasmon mode resonates at λ_{TEM13}=650 nm in a MIM cavity with R_{Au} = 160 nm (as can be seen in Table 4.3). Due to the overlap in near-field distribution and resonance wavelength, coupling occurs between the $SPP_{air/Au}(0,1)$ mode and TEM13 mode, and results in Rabi-analogue splitting in the red curve in Figure 4.8. After coupling, there are two hybridized modes at 640 nm and 680 nm, respectively. In the case of the TEM31 mode in the red curve in Figure 4.8, the strong near-field of the $SPP_{glass/Au}(0,1)$ mode is 50 nm (t_{Aufilm}) away from the 'hot spots' of mode TEM31. Besides, the resonance wavelengths are 1002 nm and 970 nm, showing a sep-

aration of 30 nm. Therefore the coupling strength between the $\text{SPP}_{glass/Au}(0,1)$ and TEM31 mode is not as strong. One can hardly determine if coupling happens between $\text{SPP}_{glass/Au}(0,1)$ and the cavity mode TEM31 in Figure 4.8.

Relating to Figure 4.10, when P= 620 nm, the resonance wavelengths of $\text{SPP}_{air/Au}(0,1)$ and $\text{SPP}_{glass/Au}(1,1)$ are $\lambda_{air/Au}(0,1)$= 647 nm and $\lambda_{glass/Au}(1,1)$= 707 nm. In Figure 4.9(a) and (b), the TEM11 mode and TEM12 mode overlap with $\text{SPP}_{air/Au}$ modes, resulting in Rabi-analogue coupling.
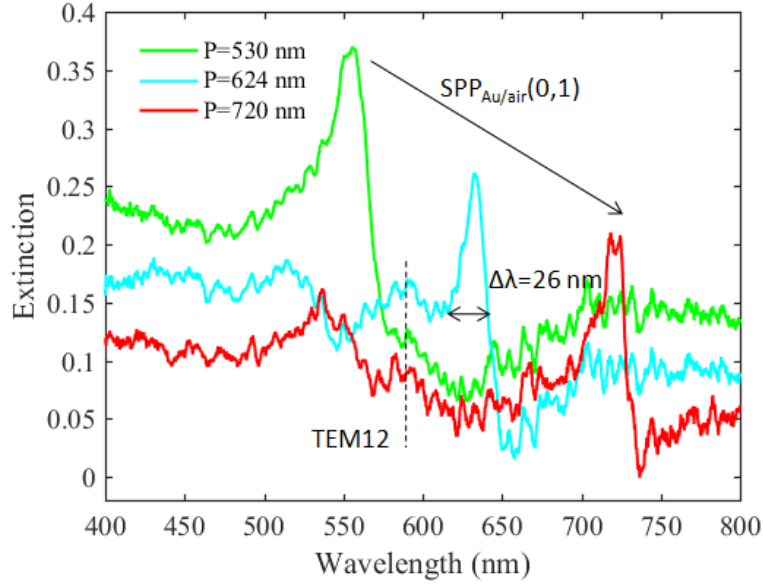
Figure 4.11: Measured extinction for MIM(I) structures with a radius of $\text{R}_{Au} \sim 100$ nm, and periodicities of P=530 nm (green curve), P=624 nm (cyan curve) and P=720 nm (red curve). The TEM12 modes and $\text{SPP}_{air/Au}(0,1)$ modes are labelled. The band width of $\text{SPP}_{air/Au}(0,1)$ at P=624 nm is estimated to be $\Delta\lambda = 26$ nm ($\hbar\gamma_{SPP}$=82 meV).

In Figure 4.11, the measured extinction spectra are shown for MIM(I) cavities with similar radii and varying periodicities. The $\text{SPP}_{air/Au}(0,1)$ modes show a red-shift as a function of increasing periodicity. The asymmetric line shape makes it problematic to obtain the precise bandwidth of SPP modes. The FWHM is then estimated to be 26 nm as shown in Figure 4.11. The line width is then calculated to be $\hbar\gamma_{SPP}$=82 meV ($\hbar\gamma_{SPP} = h(\frac{c}{\lambda_l} - \frac{c}{\lambda_r})$), where λ_l and λ_r are 615 nm and 641 nm, respectively). In Figure 4.9, the asymmetric line shapes of TEM11 mode make it problematic to evaluate the bandwidth as well. As illustrated for P=530 (green curve) in Figure 4.9, a horizontal line is drawn at half the maximum peak height $((I_{max} - I_{min})/2)$ and then the full length residing within the peak bound $(\lambda_r - \lambda_l)$ is measured to be the FWHM of the TEM11 mode. According to this evaluating method, bandwidths of TEM11 mode (41 nm spectral shift) for MIM array with P=530 nm is estimated to be $\hbar\gamma_{TEM11} = h(\frac{c}{\lambda_l} - \frac{c}{\lambda_r})$=174 meV, where λ_l and λ_r are 593 nm and 647 nm, respectively.

Similarly, $\hbar\gamma_{TEM11} = h(\frac{c}{\lambda_l} - \frac{c}{\lambda_r})$=167 meV is estimated for P=720 nm, where λ_l and λ_r are 596 nm and 648 nm, respectively. In the case of P=624 nm, the bandwidth of TEM11 mode should be 167 meV $< \hbar\gamma_{TEM11} <$ 174meV without coupling. As shown in Figure 4.9, the energy splitting for the Rabi-analog splitting is estimated to be $2\hbar g$=132 meV between two hybridized modes appearing at 614 nm and 657 nm, respectively. So the criterion that 2g$> (\gamma_{SPP} + \gamma_{TEM})/2$, for strong coupling between the SPP$_{air/Au}$(0,1) and TEM11 mode is met. Besides Rabi splitting, anti-crossing dispersion is a characteristics for strong coupling as well, which will be studied in the following subsection.

4.3.3   Anti-crossing behaviour

The Rabi-splitting and anti-crossing behaviour have been widely investigated in metallic nanosystems hybridized with QDs, dyes and fluorophores , with a focus on modifying the emission by strong coupling of emitters with plasmonic modes [171]. Similar phenomena have been observed in plasmonic microcavities and nanocavities as well [169, 177]. When the strong coupling regime is reached, Rabi-splitting happens, resulting in the fact that instead of crossing each other, the energy curves diverge from each other. This phenomenon is called anti-crossing which means that the two branches of hybridized states repel each other. This anti-crossing can be as well observed in MIM cavities consisting of gold disc arrays on a gold film system.
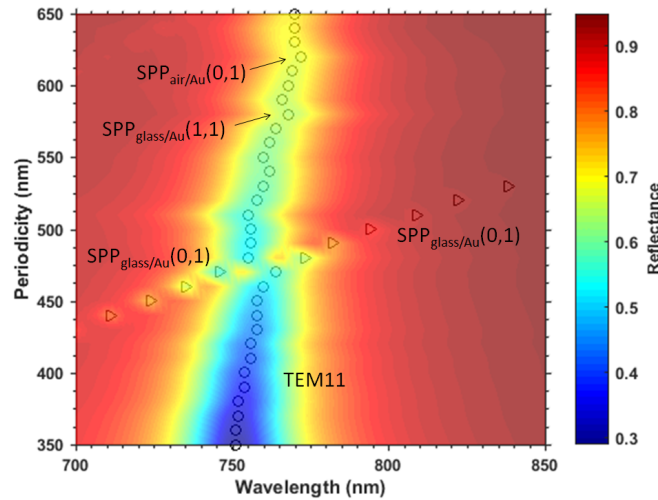
Figure 4.12: Contour plot of the simulated reflectance as a function of periodicity and wavelength for MIM cavities consisting of disc arrays on gold film. The circular and triangular markers denote the resonance position of the TEM11 mode and SPP$_{glass/Au}$(0,1), respectively. The cavity radius is R$_{Au}$=40 nm and cavity height t$_{SiO_2}$=10 nm.

Figure 4.12 shows the simulated variation of reflectance as a function of wavelength and periodicity in MIM(I) with R_{Au}= 40 nm and t_{SiO_2}= 10 nm. The resonance positions of the $SPP_{glass/Au}(0,1)$ and TEM11 mode manifest themselves in reflection spectra by the intensity minima, and are denoted by triangles and circles, respectively. On one hand, the SPP mode depends strongly on the periodicity: the resonance wavelength $\lambda_{glass/Au}(0,1)$ moves from 711 nm to 836 nm when varying the periodicity from 440 nm to 530 nm (good agreement with calculations in Figure 4.10). On the other hand, the cavity mode is hardly influenced by the periodicity in most cases. However, at the periodicity P=480 nm, the $SPP_{glass/Au}(0,1)$ mode ($\lambda_{glass/Au}(0,1) = 762$ nm in Figure 4.10) and TEM11 mode ($\sim$760 nm) coincide with each other. An anti-crossing behaviour can be observed, implying strong coupling between cavity plasmon modes and SPP modes. Two hybridized modes are formed through the coupling: one with a shorter resonance wavelength and one with a longer resonance wavelength than 760 nm. The small disturbance at periodicity P=620 nm and P=585 nm are due to hybridization of higher order $SPP_{air/Au}(0,1)$ and $SPP_{glass/Au}(1,1)$ modes with the TEM11 mode, as indicated by the arrows in the Figure 4.12.

4.3.4 Energy exchange through strong coupling

In the previous section, we presented that Rabi-analogue splitting occurs when SPP modes and cavity modes coincide with each other. This Rabi-splitting phenomenon is frequently observed in experiments as well. In this section, the efficient energy exchange between an SPP mode and cavity mode during the strong modal hybridization will be investigated.

In Figure 4.13(a) and (b), measured and simulated extinction spectra with varying periodicity are shown for MIM(I) with $R_{Au} = 38\pm2$ nm and t_{SiO_2}= 12 nm. Good agreement in the spectral profile can be found between experiments and simulations. It is worth noting that the cavity modes are exhibited as Fano resonances in extinction measurements, due to their coupling to the incident radiance (details will be shown in section 4.6). The field map for $SPP_{air/Au}(0,1)$ is shown at the resonance wavelength $\lambda_{SPP} = 670$ nm in Figure 4.13(c). The field map of the TEM11 mode is shown at the resonance wavelength λ_{TEM11}= 700 nm. The last two pictures in Figure 4.13(c) show the field maps of the two hybridized modes at their resonance wavelengths, respectively. It can be seen that the two hybridized modes obtain parts of their energy from the SPP modes (stripes pattern) and parts of their energy from the TEM11 mode (circular standing-wave pattern). Because the two hybridized modes both have energy from the SPP mode and cavity mode, one can image that the hybridized modes possess some physical properties from both the SPP mode and cavity mode. In Figure 4.12,

in the strong coupling regime from P = 450 nm to 490 nm, the originally insensitive cavity plasmon mode becomes highly dispersive as a function of periodicity, while the originally dispersive SPP mode becomes less sensitive to the periodicity in the strong coupling regime. This indicates that new plasmonic polariton quasi-particles, similar to the quantum exciton polariton in a semiconductor cavity, are formed through the Rabi-analogue splitting [171]. Our results agree well with the strong coupling between SPP mode and 1D cavity plasmon mode investigated in a nanoparticle array-planar FP cavity hybrid system [171].

$@\lambda_{spp} = 670\,nm$ $@\lambda_{TEM11} = 700\,nm$ $@\lambda = 660\,nm$ $@\lambda = 710\,nm$
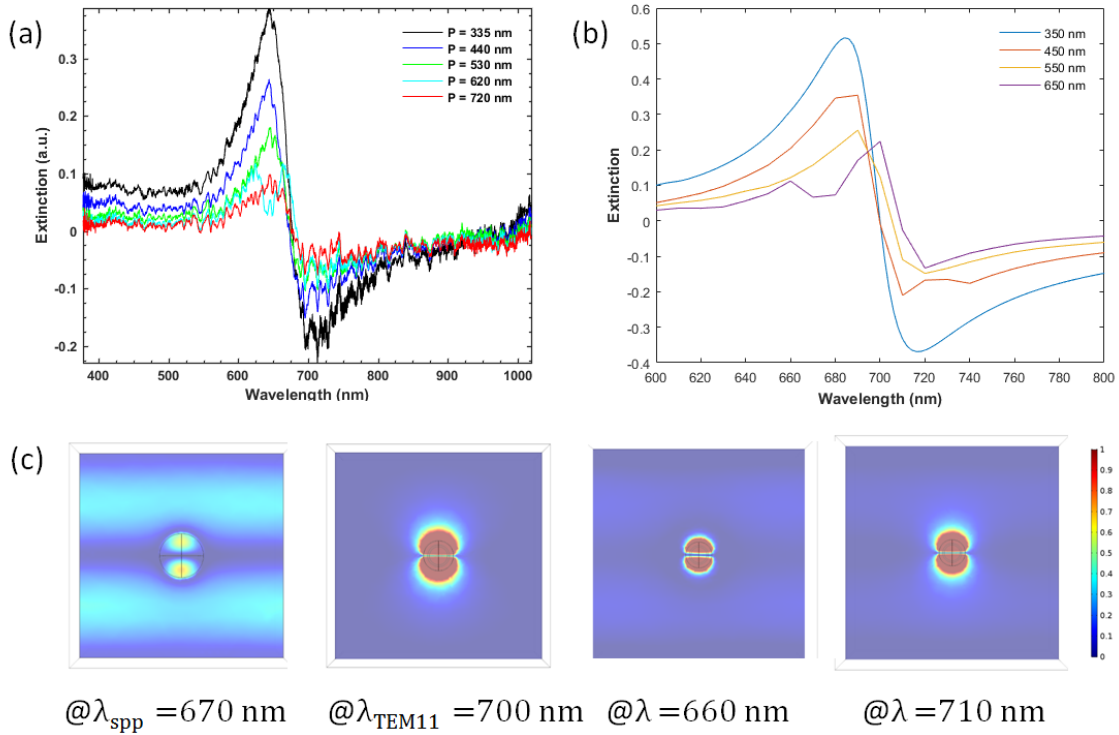
Figure 4.13: (a) Measured extinction spectra of MIM(I) cavity arrays with $R_{Au} = 38 \pm 2$ nm, t_{SiO_2}=12 nm and varying periodicity. (b) Simulated extinction spectra of MIM(I) with $R_{Au} = 40$ nm, t_{SiO_2}=10 nm and varying periodicity, wavelength sweeping step is 10 nm. (c) From left to right, the field maps for $SPP_{air/Au}(0,1)$ while P = 650 nm (with R_{Au}= 70 nm so the strong coupling is excluded), cavity plamonic TEM11 mode while R_{Au}= 40 nm (and P = 350 nm to exclude the strong coupling), and two hybridized modes after strong coupling are presented in a MIM cavity with P = 650 nm and R_{Au} = 40 nm.

4.3.5   Conclusion

The cavity plasmon modes in the visible/near-IR range are independent of periodicity in most cases. Due to the high confinement in both perpendicular and radial direction,

the energy fringe extended beyond the MIM cavity is weak, which undermines the base of near-field coupling between neighbouring cavities. Besides, the bounding nature (non-radiative) of GSPs leads to weak far-field coupling between neighbouring cavities.

However, the resonance characteristics of cavity plasmon modes are subject to a significant influence of varying periodicity when strong coupling happens between SPP modes on the Au/dielectric interfaces and cavity plasmon modes. The SPP modes are highly sensitive to the periodicity, and when the resonance position coincides with cavity modes, Rabi-analogue splitting occurs and results in two hybridized modes. The two hybridized modes both gain parts of their energy from SPP modes and parts from cavity plasmon modes, and possess physical properties of both origins.

4.4 Cavity radius dependency

4.4.1 Reflection and scattering of MIM cavities
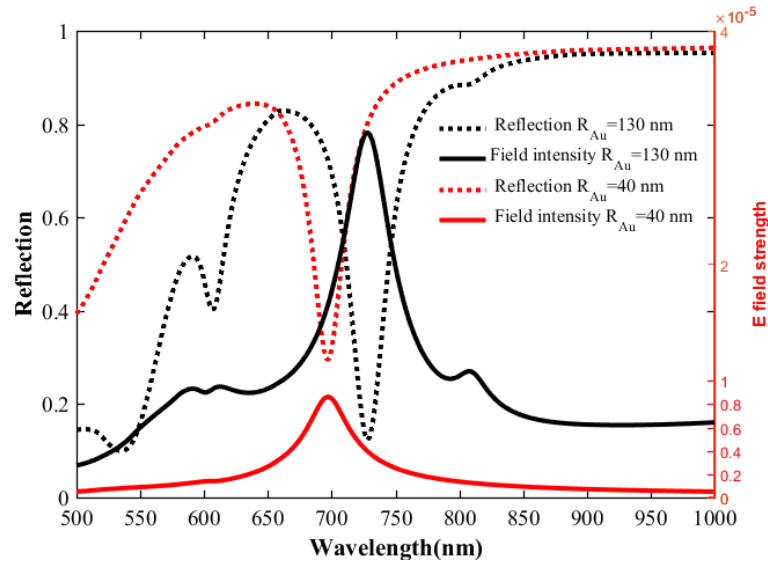
Figure 4.14: Simulated near-field strength integrated at the bottom of Au discs in MIM(II), black and red solid curves for MIM(II) with Au discs radius of 130 nm and 40 nm, respectively. P = 350 nm, t_{SiO_2} = 10 nm. The reflection spectra are shown in black and red dotted lines for the sake of comparison.

Figure 4.14 shows the simulated near-field resonance and the reflection spectra of cavity plasmon modes for MIM(II) cavity arrays with R_{Au}=130 nm and R_{Au}=40 nm. The near-field resonance shows a Lorentz profile, and the field strength maximum at the resonance wavelength, while the reflection spectra show Lorentz resonances with reflectance minima. In the MIM cavity with a radius of 130 nm, TEM31, TEM12 and

TEM13 modes appear at 810 nm, 729 nm and 607 nm as field intensity peaks and reflection dips in near-field and reflection spectra, respectively. In the case of the MIM cavity with R_{Au}=40 nm, the TEM11 mode emerges at 698 nm in both near-field and reflection spectra. It is not shown here, but the near-field and far-field reflection spectra of MIM(I) and MIM(III) show the same characteristics of no spectral shift as in MIM(II). It can be concluded that the reflection dips are straightforward indicators of the near-field resonance wavelengths of cavity plasmon modes in MIM cavities.

This property of no spectral shift between near-field resonances and reflection dip positions leads to an advantage of MIM cavities for applications for plasmon assisted spectroscopy. It has been reported that for many plasmonic substrates, the far-field resonance shows a spectral blue-shift from the near-field resonance due to the radiation and far-field effect of plasmonic modes [154, 155]. Figure 4.15 shows the simulated
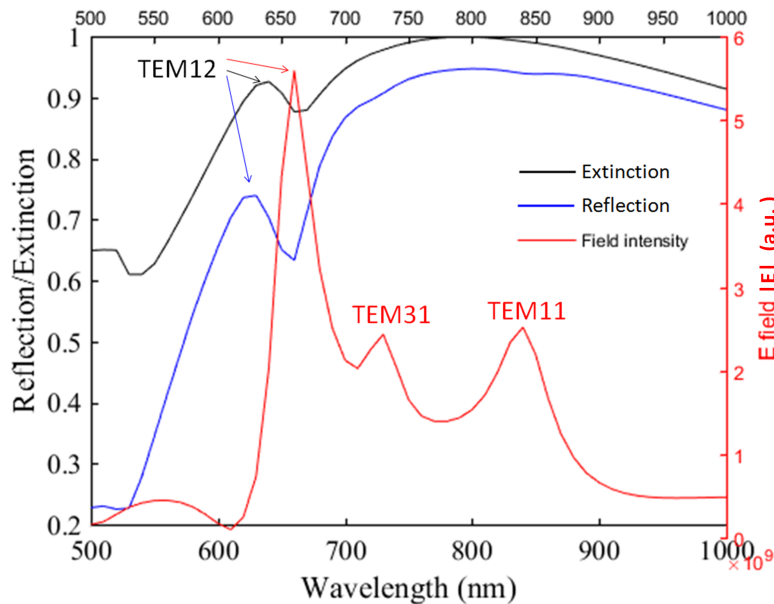
Figure 4.15: The simulated extinction (black curve) and reflection (blue curve) and field strength spectra (red curve) at the bottom corner of a gold disc are shown. R_{Au} = 160 nm.

extinction (black curve) and reflection (blue curve) and field strength spectrum (red curve) at the bottom corner of a gold disc. The disc size is R_{Au} = 160 nm. As already presented in section 4.2, the modes TEM11 and TEM31 in a large gold disc are not discernible due to the wide bandwidth and the superposition in the far-field. The TEM12 mode which is not overshadowed by other TEMmn modes can be distinguished, and appears as extinction peaks and reflection peaks. However, the peak positions in the far-field are blue shifted compared to that in the near-field spectrum. This spectral shift makes it difficult in practice to locate the near-field resonance position from the optical extinction or reflection measurements, while in the case of MIM cavities, no

shift occurs between near-field and far-field resonance maybe due to the non-radiative properties of the TEMmn modes, which makes it a more promising SERS candidate.

4.4.2   Cavity radius dependency

According to the resonance condition of TEMmn modes in equation 4.5, it is clear that the resonance wavelength red shifts with increasing R_{Au}. In Figure 4.16(a)-(b), the measured and simulated reflection spectra are presented for disc MIM(I) cavity arrays with a grating constant of 335 nm and radius of 38 nm (black curve), 73 nm (blue curve), 113 nm (green curve) and 150 nm (red curve). The reflection measurements in Figure 4.16(a) were carried out on a reflection setup as shown in Figure 3.8(b). The illumination angle is 18.5°, and the numerical apertures of the illuminating and collecting objective are 0.42 and 0.9, respectively. The corresponding simulated reflection spectra in Figure 4.16(b) were obtained with normal incidence of collimated light and a collecting N.A. of 1.

The resonance wavelengths of SPP modes are sensitive to the incidence angle. In the reflection measurement, the incidence beam comes from a wide range of angles, leading to a wide range of SPP resonance wavelengths. As a result, there is no distinct SPP resonance in the optical measurements in Figure 4.16(a). This explains why the $SPP_{glass/Au}(0,1)$ mode appears at 586 nm in Figure 4.16(b) as indicated by the dashed line, however, not in the measured spectra in Figure 4.16(a). While the difference in the incidence angles between simulations and experiments strongly affects the SPP modes, it has no influence on the position of cavity plasmon modes [80, 81], because the cavity modes are the eigen modes of the circular MIM cavity and are independent of the incident angles. The resonance wavelengths of cavity plasmon modes are indicated by reflection minima in reflection spectra. Good agreement of the resonance position of the cavity plasmon modes can be found between experiments and measurements for different R_{Au}. In Figure 4.16(a), TEM11 modes, labelled as mode (1), appear at 677 nm and 964 nm for nanocavities with radius of 38 nm and 73 nm, respectively. The field maps are shown in Figure 4.16(c). For bigger cavities, the TEM11 mode is shifted out of the range of interest. A higher order mode, TEM12 which is labelled as mode (2), appears for bigger cavities and shifts from 630 nm to 729 nm when the radius increases from 113 nm to 150 nm. Moreover, for the cavity with a radius of 150 nm, two more higher order modes, TEM31 and TEM13 modes, appear at 812 nm and 582 nm, labeled as mode (4) and (3), respectively. In conclusion, the resonance position of a certain order of cavity plasmon modes red shifts as a function of increasing radius, meanwhile, higher order cavity plasmon modes appear in the investigated spectral range.
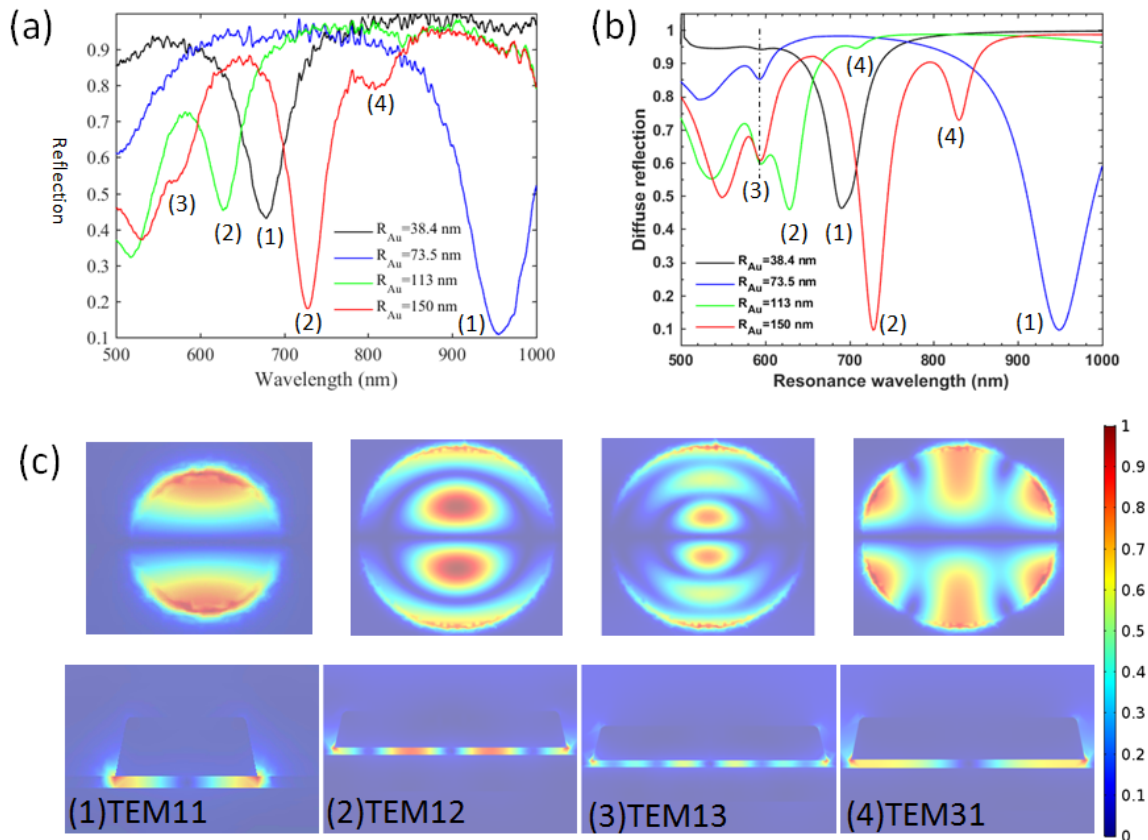
Figure 4.16: Measured and simulated resonance characteristics of plasmonic modes in disc MIM cavity arrays. (a) Measured reflection spectra for disc cavity arrays with the same array periodicity P = 335 nm, cavity height t_{SiO_2} = 12 nm and varying cavity radius: 38 nm (black curve), 73 nm (blue curve), 113 nm (green curve) and 150 nm (red curve); (b) Simulated reflection spectra in correspondence to those disc cavity arrays in (a); (c) Field maps for different orders of cavity plasmon modes.

4.4.3 Dispersion relation

In Figure 4.16(c), it can be seen that there are always fringe fields (ΔR) outside of the physical MIM cavity for each TEMmn mode. We are aware that ΔR is dependent on several parameters: the order of cavity plasmon modes, the cavity thickness, the disc radius and etc, which would influence the confinement (or the effective refractive index) of the TEMmn modes. Based on the cross-section field maps in Figure 4.16(c), the ΔR is estimated to be approximately equal to t_{SiO_2}. For simplicity, we qualitatively assume that $\Delta R \approx t_{SiO_2}$ for the TEMmn modes. The determination of ΔR can be quantitatively estimated later in Figure 5.5.

According to equation 4.5, the wave number of a TEMmn mode can be obtained by

$$k_{gsp} = \frac{\chi'_{mn}}{R + \Delta R} \tag{4.8}$$

Therefore, the dispersion relation of cavity plasmon modes can be also determined from the experimental and simulated spectra. In Figure 4.17, experimental resonance wave-
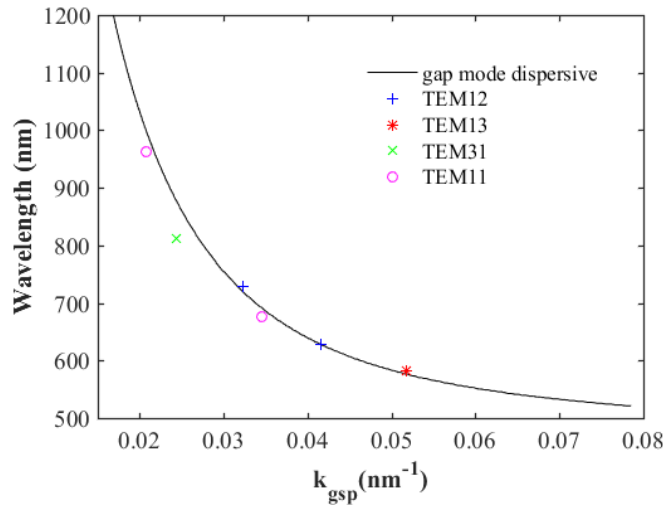
Figure 4.17: Experimental dispersion of cavity plasmon modes TEMmn in nanocavities with different sizes (circles and triangles), determined from Figure 4.16(b). The black curve shows the dispersive relation of a corresponding infinite MIM waveguide.

lengths of cavity modes λ_{TEMmn} from nanocavities with different radii were plotted by markers: TEM12 (blue markers), TEM13 (red marker), TEM31 (green marker), TEM31 (magenta marker). The black curve in Figure 4.17 is the dispersive curve for gap plasmons supported by a corresponding infinite gold (50 nm)/SiO$_2$(12 nm)/gold (50 nm) waveguide. The dispersion relation of TEMmn modes in MIM cavities is found to follow a dispersion very similar to that of the corresponding MIM waveguide. This dispersion relation has also been reported in other plasmonic resonators, such as rectangular FP cavities [151] and silver/Al$_2$O$_3$/Ag circular cavities [133]. This agreement

in experiments proves that the cavity plasmon modes are a product of continuous GSP waves supported by a MIM waveguide getting selected by the eigen modes of a circular FP cavity. As a result, cavity plasmon modes possess advantageous properties like strong near fields from their plasmonic origin and narrow resonance line shapes from their cavity modes origin. These properties make MIM cavities a very promising candidate for plasmon assisted sensing and microscopy.

4.5   Cavity height dependency

In Figure 4.3, the dispersion relation of GSP waves changes significantly with varying core thickness (t_{SiO_2}) of Au/SiO$_2$/Au MIM waveguide, due to coupling between two SiO$_2$/Au interfaces. As cavity plasmon modes arise from the interference of counter-propagating GSP modes, similar behaviour can be expected of TEMmn modes.
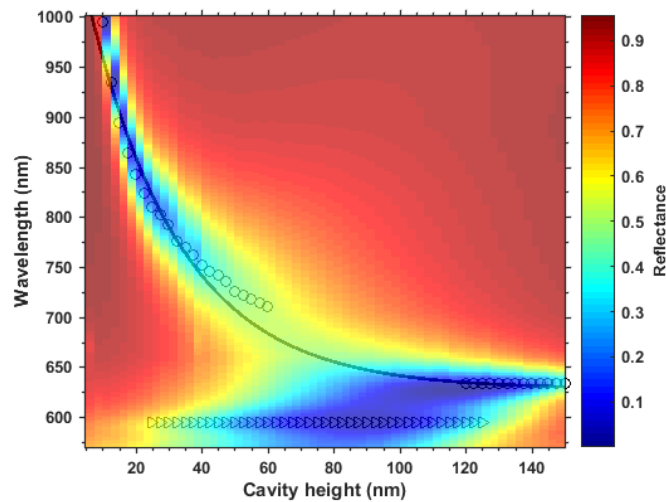
Figure 4.18: Contour plot of the reflectance as a function of cavity height and wavelength for MIM cavities consisting of disc arrays on a gold film. The periodicity is P= 335 nm and cavity radius R_{Au}= 140 nm. The circular and triangular markers are obtained by reading out the reflectance dip positions, denoting the resonance positions of the TEM11 mode and SPP$_{air/Au}$(0,1), respectively. The black curve is an exponential decay function wl = $(474\exp(-t_{SiO_2}/28\ nm)+628.1)$ nm.

Figure 4.18 shows the evolution of reflectance as a function of cavity height and wavelength for MIM(I) with R_{Au} = 140 nm and P = 335 nm. The mode appearing at 586 nm is the SPP$_{air/Au}$(0,1) mode (triangles), which is insensitive to the cavity height. The modes marked by circles are the cavity modes TEM11. It can be observed that the resonance wavelength of the TEM11 mode blue shifts with increasing t_{SiO_2}, because the GSP wave is a product of mode hybridization between two SiO$_2$/Au interfaces

with a separation of t_{SiO_2}, and the coupling strength is an exponential decay function of separation. The blue-shift of mode TEM11 can be fitted with an exponential decay of t_{SiO_2}, as the black curve in Figure 4.18. This evolution of the TEM11 mode can be understood by the mirror effect of the gold film. The gold nanodisc hybridizes with its image through the metal film, resulting in a red-shift, while the coupling strength decreases drastically as the separation increases, resulting in a blue-shift as a function of increasing t_{SiO_2}. When $t_{SiO_2} > 120$ nm, the near-fields on two metal/dielectric interfaces are decoupled, thus showing no change in λ_{TEM} with a further increasing of t_{SiO_2}.

4.6 Fano effect in MIM cavity arrays

Comparing the measured extinction spectra in Figure 4.13 and the measured reflection spectra in Figure 4.16, we find that TEMmn modes express themselves in very different profiles in extinction and reflection. In Figure 4.14, it is demonstrated that a reflection measurement is a straightforward method to determine the resonance wavelength and lineshape of cavity plasmon modes. In this section, extinction measurements of MIM cavity arrays will be studied.
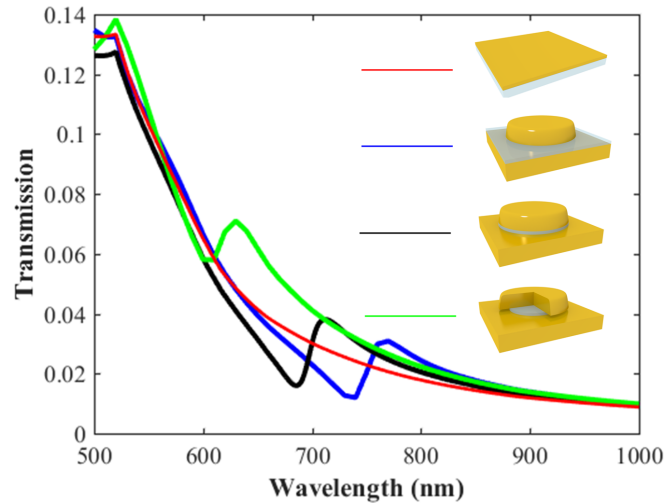
Figure 4.19: Fano profile of cavity plasmon modes in transmission. Simulated transmission spectra through three different MIM(I)-(III) and Au film t_{Au}=50 nm. The radius of the Au disc is 40 nm, the grating constant is 350 nm and the cavity height is 10 nm. The transmission spectra for MIM systems show the same tendency compared to the transmission through the gold film, except for a Fano modulation at the resonance position of the cavity modes.

Fano resonances have been extensively studied in plasmonic structures, as they contribute advantageous properties, such as a narrow resonance bandwidth, electromag-

netic induced transparency (EIT), etc. Fano resonances appear upon the interference of
a resonance with a narrow bandwidth and a broadband background. In order to under-
stand the Fano profile in extinction spectra, we investigated the transmission spectra
through MIM(I)-(III), shown in Figure 4.19. The transmission spectra through MIM
structures follow the tendency of the transmission through a Au film, except for the
Fano resonances appearing around the resonance position of cavity modes. We as-
sume that the Fano resonances in the transmission arise from the coupling between
the forward scattering of cavity modes and the transmission through the gold film. A
modified Fano formula, taking into consideration the intrinsic loss of metal, is adapted
from Martin et al [103, 178]. The spectral response is the product of the bright mode's
response with the asymmetric modulation:

$$Response = \frac{|A|^2}{(\frac{\omega^2-\omega_s^2}{\Gamma_s})^2 + 1} \frac{((\frac{\omega^2-\omega_a^2}{\Gamma_a}) + q)^2 + b}{(\frac{\omega^2-\omega_a^2}{\Gamma_a})^2 + 1} \qquad (4.9)$$

where $|A|$ is the maximum amplitude of the forced resonance if there is no coupling, ω_s
and ω_a are the resonance frequency of the bright mode with larger linewidth and dark
mode with smaller linewidth, respectively; Γ_s and Γ_a are the corresponding linewidth of
the bright mode and dark mode respectively; b is the modulation damping (or screening
parameter) and q represents the asymmetric parameter.
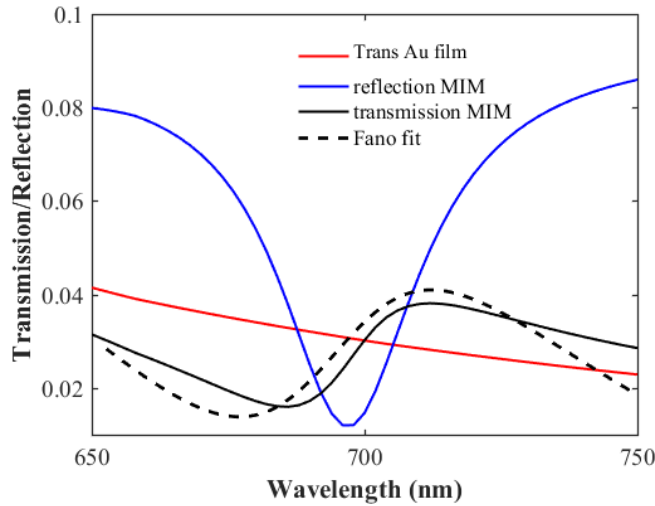
Figure 4.20: The Fano resonance for MIM(II) in Figure 4.19. The red curve is the
transmission spectrum through only 50 nm of Au film. The blue curve is the reflection
dip of MIM(II) with R_{Au}=40 nm, the amplitude has been scaled in order to be shown
together with the transmission curve. The dotted line shows a Fano fit based on the
Lorentz resonance plasmonic cavity mode and the transmission continuum. The solid
black curve is the simulated transmission through MIM(II). Good agreement can be
found between the the simulated transmission and the Fano hybridization between
transmission through the gold film and the transmission of the cavity mode TEM11.

In Figure 4.20, the Fano fit for MIM(II) is shown. The red and blue curve is the transmission through the Au film and the Lorentz reflection dip of cavity modes, which are taken as the two coupling elements for the Fano fit. The dashed black curve shows the Fano fit based on equation 4.9 with: A = 0.12, $\hbar\omega_s$= 1.59 eV (779 nm), $\hbar\Gamma_s$ = 227 meV, $\hbar\omega_a$= 1.78 eV (697 nm), $\hbar\Gamma_a$ = 252 meV, b = 0.4 and q = -0.6. The Fano fit in the dashed black curve agrees well with the transmission of the MIM(II) structure, supporting the assumption of a Fano resonance between cavity modes and the transmitted continuum, which is also referred to as incident radiance [178].
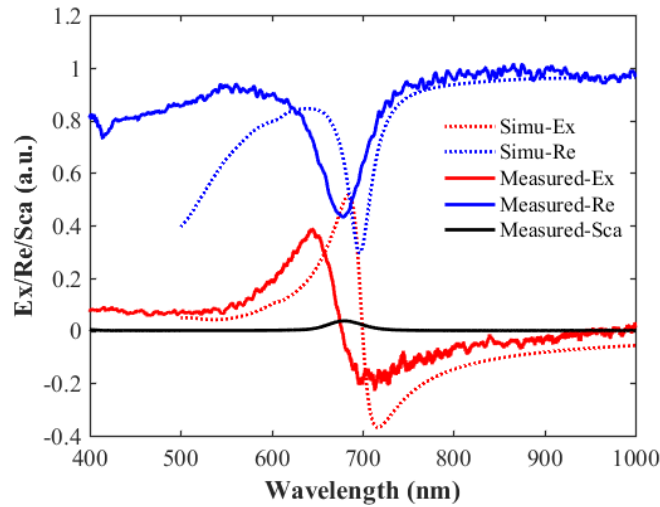
Figure 4.21: Simulated extinction (red dotted) and reflection spectra (blue dotted) for MIM(I) with R_{Au}=40 nm, t_{SiO_2}=10 nm and P=350 nm. Solid curves show the measured extinction (red), reflection (blue) and scattering (black) for MIM(I) with R_{Au}=38 nm, t_{SiO_2}=12 nm and P=335 nm. The symmetric scattering spectrum shows the same resonance characteristics as in reflection spectra: same resonance wavelength and inverse lineshape.

The measured (solid curves) and simulated (dotted curves) reflection (blue curves), extinction (red curves) and scattering (black curve) for a MIM cavity array are shown in Figure 4.21. The scattering measurement is obtained by the scattering set-up shown in Figure 3.9(a). The measured sample has parameters of R_{Au}=38 nm, t_{SiO_2}=12 nm and P=335 nm, and the simulated sample has parameters of R_{Au}=40 nm, t_{SiO_2}=10 nm and P=350 nm. The spectral profiles of the measured extinction and reflection agree well with the simulation, while the measured resonance wavelength is shorter compared to simulations. The smaller R_{Au} and bigger t_{SiO_2} in the fabricated MIM cavities lead to this discrepancy in resonance wavelength. The measured and simulated extinction spectra show negative extinction, this is because the extinction is evaluated taking transmission through a gold film and SiO_2 film as reference. The scattering measurement shown in the black curve in Figure 4.21 is another valid evidence of the Fano coupling assumption above. The scattering measurements were performed with

a transmission dark-field microscope, so the transmitted continuum through the gold film was not collected and only the forward scattering of the plasmonic cavity mode was collected. Moreover, the scattering spectrum shows the same Lorentz shape as in reflection (solid blue curve), and the resonance positions are both at 679 nm. On the contrary, the extinction spectra of cavity modes show significantly asymmetric profiles. To conclude, the plasmonic cavity modes are Lorentz shaped resonances, they appear in reflection and scattering spectra in symmetric resonance line shapes while appearing in asymmetric Fano profiles in transmission and extinction due to the coupling with the incident radiation.

4.7   Conclusion

In a coupled system consisting of arrays of gold discs on top of a gold film separated by an insulator layer, plasmonic modes with different natures can be excited. In this chapter, the cavity plasmonic modes in MIM cavities were studied. Firstly, the cavity modes in MIM structures were compared with those in simple gold discs: the presence of the Au film red-shifts the higher order cavity modes into the visible regime and decreases the resonance bandwidth by enhancing field confinement. Then, we demonstrated that the cavity plamonic modes in the visible/near-IR region are insensitive to varying periods in most cases. However, the periodicity affects the cavity modes notably when strong coupling happens between SPP modes and cavity modes. The hybridized modes obtain part of their energy from both SPP modes and cavity modes, and thus possess physical properties of both SPP and cavity modes. The TEMmn modes red-shift with increasing cavity radius, and follow the same dispersion relation as a corresponding MIM waveguide. An increasing cavity height leads to a blue-shift of the cavity modes, while the resonance wavelength of the TEMmn modes follows an exponential decay function relative to the cavity height. As to the far-field properties of cavity modes, the reflection and scattering spectra are a direct indicator of the resonance wavelengths and lineshapes of cavity modes. In extinction spectra, the cavity plasmon modes appear as Fano resonances due to the coupling with incident radiance. A sound understanding of plasmonic modes will serve as guidance in designing applications for cavity plasmon modes assisted sensing and spectroscopy.

Chapter 5

Exposing 'hot spots' of cavity plasmon modes

In the last chapter, properties of cavity plasmon modes in MIM cavity structures have been studied through experiments and simulations. In other works, similar structures have been investigated. The coupling and decoupling of LSPR and SPP modes in ordered nanoparticle arrays on gold film MIM structures have been studied in R. Nicolas' work [91]. In Ref [94], it has been shown, that it is possible to use plasmonic modes with two resonances which were created by coupling of SPP modes with a localized cavity mode. They were used for SERS measurements to achieve simultaneous enhancement at the excitation and Stokes wavelength. Cavity plasmon modes have also been used in surface enhanced infrared absorption spectroscopy [87], in which the cavity mode is tuned to match the frequency of the molecular vibration and an enhancement factor of absorption up to $2.2*10^6$ is achieved. Despite those nice results being achieved, there is still improvement to be made on these ordered MIM substrates in order to provide better performance in plasmon-assisted sensing and spectroscopy.

One can imagine when the thickness of the insulator spacer layer is less than 10 nm, the electromagnetic field is well confined and enhanced in the cylindrical dielectric spacer layer of the MIM cavities. In the previous works above, a thin continuous dielectric film was evaporated as a spacer layer. This however means, that only a very small fraction of the enhanced field of the cavity modes is accessible to the surrounding medium, since most of it is occupied by the dielectric spacer. This means that by making this part of the near-field accessible for molecule probes, the performance of this ordered nanoparticle-on-gold film MIM substrate as SERS substrates or other applications based on enhanced EM fields, can be considerably improved.

In this section, in order to address the issue that the strong EM field is not accessible

to the surrounding environment, the author studied by experiments and simulations the MIM cavity structure with an undercut, in order to expose the 'hot spot' of cavity plasmon modes. The field distribution and optical properties were compared for MIM(I)-(III).

5.1 Importance of the spacer undercut

Here we want to make the 'hot spots' of cavity plasmon modes accessible, by reducing the size of the dielectric spacer layer with wet etching. In order to validate that assumption and obtain a better understanding of the properties of the cavity modes, simulations for structures MIM(I)-(III) are performed.

5.1.1 Accessible enhanced EM field
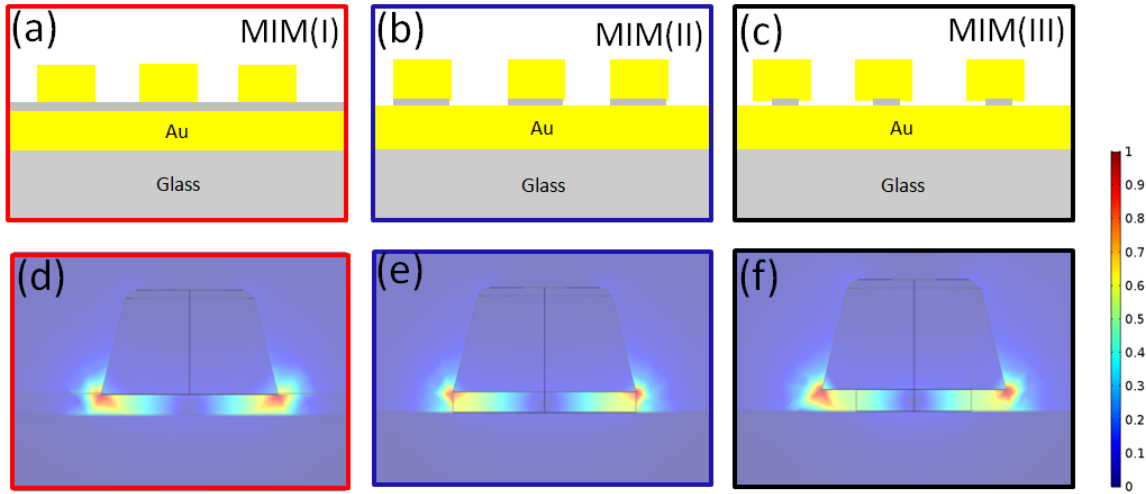
Figure 5.1: field map simulations for MIM(I)-(III). (a)-(c) schematics of MIM(I)-(III) with fixed gold disc radius R_{Au}=40 nm and grating constant P=350 nm. (a) MIM(I): dielectric film spacer; (b) MIM(II): dielectric disc spacer with radius R_{SiO_2}=R_{Au}=40 nm; (c) dielectric spacer with diameter of R_{SiO_2}=25 nm < R_{Au}. (d)-(f) Field maps of the cavity plasmon modes TEM11 in simulations for MIM(I)-(III), respectively. The field strengths are normalized to the field maximum in each map.

In Figure 5.1, MIM cavities with a gold disc radius of 40 nm and grating constant of 350 nm were studied. The spacer layer varies from a continuous silica film (a) to silica disc spacers with the same diameter $R_{SiO_2} = R_{Au} = 40$ nm (b) and smaller than that of the gold disc, $R_{SiO_2} = 25$ nm (c). Figure 5.1(a)-(c)shows the schematics of the three different MIM cavity configurations that were studied. The corresponding field maps

for the fundamental cavity mode TEM11 for each configuration are shown in Figure 5.1 (d)-(f).

The field distributions of this cavity mode are only slightly modified when the spacer geometry is changed, while the field maxima remain at their positions under the edges of the gold disc. The interpretation will be given in the following section. Here it is important to notice that in cavity configuration (c), the hot spots of the plasmonic cavity modes are exposed to the environment. This is of great importance for EM field enhanced physics where the accessibility to strongly enhanced EM fields is crucial.

5.1.2 Improving RI sensing performance
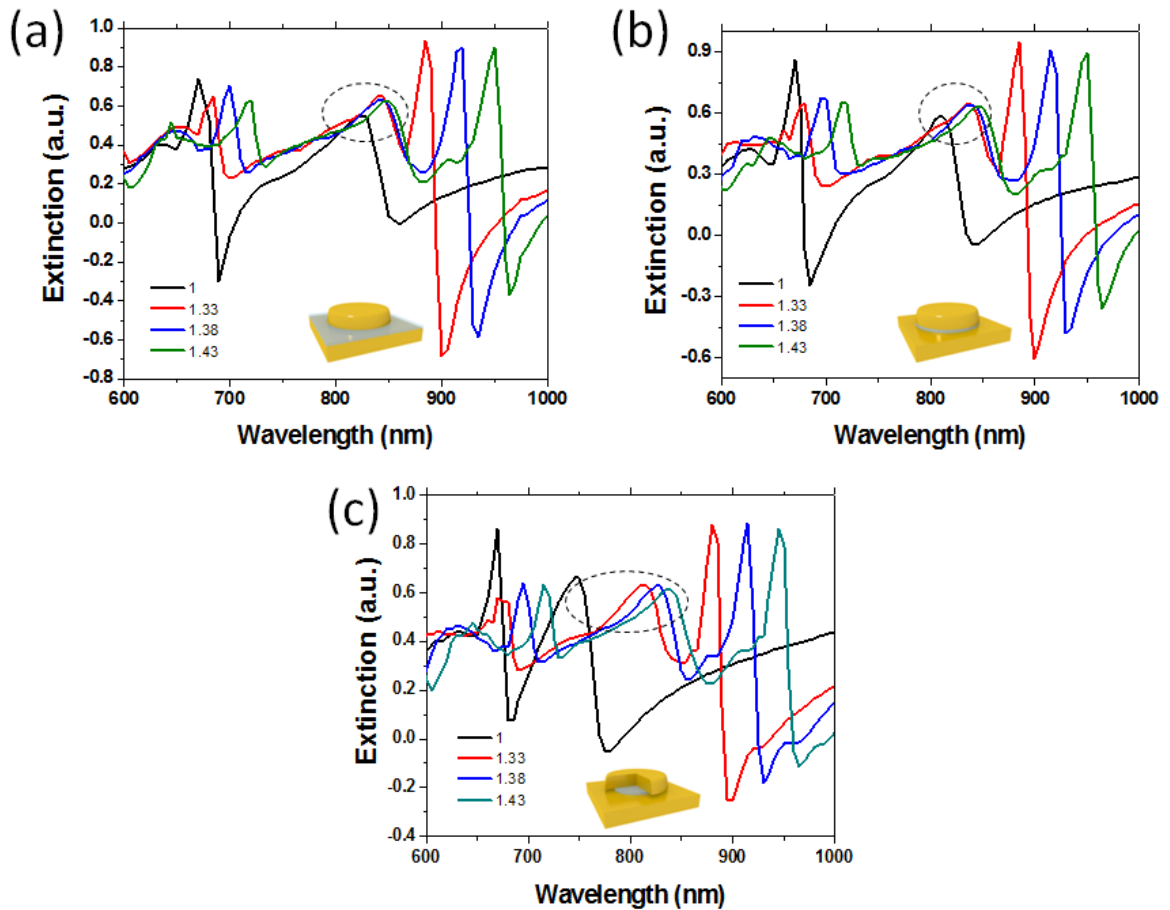
Figure 5.2: Sensing simulations for different arrays of MIM cavity structures as in Figure 5.1(a)-(c). The extinction spectra are evaluated based on equation 3.3. Radius of Au discs is $R_{Au} = 160$ nm and grating constant is P = 650 nm. The curves show extinction spectra with respect to different sensing refractive indices.

Figure 5.2 shows the simulated sensing results for different cavity configurations as showed in Figure 5.1(a)-(c). The simulated plasmonic cavities consist of Au disc array with a radius of 160 nm and grating constant of 650 nm. In simulations these cavities

are immersed in different refractive index solutions. Four different refractive indices are studied: n_1=1, n_2=1.33, n_3=1.38, n_4=1.43. The extinction responses of different MIM cavities to different refractive indices were evaluated and presented in Figure 5.2 (a)-(c). The evolution of cavity modes with respect to different refractive indices is highlighted by the dashed ellipse. It is clear that the sensitivity of cavity mode TEM12 in MIM(III) is better compared to MIM(I), with a more significant red shift of the extinction maximum as a function of increasing refractive index. The wavelengths where extinction maxima appear are recorded in Table 5.1, bandwidths are estimated, sensitivities and FoMs are evaluated in structures MIM(I)-(III).

Table 5.1: The wavelengths of simulated extinction maxima contributed by the TEM12 modes in MIM(I)-(III) are read from Figure 5.2 while the RIs of the surrounding media vary from 1 to 1.43. Senstivities (s) are evaluated by the spectral shift from n = 1 to 1.43. The band widths (FWHM) are estimated from the spectra with n = 1. FoM for TEM12 modes in MIM(I)-(III) are evaluated accordingly.

	n_1=1	n_4=1.43	S(nm/RIU)	FWHM (nm)	FoM
MIM(I)	827	852	58	76	0.76
MIM(II)	810	850	93	71	1.31
MIM(III)	749	837	205	48	4.27

In Table 5.1, it is shown that the RI sensitivities of modes TEM12 increase from 58 nm/RIU to 93 nm/RIU and 205 nm/RIU in MIM(I)-(III), respectively. The FoMs for the three different configurations were calculated based on equation 1.2: MIM(I) FoM = 0.76, MIM(II) FoM = 1.31, MIM(III) FoM = 4.27. The sensing performance of the cavity mode is notably improved after the hot spots of the cavity modes are exposed to the environment.

In conclusion, strongly enhanced EM fields can be excited in the small gaps between two metallic nanostructures. The two simulations above showed that little of the strong EM fields of cavity plasmonic modes can contribute to plasmon-assisted sensing or spectroscopy, if most of the enhanced EM field is localized inside the dielectric spacer layer. Whereas, by introducing an undercut in the MIM structure, the performance of plasmonic applications can be significantly improved.

5.2   Influence of spacer geometries

In this thesis, we propose to create the spacer undercut and expose the hot spots by wet etching, which will be presented in section 5.3. As presented in section 5.1, advantageous properties promising for plasmon assisted sensing and spectroscopy can

be obtained after an undercut is created in the MIM structure. In order to understand the physics behind these advantageous properties, it is crucial to understand the role played by the spacer layer on the resonance characteristics of cavity plasmons, so that we are aware of the change in plasmonic response of the MIM structure, before and after the etching process. In this section, the resonance characteristics of MIM structures with varying spacer geometries were studied.

5.2.1 Position of hot spots
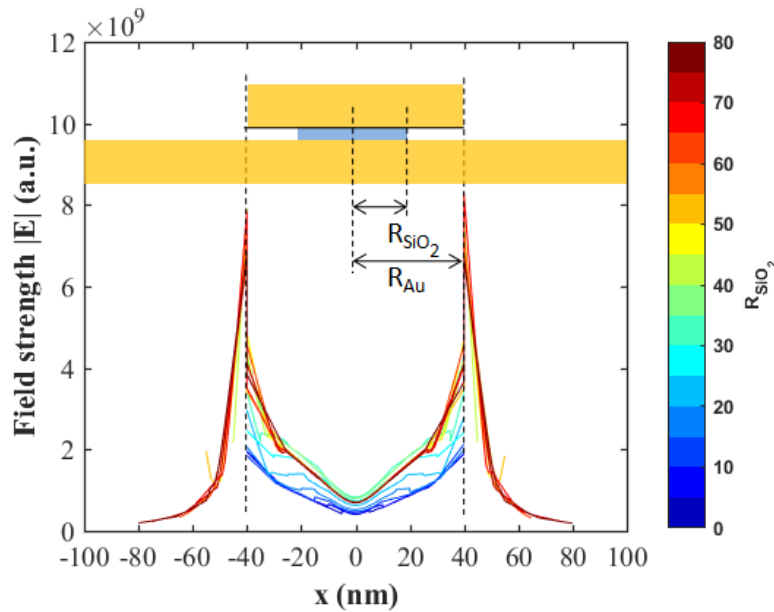
Figure 5.3: Field intensity along the diameter of a Au disc for different SiO_2 spacer discs, R_{SiO_2} varies from 5 nm to 80 nm in 5 nm steps. The R_{SiO_2} of each line is indicated by the colormap. R_{Au} = 40 nm, t_{SiO_2}= 10 nm, P= 350 nm.

In Figure 5.3, the E-field amplitude ($|E| = \sqrt{(E_x)^2 + (E_y)^2 + (E_z)^2}$) at the resonance wavelength along the diameter of a gold disc, at the position indicated by the black line, is shown for different MIM cavities. The radius of the SiO_2 disc varies from 80 nm to 5 nm in steps of 5 nm, and for each step the field strength is plotted, corresponding to when R_{SiO_2} is reduced by etching. The field maxima appear at the edges of the gold disc no matter how the size of the spacer varies. This can be explained from the nature of plasmonic cavity modes. In chapter 4, we demonstrated that the cavity plasmon modes are formed by the interference of incoming and outgoing gap plamonic modes supported by the corresponding MIM waveguide. In other words, these plasmonic modes are the result of continuous MIM waveguide modes getting selected by the discrete and sharp FP cavity resonance. The cylindrical FP cavity is defined by the two Au/dielectric interfaces and the edge of the gold disc, where the plasmonic waves are reflected. In these open FP cavities, the interference of incoming and outgoing

plasmonic waves always forms a standing wave with field maxima at the edge of the cavity, which is indicated by the edge of the gold disc [179]. As a result, there are always field maxima, also referred to as 'hot spots', of cavity plasmon modes residing at the edges of the gold disc, as can be observed in Figure 5.1 (a)-(c). We note that there is a discontinuity of the E field intensity at the edge of the gold disc, due to the sudden change of material permittivity from gold to air.

In conclusion, in an open MIM cavity the field distributions of cavity plasmon modes are insensitive to the change of spacer layer. The 'hot spots' of plamonic cavity modes can be exposed to the detecting environment by creating an undercut in the MIM cavity.

5.2.2   Resonance wavelength
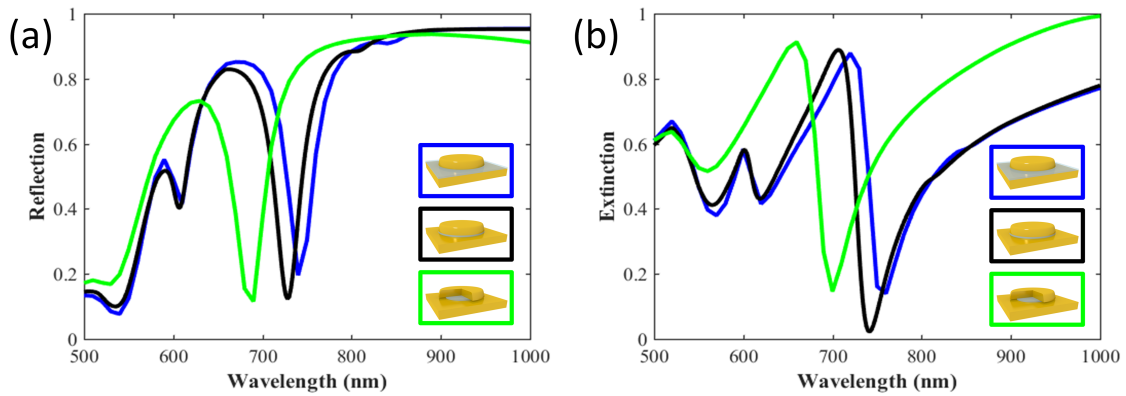
Figure 5.4: Simulated reflection (a) and extinction (b) spectra for MIM cavities with different insulator spacer geometries. Blue curve: SiO_2 film spacer (MIM(I)), black curve: SiO_2 disc spacer (MIM(II)), green curve: etched SiO_2 disc spacer $R_{SiO_2}=R_{Au}/2$ (MIM(III)). The spacer thickness, radius of gold disc and grating constant are 10 nm, 130 nm and 350 nm, respectively, in all the cases.

While the field distribution only undergoes a minor disturbance from the size variation of the insulator spacer, the cavity resonant wavelength position is notably blue shifted from MIM(I) (blue curves) to MIM(III) (green curves), as shown in Figure 5.4.

Figure 5.4 shows the simulated reflection and extinction spectra for arrays of MIM cavities with a radius of 130 nm, cavity height of 10 nm and grating constants of 350 nm, with different spacer geometry as shown in the insert. In Figure 5.4(a), the resonance position of the cavity plasmon mode (TEM12 mode) blue shifted from 744 nm to 728 nm then to 684 nm for MIM(I), MIM(II) and MIM(III), respectively. The Fano shaped resonance in extinction spectra in Figure 5.4(b) also showed similar blue-shift behaviour from MIM(I) (blue curve) to MIM(III) (green curve). This can be explained

from the characteristics of the FP cavity. As can be seen in Figure 5.1, $R_{Au} + \Delta R$ is nearly unchanged for MIM(I)-(III), thus the optical lengths of the resonance radius are $(R_{Au} + \Delta R) * n_{SiO_2}$, $(R_{Au} * n_{SiO_2} + \Delta R)$ and $(R_{SiO_2} * n_{SiO_2} + R_{Au} - R_{SiO_2} + \Delta R)$ for MIM(I)-(III), respectively. The decreasing optical length of the resonance radius leads to the blue-shift of cavity plasmonic modes TEMmn from MIM(I) to MIM(III), as observed in Figure 5.4. This means that the variation of the spacer geometry in MIM cavity structures affects the optical lengths of the resonance radius, and thus influences strongly the resonance position of cavity plasmon modes.

5.2.3 Simulations of progressive wet-etching

The progress of wet etching is simulated by investigating MIM(III) structures with decreasing R_{SiO_2}. In Figure 5.5, the wavelengths where the extinction maxima appear
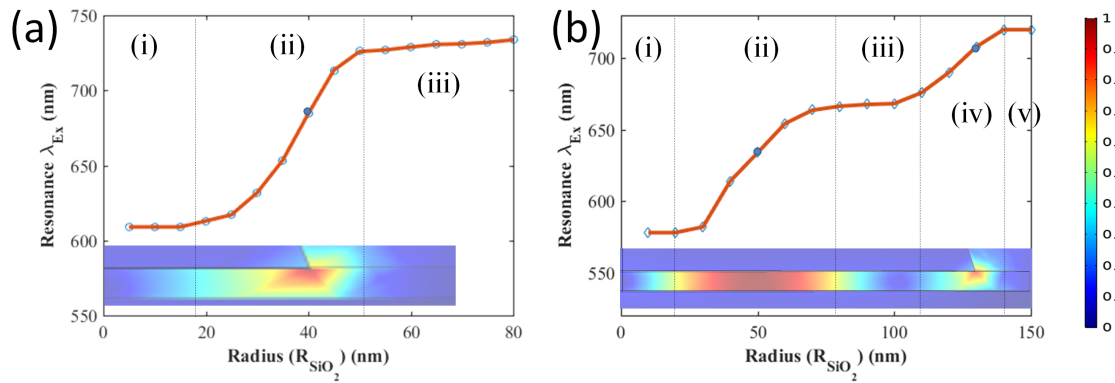
Figure 5.5: Simulating the progress of wet-etching. The simulated extinction maximum position is shown as a function of the SiO$_2$ disc spacer size R_{SiO_2} for MIM cavities with R_{Au}= 40 nm (a) and 130 nm (b). The spacer thickness and grating constant are 10 nm and 350 nm, respectively, in both cases. The side views of field maps for the TEM11 (a) and TEM12 (b) modes in MIM(I) are positioned accordingly to the coordinates of the x-axis.

are shown for the TEM11 (a) and TEM12 (b) modes as a function of the spacer radius R_{SiO_2} in MIM(III). Figure 5.5(a) depicts the evolution of the TEM11 mode position in MIM cavities with a radius of 40 nm with varying radius of the spacer from 5 nm to 80 nm. When the radius of the SiO$_2$ spacer is beyond 50 nm (regime III in Figure 5.5(a)), most of the E field energy is inside the dielectric spacer, so the resonant wavelength does not red shift as the dielectric spacer radius further increases. When the spacer radius is between 30 nm and 50 nm (regime II in Figure 5.5(a)), the field maxima are partly in the spacer and partly in the air, and the effective resonant radius decreases as the spacer radius gets smaller, resulting in a blue shift of the resonant wavelength from 733 nm to 609 nm. When the spacer disc radius is smaller than 30 nm (regime

I in Figure 5.5(a)), the field maxima are completely in air and not influenced by the size of the SiO_2 spacer anymore.

The dependency of the resonance position as a function of spacer radius was also studied for a MIM cavity with a radius of 130 nm. From chapter 4, we know that the TEM12 mode is the most predominant mode in the visible region when R_{Au} = 130 nm, and the TEM12 mode features two more modal lobes in the central region of the circular cavity, compared to the TEM11 mode. When the radius of the spacer is beyond 140 nm (regime V in Figure 5.5(b)), which is also the resonance cavity radius $R_{Au} + \Delta R$, the resonance position is independent of the spacer radius. In regime I and III, when the refractive index was modified at the nodes of the standing wave, the resonance position is hardly influenced by the change of spacer radius. In regime II and IV, when the local refractive index within the field maxima is modified by reducing the SiO_2 spacer, the resonance position of the TEM12 mode blue shifts significantly with decreasing R_{SiO_2}.

The resonance position is the most sensitive to the change of refractive index where there is the strongest E field, as marked by blue dots in both Figure 5.5(a) and (b). We conclude that the resonance position only shifts when the refractive index at the hot spots is modified. This rule applies to other cavity modes as well, regardless of the dimensions of MIM cavities. Based on this conclusion, this simulation of progressive wet-etching can be a straight-forward method to determine the fringe field region ΔR for equation $k_{gsp}(R_{Au} + \Delta R) = \chi'_{mn}$. As can be seen from Figure 5.5(a) and (b), $\Delta R \approx t_{SiO_2} = 10$ nm for both the TEM11 mode and the TEM12 mode.

5.3 Fabrication of undercut

Plamonic structures have been intensively studied over the last decades because the strong near-field inherent to plasmonic modes has been found to be very appealing for plasmonically enhanced sensing and spectroscopy. However, the 'hot spots' usually reside in the substrate or in the insulator layer and are not accessible to the analytes. In order to expose the 'hot spots' of cavity plasmon modes, wet etching and selective reactive-ion etching (RIE) were applied to reduce the size of the insulator layer [93, 95, 180]. In Ref. [180], a buffered oxide etch was used to achieve a pillar-like support for gold discs, in order to passivate the glass substrate from interacting with the sensor functionalization, more importantly, to make it possible that all the hot spot of the LSPR mode is open to molecules. In Ref. [95], a Au NPs/Al_2O_3/Au NPs composite was etched with 5% KOH solution for 120 s in order to expose the hot spots in the dielectric layer. Except for the wet etching method, a dry etching method was also used to introduce undercut in MIM structures [93].

The wet etching of evaporated SiO_2 with hydrofluoric (HF) acid has been well established in semiconductor industry, and buffered oxide etchant is also commercially available. So in this thesis, we introduced undercut in the gold/SiO_2/gold MIM cavities by wet etching because it is the most straight-forward and readily accessible method in the laboratory.

(1) Deposition
3 nm Cr
50 nm Au

(2) Spin
coating PMMA

(3) Electron beam exposure、
chemical development

(4) Deposition of
10 nm SiO_2
50 nm Au

(5) Lift-off

(6) Wet etching
buffered HF acid
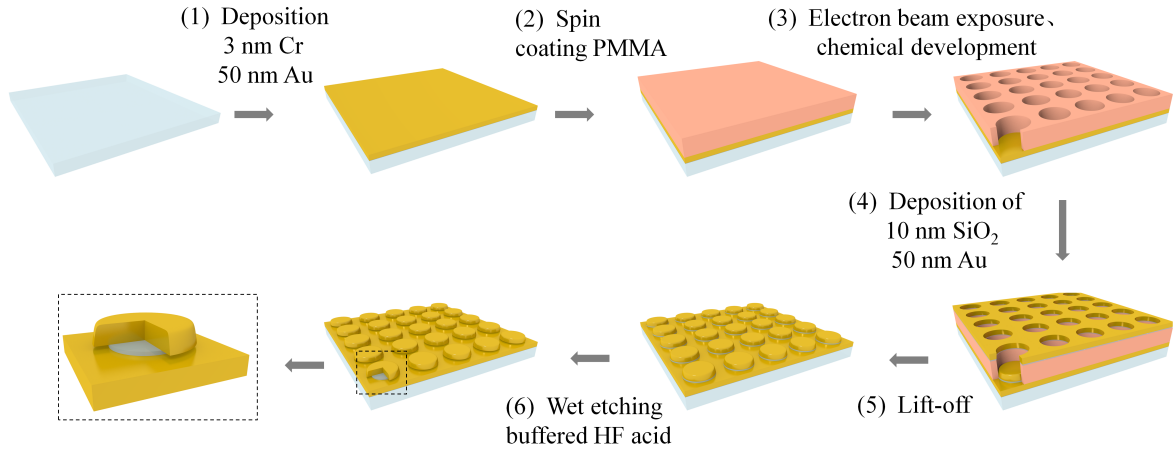
Figure 5.6: Schematic description of the fabrication of MIM structures with undercut.

Figure 5.6 depicts the fabrication process of a MIM cavity with an undercut. Arrays of MIM cavities with $R_{SiO_2} = R_{Au}$ were fabricated by standard EBL process following the steps (1) to (5). Then diluted HF with a concentration of 0.03 % (wt) in water was used to reduce the diameter of the SiO_2 spacer. The very low concentration of the etchant allows for homogeneous etching of the spacer on a well controllable time scale.

5.4 Wet etching experiments

The influence of decreasing R_{SiO_2} by wet etching on the location of 'hot spots' and the resonance wavelength has been investigated through simulations in the previous sections. Here, the optical properties of MIM(II) (before wet etching) and MIM(III) structures (after etching) are presented. The extinction spectra of arrays of MIM cavities were recorded taking transmission through a 50 nm gold film as reference, before and after the arrays of MIM structures were etched for 40 s. A collimated illumination was used and the numerical aperture of the collecting objective is 0.4.

Figure 5.7 shows the evolution of extinction spectra for MIM cavities with a radius around 130 nm and varying grating constants, before and after the etching process. The dimensions of the cavities are shown in the legend with R_{Au} and P indicating the cavity radius and periodicity, respectively. The resonance positions of LSPR modes with 'hot spots' residing at the top edge of the gold discs are not influenced by the

etching process when grating constants are 335 nm (blue curve) and 440 nm (black curve). In the case of P = 530 nm (red curve), there is one mode showing an extinction maximum at 559 nm which is a hybridized mode of a LSPR mode and $SPP_{air/Au}(0,1)$. Moreover, this hybridized mode is insensitive to the etching process as well. This can be easily understood by the resonance conditions of the LSPR mode and SPP mode. The LSPR mode is highly sensitive to the refractive index change inside its 'hot spots', which are ∼ 50 nm away from the varying RI in the insulator. The RI sensitivity of the LSPR mode will be shown in details in chapter 6. On the other hand, the grating induced SPP modes are dependent of the grating constants, incident angle, and refractive index change inside their near-field. Therefore, both LSPR modes and SPP modes are insensitive to the change of the refractive index in the insulator layer. As a result, these modes stay at the same positions before and after etching as can be observed in Figure 5.7.
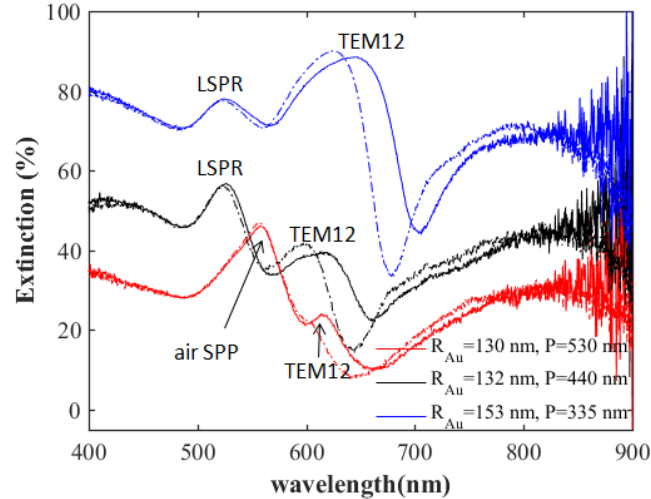
Figure 5.7: Extinction spectra for arrays of MIM cavities, before (solid curves) and after (dashed curves) the wet etching step, respectively. The blue, black and red curves present the extinction spectra obtained from MIM(II) (solid curve) and MIM(III) (dashed curve) with R_{Au} = 153 nm, 132 nm and 130 nm, respectively.

On the other hand, the TEM12 modes as labelled in Figure 5.7, blue shift notably after the etching process, agreeing well with the simulations in section 5.2. The extinction maxima resulting from the TEM12 mode blue shifted from 647 nm to 626 nm, from 619 nm to 598 nm and 616 nm to 600 nm for MIM cavities with R_{Au} = 153 nm, 132 nm and 130 nm, respectively. For the array of MIM cavities with a radius of 130 nm and grating constant of 530 nm, the resonance position blue shifted by 16 nm. Relating to the simulated results in Figure 5.5 (b), the radius of the SiO_2 disc is thus reduced by ∼ 14 nm. Because the etching process is isotropic, we assume that the radius of the SiO_2 spacer was reduced by 14 nm in all the arrays of MIM cavities for simplicity.

This assumption will be used in chapter 7 when calculating the relative enhancement factor of undercut MIM cavities.

5.4.1 Response of different TEMmn modes

In chapter 4, we presented that the edge cavity modes and the surface cavity modes show very different field distribution characteristics: the edge modes have their strong near-field distributed in the modal lobes around the circumferences of the MIM cavities, on the other hand, the surface cavity modes have most of their energy confined in the central modal lobes rather than the edge lobes. Moreover, different orders of surface cavity modes show different confinement strength as shown in section 4.3.1. In this section, the sensitivities of different orders of cavity modes to wet etching will be investigated through experiments and simulations.
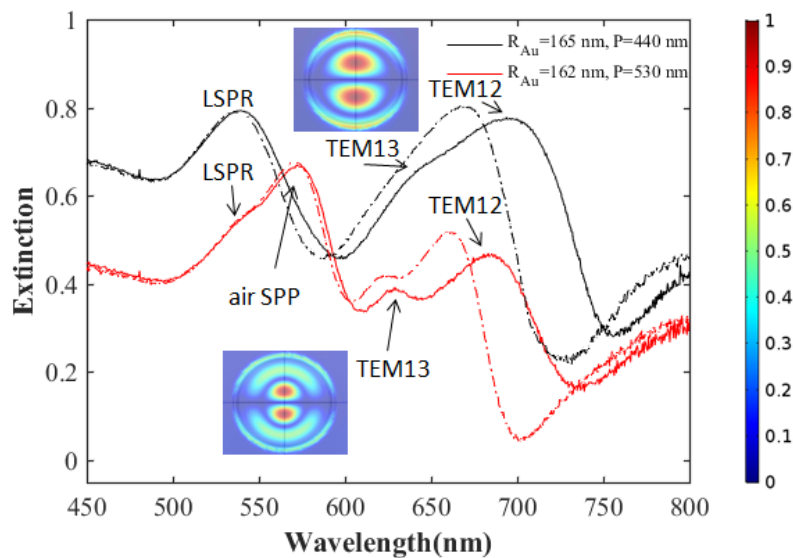
Figure 5.8: Measured extinction spectra for arrays of MIM cavities with R_{Au}= 165 nm, P = 440 nm (black curve) and R_{Au}= 162 nm, P = 530 nm (red curve) are shown, before (solid curves) and after (dashed curves) the wet etching step, respectively. Inserts are the field maps of the TEM12 and TEM13 modes.

Figure 5.8 shows the extinction spectra before (solid curves) and after (dashed curves) etching for arrays of MIM cavities with diameters around 320 nm and grating constants of 440 nm (black) and 530 nm (red). Similar to Figure 5.7, the LSPR mode and hybrid mode did not move before and after the etching step, while for the plasmon cavity mode TEM12, the extinction peaks blue shifted from 696 nm to 670 nm for the cavity array with a diameter of 331 nm, and shifted from 686 nm to 661 nm when the cavity diameter is 324 nm. The TEM12 modes blue shifted by 26 nm and 25 nm after etching respectively. The cavity plasmon mode TEM13 in the red curves blue shifts from

629 nm to 623 nm. The resonance position of the TEM13 mode shifted by 6 nm, significantly less influenced compared to the TEM12 mode. This can be explained by the energy distributions of mode TEM12 and TEM13. In chapter 4, we demonstrated that for higher order modes TEM12 and TEM13, the mode energy resides rather in the central modal lobes than the edge lobes, as can be seen in the inserts of Figure 5.8. A bigger portion of the near field is distributed at the edge of MIM cavities for mode TEM12 than for TEM13. As a result, mode TEM12 is more sensitive to the change of refractive index at the rim of MIM cavity than mode TEM13. In order to provide theoretical support for the explanation, simulations were performed to investigate the behaviours of different modes in response to the etching process.
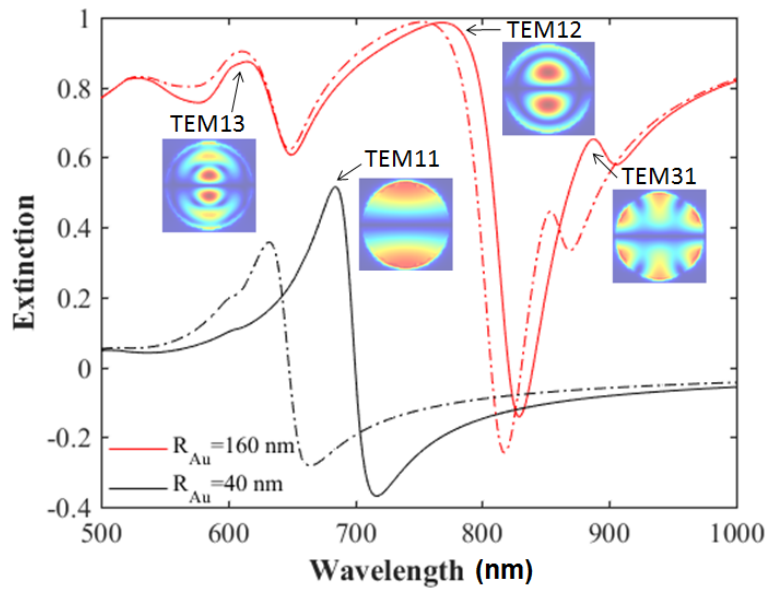
Figure 5.9: Simulated extinction spectra for arrays of MIM cavities with radius of 160 nm (red) and 40 nm (black), before (solid curves) and after (dashed curves) the SiO_2 spacer is reduced by 10 nm, respectively. Array constant is 350 nm. Inserts are the field maps of plasmonic cavity modes.

Figure 5.9 shows the simulated extinction change when the SiO_2 spacer is reduced by 10 nm, MIM cavities with radius of 40 nm and 130 nm are studied.

Table 5.2: The positions of extinction maxima resulting from the TEMmn modes in the simulated extinction spectra before and after wet etching in Figure 5.9.

TEMmn	before etching	after etching	shift
TEM11	684 nm	632 nm	52 nm
TEM12	780 nm	766 nm	14 nm
TEM13	616 nm	612 nm	4 nm
TEM31	886 nm	854 nm	32 nm

The extinction peak blue shifts from 684 nm to 632 nm for the TEM11 mode when R_{Au} = 40 nm. The extinction peaks shift from 886 nm to 854 nm, 780 nm to 766 nm and 616 nm to 612 nm for plasmonic modes TEM31, TEM12 and TEM13, respectively. When the SiO_2 spacer is etched by 10 nm, the TEM11, TEM12, TEM13 and TEM31 mode shift to a shorter wavelength by 52 nm, 14 nm, 4 nm and 32 nm. Comparing the field maps of different modes, we can draw the conclusion that the modes with more energy distributed at the edge of the MIM cavities, like the edge modes TEM11 and TEM31, show a higher sensitivity to the modification of the refractive index by etching. For surface cavity modes TEM12 and TEM13, most of the energy resides in the central modal lobes, these modes show a relatively moderate sensitivity.

We note that the blue-shift in simulations, assuming R_{SiO_2} is reduced by 10 nm, is larger than the blue-shift in experiments, where the radius is assumed to be ∼14 nm smaller after etching. This maybe due to the slanted wall of the SiO_2 disc spacer in the experiment, while this is not considered in the simulations in Figure 5.9. As presented in chapter 4, the slanted side wall of the SiO_2 disc makes the radius of the gold disc smaller than R_{SiO_2}. This is also assumed to be the reason why the positions of extinction maxima are at a shorter wavelength in experiments than in the simulations.

5.5 Conclusion

In this chapter, the author discussed the importance of exposing the 'hot spots' for plasmon-assisted spectroscopy and sensing. The influence of the spacer geometry on the position of the 'hot spots' and resonance wavelengths of cavity plasmon modes was investigated. The cylindrical cavities for cavity modes are defined by the thickness of the spacer layer and the diameter of the gold disc, instead of the diameter of the dielectric spacer. The MIM cavity can be seen as a metal/insulator/metal waveguide with finite dimensions, and the nature of the cavity resonant modes is due to formation of standing waves by the interference of incoming and outgoing guided modes of the MIM waveguide which were reflected at the edges of the MIM cavity. Thus, however the geometry of the dielectric spacer changes, waveguide modes will always get mainly reflected at the edges of the gold discs, forming field maxima at the end of an open cavity. As a result, the change of refractive index in the spacer layer does not effect much the field distribution, but affects significantly the resonance position. When the size of the insulator spacer gets reduced by etching, the resonance positions of cavity plasmon modes blue shift when the local refractive index at the modal lobes gets modified, while the resonance positions stay unchanged if only the refractive index at the modal nodes was changed by etching. Due to the fact that edge cavity modes

possess more modal energy at the edges MIM cavities compared to surface cavity modes, edge modes TEM11 and TEM31 show higher sensitivity to the decreasing R_{SiO_2} than surface modes TEM12 and TEM13.

From the point of application for plasmon-assisted sensing and spectroscopy, configuration MIM(III) is superior to MIM(I) and MIM(II), because not only the strongest near field is now accessible to the surrounding environment, also the accessible mode volume is increased.

Chapter 6

Sensing performance of MIM structure

In Chapter 4, we studied the physical properties of cavity plasmon modes in MIM cavities. It has been show through simulations and experiments that the cavity plasmon modes show advantageous properties such as strong near-field and narrow bandwidth. However, the near-fields of the TEMmn modes are mostly confined in the continuous insulator film in the MIM(I) structure, which is beyond the reach of the surrounding medium. Then in chapter 5, we showed that the sensing capabilities of the TEMmn can be significantly increased by exposing the near-field of cavity plasmon modes. The TEMmn modes show increasing sensitivity in the order of MIM(I), MIM(II) and MIM(III), indicating that the sensitivity of plasmonic modes increases continuously as a function of increasing sensing volume where the plasmonic near-field interacts with the detecting medium.

As has already been demonstrated in the measured or simulated far-field spectra in the last chapters, several different types of modes can be identified through far-field spectra: cavity plasmon modes, SPP modes on Au/glass and Au/air interfaces, SLR modes resulting from the diffraction of metal gratings and LSPR modes of gold discs. These plasmonic modes possess different dependencies on the surrounding media and different 'hot spots' locations. The goal of this chapter is to compare the sensing capabilities of different plasmonic modes. The sensing performance of different modes is studied in bulk RI sensing through simulations and experiments, where RI changes in the bulk medium are detected. Then, their sensing performance in molecular sensing configurations, where the RI is only modified locally in the vicinity of the metallic structures, will be investigated by simulations.

6.1   Sensing capability

In section 1.1.1, we presented two of the most common methods to describe the sensing capability of a plasmonic mode. One is RI sensitivity S, defined by $\frac{d\lambda}{dn}$ as shown in Figure 6.1(a), which describes how much the resonance wavelength would shift in response to the refractive index change of one RI unit. The other most commonly used standard is the FoM, which is obtained by dividing the sensitivity by the line width $\Delta\lambda$ (FWHM) of the resonance: FoM$=\frac{S}{\Delta\lambda}$. The definition for S and FoM can
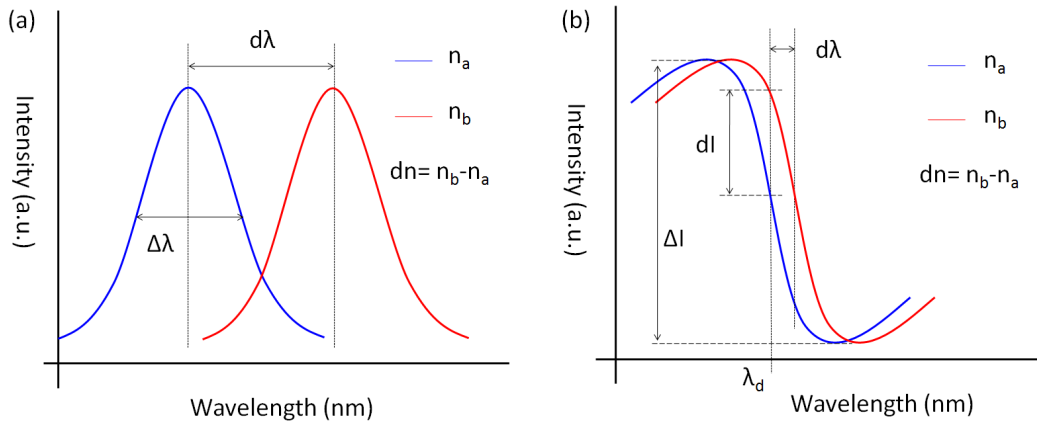
Figure 6.1: (a) Definition of the S and FoM for a Lorentz-shaped resonance: $S = \frac{d\lambda}{dn}$, FoM $=\frac{S}{\Delta\lambda}$; (b) Definition of FoM* for asymmetric plasmonic response: FoM* $= \frac{S\frac{dI}{d\lambda}}{I}$, FoM* is not necessarily defined at the peak/dip position, but the wavelength that gives the maximum intensity change with the refractive index change. $S_I = dI/dn = S\frac{dI}{d\lambda}$ is defined for intensity modulated sensors.

be seen in Figure 6.1. For the plasmonic modes appearing as a single sharp resonance in the spectra, the S and FoM can be easily determined. However, it is difficult to determine a consistent line width (FWHM) for complex plasmonic nanostructures with complicated plasmonic resonances, in order to calculate the FoM. To settle this issue for asymmetric plasmonic responses, Becker et al. suggested an alternative figure of merit FoM* [11, 181]:

$$FoM^* = (\frac{\frac{dI}{dn}}{I})_{max} = (\frac{\frac{dI}{d\lambda}\frac{d\lambda}{dn}}{I})_{max} = (\frac{S\frac{dI}{d\lambda}}{I})_{max} \tag{6.1}$$

In their concept of FoM*, the relative intensity change dI/I which is proportional to the relative resonance shift $d\lambda/\Delta\lambda$ is measured at a fixed wavelength λ_d which gives the maximum intensity change in response to an index change dn. Then there is no necessity to measure the bandwidth of the plasmonic resonance. Moreover, the sensing performance of sensors based on intensity change and those based on resonance shift can be directly compared. From chapter 4 and chapter 5, we know that MIM

cavities give a very complicated plasmonic response with different modes coupling to each other, besides, the TEMmn modes appear as Fano shapes in extinction spectra of MIM structures. FoM* suits our situation better than FoM. However, there are negative values in extinction spectra because the transmission through a gold film is taken as reference (as can be seen in Figure 4.13 and 4.21), which leads to a singularity of FoM* at I$\rightarrow$0. In this thesis, we make a modification on the basis of FoM*: the relative intensity change dI/ΔI is measured instead of dI/I. So $FoM^* = (\frac{S\frac{dI}{d\lambda}}{\Delta I})_{max}$ can be obtained. Moreover, we take into consideration the limit of detection (LOD) and dynamic sensing range of sensors, which depend on the signal/noise ratio and are proportional to ΔI, as in Figure 6.1. Then we obtain from FoM* the sensitivity of an intensity modulated sensor $\bar{S}_I$. The definition can be seen in equation 6.2.

$$\Delta I * FoM^* = \Delta I * (\frac{S\frac{dI}{d\lambda}}{\Delta I})_{max}) = (S\frac{dI}{d\lambda})_{max} = dI/dn = \bar{S}_I \qquad (6.2)$$

The positive or negative signs of $\frac{dI}{d\lambda}$ and $\bar{S}_I$ represent that either an intensity decrease of increase is detected at the detecting wavelength λ_d. In this thesis, the modulus of sensitivity is interested and is defined as:

$$S_I = S(|\frac{dI}{d\lambda}|)_{max} \qquad (6.3)$$

In order to facilitate the comparison of sensing capability between different modes, S_I is used as a standard together with the sensitivity S and FoM to evaluate the performance of plasmonic sensors. In this thesis, S_I is obtained by evaluating the spectral shift S and identify $(|\frac{dI}{d\lambda}|)_{max}$ by matlab calculation, and then S_I is calculated based on equation 6.3 by $S_I = S(|\frac{dI}{d\lambda}|)_{max}$.

6.2 Sensitivities of modes in smaller MIM cavity

In this chapter, we will focus mainly on MIM(III) and MIM(II) where the advantageous plasmonic properties of cavity plasmon modes are better exploited. For the MIM(III) cavity studied in this chapter, $R_{SiO_2} = 1/2R_{Au}$. We start to characterize the sensing performance of MIM cavities with smaller R_{Au}, because their plasmonic response is relatively simpler with the TEM11 mode predominating in the visible/near-IR region. In this section, we choose MIM cavity arrays with a cavity radius of R_{Au}=40 nm and periodicity of P=450 nm and P=550 nm to study their sensing capabilities based on extinction measurements and reflection measurements. The periodicity of 450 nm is chosen so that we can compare the sensitivities of TEM11 mode and SPP$_{Au/envir}$(0,1)

mode. And in MIM(III) with R_{Au}=40 nm, strong coupling will occur between SPP and cavity modes when P=550 nm, providing a platform to study if the strong coupling can improve the sensitivity of the TEMmn mode.

6.2.1   Sensing without strong coupling

6.2.1.1   Sensor properties based on reflection

The reflection dip is a straightforward indicator of the resonance wavelength of the TEMmn modes, making it easier to identify each mode in sensing. We start from the MIM(III) cavity array that gives a simpler plasmonic response with R_{Au}=40 nm and P=450 nm. We characterize the sensing capabilities of plasmonic resonances appearing in the reflection spectra of a MIM(III) cavity. The RI of the surrounding medium n_s varies from 1, 1.33, 1.35, 1.38 to 1.43. The near-field resonance spectra are shown with n=1.33, in order to identify the plasmonic modes.
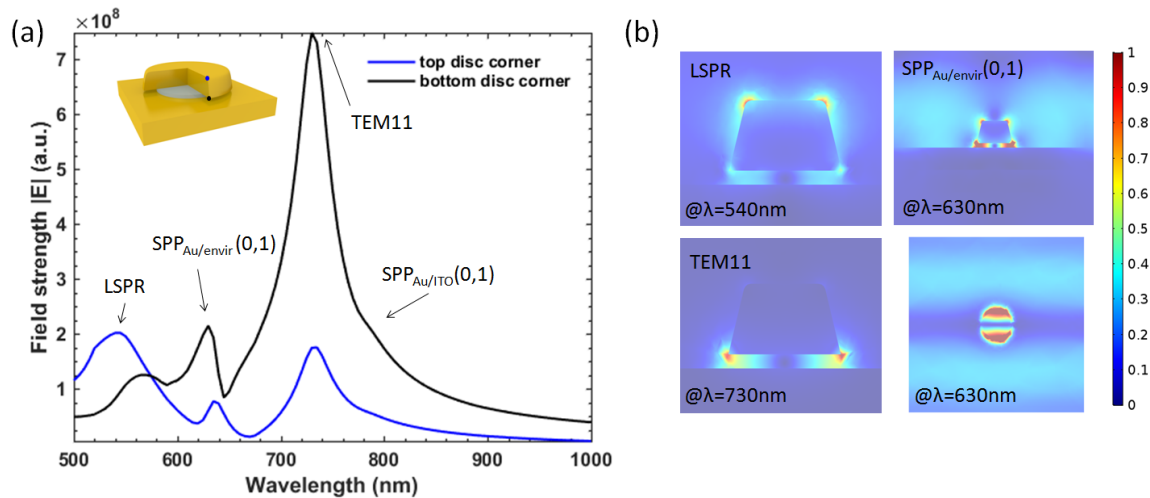
Figure 6.2: (a) The near-field strength ($|E| = \sqrt{E_x^2 + E_y^2 + E_z^2}$) on the top corner and bottom corner of the gold disc, as indicated by the black and blue dots in the inserted picture. The MIM(III) has $R_{Au}=2R_{SiO_2}$=40 nm, P=450 nm, and the MIM structure is on top of an ITO substrate (t_{ITO}=50 nm). The nature of each resonance is labelled: a LSPR mode, TEM11 mode, and $SPP_{Au/envir}(0,1)$ and $SPP_{Au/ITO}(0,1)$. Weak coupling occurs between the TEM11 mode and $SPP_{Au/envir}(0,1)$ mode, resulting in the Fano shape of the SPP, while the TEM11 mode is hardly disturbed. (b) The field maps in side view for each plasmonic resonance peak: LSPR mode with strong near-field on the top of the gold disc (λ=540 nm), TEM11 mode (λ=730 nm) with strong near-field confined in the cavity. The field maps for $SPP_{Au/envir}(0,1)$ (λ=630 nm) from both the top view and side view are shown.

In Figure 6.2(a), the E field strength ($|E| = \sqrt{E_x^2 + E_y^2 + E_z^2}$) on the top corner and bottom corner of the gold disc as shown by the insert picture, are presented

for MIM(III) with R_{Au}=40 nm and P=450 nm. The MIM cavity is on top of an ITO substrate, which is sometimes used in practice to promote the adhesion between gold film and glass substrate. It influences the resonance position on the Au/ITO substrate (50 nm ITO film on glass substrate), while it has no influence on the cavity modes except when strong coupling occurs. The nature of the plasmonic resonance is identified by checking the field maps at each resonance and is labelled accordingly in the resonance spectra. Figure 6.2(b) shows the corresponding near-field distributions. In this MIM cavity array which is immersed in water, three types of plasmonic modes are excited. The most pronounced mode is the TEM11 mode, appearing at 730 nm with its strong near-field squeezed inside the cavity. A SPP mode on the Au film and sensing environment interface, which is referred as Au/envir interface later, is excited. The $SPP_{Au/envir}(0,1)$ couples with the TEM11 mode in the weak coupling regime, leading to a Fano resonance from 610 nm to 660 nm (The original resonance wavelength $\lambda_{Au/envir}(0,1) = 646$ nm, according to equation 4.1). There is a $SPP_{Au/ITO}(0,1)$ mode excited at 795 nm. A LSPR mode with 'hot spots' on the top of the gold disc is excited at 540 nm.
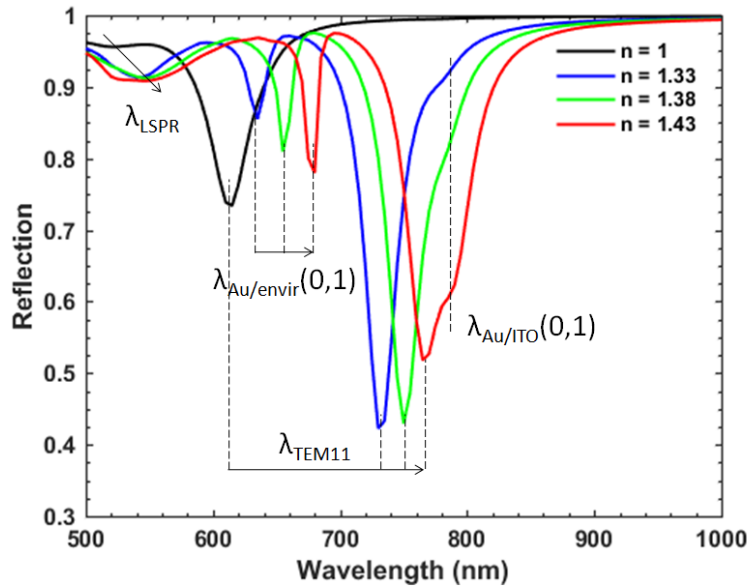
Figure 6.3: The simulated sensing spectra based on reflection for a MIM(III) cavity with $R_{Au}=2R_{SiO_2}$=40 nm, P=450 nm and t_{SiO_2}=10 nm. The RI of the detecting solution varies from 1 (black curve) to 1.33 (blue curve), 1.38 (green curve) and 1.43 (red curve). The nature of the plamonic modes is labelled accordingly.

In Figure 6.3, the reflection spectra for the MIM cavity are presented with the RI of the surrounding medium varying from 1 to 1.33, 1.38 and 1.43. The wavelength shift of each plasmonic mode is labelled. It is clear that the $SPP_{Au/envir}(0,1)$ mode and the TEM11 mode show notable red-shifts with increasing detecting RI, while the $SPP_{Au/ITO}(0,1)$ mode hardly shows a response to the RI change. The LSPR mode at

short wavelengths shows resonance wavelength shifts to the RI change, however, not as sensitive as the $SPP_{Au/envir}$ mode and the TEM11 mode. As it can be seen in Figure 6.3, the $SPP_{Au/envir}$ mode and TEM11 mode appear in the sensing spectra as discrete reflection dips, which makes it possible to estimate their FWHM and evaluate the FoM. The resonance positions of each mode and FWHMs are summarized in Table 6.1, and the sensitivities S, FoM and S_I are accordingly evaluated. The $SPP_{Au/envir}(0,1)$ shows

Table 6.1: The resonance wavelengths of plasmonic modes that are excited on a MIM cavity array with R_{Au}=40 nm, periodicity P=450 nm, with the surrounding RI varying from 1 to 1.33, 1.38, 1.43. The bandwidths FWHM ($\Delta\lambda$) of these modes are estimated at n=1.33. The sensor qualities of sensitivities S, FoM and S_I are evaluated. The maximum $|dI/d\lambda|$ can be achieved when the intensity change is detected at λ_d.

variables	LSPR	$SPP_{Au/envir}$	TEM11	$SPP_{Au/ITO}$
n=1			613	776
n=1.33	542	633	732	776
n=1.38	547	656	750	776
n=1.43	550	678	767	776
FWHM (nm)	53	20	31	
S (nm/RIU)	80	450	350	0
FoM (RIU^{-1})	1.51	21.5	11.3	0
$(|dI/d\lambda|)_{max}$ (%/nm)	0.13	1.1	2.58	0.26
λ_d (nm) (n=1.33)	558	640	724	790
S_I(%/RIU)	10.4	495	903	0

the best sensitivity of 450 nm/RIU. This can be roughly predicted from the resonance condition equation 4.1. $S = \frac{\partial \lambda_{res}}{\partial n_d} \sim |\sqrt{\frac{\epsilon_m}{\epsilon_m+\epsilon_d}}|\frac{P}{\sqrt{i^2+j^2}} \sim \frac{P}{\sqrt{i^2+j^2}}$ when $|\epsilon_m| \gg \epsilon_d$, thus the sensitivity of $SPP_{Au/envir}(0,1)$ can be estimated to be 450 nm/RIU. The $SPP_{Au/envir}$ mode shows a high sensitivity due to its strong dependency on the surrounding RI and its big sensing volume. On the other hand, the $SPP_{Au/ITO}$ mode is insensitive to the RI change in the surrounding environment, because the near-field of $SPP_{Au/ITO}(0,1)$ is mostly on the substrate side and hardly disturbed by the RI change in the detecting medium. The TEM11 mode shows a sensitivity of 350 nm/RIU due to the sensing volume being increased by decreasing R_{SiO_2} and making the near-field accessible to the surrounding medium. The sensitivity of the LSPR mode is roughly estimated to be 80 nm/RIU, the broad line shapes make it hard to maintain high precision in reading out the resonance position.

In Table 6.1, a FoM of 1.51 is estimated for the LSPR mode, while the $SPP_{Au/envir}(0,1)$ shows the highest FOM of 21.5, due to its high sensitivity and narrow bandwidth. On the other hand, the TEM11 mode shows a S_I of 903, which is much better than 10.4 for the LSPR mode and 495 for the $SPP_{Au/envir}(0,1)$ mode. The best FoM and S_I occurs for different resonance modes, because they evaluate the resolution in the spectral shift and

intensity change, respectively. Even though the TEM11 mode does not show better S than $SPP_{Au/envir}$ and possesses a broader bandwidth as well, it has a deep reflection dip which provides promising resolution in intensity change and a steep resonance profile which provides high sensitivity as an intensity-modulated sensor. This result means that the $SPP_{Au/envir}(0,1)$ would be suited better for applications based on spectral shift, and the TEM11 mode would give better performance in sensing based on measuring the intensity changes at a fixed wavelength.

6.2.1.2 Sensor properties based on extinction

In chapter 4, it is demonstrated that the Lorentz shaped resonance appears as a Fano line shape in extinction spectra of MIM structures due to the coupling with incident radiance through the gold film. Engineering Fano line-shaped resonances in metallic nanostructures has been one of the most common ways to improve the sensing capabilities of plasmonic sensors. Better sensing capabilities can be expected of MIM structures with extinction measurements because the Fano profile provides a narrower bandwidth and steeper resonance profile.
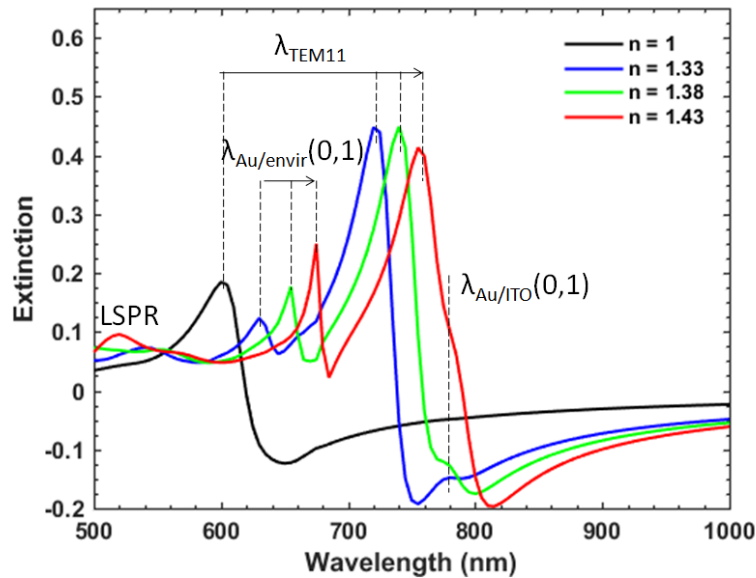
Figure 6.4: (a) The simulated sensing spectra based on extinction for MIM(III) cavity with $R_{Au}=2R_{SiO_2}=40$ nm, P=450 nm and $t_{SiO_2}=10$ nm. The RI of the detecting solution varies from 1 (black curve) to 1.33 (blue curve), 1.38 (green curve) and 1.43 (red curve). The nature of the plamonic modes is labelled accordingly.

The simulated effect on the extinction spectra of a RI change of the bulk immersion liquid from 1 to 1.43 is shown in Figure 6.4, for the same MIM cavity array as in the last section. The corresponding modes are labelled, and the red-shift is indicated by an

arrow as a function of increasing RI. The plasmonic modes shift in the same manner as in Figure 6.3: the $SPP_{Au/envir}(0,1)$ shows the strongest wavelength shift, followed by the TEM11 mode, while the $SPP_{Au/ITO}(0,1)$ is insensitive to the RI change of the detecting medium and the LSPR mode shows a slight red-shift.

Table 6.2: The position of the extinction maximum of plasmonic modes is recorded for the same MIM(III) cavity array as in Table 6.1, while the detecting bulk RI varies from 1 to 1.33, 1.38, 1.43. The sensor qualities of sensitivities S and FoM* are evaluated.

variables	LSPR	$SPP_{Au/envir}$	TEM11	$SPP_{Au/ITO}$
n=1			602	776
n=1.33	542	630	722	776
n=1.38	551	655	740	776
n=1.43		675	757	776
S (nm/RIU)	180	450	350	0
$(|dI/d\lambda|)_{max}$ (%/nm)	0.14	0.68	4.12	0.1
λ_d (nm)	556	636	734	790
S_I (%/RIU)	25.2	306	1442	0

In Table 6.2, the maximum position of the Fano resonance is read for each RI of the detecting medium. As it is difficult to estimate the FWHM of Fano resonances for the FoM, we compare the sensing capabilities of each plasmonic mode by sensitivities S and S_I. The sensitivities of the $SPP_{Au/envir}$, $SPP_{Au/ITO}$ and the TEM11 mode are the same compared to those based on reflection sensing in Table 6.1, showing a value of 450 nm/RIU, 0 and 350 nm/RIU, respectively. While, the sensitivity of the LSPR seems to be improved by extinction, it might result from estimation errors due to its shallow and broad resonance. The TEM11 mode shows the highest S_I of 1442 due to its drastic intensity drop as a function of increasing RI of the surrounding medium. By comparing the S and S_I in Table 6.2 to Table 6.1, we find that the sensitivity S in the spectral shift is mostly the same for reflection- and extinction-based sensors, while the Fano-shaped extinction provides steeper profiles than Lorentz-shaped reflection, leading to better sensitivity and resolution in intensity-modulated sensing for the TEM11 mode.

6.2.2   Sensing with strong coupling

In section 4.3.2, we demonstrated that Rabi-analogue mode splitting occurs when the SPP and the TEMmn modes hybridize with each other. As a result, resonances with narrower bandwidth and steeper profile can be created out of the coupling, showing potential as a promising plasmonic sensor. In this section, the sensing capabilities of plasmonic modes supported by MIM structures with R_{Au}=40 nm and P =550 nm are investigated.
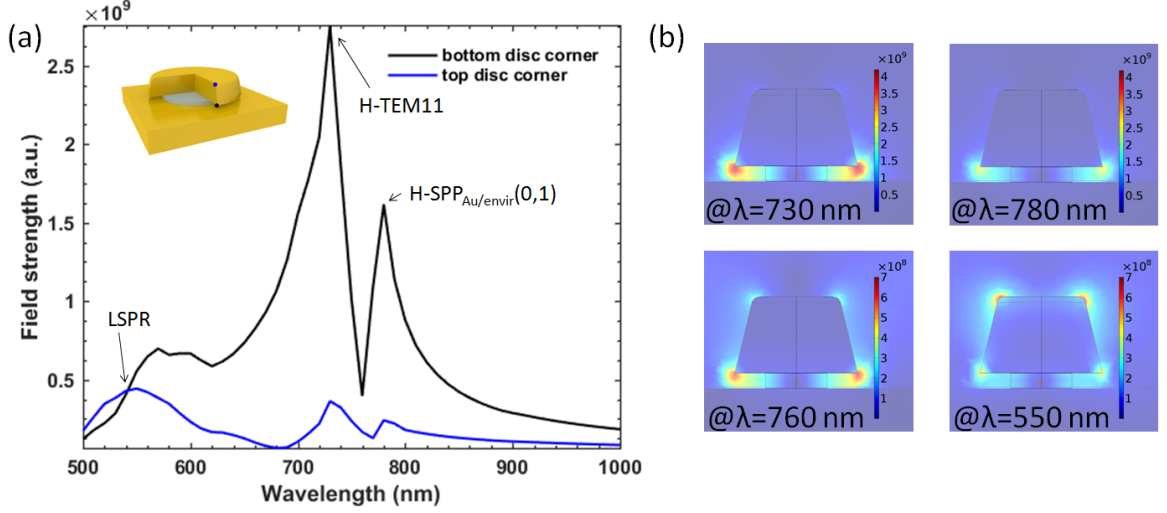
Figure 6.5: (a) The near-field strength ($|E| = \sqrt{E_x^2 + E_y^2 + E_z^2}$) on the top corner and bottom corner of the gold disc, as indicated by the black and blue dots in the inserted picture. The MIM(III) structure has $R_{Au} = 1/2R_{SiO_2}$=40 nm, P =550 nm and t_{SiO_2}= 10 nm; (b) The field maps for each plasmonic resonance peak: two hybridized modes (λ= 730 nm and λ= 780 nm) arise from the strong coupling of the SPP mode and TEM11 mode, a LSPR mode shows a strong near-field on the top of the gold disc (λ= 550 nm). The field map at the resonance dip (λ= 760 nm) between the two hybridized modes is shown as well. The simulating wavelength step is 10 nm.

Figure 6.5 shows the near-field resonance characteristics of a MIM(III) cavity array with $R_{Au} = 1/2R_{SiO_2}$=40 nm, P =550 nm and t_{SiO_2}= 10 nm. In Figure 6.5(a), the near-field strength ($|E| = \sqrt{E_x^2 + E_y^2 + E_z^2}$) is plotted both on the top and bottom corner of a gold disc. The mode hybridization can be seen in both near-field spectra: the Lorentz shaped SPP mode and TEM11 mode hybridized and formed two hybridized modes with Fano line shapes, and both contain part SPP energy and part TEM11 mode energy. We refer to the resonance with peak position at 730 nm as the hybridized TEM11 (H-TEM11) mode, because it contains more TEM11 energy compared to the one at 780 nm, which is referred to as hybridized SPP mode (H-SPP). The LSPR mode still appears at short wavelengths with its 'hot spot' on top of the disc, as can be seen in Figure 6.5(b).

Table 6.3: The positions of the extinction maxima of plasmonic modes are recorded from Figure 6.6, with the detecting bulk RI varying from 1 to 1.33, 1.38, 1.43. The $(|dI/d\lambda|)_{max}$ (%/nm) and λ_d (nm) are determined by calculation. The sensor qualities of sensitivities S (nm/RIU) and S_I (%/RIU) are evaluated.

RI	1	1.33	1.38	1.43	S	$(|dI/d\lambda|)_{max}$	λ_d	S_I
H-TEM11	612	722	742	762	400	3.5	732	1400
H-SPP$_{Au/envir}$(0,1)		770	800	820	500	2.27	774	1135

In Table 6.3, it is interesting to find out that the sensitivity S of H-SPP$_{Au/envir}$(0,1)
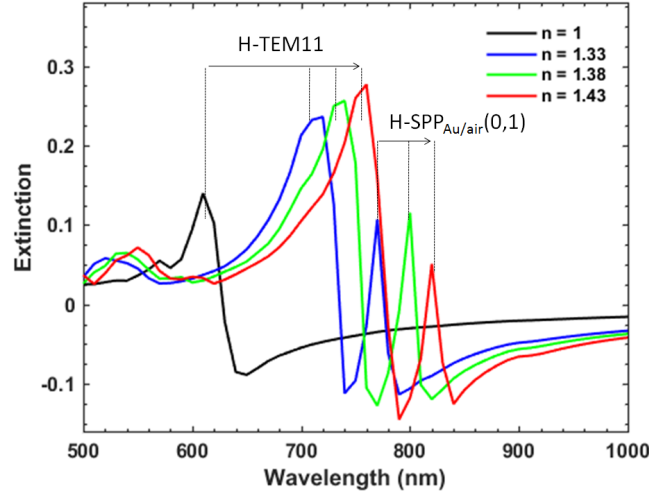
Figure 6.6: The simulated sensing spectra for MIM(III) cavity with $R_{Au}=2R_{SiO_2}=40$ nm, P =550 nm and $t_{SiO_2}=10$ nm. The RI of detecting solution varies from 1 (black curve), to 1.33 (blue curve), 1.38 (green curve), 1.43 (red curve). The nature of the plamonic modes is labelled accordingly.

is 500 nm/RIU, which is decreased compared to 550 nm/RIU ($S \approx \frac{P}{\sqrt{i^2+j^2}}$). On the other hand, a sensitivity of 400 nm/RIU is achieved by the H-TEM11 mode, which is increased compared to 350 nm/RIU without strong coupling (in Table 6.2). By comparing the S_I of Table 6.3 and Table 6.2, the S_I of the TEM11 mode decreased after hybridization and the S_I of the SPP mode increased after hybridization. This means the hybridized modes have part of the sensitivity from the TEM11 mode and part of its sensitivity from the $SPP_{Au/envir}$ mode. This mode hybridization provides a way to tune the sensitivity of plasmonic modes: to make the originally insensitive mode show high sensitivity to the RI change in detecting medium, and make the highly sensitive mode more stable to the environment change. This strong coupling effect will be observed as well in experiments in section 6.4.6.

6.2.3   Conclusion

In small MIM(III) cavity arrays, the TEM11 mode is the most pronounced mode showing a deep and narrow resonance dip in reflection spectra. Thus, it shows potential for high resolution sensing due to high signal/ noise ratio and high precision in determining the spectral shift. With $R_{Au} = 2R_{SiO_2}$, the sensing volume of the TEMmn modes is significantly increased compared to those in MIM(I) by exposing the strong near-field. A sensitivity of 350 nm/RIU, and a FoM of 11.3 in spectral shift based sensing is predicted for a MIM(III) cavity with $R_{Au}=40$ nm, P = 450 nm. A sensitivity of 903 %/RIU in intensity-modulated sensing can be achieved in reflection based

sensing. While in extinction measurements, a Fano profile with high asymmetric factor is created by coupling with the incidence radiance. In extinction based sensing, the spectral sensitivity is the same as in the reflection sensing. However, the S_I is notably improved because the extinction spectra have steeper resonance profiles.

The LSPR mode in small MIM(III) arrays appears as a shallow and broad extinction peak, which leads to poor resolution in both intensity change and spectral shift. It is not the most promising candidate in MIM(III) cavity arrays with respect to resolution and sensitivity. Whereas, the sensitivity of the LSPR mode increases with the disc size and shows good performance in MIM(I) and MIM(II) when the sensitivity of the TEMmn modes is restricted by its sensing volume, as will be seen in section 6.4.

The SPP modes show narrow resonance line shapes due to their non-radiative nature. The $SPP_{Au/substrate}$(i,j) mode is insensitive to the RI change in detecting medium due to the fact that its near-field is in the substrate, resulting in almost no sensing volume. The sensitivity of the $SPP_{Au/envir}$(i,j) mode strongly depends on the periodicity P with $S \approx \frac{P}{\sqrt{i^2+j^2}}$ when mode hybridization does not occur. When the $SPP_{Au/envir}$(i,j) mode coincides with the TEMmn mode, strong coupling occurs and the new hybridized modes have physical properties of both their origins, including the sensitivity versus RI changes. As a result, the two hybridized modes show sensitivities between the original sensitivities of the SPP mode and the TEMmn mode.

6.3 Sensitivities of modes in larger MIM cavity

In a MIM(III) cavity with larger R_{Au}, higher order TEMmn modes will be excited, more higher order SPP modes will be excited as well with a larger periodicity. In this section, the sensing performance of higher order TEMmn modes and SPP modes will be studied. The near-field resonance spectra for a MIM(III) cavity with $R_{Au}=$ 160 nm, P = 650 nm are presented in Figure 6.7, when the detecting bulk RI is 1.33. In Figure 6.7, two higher order cavity plasmon modes can be distinguished: the TEM12 and TEM31 mode and two pronounced SPP modes: $SPP_{Au/envir}$(0,1) and $SPP_{Au/envir}$(1,1) are identified. Strong coupling occurs between $SPP_{Au/envir}$(0,1) and TEM31 as can be seen from the near field distribution. We name the hybridized mode at $\lambda=$ 890 nm the H-$SPP_{Au/envir}$(0,1) mode because it has more energy thus more physical properties inherited from SPP modes, likewise, the one at $\lambda=$ 930 nm is named H-TEM31.

It is worth noting that the field maps at the resonance wavelength of $SPP_{Au/envir}$ modes show a localized near field at the disc edges together with their propagating near-field, as can be seen in the side view field maps in Figure 6.7(b). I believe these strong 'hot
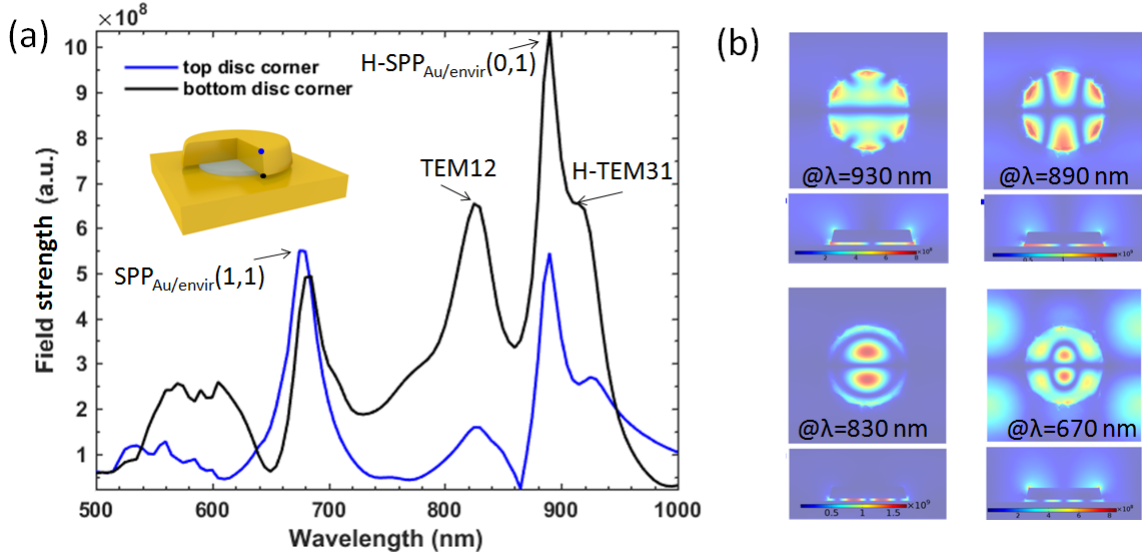
Figure 6.7: (a) The near-field strength ($|E| = \sqrt{E_x^2 + E_y^2 + E_z^2}$) on the top corner and bottom corner of the gold disc, as indicated by the black and blue dots in the inserted picture. (b) The field maps from top view and side view are shown for each plasmonic resonance peak: hybridized TEM31 (H-TEM31) at λ= 930 nm, hybridized $SPP_{Au/envir}(0,1)$ at λ= 890 nm, the TEM12 mode at λ= 830 nm, and the $SPP_{Au/envir}(1,1)$ mode at λ= 670 nm. The LSPR mode with strong near-field on top of the gold disc (around λ= 550 nm) is not specifically shown due to complicated coupling with the modes $SPP_{Au/glass}(0,1)$ and $SPP_{Au/glass}(1,1)$.

spots' on the edges of the disc arise from the collective oscillation in the gold discs in response to the near-field of the adjacent propagating SPP mode. As can be seen in the black curve (or the blue curve), the near field intensity of SPP modes at the gold disc edges can even surpass that of the cavity modes even at the bottom corner where the 'hot spots' of the TEMmn mode reside, same at the upper corner. (It is not shown in this thesis, but in the case of MIM(I), the near-field on the top edge is very strong due to the near-field induced electron oscillation in the gold disc, nevertheless the near-field at the bottom edge at λ_{SPP} is very weak due to the momentum mismatch between Au/*air* interface in SPP and Au/*glass* interface at the bottom of disc. This can be a supporting evidence of our assumption about the near-field induced LSPR in discs.) This makes MIM arrays a promising candidate for plasmon assisted spectroscopy due to its strong 'hot spots' and easy accessibility. This can be the reason that in both Figure 7.4 (before undercut) and Figure 7.9 (after undercut), the MIM cavities with larger P (P= 440 nm, 530 nm and 624 nm) showed higher SERS signals even though less MIM cavities contributed to the signal: Because the LSPR mode excited by the near-field of the $SPP_{air/Au}$ contributed to the enhancement as well. In the case of P=335 nm, the $SPP_{air/Au}(0,1)$ mode appears around 450 nm, so does the SPP induced LSPR. Neither the excitation process (λ_{laser}=633 nm) nor emission process (λ_{Raman}=685 nm, 704 nm) of the Raman scattering can benefit from the strong near-field of this LSPR

mode. While in the case of larger P, the $\lambda_{air/Au}$ appear closer to the laser and Raman wavelengths, thus the SPP excited LSPR mode can contribute to the SERS scattering as well.

On the other hand, the RI sensitivity of this SPP mode is exclusively dependent of the physical properties of the SPP resonance, but not at all influenced by this near-field induced LSPR on the gold disc. As we already showed in the last section, the sensitivity of $\text{SPP}_{Au/envir}$ is $S \approx \frac{P}{\sqrt{i^2+j^2}}$. More details about the sensitivities of $\text{SPP}_{Au/envir}$ modes will be given in section 6.5.
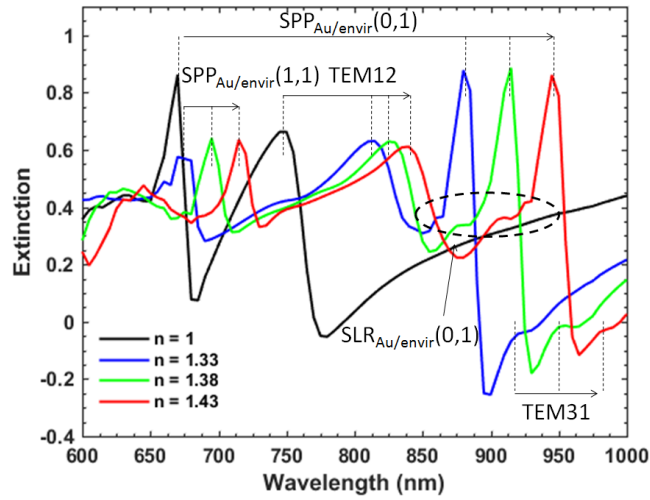
Figure 6.8: The simulated sensing spectra for a MIM(III) cavity with $R_{Au}=2R_{SiO_2}=160$ nm, P =650 nm and $t_{SiO_2}=10$ nm. The RI of the detecting solution varies from 1 (black curve) to 1.33 (blue curve), 1.38 (green curve), 1.43 (red curve). The nature of the plamonic modes is labelled accordingly.

Table 6.4: The positions of the extinction maxima of plasmonic modes are recorded from Figure 6.8, with the detecting bulk RI varying from 1 to 1.33, 1.38, 1.43. The sensor qualities of sensitivities S (nm/RIU) and S_I ($\%/RIU$) by detecting the intensity changes at λ_d (nm) are evaluated.

RI	1	1.33	1.38	1.43	S	$(|dI/d\lambda|)_{max}$	λ_d	S_I
$\text{SPP}_{Au/envir}(1,1)$		675	696	717	420	4.6	680	1932
TEM12	751	814	829	841	270	1.9	826	513
$\text{SPP}_{Au/envir}(0,1)$	670	882	913	945	630	14.8	888	9324
TEM31		917	950	985	680	0.009	922	6.12

The extinction spectra for a MIM(III) cavity array with $R_{Au}=160$ nm immersed in detecting solution with RI of 1 (black curve), 1.33 (blue curve), 1.38 (green curve) and 1.43 (red curve), are presented in Figure 6.8. The different sets of plasmonic modes are labelled and also mode $\text{SLR}_{Au/envir}(0,1)$ appeared at $\lambda_d = \frac{P\sqrt{\epsilon_d}}{\sqrt{i^2+j^2}} = nP$. The peak position of each mode is read and the spectral shift sensitivities S (nm/RIU) and

intensity-modulated sensitivities S_I are evaluated in Table 6.4. A spectral shift sensitivity of 680 nm/RIU and 270 nm/RIU are obtained for the TEM31 mode and TEM12 mode, respectively. This sensitivity difference can be explained by the field distribution of edge cavity mode and surface cavity mode: for edge modes, the strong near-field is distributed along the circumference of the MIM cavity, while the surface modes have their 'hot spots' along the diameter. Besides, as can be seen in the field map in Figure 6.7, the central modal lobes provide hotter 'hot spots' compared to those at the edge of the cavity for surface modes TEM1n. As a result, the sensing volume of the TEM31 mode is much bigger than that of TEM12 in the MIM(III) cavity, therefore, resulting in a higher sensitivity for edge plasmonic mode TEM31 compared to surface mode TEM12. The sensitivities of the SPP$_{Au/envir}$(0,1) mode and SPP$_{Au/envir}$(1,1) mode are evaluated as 630 nm/RIU and 420 nm/RIU, which are roughly in agreement with the prediction by S$\approx \frac{P}{\sqrt{i^2+j^2}}$. In the case of the SPP$_{Au/envir}$(1,1) mode, its sensitivity is decreased a bit by coupling with the TEM13 mode, which is a not very pronounced but quite insensitive surface cavity mode with wavelength around 745 nm as in Figure 6.8. In the case of the SPP$_{Au/envir}$(0,1) mode, both the H-SPP mdode and TEM31 mode show high sensitivities.

6.4   Experimental RI sensing

6.4.1   Sensing method

In this section, we present the experimental RI sensing results. We fabricate MIM(II) cavities with different diameters and different periods and conduct RI sensing in bulk immersion configuration. The standard RI solution is prepared by glycerin aqueous solution with different concentrations: 7%, 22% and 37%. The refractive index is then confirmed by a refractometer to be 1.34, 1.36 and 1.38 for these three mixtures respectively. The sensing experiments are conducted based on extinction measurements and the measuring configuration can be seen in Figure 6.9.

The incident light is from a Halogen lamp, it is illuminated from the bottom of vertical MIM(III) cavity arrays. The transmission through the substrate is then collected by a 10× objective. A beam splitter then divides the transmitted light into two parts, one part goes into a camera for the real-time imaging. The other part passes through a confocal pinhole and a spectrometer entrance slit to get rid of the stray light before it enters the spectrometer. The sensing area is shown in the insert image of Figure 6.9, the MIM cavity array is immersed in 20 µL of glycerin aqueous solution. We recorded the transmission through MIM substrate for 5 refractive indices, in the order of: n=1 (air),
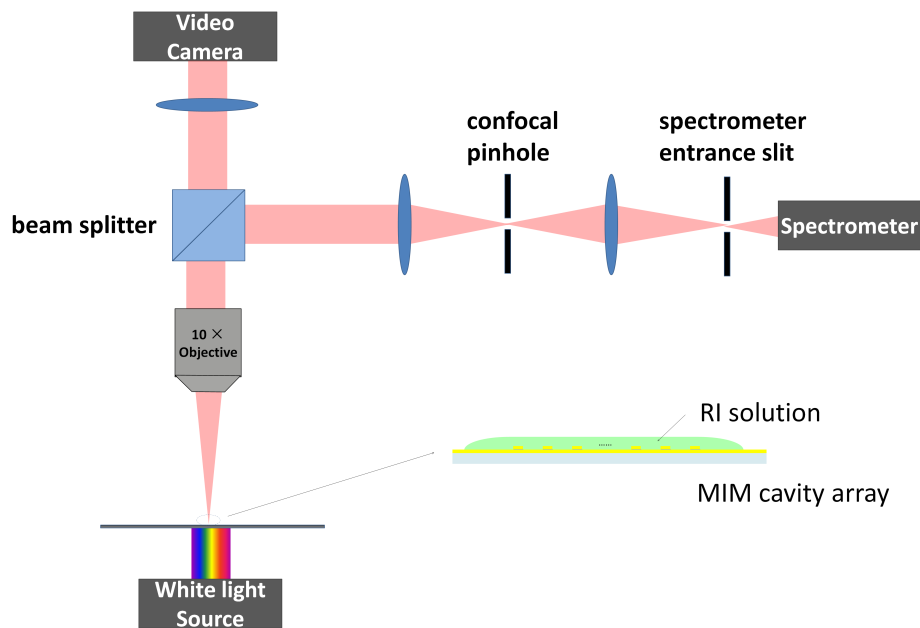
Figure 6.9: The RI sensing configuration. The extinction based sensing is conducted on a confocal microscope. The white light source is illuminated from the bottom of vertical MIM structures, and the transmission is collected by a $10\times$ objective with a N.A. of 0.3. The collected signal is then split into two parts: part of the signal goes into the camera for imaging of the structures and part of the signal is passed through a confocal pinhole and a spectrometer entrance slit into the spectrometer. The sensing area is enlarged in the insert image, the MIM cavity array is immersed by the detecting RI solution.

n=1.33 (water), n=1.34 (7% glycerin/water), n=1.36 (22% glycerin/water), n=1.38 (37% glycerin/water). The transmission through 50 nm Au film where there is no SiO_2 and Au discs was also recorded for each refractive index as reference. The extinction is evaluated by equation 3.2: the transmission difference between the 50 nm Au film area and MIM cavity array divided by the transmission through 50 nm Au film. It is worth noting that the glycerin solution becomes viscous at higher concentration, it helps to decrease the influence from different RI solutions to start from the lower concentration to higher ones. The influence is further eliminated by flushing the substrate with the detecting solution for 5 times before the transmission spectra were recorded.

6.4.2   Resolution of MIM sensors

The resolution of plasmonic sensors is an important parameter to evaluate its sensing performance, because it determines the limit of detection (LOD) which is the lowest quantity of a substance that can be distinguished. The resolution of a sensor includes the spectral resolution which can be evaluated by S and FoM. Besides, the signal/noise ratio strongly affects the resolution as well.

In Figure 6.10, the sensing spectra for MIM cavities with a R_{Au} of (a) 35 nm, (b) 68 nm, (c) 92 nm and (d) 131 nm, in different immersion bulk RIs are presented. The cavity arrays have the same cavity height of t_{SiO_2}=12 nm and periodicity of P=335 nm. The refractive index varies from 1 to 1.38. The plasmonic modes are labelled accordingly. It can be found that the extinction efficiency increases with increasing disc size R_{Au}. For instance, the extinction efficiencies of the LSPR mode are 0.08, 0.45, 0.79 and 0.92 at n=1.33 for R_{Au}=35 nm, 68 nm, 92 nm and 131 nm, respectively. The higher extinction efficiency results in a better resolution of signal from the intrinsic noise of the measuring system. It is a general rule that we found out during the sensing that the MIM(II) arrays with bigger disc size and denser gold coverage show stronger signal, which leads to a better signal/noise ratio and better resolution.

6.4.3   Sensitivity of LSPR mode

In Rana Nicolas' earlier work, the LSPR mode in MIM(I) structures has been studied, and a highest sensitivity of 192 nm/RIU and a FoM of 3.76 has been achieved with R_{Au}=85 nm and P=350 nm [91]. In this section, we study the sensing capabilities of MIM(II) structures with many different disc radii R_{Au} and different periodicity. It can be seen in Figure 6.10, that the LSPR mode in a MIM(II) cavity with its 'hot spots' on top of the gold disc demonstrates high sensitivity as well.
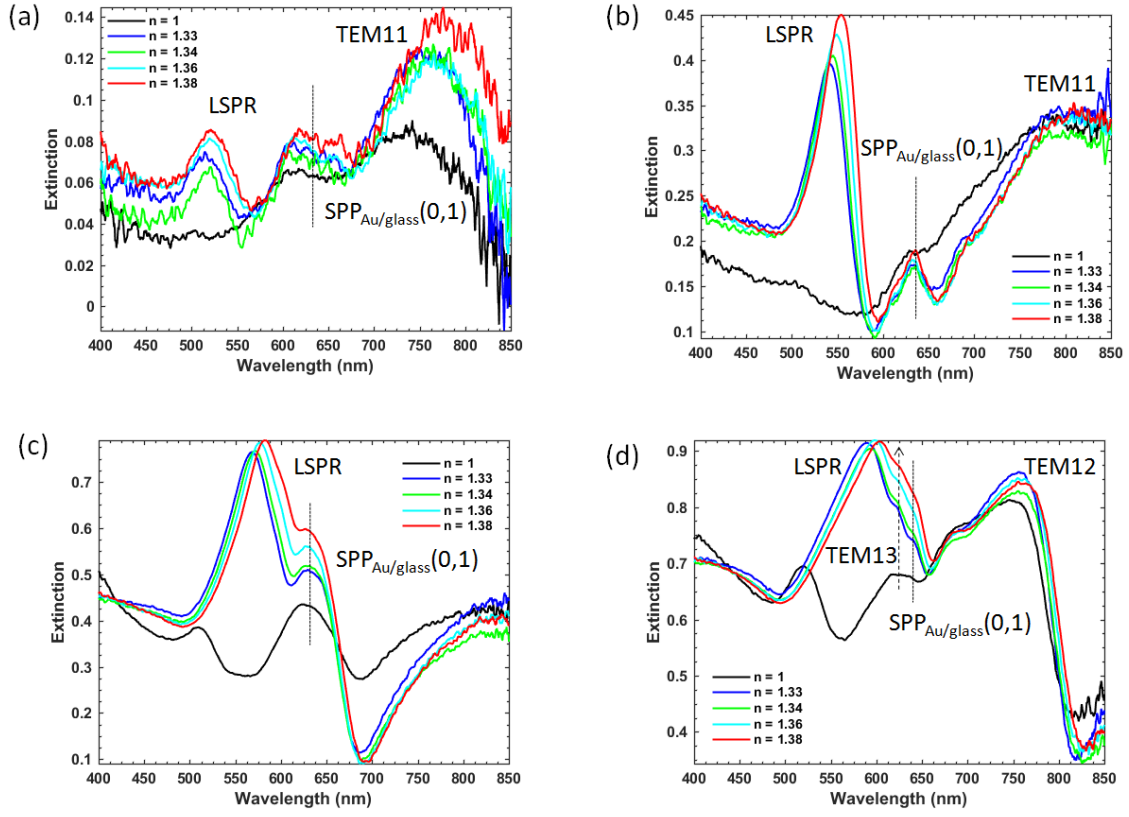
Figure 6.10: Sensing performance of LSPR mode. Measured extinction spectra through MIM(II) cavity array with periodicity P=335 nm, (a) R_{Au}=35 nm, (b) R_{Au}=68 nm, (c) R_{Au}=92 nm, (d) R_{Au}=131 nm, for different immersion bulk refractive index: 1 (black curve), 1.33 (blue curve), 1.34 (green curve), 1.36 (cyan curve), 1.38 (red curve). The plasmonic modes are labelled accordingly.

Table 6.5: The positions of the extinction maxima of the LSPR modes (nm) are recorded for the spectra shown in Figure 6.10. The bandwidth FWHM (nm) is estimated at n=1.33 by measuring the bandwidth at the middle point of the wider side of the resonance band, and the sensitivities S (nm/RIU) and FoM are evaluated.

RI	1	1.33	1.34	1.36	1.38	FWHM	S	FoM
R_{Au}=35 nm	504	513	519	522	525	39	232	6
R_{Au}=68 nm		542	545	550	554	38	248	7
R_{Au}=92 nm	509	568	572	577	583	59	310	5
R_{Au}=131 nm	520	590	595	598	603	80	245	3

In Table 6.5, the position of the extinction maxima of the LSPR mode is recorded for the spectra shown in Figure 6.10. The bandwidth $\Delta\lambda$ is estimated at n=1.33 by measuring the bandwidth at the middle point of the wider side of the resonance and the sensitivities S and FoM are evaluated (based on the shift between n=1.33 and 1.38). The extinction efficiency and bandwidth, as well as sensitivity increases with increasing disc size. The S increases from 232 nm/RIU, to 248 nm/RIU and 310 nm/RIU for R_{Au} = 35 nm, 68 nm and 92 nm, respectively. Then the S decreases to 245 nm/RIU for R_{Au} = 131 nm due to coupling with an insensitive mode TEM13, as can be seen in Figure 6.10(d). A much higher FoM (7) is obtained from MIM(II) compared to our previous work with MIM(I) (3.76). In order to understand the mechanism of this improvement, we conducted sensing simulations based on MIM(I) and MIM(II) with R_{Au} = 68 nm P = 335 nm, as shown in Figure 6.11.
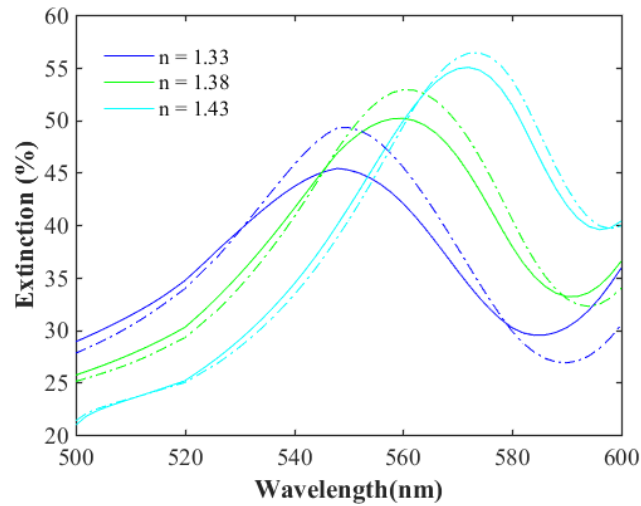
Figure 6.11: Simulated sensing performance of LSPR mode in MIM(I) (dashed curves) and MIM(II) (solid curves). The R_{Au}=68 nm, t_{SiO_2}= 12 nm and periodicity P = 335 nm for both MIM(I) and MIM(II). The spectra are presented for n = 1.33, 1.38 and 1.43.

From Figure 6.11, the simulated sensitivities for LSPR modes in both MIM(I) and MIM(II) are 240 nm/RIU. The bandwidths of the LSPR mode in MIM(I) and MIM(II) hardly changed, so the FoMs of the LSPR modes are similar in MIM(I) and MIM(II) as well. This means the sensitivity of the LSPR mode cannot get improved by under-etching, which is different from the TEMmn modes. The improvement in sensitivity of the LSPR mode we achieved in MIM(II) compared to previous work on MIM(I) is maybe due to the better resolution of the confocal measuring setup and the better homogeneity of MIM structures fabricated with better EBL equipment.

Zhang et al. has developed a theory about achieving a LSPR mode with 'hot spots' on top of the gold disc by creating hybridization between a dipolar mode and a quadrupo-

lar mode of the gold disc. As a result, the sensitivity of the LSPR mode has been siginificantly improved by shifting the 'hot spots' from the substrate to the top of the disc [156]. The LSPR mode in MIM systems may as well arise from the strong coupling between a quadrupolar mode of the gold disc and the gap plasmon polariton of the cavity. This hybridized mode shows weak dependence on the disc size, as can be seen in Table 6.5 for n=1, where the LSPR mode shifts from 504 nm to 520 nm with a large disc size change from 35 nm to 131 nm. At the same time, this LSPR mode is insensitive to the refractive index change under the gold disc, as can be found by comparing the dashed curves and solid curves in Figure 6.11. These sensitivity dependencies are in god agreement with the hybridized modes in Zhang's work [156].

6.4.4   Intensity sensitivities of LSPR mode

As presented in the sensing simulation sections, the Fano extinction resonance with steep resonance line shape suits well for the intensity modulated plasmonic sensor. The sensitivities S_I of the LSPR modes in Figure 6.10 based on intensity change are shown in Table 6.6.

Table 6.6: The wavelength λ_d (n = 1.33) which gives rise to the maximal $(|dI/d\lambda|)_{max}$ are determined for the spectra in Figure 6.10. The sensitivities S_I are evaluated then based on equation 6.1.

RI	S (nm/RIU)	$(|dI/d\lambda|)_{max}$(%/nm)	λ_d (nm)	S_I(%/RIU)
R_{Au}=35 nm	232	0.12	538	27.8
R_{Au}=68 nm	248	1.26	559	312.5
R_{Au}=92 nm	310	0.95	583	294.5
R_{Au}=131 nm	245	0.65	605	159.3

In Table 6.6, the $(|dI/d\lambda|)_{max}$ is obtained at wavelength λ_d (n = 1.33), and the S_I are calculated based on equation 6.1. The sensitivity based on intensity change is a product of S and $|dI/d\lambda|$, so it is determined by the overall effect of spectral shift sensitivity and the slope of the resonance profile. The highest S_I of 312.5 $\%/RIU$ is obtained by the MIM cavity with R_{Au}= 68 nm, when the intensity increase at a fixed wavelength of 559 nm is detected as increasing RI. The MIM cavity with R_{Au}=92 nm provides a slightly smaller S_I of 294 $\%/RIU$ by measuring the intensity change at 583 nm with increasing detecting RI. The MIM cavity with R_{Au}= 35 nm shows low sensitivity S_I compared to other bigger cavities. Besides, it does not hybridize with other modes to create steep Fano profiles as shown in Figure 6.10, nevertheless, the LSPR modes in other cavities all hybridized with the $SPP_{Au/glass}$(0,1) mode to create Fano profiles with higher asymmetry factor. As an overall effect, the R_{Au}= 35 nm cavity provides

the poorest LSPR sensing performance in both spectral shift modulated sensor and intensity modulated sensor, and the R_{Au}=68 nm cavity excels for both modulations.

6.4.5   Sensitivities of cavity plasmon modes

In Figure 6.10, a TEM11 mode appears in MIM(II) with R_{Au}=35 nm, and a TEM12 and TEM13 mode appears in the cavity array with R_{Au}=131 nm. The positions of extinction maxima for the modes TEM11, TEM12 and TEM13 at n=1 and n=1.38 are read out and sensitivities are evaluated in Table 6.7. The TEM11 mode shows the highest sensitivity of 108 nm/RIU which decreases to 33 nm for the TEM12 mode, and to around 0 for the TEM13 mode. (The evaluation of TEM13 mode is problematic due to the multiple resonance shoulders. I visually estimated the sensitivity to be 0). From Chapter 4, we know that the confinement of MIM cavities on the TEMmn modes increases from the TEM11 mode, to TEM12 mode and TEM13 mode with increasing n_{gsp}. For the higher order surface cavity modes TEM1n, most of their near-field energy is confined in the central modal lobes rather than the edge lobes. As a result the near-field of higher order surface TEM1n modes is less disturbed by the RI change in the detecting medium. In Figure 5.8, the TEM13 mode only shifts 7 nm when the SiO_2 spacer disc is reduced by $\approx$14 nm in experiments. The insensitivity of a TEM13 mode in MIM(II) can be expected.

Table 6.7: The maxima positions (nm) of the Fano extinction resonances of the TEMmn modes are recorded from spectra shown in Figure 6.10. The sensitivities S are evaluated.

	n=1	n=1.33	S (nm/RIU)
TEM11	744	785	108
TEM12	755	767	33
TEM13	623	623	0

It is worth noting that the sensitivity of the TEMmn mode can be significantly improved from MIM(II) to MIM(III), because only the fringe field (near-field in the region of ΔR) of the TEMmn mode is exposed in MIM(II) compared to MIM(I). In MIM(III), the field maxima at the edge of the gold disc will be accessible to the detecting medium and show higher sensitivity. For the higher order surface cavity modes TEM1n, they are not as sensitive compared to the edge cavity modes TEMm1 with most of their energy residing in the center of the cavity, however they provide a narrower band width which is good for resolution. From last section, we learnt that MIM(II) with smaller R_{Au} does not show promising sensing capability based on LSPR sensing. However, the

TEM11 mode in small MIM(II) cavities shows higher sensitivity with sensing based on cavity plasmon modes, compared to higher order surface cavity modes in bigger MIM(II) arrays.

6.4.6 Sensitivities of SPP modes

In this section, we study the sensitivity of SPP modes by experiments. MIM(II) cavities with the varying periodicity ranging from 440 nm, 530 nm, 625 nm to 720 nm, and radius of $R_{Au} = 162 \pm 5$ nm are fabricated. The extinction spectra through the MIM(II) arrays with varying bulk RI are presented in the following figure.
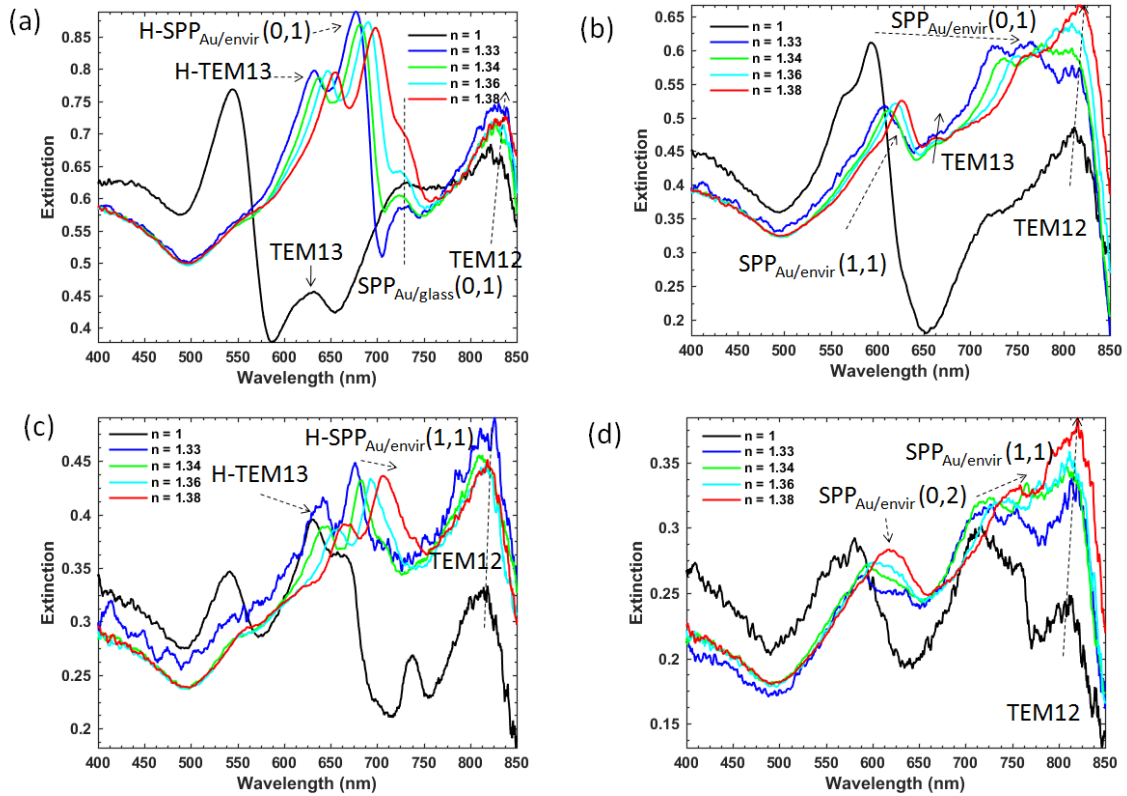
Figure 6.12: Sensing performance of SPP mode. Measured extinction spectra through MIM(II) cavity array with radius and periodicity of (a) P=440 nm, R_{Au}=166 nm, (b) P= 530 nm, R_{Au}=162 nm, (c) P=625 nm, R_{Au}=157 nm, (d) P=720 nm, R_{Au}=157 nm, for detecting solution with different bulk refractive index: 1 (black curve), 1.33 (blue curve), 1.34 (green curve), 1.36 (cyan curve), 1.38 (red curve). The plasmonic modes are labelled accordingly.

In Figure 6.12, the sensing spectra are shown for MIM(II) cavities with (a) P=440 nm, R_{Au}=166 nm, (b) P=530 nm, R_{Au}=162 nm, (c) P=625 nm, R_{Au}=157 nm, (d) P=720 nm, R_{Au}=157 nm. It can be seen that the TEM12 modes appear at around 830 nm with poor sensitivity for all the four arrays. The plasmonic modes are labelled

correspondingly next to the spectra, and the peak position of the sensitive SPP modes or hybridized SPP modes are recorded in Table 6.8.

Table 6.8: The positions of extinction maxima of the $SPP_{Au/envir}$ modes for a MIM(II) cavity array with periodicities of 440 nm, 530 nm, 625 nm and 720 nm and a radius of $R_{Au} = 162 \pm 5$ nm. The spectral shift sensitivities S (nm/RIU) are evaluated.

P (nm)	mode	1.33	1.34	1.36	1.38	S
440	$H\text{-}SPP_{Au/envir}(0,1)$	677	682	690	699	425
	H-TEM13	632	638	647	655	425
530	$SPP_{Au/envir}(0,1)$	727	736	749	762	650
	$H\text{-}SPP_{Au/envir}(1,1)$	608	613	620	627	350
625	H-TEM13	640	646	657	668	550
	$H\text{-}SPP_{Au/envir}(1,1)$	676	683	694	706	575
720	$SPP_{Au/envir}(0,2)$			615	622	350

We firstly look at Figure 6.12(a) and (c) where the mode hybridization occurs. From the simulations earlier (Figure 4.2 and 5.9), we know that for a MIM cavity with R_{Au}=160 nm, a TEM13 mode appears at around 650 nm. According to equations 4.1 and 4.2, resonance wavelength of $SPP_{Au/envir}(0,1)$ and $SLR_{Au/envir}(0,1)$ should appear at around 640 nm and 585 nm, respectively, when n=1.33 (blue curve) for P=440 nm (Figure 6.12(a)). So the double-band structure from 630 nm to 700 nm arise from the hybridize of $SPP_{Au/envir}(0,1)$ mode (originally ∼640 nm) and TEM13 mode (originally ∼650 nm), resulting in two hybridized modes $H\text{-}SPP_{Au/envir}(0,1)$ at 677 nm and H-TEM13 mode at 632 nm, respectively. This hybridization rule applies to the double-band structures around 650 nm in both Figure 6.12(a) and (c). It is worth noting that this hybridization results in notably increased sensitivity for the TEM13 mode and decreased sensitivity for the SPP mode. In the case of P= 440 nm, the sensitivity of $SPP_{Au/envir}(0,1)$ is predicted by $S \sim |\sqrt{\frac{\epsilon_m}{\epsilon_m+\epsilon_d}}|\frac{P}{\sqrt{i^2+j^2}}$ to be around 470 nm/RIU (ϵ_m and ϵ_d are -15.7 and 1.9, respectively), while the sensitivity of the TEM13 mode can be predicted to be 0 as in Table 6.7. After strong coupling, the hybridized modes show both high sensitivity due to their SPP origin: the $H\text{-}SPP_{Au/envir}(0,1)$ shows a sensitivity of 425 nm/RIU and the H-TEM13 mode shows a sensitivity around 425 nm/RIU as well. The same phenomenon happens when P=625 nm in Figure 6.12(c), then the TEM13 mode hybridizes with $SPP_{Au/envir}(1,1)$. As a result of the mode hybridization, the H-TEM13 mode shows a sensitivity of 550 nm/RIU and the $H\text{-}SPP_{Au/envir}(1,1)$ shows a sensitivity of 575 nm. The sensitivity of TEM13 mode has been significantly increased after hybridizing with SPP modes. These sensing results means that the sensitivity of cavity plasmon mode can be increased as well by mode hybridization with a delocalized SPP mode, besides creating a spacer undercut shown in chapter 5.

In Figure 6.12(b), when P=530 nm, the $\text{SPP}_{Au/envir}(1,1)$ mode couples to the TEM13 mode as well. A sensitivity of 350 nm/RIU is obtained for $\text{H-SPP}_{Au/envir}(1,1)$ mode, which is smaller than 401 nm/RIU predicted by $|\sqrt{\frac{\epsilon_m}{\epsilon_m+\epsilon_d}}|\frac{P}{\sqrt{i^2+j^2}}$. This results from coupling to the less sensitive cavity modes. A sensitivity of 650 nm/RIU is obtained for $\text{SPP}_{Au/envir}(0,1)$, which is similar to 567 nm/RIU by prediction. In Figure 6.12(d), the resonance wavelength of the $\text{SPP}_{Au/envir}(0,2)$ mode appears at 620 nm when the detecting medium is 1.38, so the $\text{SPP}_{Au/envir}(0,2)$ mode is almost decoupled with TEM13 mode, and a sensitivity is evaluated to be around 350 nm/RIU, which roughly agrees with the prediction of S$\approx |\sqrt{\frac{\epsilon_m}{\epsilon_m+\epsilon_d}}|\frac{P}{\sqrt{i^2+j^2}}$.

6.5 Molecular sensing

It is widely known that the SPP mode is a better candidate for bulk sensing attributed to its well-defined line shapes and big sensing volume interacting with bulk media, however, the LSPR mode suits better for molecular sensing, for instance, immuno-essay sensing in biomedicine, where the effective sensing volume is within ∼10 nm in most cases. In MIM cavity arrays, the TEMmn mode has well confined strong near-fields inside the cavity, which can result in promising sensing performance in molecular sensing. In bio-molecules sensing, the sizes of most proteins, for instance antibodies, are known to be around $5 \sim 10$ nm diameter, and the refractive index of a monolayer of these proteins is estimated to be around 1.5 [90, 181]. The molecular sensitivities depend on the size and refractive index of the detecting molecules. In order to numerically investigate the performance of MIM cavity arrays in biosensing, we put a thin layer with a thickness of 10 nm and refractive index of n=1.5 on the top of MIM arrays. In this section, we simulated a MIM(III) cavity with periodicity P=650 nm, and R_{Au}=70 nm and 160 nm respectively, to compare the sensitivities of different orders of cavity plasmon modes, SPP modes and LSPR mode in the molecular sensing configuration.

In Figure 6.13, the reflection spectra of MIM(III) cavity arrays with (a) R_{Au}=160 nm, (b) R_{Au}=70 nm, when they are in air (n=1) and when the arrays are covered with a 10 nm thick layer of organic molecules (n =1.5), are shown. The plasmonic modes are labelled accordingly. The resonance wavelengths indicated by the reflection dips in Figure 6.13 are recorded in Table 6.9 and the sensitivies S are evaluated. In Table 6.9, as one would predict, the TEM11 mode and TEM12 mode show the highest sensitivities of 520 nm/RIU and 168 nm/RIU, respectively, due to their strongly enhanced near-field within 10 nm distance from the Au surface. The TEM11 mode shows a higher sensitivity because it has 'hot spots' at the ends of the cavity which are accessible
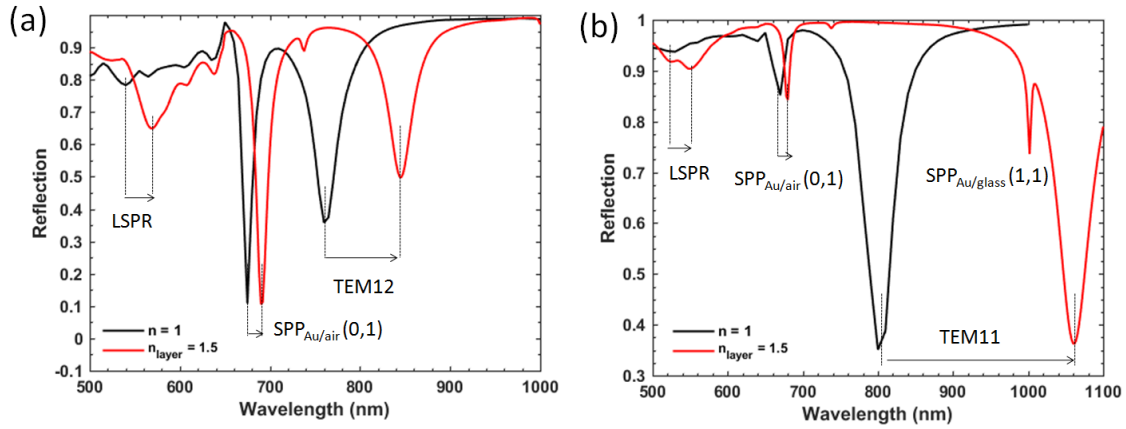
Figure 6.13: Simulated molecular sensing for MIM(III) cavities with (a) $R_{Au} = 2R_{SiO_2}$=160 nm, (b) $R_{Au} = 2R_{SiO_2}$=70 nm and fixed periodicity of 650 nm, cavity height t_{SiO_2}=10 nm. The black curves present the reflection spectra without molecules (n=1), while the red curves present the reflection when molecules bond to the metal surface and form an organic layer with a thickness of 10 nm and effective refractive index of 1.5. The TEMmn modes show much higher sensitivities compared to those of SPP modes and LSPR modes.

Table 6.9: The reflection positions of the different plasmonic modes in MIM(III) are recorded from Figure 6.13. The simulated molecular sensing sensitivities S are evaluated.

R_{Au}	modes	n=1	n=1.5	S (nm/RIU)
	LSPR	538	568	60
160 nm	SPP$_{Au/air}$(0,1)	675	691	32
	TEM12	762	846	168
	LSPR	530	550	40
70 nm	SPP$_{Au/air}$(0,1)	670	680	20
	TEM11	802	1062	520

to the molecules with R_{Au}=2R_{SiO_2}, while the TEM12 mode has most of its near-field confined in the central modal lobes, which are only partly accessible to the molecules. As a result, the TEM11 mode shows a higher molecular sensitivity than the TEM12 mode. The LSPR mode at a short wavelength around 535 nm also showed a sensitivity of 60 nm/RIU and 40 nm/RIU in cavities with R_{Au}= 160 nm and R_{Au}= 70 nm, the sensitivity of the LSPR mode increases when the disc size increases. The SPP$_{Au/envir}$ mode shows the poorest molecular sensitivities. In section 6.3, we discussed about the interesting near-field of SPP modes in a gold disc-on-film system, and there is a LSPR mode that gets excited on the gold disc by the near-field of SPPs, which shows impressive near-field intensity at the top and bottom corner of the disc. From the small molecular sensitivities of the SPP$_{Au/envir}$ mode, we can conclude that the sensitivity of the SPP mode is not affected by the LSPR mode excited by it at the same wavelength, even though this LSPR shows very high localized near-field intensity. Nevertheless, the high field strength of the near-field induced LSPR on the gold disc can improve the performance of plasmon-assisted spectroscopy, as in Figure 7.4 and Figure 7.9.

6.6 Conclusion

From chapter 5, it is clear that the sensitivity of TEMmn modes gets improved from MIM(I) to (III), by increasing their sensing volume through exposing the 'hot spots'. In this section, we discussed the sensing performance of the improved structures: MIM(III) and MIM(II). Firstly, the bulk RI sensing capability is studied. We showed by simulation in MIM(III), that the reflection measurements are suitable for sensing based on spectral shifts due to the narrow Lorentz resonance band of the TEMmn mode and SPP mode, while sensing based on extinction provides the same spectral shift sensitivity, but higher intensity modulated sensitivity due to the steeper spectral profile created by coupling with the incidence radiance. Then we show that the sensitivities of the TEMmn mode and SPP$_{Au/envir}$ can be tuned by mode hybridization. The hybridized modes through Rabi-splitting have part of the energy and physical properties inherited from both their origins, including sensitivity. After that we studied the sensitivity of higher order cavity modes and higher order SPP$_{Au/envir}$ modes in larger MIM(III) cavity arrays with larger periodicity as well. It is shown that the higher order edge modes TEMm1 possess a better sensitivity than the higher order surface modes TEM1n due to differences in field distribution. The sensitivities of different orders of SPP$_{Au/envir}$(i,j) can be roughly estimated by $S \approx |\sqrt{\frac{\epsilon_m}{\epsilon_m + \epsilon_d}}| \frac{P}{\sqrt{i^2 + j^2}}$ if mode hybridization does not occur.

In the next section, we showed the bulk RI sensing with MIM(II) cavity arrays. We

found that the sensitivity of the LSPR mode increases with increasing R_{Au} before it couples with the insensitive TEM13 mode. A FoM of 6.53 is achieved in experiments with a MIM(II) cavity array with $R_{Au} = 68$ nm. It is also proved by simulation that the sensitivity of the LSPR mode would not be improved by underetching. Then we compared the sensitivities of different orders of surface cavity modes TEMm1, where the sensitivity decreases drastically with increasing orders due to decreasing sensing volume. For the $SPP_{Au/envir}$(i,j) modes, it is proved in the experiments that the RI sensitivity exchanges between the SPP mode and TEMmn mode through mode hybridization. The originally insensitive TEM13 mode gets very sensitive to bulk RI change with a sensitivity of 299 nm/RIU, while the highly sensitive SPP modes gets more stable to the RI change of the surrounding environment.

In the last section, the molecular sensitivities of different plasmonic modes are studied. The TEMmn modes with strong localized near-field present the best sensing performance. The TEM11 mode has a high sensitivity which is three times that of the TEM12 mode. While the SPP modes show impressive sensing capabilities in bulk sensing, their sensitivity in the molecular sensing configuration is poor due to the near-field not being as strong within 10 nm distance from the Au surface. In this chapter, we also discussed the interesting LSPR mode which is excited at λ_{SPP} on the gold disc by the near-field of SPP modes. It possesses near-fields even stronger than the TEMmn modes, which makes disc arrays on gold film a promising candidate for plasmon-assisted spectroscopy. On the other hand, the molecular sensitivity of $SPP_{Au/envir}$ modes is not improved by the strong near-field of this LSPR mode.

Chapter 7

SERS based on MIM structures

Surface enhanced Raman scattering (SERS) can yield valuable structural and chemical information about detected molecules. Raman scattering is an inelastic scattering process, which delivers spectra with distinct features, that are specific to the investigated molecules. Therefore, the technique can e.g. be used in sensing applications for human gene analysis, clinical diagnosis, pharmacology, forensic investigation and others [64]. As presented in section 1.1.2, the intensity of Raman scattering however is very low, compared to the intensity of elastic scattering. Therefore, many attempts for enhancing the signal have been pursued [182]. It is widely believed that the enhancement factor (EF) of SERS substrates arises from two mechanisms: electromagnetic (EM) enhancement by strong local electromagnetic fields and chemical enhancement, while the former mechanism dominates by many orders of magnitude in most applications [4]. In most cases, the EF can be roughly estimated as being proportional to the fourth power of the electric field enhancement, since the Raman wavelengths are usually close to the laser wavelength and both the intensity of the exciting and the scattered field are enhanced. Therefore, a common approach is to make use of the strong near-fields in the vicinity of plasmonic nanoparticles. Thus, in order to boost the enhancement of local electromagnetic (EM) fields, nanostructures with gaps on the scale of few nanometers, such as homo-dimers, hetero-dimers, trimers, and vertical metal-insulator-metal (MIM) structures were investigated extensively, due to the particularly strong EM near-field in nanogaps. These SERS substrates were presented in section 1.1.2.2 and MIM structures have shown great study interest. In this section, SERS performance of MIM(II) and MIM(III) will be investigated with different Raman active molecules.

7.1   Evaluation of SERS EF

The estimation of the SERS EF in most cases, where the contribution of chemical enhancement can be neglected, has been given by equations 1.4 and 1.5. However, these definitions fail to take into consideration that SERS is a type of surface spectroscopy, and only the absorbed molecules which are accessible to the enhanced EM field can contribute to the SERS signal. To fix this problem, the experimental approach to define the average SERS EF for a given SERS substrate has been given by [4] :

$$EF = \frac{I_{SERS}/N_{Surf}}{I_{Raman}/N_{Raman}} \tag{7.1}$$

Here, N_{Surf} and N_{Raman} represent the average number of Raman molecules involved in SERS and normal Raman experiments, respectively, I_{SERS} and I_{Raman} mean the measured intensity of SERS signal and normal Raman signal, respectively.

7.1.1   Relative enhancement factor

In the case of molecules with big Raman cross sections, for instance dyes, normal Raman signal can be obtained easily. Nevertheless, for most Raman molecules like 4-mercaptobenzoic acid (4-MBA) and trans-1,2-bi-(4-pyridyl) ethylene (BPE), Raman scattering cross sections are small. Besides, the solubility of these molecules in water is not high enough to obtain high concentration aqueous solutions in order to generate distinguishable normal Raman signal (I_{Raman}). Some groups obtained normal Raman intensity (I_{Raman}) and the involved molecule numbers N_{Raman} of these molecules by dissolving Raman molecules in ethanol. However, the fast evaporation rate of ethanol under room temperature and the fact that heat is produced by the laser during Raman measurements undermines the credibility of the estimation of N_{Raman}.

Thus, in this work, 5 nm Au island films are taken as reference sample to evaluate the relative enhancement factor (REF) of MIM structures. As already presented in section 1.1.2.2, thin metallic island films are very well known SERS substrates. These nano-islands separated by nanometric gaps, when under illumination with visible light, give rise to 'hot spots' in the gaps. The highly dense 'hot spots' feature strongly enhanced electric fields resulting in a high EF for SERS, which makes island films good reference samples. Another advantage of REF is that Raman signals arise from the Au/molecule complex composites in both MIM structures and reference substrate, leading to no Raman band position shift between the SERS substrate under evaluation and that of the reference Raman substrate. Details can be seen in section 7.2.

The reference samples were prepared according to the following process: firstly, a glass substrate (22 mm × 22 mm) was cleaned the same way as stated in section 3. Then 5 nm of gold were thermally deposited on the glass substrate with a rate of 0.2 nm/s, and island films instead of continuous gold films were obtained [183]. Figure 7.1 shows
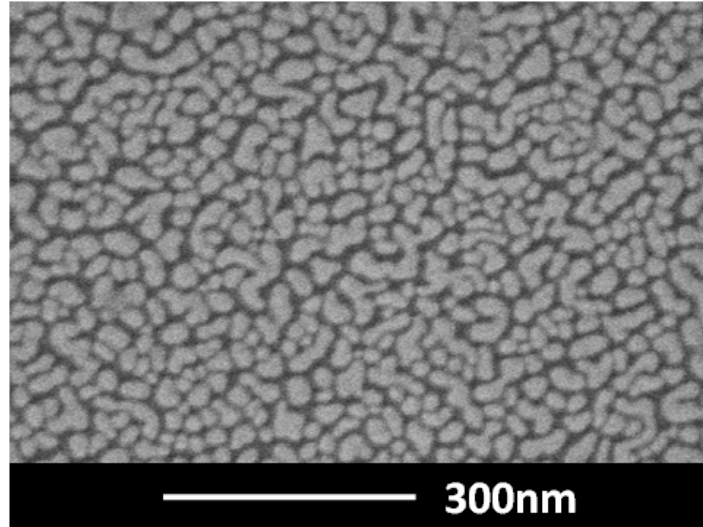

Figure 7.1: SEM image of 5 nm Au island film. The coverage of Au islands is evaluated to be 91% using imageJ. Acknowledgement to Dr. Sergei Kostcheev for helping me with this SEM image.

a SEM image of an as-fabricated 5 nm Au island film following the process presented above (with sincere acknowledgement to Dr. Sergei Kostcheev for kind help). As can be observed in Figure 7.1, the reference SERS substrate is covered by nano-islands separated by nano-gaps, which can give rise to high SERS signal. The Au coverage is estimated to be 91% by software imageJ. The 5 nm gold island films are immersed in 4-MBA/ethanol mixture with a concentration of 1 mM for 24 h, in order to get a monolayer of molecules on top of the gold nano-structures. The reference SERS signals of the island films were averaged over 5 measurements on 5 spots on each island film and further averaged over 2 island films for each Raman molecule. The relative EF of the MIM structure compared to 5 nm Au island film, was then evaluated in this work by

$$REF = \frac{I_{MIM}/N_{MIM}}{I_{island}/N_{island}} \tag{7.2}$$

Here, N_{MIM} and N_{island} represent the average number of Raman molecules covered by the laser spot. I_{MIM} is the Raman intensity for the MIM substrate and I_{island} for the island film, respectively.

The MIM(II) and (III) samples are prepared following the same protocols as in the case of the 5 nm Au island film, in order to achieve a monolayer of 4MBA or BPE

molecules on the surface of the MIM(II) substrates. Besides, the SERS experiments were performed under the identical measuring configuration using a LabRam from Horiba JobinYvon, so the laser spot size is consistent in the experimental and reference group. Based on the high Au coverage of 91% of the 5 nm Au island films and 100% in the cases of the MIM(II) and MIM(III) structures, we assume that the average numbers of molecules covered by the laser spot on the MIM susbtrates and gold islands are approximately the same, $N_{MIM} \approx N_{Raman}$. Thus, the relative enhancement factor REF can be given by:

$$REF = \frac{I_{MIM}}{I_{island}} \tag{7.3}$$

7.1.2   Effective relative enhancement factor

REF evaluates the average SERS EF of MIM structures with respect to 5 nm island films on the scale of the laser spot sizes. However, not all the Raman molecules covered by the laser spot contributed to the SERS signal. Figure 7.2 shows the Raman signal
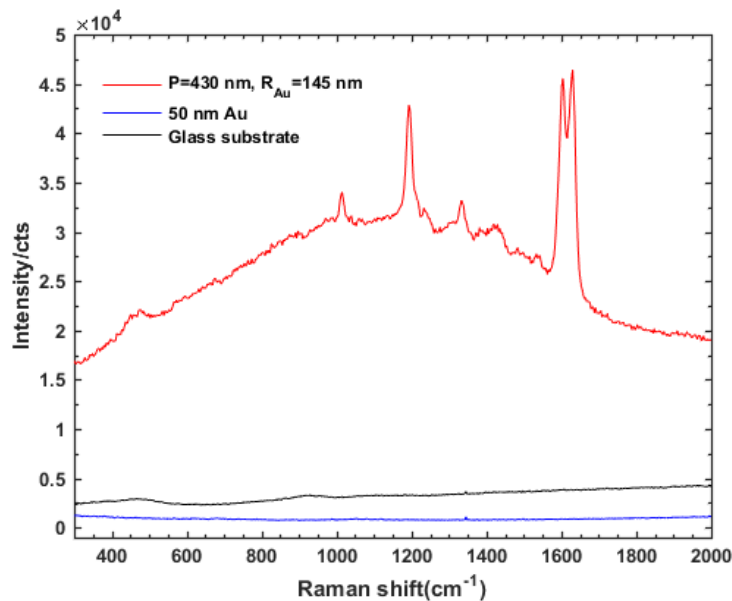
Figure 7.2: Raman signals recorded on MIM(II) structure (red curve) with a periodicity of 430 nm and cavity radius of 145 nm, on glass substrate (black curve) and 50 nm continuous Au film (blue curve) under the same SERS measuring configuration. The Raman spectra are not treated with baseline correction.

for a MIM(II) structure (red curve) with a periodicity of 430 nm and cavity radius of 145 nm, recorded on glass substrate (black curve) and 50 nm continuous Au film (blue curve) under the same treatment procedure and measuring configuration. The Raman spectra in Figure 7.2 are not treated with baseline correction. We found that the baseline intensity is reduced on the 50 nm continuous Au film (blue curve) compared

to the glass substrate (black curve). The nature of the baseline in Raman spectra is still partly unknown and under debate [4]. It is possible that the baseline in our Raman spectra arises from fluorescence of the Raman molecules. The fluorescence gets quenched on the continuous Au film which leads to reduced baseline intensity compared to the glass substrate, nevertheless, in the case of the MIM structure, the fluorescence gets enhanced together with the Raman bands. In order to improve the signal/noise ratio of Raman peaks, the subtraction of fluorescence from Raman spectra is performed by applying and subtracting a polynomial fit to the spectra in the SERS spectra presented in the following chapter. This polynomial fit allows to reduce the signal without losing information of small peaks and changing the peak ratio which holds important information [184].

As for the enhancement of the continuous Au film, it can be seen from Figure 7.2, no SERS enhancement is obtained (blue curve). This means: although the MIM(II) structure provides high SERS signal (red curve), the molecules adsorbed on Au film (blue curve) rather than gold discs, have negligible contribution to the SERS signal of the MIM substrate. We know that the number of molecules that contribute to the SERS EF is proportional to the enhanced area, or the size of the hot spots. Therefore, in order to take into consideration the number of molecules that contribute to SERS EF, the concept of REF_{eff} is introduced, which is defined by:

$$REF_{eff} = \frac{I_{MIM}/A_{eff}}{I_{island}/A_{laser}} = \frac{I_{MIM}}{I_{island}} * \frac{A_{laser}}{A_{eff}} \tag{7.4}$$

where, A_{laser} and A_{eff} present the areas of accessible enhanced near-field covered by laser spot in island film and MIM structures, respectively.

In this thesis, A_{laser} is taken for the enhanced area of the island films assuming that the surface of the island film is covered by accessible 'hot spots'. In Ref. [185], Enders et al. showed that a strong near-field appears around the gold islands at low coverage of Au islands. Also a huge electromagnetic enhancement occurs in the nanometric gaps of the densely packed islands due to near-field interaction. As a result, the field enhancement (as shown in Figure 1.11(a)) and the Raman scattering enhancement (as shown in Figure 1.11(b)) on the island film fluctuates strongly on the nanometer scale [67]. Even though the field enhancement of the island film is macroscopically homogeneous [67], the strong enhancement fluctuation in the nanometer scale makes it difficult to make a simple and precise approximation about its effectively enhanced area. We note, that the assumption, that the enhanced area of the island film is equal to A_{laser} may result in an overestimated REF_{eff}.

In the case of MIM(II), the accessible near-fields of cavity plasmon modes are only at

the edges of the SiO_2 discs, while we take the effective area A_{eff} to be the area of the Au discs in MIM structures which may result in an underestimated REF_{eff}. So we get $A_{eff} = C_{eff} * A_{laser} = \frac{\pi R_{Au}^2}{P^2} * A_{laser}$, where C_{eff} means the coverage of Au discs in MIM structures. Then we get $\frac{A_{eff}}{A_{laser}} = \pi R_{Au}^2 / P^2$, and the REF_{eff} for MIM(II) can be evaluated as:

$$REF_{eff} = \frac{I_{MIM}}{I_{island}} * \frac{P^2}{\pi R_{Au}^2} \tag{7.5}$$

Evaluating or comparing of the overall EF of a SERS substrate to a common and well-performing SERS substrate can be seen as well in the literature [186, 187], which are similar to the method presented in this thesis in section 7.1.1. To the author's knowledge, there is no widely accepted approximation of the enhanced area of an island film available. In this thesis, the REF_{eff} is an estimated relative enhancement factor based on approximations of the enhanced area in both MIM structures and a 5 nm Au film, in an attempt to compare the 'hot spots' intensity in these two SERS substrates. We are well aware that the values of REF_{eff} might vary with a more accurate approximation of the enhanced near-field of the island film. Nevertheless, despite the compromised accuracy of the values of REF_{eff}, the variation trend of REF_{eff} of MIM cavities with different cavity radii and periodicities would be realistic because they are obtained by taking the effective enhancement factor of an island film as unity (which is a constant). Therefore, it is possible to relate the variation of REF_{eff} of different MIM cavities, for both cavities with and without undercut and with different geometrical parameters, to the SERS EM enhancement theory as shown in section 1.1.2.1.

7.2   SERS experiments with 4-MBA

The SERS spectra were recorded using a LabRam from HORIBA Jobin-Yvon with a He-Ne laser source. The laser wavelength is 633 nm and the full laser power is 8.3 mW. There are a sequence of attenuating filters to decrease the excitation power by 2, 4, 10, 100, 10^3 and 10^4 times. Different sizes of laser spots can be chosen by applying different objectives. In this work, the 10 times objective was used if not stated otherwise. This means the SERS measurements were performed in reflection confocal geometry with the 10 times objective for sample illumination and the scattered light collecting. The laser spot at the focus plane is around 10 μm. The typical acquisition times range from 5 s to 20 s, while the spectra were later normalized to 20 s acquisition time for the sake of comparison. All SERS measurements were designed to record with averaging over 5 spectral sets. The SERS spectra in this work are presented after baseline correction,

that was performed by fitting polynomial baselines to the SERS spectra to determine the background and then subtracting it.

The SERS EFs of MIM structures with Au discs on the top of a Au film separated by a SiO_2 spacer disc ($R_{SiO_2} = R_{Au}$), were investigated with 4-MBA molecules. MIM structures with different radius (R_{Au}) and grating constants P ranging from 350 nm to 750 nm in 100 nm steps, were studied.
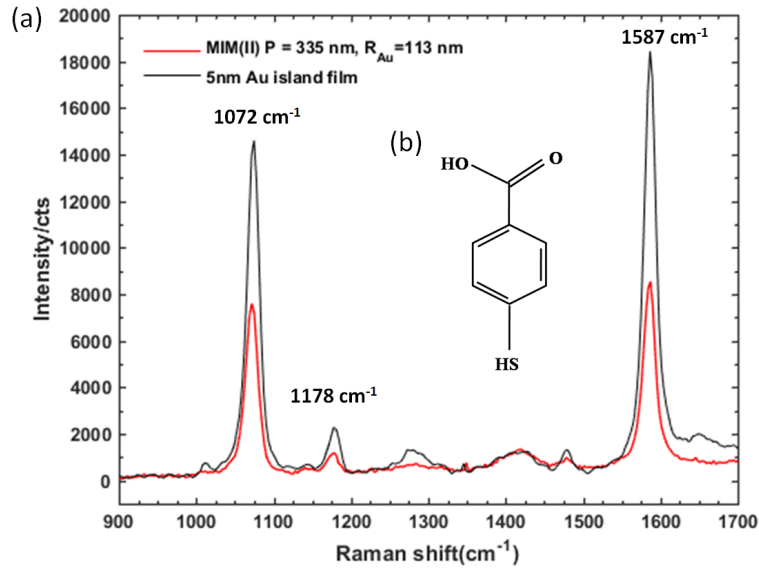

Figure 7.3: (a) Enhanced Raman spectra of 4-MBA on Au MIM(II) structure with P = 335 nm and R_{Au}=113 nm (red curve) and 5 nm Au island film (black curve), (b) chemical structure of 4-MBA.

4-mercaptobenzoic acid (4-MBA) is a widely used Raman analyte due to its well-defined Raman peaks and the fact that idealized, ordered self-assembled monolayers (SAMs) can be easily achieved with a simple treatment process [188]. A 4-MBA molecule consists of a thiol group, an aromatic ring and a carboxyl group, as shown in Figure 7.3 (b). The thiol group will covalently adsorb on the gold surface forming a gold-thiolated complex. Freshly fabricated MIM structures and 5 nm gold island films were immersed in 4-MBA/ethanol mixture with a concentration of 1 mM for 24 h, in order to get a monolayer of molecules on top of the gold nano-structures. Then the structures are rinsed with ethanol to remove the molecules adsorbed on the substrate surface through physical absorption, so that a better control of the involved Raman molecules was assured. Samples are then dried by a diffuse stream of high purity nitrogen. Figure 7.3 (a) show a SERS spectrum recorded on a gold disc MIM array with R_{Au}=113 nm and P=335 nm. The SERS spectra were similar to the previously reported spectra of 4-MBA on the surface of other gold nanostructures [189–192].

The Raman band positions of bulk 4-MBA are adapted from Ref. [193] and presented in

Table 7.1: Raman bands assignment for bulk 4-MBA and 4-MBA/Au complex, ν – stretch; δ – in-plane bend.

Bulk 4-MBA	4-MBA/Au complex	Assignment
1087 cm^{-1}	1072 cm^{-1}	ring-breathe + $\nu(C-S)$
1182 cm^{-1}	1178 cm^{-1}	δ(C-H)
1596 cm^{-1}	1587 cm^{-1}	$\nu(C-C)_{ring}$

Table 7.1, together with the Raman bands position of 4-MBA/Au complexes obtained from Figure 7.3. It is worth noting that there is a blue shift of the Raman bands of 4-MBA molecules adsorbed on the Au surface compared to the bulk 4-MBA. Our observation of the Raman bands shift between SERS and normal Raman spectra is in agreement with other SERS experiments, and the spectral shift is attributed to the charge transfer effect [4, 191, 194]. On the contrary, there are no band position variations between MIM structures and the Au island film because both the Raman bands arise from the vibrational modes of 4-MBA/Au complexes. This is one of the advantages of evaluating REF rather than absolute EF as stated in the previous section.

The peak in the spectrum at around 1072 cm^{-1} is assigned to the overall effect of (C-C)ring ring-breathing modes and vibration of C-S bonds. The band at 1178 cm^{-1} is due to the bending of C-H bonds, and the Raman band at 1586 cm^{-1} arises from the aromatic ring breathing mode [190]. The SERS performances of SERS substrates are later evaluated at the Raman bands with higher intensity: 1072 cm^{-1} and 1586 cm^{-1}, which are referred to as Peak 1 and Peak 2 later.

7.2.1   SERS experiments with unetched MIM

7.2.1.1   Experimental EF

MIM(II) structures with different radii of the Au discs R_{Au} and periods were investigated for their SERS performance under identical SERS measuring configuration. The cavity thickness was t_{SiO2}=12 nm for all the experimentally investigated MIM(II) cavities. The REFs and REF$_{eff}$s of MIM(II) substrates with respect to the island film are calculated according to formula 7.3 and 7.5.

Figure 7.4 presents the measured SERS performance of MIM(II) with respect to gold island films, the relative enhancement factor (REF) and effective REF (REF$_{eff}$) are shown in Figure 7.4(a) and (b), respectively. In Figure 7.4(a), the intensity of the SERS signal showed a trend of increasing first then decreasing as a function of increasing R_{Au}, for both grating constant P=335 nm and P=430 nm. The SERS signal of the
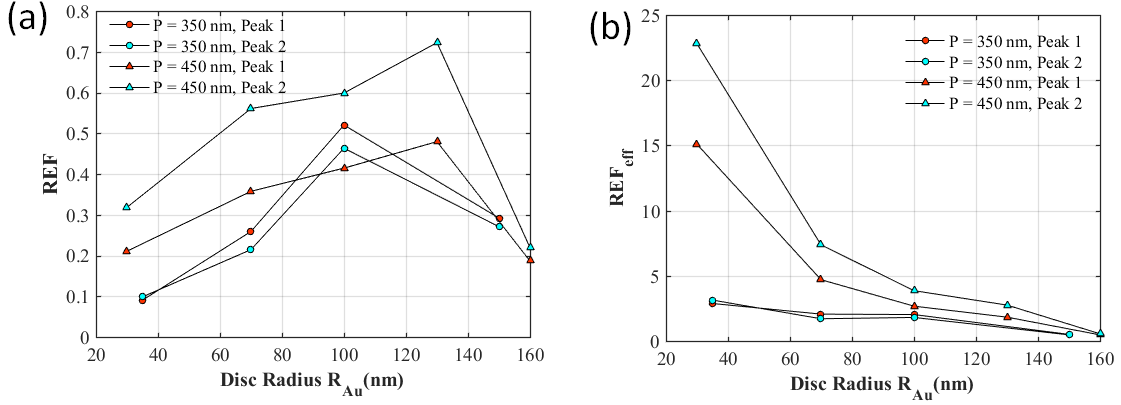
Figure 7.4: Measured (a) REFs and (b) REF$_{eff}$s with respect to island film for MIM (II) with different radii of the Au disc R$_{Au}$ and grating constant P. A_{eff}/A_{laser} was given by $\pi R_{Au}^2/P^2$ as in equation 7.5

investigated MIM(II) was not as strong as that of island films. The best REF of 0.72 occurs for MIM(II) with R$_{Au}$=130 nm and P=430 nm.

The REF$_{eff}$s were calculated based on formula 7.5, while taking the area covered by Au discs as the effective Raman enhancing area ($A_{eff}/A_{laser} = \pi R_{Au}/P^2$). In Figure 7.4(b), the MIM(II) structure with a R$_{Au}$ of 40 nm shows a high REF$_{eff}$ of 23, though the REF is quite small due to its small effective area. It can be observed that the evaluated REFs at Raman peak 1 and peak 2 show the same variation profile as a function of cavity radius in Figure 7.4(a), also the same variation can be found for the REF$_{eff}$s in Figure 7.4(b). This is because the Raman wavelengths of peak 1 (1072 cm^{-1}) and peak 2 (1587 cm^{-1}) are 680 nm and 704 nm, respectively, and it is possible that the two closely separated Raman bands receive comparable enhancement factors from the near-field of plasmonic modes. More details can be found in the simulated EF. In Figure 7.4(b), the magnitudes of REF$_{eff}$ showed a complicated behaviour as a function of R$_{Au}$. Here, in order to understand the variation of the REF$_{eff}$s, simulations were performed to theoretically determine the REF$_{eff}$s at peak 1 and peak 2 with varying cavity radius.

7.2.1.2 Simulated EF

According to formula 1.4, the Raman signal enhancing capability of SERS substrates can be estimated by $|\tilde{E}_{Loc}(\omega_L)|^2 \times |\tilde{E}_{Loc}(\omega_R)|^2$. As the enhancement of the E field at the laser and Raman wavelengths is crucial to the SERS EF, in the FEM simulations, $|E|^2$ ($|E| = \sqrt{E_x^2 + E_y^2 + E_z^2}$) was integrated over the Au discs surface (top surface and side wall).

The integrated field intensities as a function of R$_{Au}$ are presented in Figure 7.5 for dif-
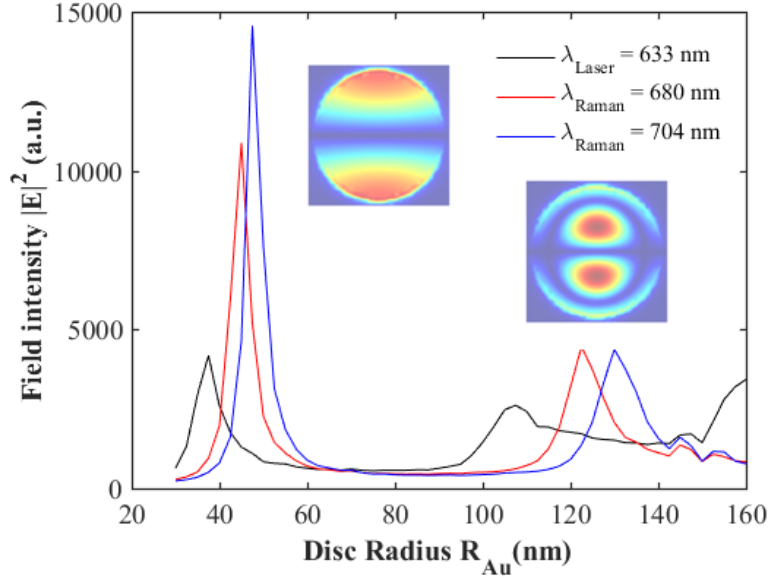
Figure 7.5: The near-field intensity is presented as a function of R_{Au}, at the laser wavelength λ_{laser}= 633 nm (black curve), the Raman wavelength of peak 1 λ_{R1}= 680 nm (red curve), and peak 2 λ_{R2}= 704 nm (blue curve), respectively. The near-field intensity is obtained by integrating $|E|^2$ over the discs surface (top surface and side wall).

ferent wavelengths: $|\tilde{E}_{Loc}(\omega_L)|^2$ at λ_{laser}=633 nm (black curve), $|\tilde{E}_{Loc}(\omega_R)|^2$ at λ_{R1}=680 nm (red curve) and λ_{R2}=704 nm (blue curve). In chapter 4, it is presented that cavity plasmon mode TEM11 dominates in the visible region for smaller discs ($R_{Au} \sim$ 40 nm, 70 nm) and the TEM12 mode dominates the spectra of larger discs ($R_{Au} \sim$ 100 nm, 130 nm, and 160 nm), respectively. For the near-field integrated at 633 nm (black curve), there are two pronounced peaks through the investigated R_{Au} range. The E field resonance appearing for the smaller disc size R_{Au}= 38 nm results from the cavity mode TEM11, which can be confirmed by the inserted field map. Similarly, the field resonance at R_{Au}= 108 nm is due to cavity plasmon mode TEM12. The E field increases again for $R_{Au} \geqslant$ 150 nm, which may result from the TEM31 or TEM13 mode of larger cavities. The near-field resonances at the Raman wavelengths (red and blue curves) show the same profile except the resonance R_{Au} for the modes TEM11 and TEM12 shifted to larger radii due to increasing wavelength. For increasing wavelength, the resonance R_{Au} also increases, as can be deduced through the formula $k_{gsp}(R_{Au} + \Delta R) = \chi'_{mn}$. On the other hand, the integrated E field is significantly smaller for MIM structures with Au disc radii around 70 nm and 160 nm, because both the laser and Raman wavelengths are out of the plasmonic resonance of TEM11 ($R_{Au} = 70$ nm) and TEM12 mode ($R_{Au} = 160$ nm).

It is worth noting that the E field resonances attributed to the TEM11 mode show a notably stronger field enhancement at the smaller R_{Au} compared to those resulting

from the TEM12 mode at the larger R_{Au}. In the case of the near-field at $\lambda_{R2} = 704$ nm (blue curve), the $|E|^2$ at the resonance R_{Au} of the TEM11 mode is 3 times that of the TEM12 mode. In chapter 4, it is presented that surface cavity mode TEM12 shows a better field confinement than the TEM11 mode. Different from the edge mode TEM11, the surface mode TEM12 has most of its energy in its central modal lobes rather than the edge lobes, which can be seen by comparing the inserted field maps. As a result, the local field strength of the TEM12 mode at the cavity ends is found to be considerably lower than that of the TEM11 mode. As a result, the integrated field at the surface of the Au disc is lower for the TEM12 mode than that of the TEM11 mode, as can be seen in Figure 7.5.
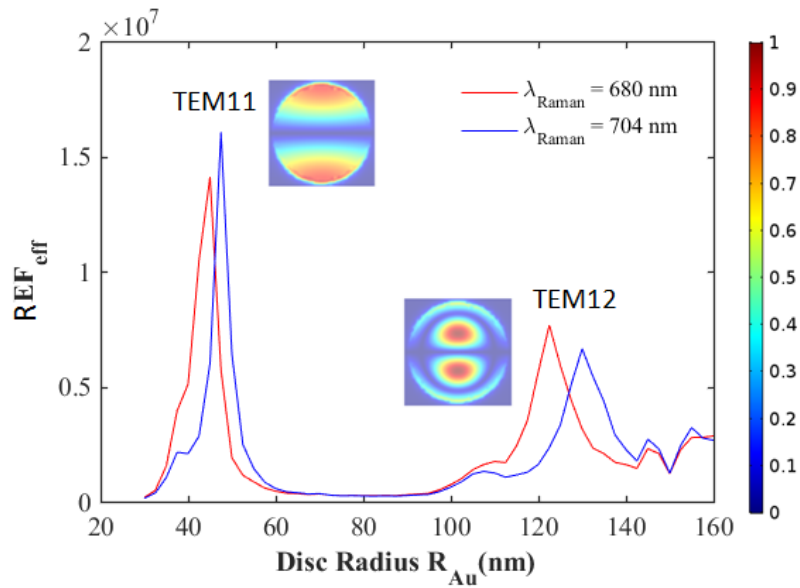

Figure 7.6: Simulated REF_{eff} for MIM(II) are presented as a function of varying radius of Au disc R_{Au} for peak 1 (red curve) and peak 2 (blue curve), the periodicity is fixed at P = 335 nm. $REF_{eff} = |\tilde{E}_{Loc}(\omega_L)|^2 \times |\tilde{E}_{Loc}(\omega_R)|^2$ based on equation 1.4.

The EFs in Figure 7.6 are the products of the integrated field intensity at the laser wavelength and corresponding Raman wavelengths, $REF_{eff} = |\tilde{E}_{Loc}(\omega_L)|^2 \times |\tilde{E}_{Loc}(\omega_R)|^2$. For Raman peak 2, the MIM structures with R_{Au} of 48 nm and 130 nm show peaks of REF_{eff}, resulting from enhanced E fields of cavity plasmon modes TEM11 and TEM12. MIM(II) with radius R_{Au} out of the resonance range show not very impressive enhancement factors, due to the fact that no cavity plasmon mode is excited at neither laser wavelength nor Raman wavelengths. Consequently, the REF_{eff} decreases and then increases, and again decreases as a function of increasing R_{Au}. The same variation pattern can be seen for peak 1, except with smaller resonance R_{Au} due to the smaller Raman wavelength.

The enhancement peak due to the TEM11 enhancement at smaller R_{Au} is much stronger than that of the TEM12 mode at the larger R_{Au}. It can be explained by the same reason

as in Figure 7.5: because of the field distribution difference between edge cavity mode
TEM11 and surface cavity mode TEM12. The nature of the small bumps at R_{Au}=38
nm, 143 nm, 155 nm are not clear yet, they may arise from the LSPR mode of the Au
disc, or SPP modes or higher order cavity plasmon modes, or maybe just because the
calculation mesh size is not fine enough.

7.2.1.3   Comparison between Experimental and Simulated EF

In the experiments (Figure 7.4(b)), the steps between two investigated R_{Au} are too
large to show as much details as in the simulation (Figure 7.6). The REF_{eff} peak
due to enhancement of the TEM12 mode is hardly visible for the MIM structures
with big R_{Au} between 100 nm and 160 nm. The REF_{eff} contributed by the TEM11
mode between R_{Au} = 40 nm and 60 nm did not appear as a peak in experiments,
because only R_{Au} = 35 nm and 70 nm were investigated experimentally. However, the
trend of higher REF_{eff} due to enhancement of the TEM11 mode at smaller disc radius
and lower REF_{eff} due to enhancement of the TEM12 mode is in good agreement as
predicted by simulations.

In Figure 7.4(b), the same $\frac{A_{eff}}{A_{laser}} = \pi R_{Au}^2/P^2$ were applied for the TEM11 mode and
TEM12 mode when the REF_{eff} is calculated based on equation 7.5. However, the field
distribution difference between edge cavity modes and surface cavity modes makes
the enhanced near-field of the TEM12 mode less accessible at the MIM(II) structure
surface compared to that of the TEM11 mode. In Figure 7.7(a), field maps for TEM11
mode and TEM12 mode are presented at their resonance wavelengths. An energy
threshold is set so that the energy above this threshold would appear in dark red. The
accessible enhanced near-field is outlined by black lines. The TEM12 mode is not as
accessible as TEM11 mode because the energy of surface mode TEM12 is strongly
confined in the center of the MIM cavity, whereas the energy of edge mode TEM11 is
distributed at the cavity edge. To evaluate the experimental REF_{eff}, for simplicity,
we take $\frac{A_{eff}}{A_{laser}} = \pi R_{Au}^2/P^2$ for $R_{Au} \leqslant 100$ nm where the TEM11 mode dominates, and
$\frac{A_{eff}}{A_{laser}} = 0.5\pi R_{Au}^2/P^2$ for 100 nm $< R_{Au} < 160$ nm where the TEM12 mode dominates.
The evaluated REF_{eff}s are then presented in Figure 7.7(b). Compared to Figure 7.4(b),
the REF_{eff} peak attributed to the TEM12 mode can be distinguished at R_{Au} = 130
nm, after the different accessible enhanced areas of TEM12 and TEM11 are taking into
consideration.

To conclude, the experimental REF_{eff} follows the prediction of FEM simulations,
while more different radii would be required to compare the curve shapes. For the
smaller R_{Au}, the TEM11 mode dominates at the laser and Raman wavelengths, and
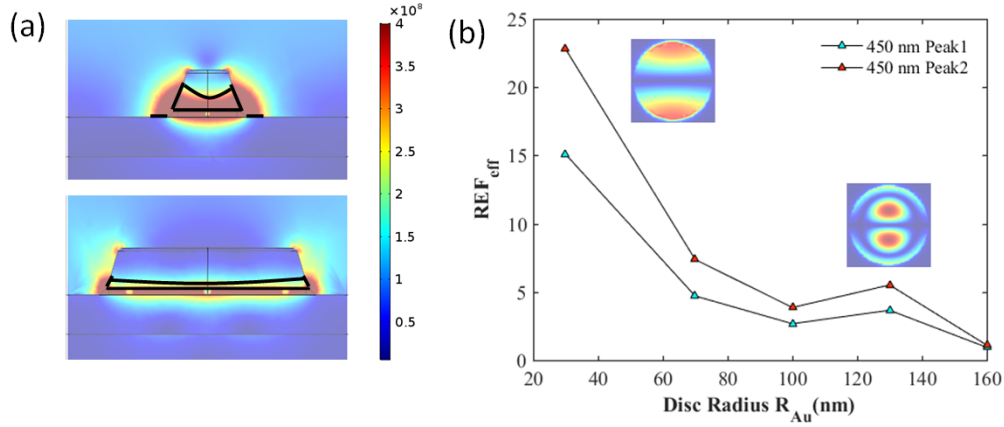
Figure 7.7: (a) Field maps of TEM11 mode and TEM12 mode at resonance wavelengths. An energy threshold is set, and the energy above this threshold appears in dark red. The enhanced field of TEM11 is more accessible at the MIM structure surface than that of TEM12 mode. (b)The REF_{eff} evaluated based on equation 7.5 while taking into consideration of the accessible enhanced area of TEM12 and TEM11 mode: $\frac{A_{eff}}{A_{laser}} = \pi R_{Au}^2/P^2$ for $R_{Au} \leqslant 100$ nm, and $\frac{A_{eff}}{A_{laser}} = 0.5\pi R_{Au}^2/P^2$ for 100 nm $< R_{Au} < 160$ nm.

the TEM12 mode dominates in the case of larger R_{Au}. Compared to the TEM12 mode, the enhanced near-field of the TEM11 mode is more accessible for molecules adsorbed on the MIM structure surface, resulting from the fact that the near-field of edge cavity mode TEM11 resides at the edges of the MIM(II) cavity and that of the TEM12 mode resides at the center of the MIM(II) cavity. As a result, the REF_{eff} peak attributed to the TEM11 mode shows a higher amplitude than the peak attributed to the TEM12 mode.

7.2.2 SERS experiments with under-etched MIM

7.2.2.1 SERS experiments

While the MIM(II) shows good REF_{eff} compared to island films, even better SERS performance can be expected, as stated in chapter 5. In this section, another MIM(II) sample was fabricated in parallel to the SERS sample investigated in the previous section. It was then studied in chapter 5 for exposing the hot spot by wet etching. By comparing the blue shift of the extinction measurements to the simulated extinction spectra, it was estimated that the R_{SiO_2} was decreased by 14 nm after etching by HF acid with a concentration of 0.03 % (wt) for 50 seconds. Because it is an isotropic etching process, we assume that R_{SiO_2} for different MIM structures were all reduced by 14 nm. This sample was then treated with 4-MBA with the same method as for the unetched sample, and SERS signals were recorded under the identical measuring

configuration.
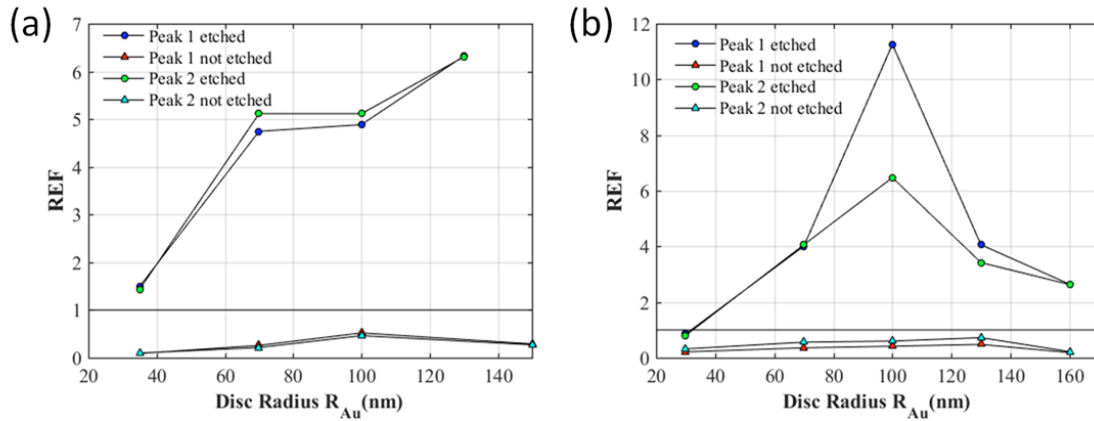
Figure 7.8: the REFs of MIM structures before and after wet etching for different Au disc radius and grating constants (a) P = 335 nm and (b) P = 440 nm.

Figure 7.8 presents the REFs of MIM structures before and after wet etching for different disc radius and periods. It is quite clear that the underetched MIM structures show better SERS capability than island films (REF > 1), whereas their non-etched counterparts show weaker SERS signal than island films, with REF below 1.
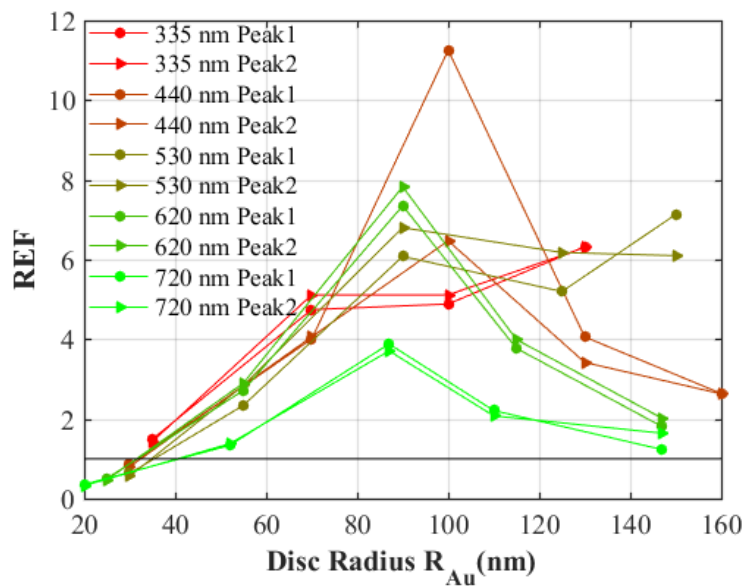
Figure 7.9: The REFs of MIM(II) structures after wet etching (MIM(III)) for different Au disc radii R_{Au} ranging from 20 nm to 160 nm, and grating constants P ranging from 335 nm to 720 nm.

SERS signals were also recorded and evaluated for higher grating constants, P = 530 nm, 620 nm and 720 nm. In Figure 7.9, REFs for different etched samples with different geometrical parameters are presented. Stronger SERS signals than those obtained with island films were achieved for MIM structures with big grating constants, even though

these substrates have a very small enhancing effective area compared to island films. It is interesting to notice that for grating constants P = 620 nm, 530 nm and 440 nm, the recorded maxima SERS signals are stronger than those of MIM with P = 335 nm, even though less Au disc MIMs were involved (laser spot size around 10 μm). For the nonetched MIM, in Figure 7.4(a), the SERS signal was also stronger for P = 440 nm than that of P = 335 nm. In chapter 4, it was stated that the near-field and resonance position of cavity plasmon modes is independent of the grating constants except when strong coupling occurs. The position of SPP modes can be easily calculated based on equation 4.1. The grating induced surface polaritons at the substrate/Au film interface (SPP$_{Au/glass}$(0,1)) occur at 709 nm for P = 440 nm and the SPP$_{Au/glass}$(1,1) mode appears at 632 nm for P = 530 nm, respectively. Although these resonances are close to the wavelengths of interest (λ_{laser} = 633 nm, λ_{R2} = 704 nm), the SPP field is propagating on the glass/Au film interface, beyond the reach of Raman molecules. For P = 620 nm, SPP$_{Au/glass}$(1,1) and SPP$_{Au/air}$(0,1) appears at 702 nm and 647 nm, respectively. The near-field of SPP$_{Au/glass}$(1,1) is not accessible to the molecules, and SPP$_{Au/air}$(0,1) is out of the wavelengths of interest (bandwidths of SPP modes are ∼30 nm as in Figure 4.11). For P = 720 nm, SPP$_{Au/glass}$(0,2) and SPP$_{Au/air}$(0,1) appear at 612 nm and 741 nm, respectively, both out of the range of interesting wavelengths. So the stronger SERS signals for higher grating constants do not come directly from the near-field contribution of SPP modes. There are two possible reasons to explain the stronger SERS signal for larger periodicity: first, the mode hybridization between SPP mode and cavity mode shifts the resonance positions of hybridized modes to a more beneficial position for the electromagnetic enhancement effect. Second, the strong localized field of the LSPR mode induced by SPP$_{Au/air}$ modes contributes to the higher SERS signal. Details about this LSPR mode at $\lambda_{SPP_{Au/air}}$ were presented in section 6.3.
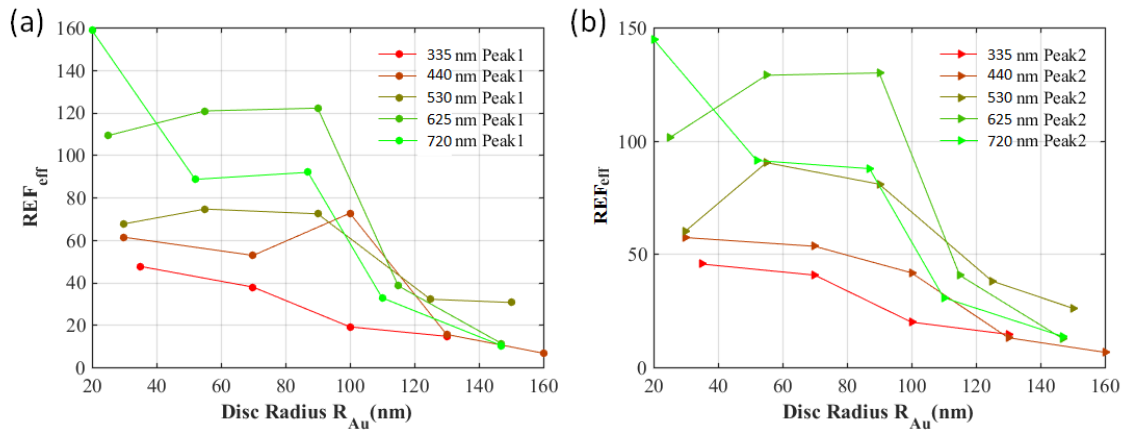

Figure 7.10: REF$_{eff}$ evaluated from Figure 7.9 with $A_{eff}/A_{laser} = \pi R_{Au}^2/P^2$: (a) Raman peak at 1084 cm^{-1}, (b) Raman peak at 1586 cm^{-1}.

Figure 7.10 presents the measured SERS REF_{eff}s with respect to island films with $A_{eff}/A_{laser} = \pi R_{Au}^2/P^2$ based on formula 7.1. REF_{eff} up to 160 were found compared to island film, which is much higher than the best REF_{eff} of 23 of the unetched MIM structures. It can be seen in Figure 7.10 that MIM(III) structures with smaller R_{Au} show higher REF_{eff}s than MIM(III) with larger R_{Au}. The REF_{eff} peaks evaluated for Raman bands at 1084 cm^{-1} (Figure 7.10(a)) and 1586 cm^{-1} (Figure 7.10(b)) seem to appear between $R_{Au} = 40$ nm to 80 nm. Simulations were performed to understand the dependency of REF_{eff} on the Au disc size R_{Au} in MIM(III) structures.

7.2.2.2   Simulated SERS EF

In Figure 7.11, the simulated E field intensity and REF_{eff}s for the investigated MIM(III) structures in Figure 7.10 are presented. The simulated E field intensity and REF_{eff}s for corresponding MIM(II) in Figure 7.5 and 7.6 are also shown for comparison purposes. In chapter 5, it is shown by experiments and simulations that the resonance wavelengths of cavity plasmon modes shift to a shorter wavelength after the undercut is created by wet etching. That means the resonance R_{Au} for a given investigated wavelength shift to a larger R_{Au}. As shown in Figure 7.11(a), after the effective refractive index inside the plasmonic resonator MIM(III) is smaller than that of MIM(II), the resonance R_{Au} for laser wavelength and Raman wavelengths shift to bigger R_{Au}. It is worth noting that the accessible enhanced E field increased from MIM(II) to MIM(III). This can be explained by the fact that the near-fields of cavity plasmon modes are partially exposed to the Raman molecules after wet etching. In Figure 7.11(b), the simulated REF_{eff} were shown for the etched (MIM(III)) and unetched sample (MIM(II)). It can be seen that the resonant REF_{eff} due to enhancement from the cavity modes TEM11 and TEM12 both shifted to bigger R_{Au} after etching, and the REF_{eff}s in MIM(III) structures are higher than in the corresponding MIM(II) structures.

Now back to the experiment REF_{eff} in Figure 7.10. By comparing the peak position attributed to the TEM11 mode for etched and unetched MIM structures (Figure 7.10 and 7.4(b), respectively), the corresponding REF_{eff} shifted to a larger R_{Au} after etching and appear at R_{Au} between 40 nm and 90 nm. The red shift of REF_{eff} attributed to the TEM11 mode is in good agreement with simulations, while the resonance position of REF_{eff} is moved a bit more to bigger disc radii, and the band width of the resonance is wider than the simulated resonance. The wider resonance bandwidth in experiments compared to the simulations may arise from the smaller quality factors of fabricated MIM cavities compared to the perfect cavity in simulations. In the simulations, a red-shift of ~ 5 nm and a REF_{eff} improvement of 2 are predicted. Nevertheless, by comparing Figure 7.10 and 7.4(b), a red-shift of ~ 20 nm and a REF_{eff} improvement
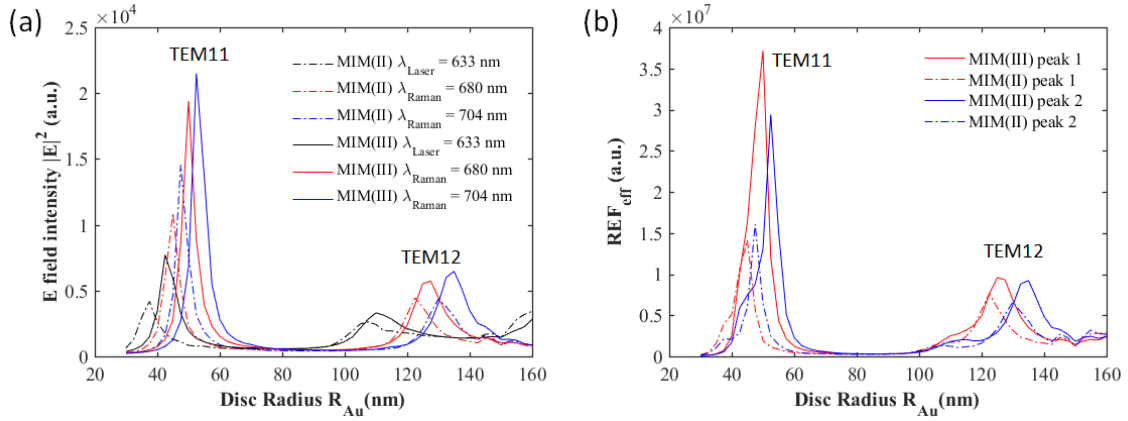
Figure 7.11: (a) The E field was integrated on the Au disc and Au surface exposed by wet etching. The integrated field intensities are shown for laser wavelength and Raman wavelengths for nonetched and etched MIM structures; (b) Simulated REF_{eff} for nonetched and etched MIM structures at two Raman bands. Solid and dotted curves for etched and unetched MIM structures respectively.

of 7 are achieved in experiments after wet etching. This may result from the different SiO_2 disc profile after etching in experiments and simulations. In simulations, a side wall with right angle is applied as can be seen in Figure 3.11. However, in experiments, excessive etching occurs at the Au/SiO_2 interface due to the fact that the HF etchant is drawn along the interface by capillary action [195], which can result in larger exposed enhanced area in the cavity than we estimated based on the resonance shift after etching in Figure 5.7. As a result, better REF_{eff} enhancement and stronger red-shift of the REF_{eff}s are observed in experiments. For etched MIM structures, it is similar to unetched MIM structures that the REF_{eff}s attributed to the enhancement of the TEM11 mode are much stronger than those contributed by the TEM12 mode.

It is worth noting that the TEM11 mode enhanced REF_{eff} is not always stronger than the one enhanced by the TEM12 mode in etched samples. It is true that mainly the hot spots of cavity plasmon modes localized under the edges of Au discs will be exposed by wet etching, thus the SERS EF can benefit more from the strong field of the TEM11 mode than the TEM12 mode at the disc edge. Whereas, when the TEM12 mode is excited in the visible spectral range, that means the Au disc is big and a larger exposed area (enhanced area by cavity modes) can be achieved by etching compared to small discs, resulting in more binding spots for the Raman molecules. In our experiments and simulations, the SiO_2 disc is reduced by 14 nm, however, only 2 nm into the edge of the Au disc because of the slanted side wall of the SiO_2 disc, as showed in Figure 3.11. Consequently, in our experiments, the EF contributed by the TEM11 mode is stronger than that of TEM12 mode. If the etching time was increased, R_{SiO_2} would be reduced more. There is a possibility that the bigger exposed area for the TEM12 mode will compensate for the fact that the local field at the disc edges is not as strong

as for the TEM11 mode, and the REF_{eff} contributed by the TEM12 mode dominates.

7.3   SERS experiments with BPE

The SERS EFs of disc-on-film MIM structures with Au discs on top of a Au film separated by a SiO$_2$ spacer disc ($R_{SiO_2} = R_{Au}$), were investigated with BPE molecules. MIM structures with different radii (R_{Au}) and grating constants were studied. The MIM structures and island films were incubated in 1 mM BPE(trans-1,2-bis(4-pyridyl)-ethylene)/ethanol solution. The surface treatment times were optimized by measuring the SERS signal after incubating for different times. It is found that the SERS intensity stopped increasing after incubating for 15 min. We assume that a monolayer of molecules was formed on the substrate surface after 15 min of incubation. After 15 min, there remain no free binding spots on metallic structures for more BPE molecules, though the substrates were immersed in BPE solution for 2 h or 2 weeks.

SERS measurements were performed on island films rinsed or without rinsing after the incubation process as well. It is found that a better homogeneity of the SERS signal can be obtained on island films which were rinsed after incubation. This is due to the fact that the BPE molecules that were adsorbed randomly on the surface through physical absorption were washed away during the rinsing process, while the monolayer of BPE molecules bound through chemical covalent bonds remained. Therefore, the rinsing process is important to have a homogeneous monolayer of BPE molecules, thus approximately equal numbers of BPE molecules are involved in each SERS measurement when the size of the laser spot is kept the same.

According to the optimized surface treatment process, MIM structures and island films were immersed in 1 mM BPE ethanol for 2 h, then rinsed with ethanol and blown dry by nitrogen gun. The BPE molecules are believed to bind to the metallic surface through the nitrogen atom with the long-axis of the BPE molecule along the Au-N bond. A schematic of a BPE molecule can be seen in the insert of Figure 7.12(a).

Figure 7.12(a) presents the averaged SERS spectra for Au island films and a connected MIM structure, where $2R_{Au} > P$. The SERS spectra for island films were averaged over 5 different locations on each sample, and further averaged over 3 different 5 nm Au island films, in order to rule out too high or too low reference SERS signals. The SERS spectrum for a connected MIM structure was also averaged over three different measurements at different locations. The SERS signal shows distinct Raman peaks in accordance with other works [106, 196]. The most dominant Raman peaks appeared at 1636, 1607 and 1199 cm^{-1}, the corresponding assignment of the Raman bands can
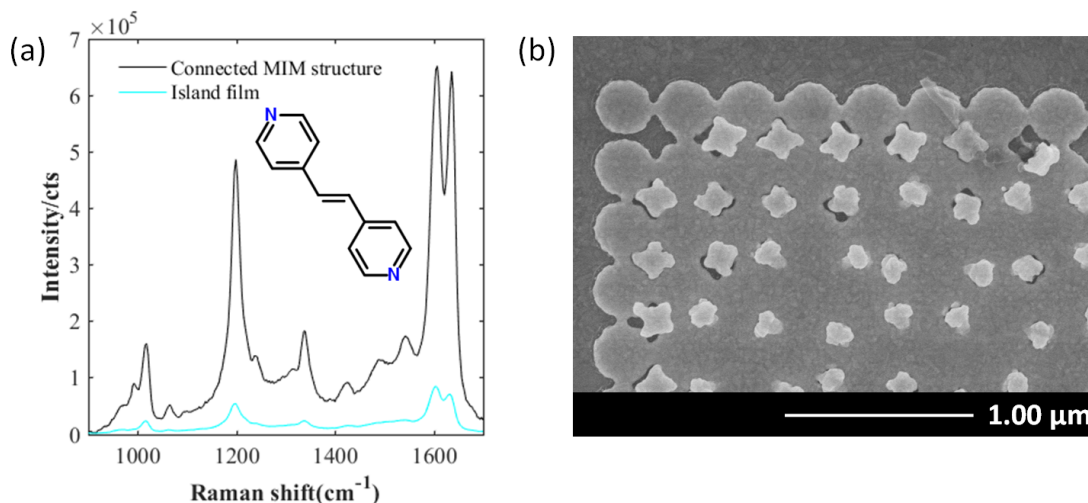
Figure 7.12: (a) Averaged SERS spectra recorded for connected MIM structures and island films, insert is a schematic of a BPE molecule, (b) a SEM image of connected MIM structures

be seen in Table 7.2. The Raman band at 1636 cm^{-1} is attributed to stretching of the C=C bond in the vinyl group. The Raman band at 1607 cm^{-1} is assigned to the stretching of the C-C bond in the pyridine ring and C-H in-plane bending vibration. The stretching of the C-C bond in the pyridine ring and the in-plane deformation of the C-N bond in the pyridine ring contribute altogether to the Raman band at 1199 cm^{-1} [197].

Table 7.2: Raman bands assignment for Au-BPE complex. ν – stretch; δ – in-plane bend; v – vinyl; p – pyridyl ring.

Raman bands	Assignment
1636 cm^{-1}	$\nu(C=C)_v$
1607 cm^{-1}	$\nu(C\text{–}C)_p, \delta(C\text{–}H)$
1199 cm^{-1}	$\nu(C\text{–}N)_p, \nu(C\text{–}C)_p$

The connected MIM structure was produced when the EBL exposure dose was too high to generate hole patterns with disc sizes of 320 nm and grating constants of 350 nm. As a result, connected discs on top of a Au film separated by a SiO$_2$ insulator layer and additional gold particles from incomplete lift-off are obtained, instead of the designed MIM cavity array. Here we can assume that the average numbers of BPE molecules covered by the laser spot in each SERS measurement are approximately the same due to the molecular monolayer formation and the same laser spot size. So the REFs can be calculated using formula 7.2. The REFs of connected MIM structures are evaluated to be 9.7, 8 and 9.1 at Raman bands 1636, 1607 and 1199 cm^{-1}, respectively. The good SERS enhancement factor of this connected MIM structure may arise from its special

structural configuration or from the high EM field in nanogaps which were formed accidentally from the high exposure dose. Similar high REFs appeared for connected MIM structures investigated with 4-MBA in the previous section as well (not shown). A further investigation in this connected MIM structure may suggest a possibility for excellent SERS substrates (outlook).

For all the MIM(II) cavities investigated with different radii of Au discs R_{Au} and grating constants P, in most cases, the effective relative EFs are either comparable to or smaller than that of the 5 nm Au island film, as in the case of 4-MBA enhanced by unetched MIM structures. Just two MIM(II) structures were found showing better SERS performance than island films. In Figure 7.13, the solid curves show the REF_{eff}s
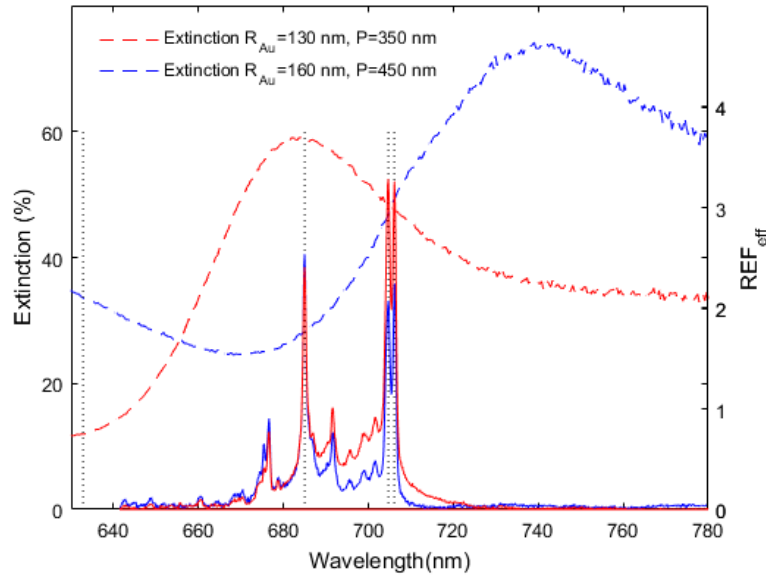
Figure 7.13: The REF_{eff} of two MIM(II) structures with respect to the island film is shown as a function of wavelength. Corresponding extinction measurements were shown to indicate the resonance positions of plasmonic modes. The laser wavelength and Raman wavelengths are marked by the dotted black lines at 633 nm, 685 nm, 704 nm and 706 nm.

for two different disc-on-film MIM structures: R_{Au}= 130 nm, P = 350 nm (solid red curve) and R_{Au}= 160 nm, P = 450 nm (solid blue curve). The REF_{eff}s were calculated according to formula 7.3. The corresponding extinction measurements were presented in dashed curves to indicate the resonance wavelengths of the plasmonic modes. The black dotted lines mark the important wavelengths for SERS: laser wavelength $\lambda_L =$ 633 nm, Raman scattering wavelengths $\lambda_R = 685$ nm, $\lambda_R = 705$ nm and $\lambda_R = 706$ nm for Raman bands at 1199 cm^{-1}, 1607 cm^{-1} and 1636 cm^{-1}, respectively. A REF_{eff} of 3.3 was observed for MIM structures with R_{Au}= 130 nm, P = 350 nm at Raman bands 1636 and 1607 cm^{-1}. As explained in chapter 4, the resonance wavelength of the cavity plasmon mode lies between the peak and dip position of the asymmetric

extinction spectra: between 680 nm and 730 nm for R_{Au}= 130 nm, and at a wavelength longer than 740 nm for R_{Au}= 160 nm. So, the Raman scattering wavelengths $\lambda_R = 705$ nm and $\lambda_R = 706$ nm are relatively closer to the cavity plasmon resonance when R_{Au}= 130 nm. As a result, MIM structures with R_{Au}= 130 nm showed a larger REF_{eff} (3.8) than R_{Au}= 160 nm (3.2).

7.3.1 SERS based on vertical disc dimer

Vertical dimer samples with different R_{Au} and P were fabricated by the lift-off method as stated in section 3.1. The as-fabricated structures were treated with BPE/ethanol solution following the same protocol as in the last section, and the SERS capabilities are investigated under identical measuring configuration. In Figure 1.21, it is shown that the field intensity at the edges of the vertical Au disc dimer is not as strong as that for a disc-on-film structure at the cavity resonance wavelength. However, the accessible hot spot on the disc dimer is bigger than on the disc-on-film system. So it is interesting to study the SERS performance of vertical dimers.
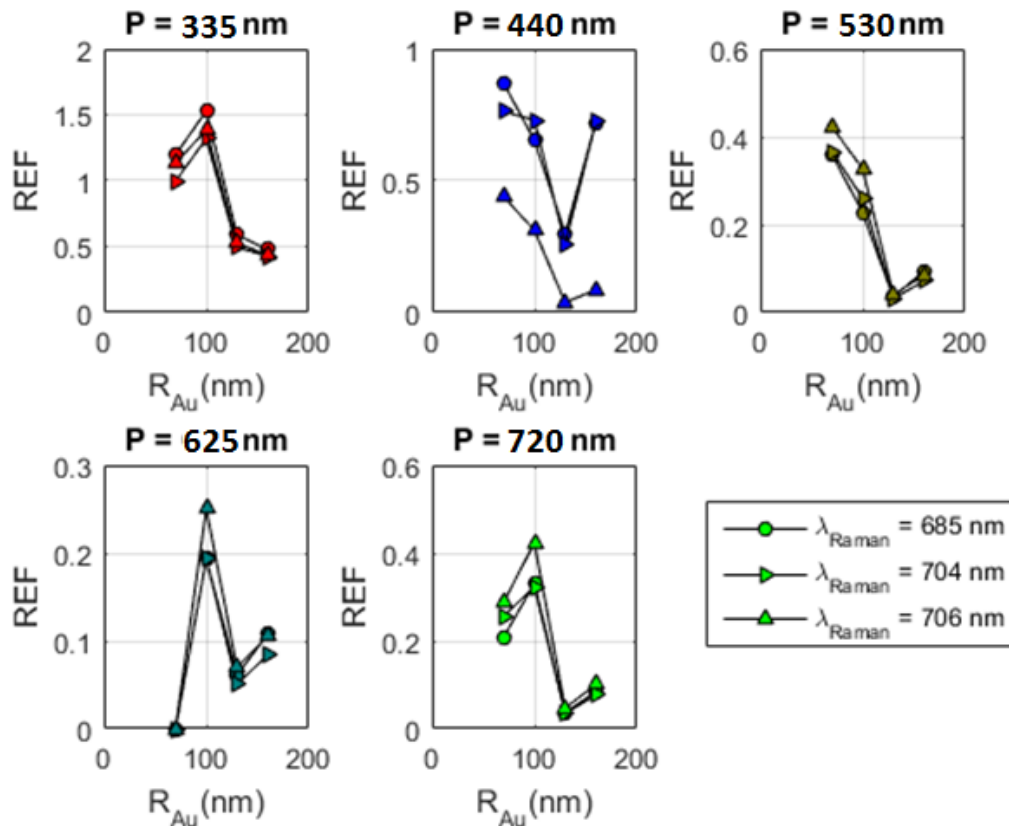

Figure 7.14: REFs of vertical dimers as a function of Au disc radius R_{Au} and varying grating constant P = 335 nm, 440 nm, 530 nm, 625 nm, 720nm, with respect to island films

Figure 7.14 shows the measured REFs of vertical dimers with varying geometrical parameters, calculated based on formula 7.3. The highest REF appears for a substrate with a disc radius of $R_{Au} = 100$ nm and grating constant P = 335 nm. The highest REF of vertical dimers of $\sim$1.5 is a bit smaller than for the unetched MIM(II) structure, as REF of 3.3 was observed in Figure 7.13.
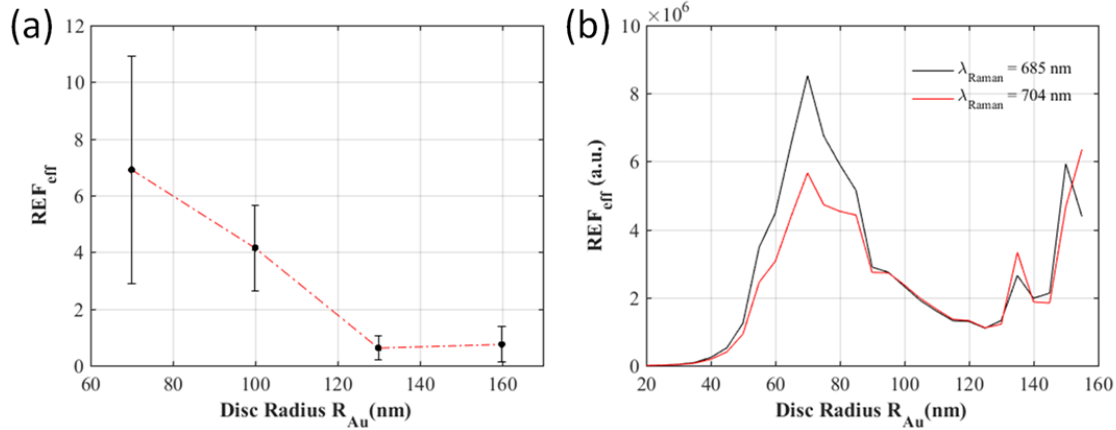

Figure 7.15: (a) Measured REF_{eff}s of vertical dimers with different Au disc radii R_{Au}, for Raman band $\lambda_{Raman} = 704$ nm with respect to island films. (b) Simulated REF_{eff} for vertical dimers as a function of increasing R_{Au} for two Raman bands: $\lambda_{Raman} = 685$ and $\lambda_{Raman} = 704$ nm.

The corresponding REF_{eff}s were evaluated from Figure 7.14 based on formula 7.1 and presented in Figure 7.15(a). The effective Raman enhancing area fraction is given by $A_{eff}/A_{laser} = \pi R_{Au}/P^2$. The REF_{eff} shows a decrease from $R_{Au} = 70$ nm to $R_{Au} = 130$ nm, then slightly increases from $R_{Au} = 130$ nm to $R_{Au} = 160$ nm. This evolution trend of REF_{eff} as a function of R_{Au} is in good agreement with simulations in Figure 7.15(b).

In the vertical disc dimers, the circular FP cavity is defined by the two Au/SiO_2 interfaces and the edge of the Au disc R_{Au}, the resonance condition of TEMmn modes is the same as that in MIM(II) structures. As a result, the vertical disc dimer shows identical near-field distributions and resonance wavelengths (also shown in Figure 1.21) as the MIM(II) structure when the FP cavity has the same insulator thickness and Au disc radius, even though the far-field spectra are very different from each other. SERS is more about near-field enhancement, so the dependency of REF_{eff} on R_{Au} should be very similar. This is proven by the fact that the simulated REF_{eff} for these two structures, presented in Figure 7.15(b) and 7.6 respectively, show similar profiles. Nevertheless, the REF_{eff} peaks in vertical MIM structures appear at a larger R_{Au}. This is because the simulations are adapted to the fabricated structures in shape and size. It is inevitable for structures fabricated by EBL and evaporation to feature slanted side walls. For a vertical dimer consisting of a 50 nm Au disc/10 nm SiO_2 disc/50 nm

Au disc in height, the side walls of Au discs show a tilting angle of $\sim 75°$ and the side walls of SiO$_2$ discs show an angle of $\sim 45°$ due to different evaporation rates of metal and dielectric in experiments. If the base radius of the bottom disc is R$_{Au}$, then the base radius of the upper disc is only (R$_{Au}$ - 23.4) nm. The radius of a plasmonic resonator is determined by this smaller radius. This means when the vertical dimer and MIM(II) structure with a disc spacer have the same R$_{Au}$, the resonance radius in the vertical disc dimer is ~ 23.4 nm smaller. This is the reason why the REF$_{eff}$ shifted to a bigger R$_{Au}$ in Figure 7.15(b) compared Figure 7.6.

Similar to the MIM(II) structures, the REF$_{eff}$ attributed to the TEM11 mode is also stronger than the one attributed to the TEM12 mode. As a result, vertical dimers with a smaller R$_{Au}$ show a relatively higher REF$_{eff}$ in Figure 7.15. The SERS capability of vertical dimers can be significantly improved by exposing the hot spots of cavity modes.

7.4 Conclusion

In this chapter, SERS capabilities of cavity plasmon modes in unetched MIM(II) structures and etched MIM structures (MIM(III)) were investigated with 4-MBA and BPE molecules. The dependency of the SERS EFs on geometrical parameters were evaluated from measurements and explained with simulations. Notable SERS EF improvements have been achieved by MIM(III) structures which are obtained by wet etching MIM(II) structures. The R$_{Au}$ which gives rise to the highest REF$_{eff}$ shifts to a larger R$_{Au}$ after wet etchig. Good qualitative agreement has been found between measured and simulated REF$_{eff}$s. The TEM11 mode enhanced REF$_{eff}$ peaks appear at a smaller R$_{Au}$ and have bigger magnitude than those enhanced by the TEM12 mode. However, a dominant REF$_{eff}$ at a bigger R$_{Au}$ attributed to the enhancement of the TEM12 mode may be expected by greatly reducing the radius R$_{SiO_2}$. Much stronger EFs can also be expected from greatly reducing R$_{SiO_2}$ with increasing the accessible enhanced area. The content presented in this chapter will provide us with a guidance to optimize the geometrical parameters of plasmonic resonators according to different measuring situations.

Appendix A

Cones-on-film MIM structure

Cones-on-film MIM structures are studied experimentally and theoretically as well, the detailed results are not shown here due to the length of this thesis. However, the fabrication process is shown here.

Besides the advantageous properties of strong field confinement and enhancement, cone MIM cavities provide more tunability compared to disc MIM cavities, thanks to their sharp-tipped geometry. Both in-plane base plasmonic modes and out-of-plane modes are excited with proper excitation conditions. The out-of-plane plasmonic mode in nanocones with a well-defined localized excitation area and high field intensity is of great interest for research on single photon light sources, near-field microscopes and plasmon-assisted spectroscopy [198].

Fabrication of gold cones on a gold film sandwiched with a dielectric insulator layer is very similar as for gold discs on gold film, as presented in Figure 3.1. To fabricate a gold cones MIM structure, firstly, glass substrates were cleaned, 50 nm ITO were deposited as adhesion layer and also to promote the conductivity for EBL. 50 nm gold and 10 nm SiO_2 were subsequently deposited. For the spin coating process, after the first layer of PMMA was spin coated with the same parameters as in the last section, the substrate was placed in the oven at 150 °C for 10 min. Then the same spin coating process was repeated on top of the first PMMA layer, then postbake in the same oven for 1 h. The thickness of this two-layer PMMA was around 300 nm. According to the experience that when the height of the deposited structures is less than 1/3 of that of the PMMA layer, lift-off works out the best, this height of 300 nm PMMA fits well to produce cones with 100 nm height. E-beam lithography and development were performed. A deposition rate of 0.02 nm/s was applied to fabricate gold cones, which is only 1/15 of the deposition rate for fabricating nano discs. As the thickness of the gold film is growing thicker on top of the PMMA layer, the mask holes are also closing

up with time until they are completely closed, resulting in a nanocone structure with a sharp tip. The lift-off process yields gold nanocones on a gold film sandwiched with an insulator layer.

While the same methods, e-beam lithography and deposition, are used for the fabrication of gold discs and cones, the aspect ratio of the PMMA height and structure diameters, as well as the deposition rate of gold play an important role in the final structure geometry. The reason behind the structural difference is that the deposited gold on the PMMA mask reduces the hole size constantly as the gold film grows thicker, until it is closed completely. Attributed to the same reason, gold discs obtained by this method cannot achieve straight side walls. Instead, those discs have sloped side walls and rounded corners on the edge, more like truncated cones.
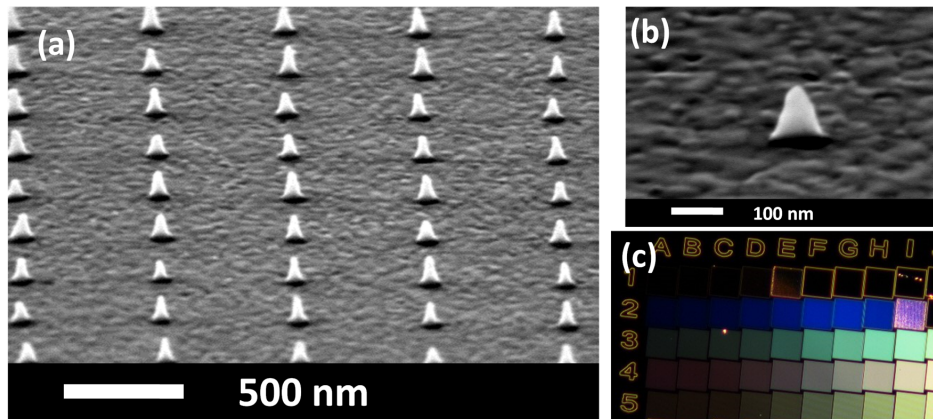
Figure A.1: Arrays of cone MIM cavities. (a) SEM image of cone array on gold film with a SiO_2 film spacer, the radius of the cone base is 50 nm, the height of the cones is 130 nm and the grating constant is 550 nm. (b) SEM image of a single cone MIM cavity of 50 nm radius and 130 nm height. (c) Dark-field image for arrays of cone MIM cavities consisting of cones with heights of 130 nm on gold film separated by a 10 nm SiO_2 layer, the radius increases gradually from the first row to the fifth row and the grating constant increases from left to right. Area size in (c): 25 $\mu m \times 25$ μm.

Figure A.1 (c) shows a dark field image for arrays of cone MIM cavities where the height of the cones is 130 nm, the height of the gold film is 50 nm and the insulator layer is an evaporated 10 nm SiO_2 film. The radius of the cone base is 50 nm.

Appendix B

French summary

B.1   Nos objectifs

Les résonances plasmoniques de surface (SPR) sont des oscillations collectives de gaz d'électrons, qui peuvent être excitées à des interfaces métal noble/diélectrique lorsque la lumière interagit avec des nanostructures métalliques. Le gaz d'électrons libres dans le métal oscille en fonction du champ électrique local par rapport aux noyaux ioniques fixes, ce qui crée un champ électromagnétique (EM) bien confiné et renforcé à la surface des nanostructures métalliques. En raison du mécanisme de cette oscillation plasmonique, la position de résonance et l'intensité sont très sensibles au changement de milieu environnant, ainsi que la taille et la forme des nanostructures [1–4]. Ces propriétés permettent de créer des capteurs biomédicaux et des capteurs Raman s'appuyant sur des plasmons générés par de telles nanostructures. Ainsi, depuis la découverte des SPR, de nombreux efforts ont été consacrés à l'utilisation de capteurs plasmoniques pour le diagnostic clinique, la sécurité alimentaire ou la surveillance de l'environnement.

Dans l'état actuel des connaissances, il n'est pas surprenant que les structures métal-isolant-métal (MIM) offrent en général de meilleures performances de détection indice de réfraction (IR) et améliorent le signal Raman par rapport aux nanostructures monomères dans les mêmes conditions. Ensuite, les applications basées sur des structures MIM verticales, qui sont relativement faciles à fabriquer en laboratoire, ont été brièvement passées en revue. Poussé par la volonté d'améliorer les capacités de détection, il a été conclu qu'il était nécessaire d'exposer le 'point chaud' dans les structures MIM verticales.

Notre objectif est de développer un substrat plasmonique ordonné et reproductible,

tout en offrant des champs proches fortement renforcés et des largeurs de raies étroites pour des applications de détection plasmoniques performantes. Différents modes plasmoniques, tels que les SPR induits par réseau, les modes résonance plasmonique de surface localisée (LSPR) au niveau de nanoparticules d'or et les modes de cavité dans la cavité isolante seront identifiés lors d'expériences et de simulations. L'influence de chaque élément de construction de la structure MIM sur les propriétés plasmoniques, en particulier la géométrie de la couche isolante, sera étudiée. Une meilleure compréhension de la physique fondamentale de la structure MIM de la cavité nous guidera la voie vers une géométrie d'échantillon optimisée. Un vide sera créé par gravure humide de la couche d'espacement. Le potentiel de cette structure MIM dans la détection IR et le SERS sera étudié.

B.1.1 'Hot spot' reproductible et accessible

De nombreux efforts ont été consacrés à la fabrication et à la valorisation des 'points chauds' des structures MIM latérales [37, 39, 40]. La force de couplage des modes plasmoniques dépend fortement de la distance de l'intervalle entre les nanostructures. Le confinement et l'amélioration du champ augmentent considérablement à mesure que la distance est réduite.
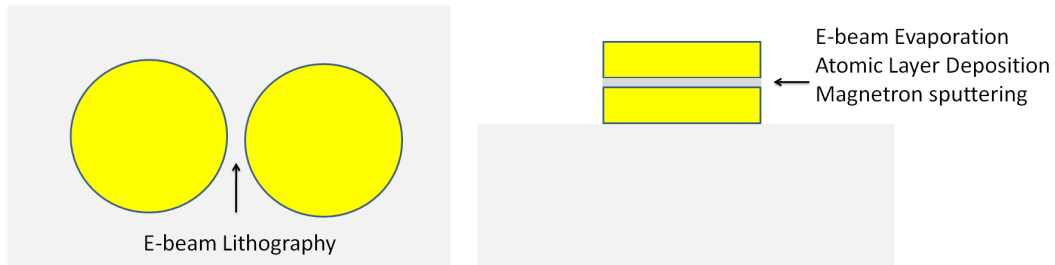
Figure B.1: Schématique du dimère latéral (à gauche) et dimère vertical (à droite).

Pour les structures MIM latérales ordonnées, comme le montre la figure B.1, les lacunes sont le plus souvent créées par lithographie à faisceau électronique (EBL), ce qui signifie que les espaces inférieurs à 10 nm ont une faible reproductibilité, limités par la résolution de la technique EBL. En revanche, dans le cas de structures MIM verticales, le contrôle précis d'un intervalle jusqu'à quelques nanomètres est mieux contrôlable, car l'intervalle dans une structure MIM verticale est défini par des techniques de dépôt en couche mince, telles que l'évaporation thermique par faisceau d'électrons, la pulvérisation cathodique ou le dépôt de couche atomique, comme indiqué pour un dimère vertical dans la Figure B.1. Un espace inférieur au nanomètre peut être obtenu lorsqu'une couche isolante d'épaisseur inférieure à un nanomètre est prise en sandwich entre deux nanostructures métalliques par dépôt atomique [96, 97]. De plus,

la réalisation reproductible d'espaces supérieurs à 5 nm peut être obtenue avec un contrôle d'épaisseur suffisant par des techniques éprouvées telles que l'évaporation et la pulvérisation cathodique.

Outre l'avantage du contrôle de l'espacement et de la reproductibilité, les structures MIM verticales constituent également une meilleure configuration pour la fabrication d'hétérodimères. Les hétérodimères sont un moyen d'obtenir plus d'accordabilité de la résonance plasmonique en utilisant des métaux différents pour deux nanostructures. Dans le cas des hétérodimères latéraux, on utilise généralement une méthode à double exposition qui nécessite une grande précision d'alignement, un équipement sophistiqué et une expertise des opérations. En comparaison, les structures MIM verticales peuvent être facilement obtenues en utilisant une source de dépôt différente.

Enfin, les structures MIM verticales peuvent présenter des volumes de modes plus importants dans l'espace (une carte de champ sera présentée au chapitre 4) par rapport aux MIM latéraux, tels que les nœuds papillons. De plus, le chevauchement spatial de différentes résonances plasmoniques peut être important, ce qui permet à une molécule Raman résidant à cet emplacement d'avoir signal exalté simultanément aux longueurs d'onde d'excitation et d'émission de la diffusion Raman [94].

Les 'points chauds' ordonnés dans les structures MIM verticales seront exposés à l'environnement de détection après une gravure humide bien contrôlée dans cette thèse. Le changement d'indice de réfraction dans le 'point chaud' modifiera considérablement la condition de résonance des modes plasmoniques de la cavité, entraînant de forts changements de position de résonance. Ceci est montré dans le chapitre de detection LSPR. Dans le cas d'applications SERS, les molécules Raman immobilisées dans le 'point chaud' de la structure MIM verticale diffuseront un signal Raman considérablement augmenté, conformément à la formule $EF \sim |E_{loc}|^4$.

B.1.2 Physique fondamentale dans les structures MIM verticales

Dans une structure MIM verticale , par exemple des matrices de disques d'or sur un film d'or séparées par une mince couche isolante, un ensemble riche de modes plasmoniques de différentes natures peut être excité. Ceux-ci comprennent des résonances de plasmon de surface localisées (LSPR) de nanoparticules d'or, des modes de réseau de surface résultant de l'interaction de champ lointain du rayonnement plasmonique entre voisins nanoparticules et plasmons de surface polaritons (SPR) des deux côtés du film d'or excité par les matrices de disques d'or.

En faisant varier les paramètres géométriques ou les matériaux des structures MIM, les modes plasmoniques peuvent être perturbés et interférer les uns avec les autres, entraînant des positions de résonance décalées, des profils d'extinction de type Fano et un champ proche encore exalté. Les applications plasmoniques optimales de MIM pour les substrats de spectroscopie Raman exaltée de surface (SERS) peuvent être conçues en fonction de différentes conditions d'éclairage et de molécules à détecter, sur la base d'une meilleure compréhension de la manière dont ces différents modes se couplent et s'hybrident.

Parmi tous les modes excités des structures MIM, les modes plasmoniques à cavité sont les plus intéressants avec des champs localisés hautement confinés et améliorés, pris en sandwich entre des nanostructures en or. Il est nécessaire d'étudier systématiquement les modes et sa dépendance aux dimensions des structures MIM .

Étant donné que nous souhaitons introduire un défaut dans la couche isolante et exposer les 'points chauds' des structures MIM , il est essentiel de savoir comment le champ proche serait modifié lors de la réduction des dimensions de l'isolant.

B.1.3   Amélioration des performances du capteur LSPR

Selon l'équation $FoM = \frac{S}{\Delta\lambda}$ (FoM est la figure de mérite, S est la sensibilité et $\Delta\lambda$ est la largeur de raie.), la capacité de détection IR peut être améliorée en réduisant la largeur de raie ou en augmentant la sensibilité IR des modes plasmoniques. Comme cela a déjà été dit précédemment et sera démontré en détail dans cette thèse, on peut s'attendre à une sensibilité élevée du IR lorsqu'un champ local fortement renforcé est soumis au changement d'indice de réfraction du milieu environnant. De plus, les structures MIM offrent un moyen très simple d'obtenir une largeur de raie très étroite en confinant les modes plasmoniques dans une cavité de Fabry-Pérot.

La figure B.2 montre les spectres d'extinction et de réflexion simulés pour des matrices de nanodisques Au sur un substrat de verre et sur un film d'or séparé par un disque isolant SiO_2, le rayon du disque Au et l'isolateur SiO_2 isolant sont de 40 nm pour les deux exemples de configuration. Les spectres d'extinction ont été évalués en prenant la transmission à travers le film Au comme référence (c'est pourquoi l'extinction négative apparaît dans les spectres d'extinxtion). L'extinction des réseaux de nanodisques Au, courbe rouge dans la figure B.2, montre un pic d'extinction avec une largeur de raie de 37 nm et une valeur d'extinction d'environ 0,28, tandis que dans le cas de la structure MIM le spectre d'extinction (La courbe noir de la figure B.2) fournit une largeur de raie de 37 nm pour les spectres à extinction positive et une valeur d'extinction de 0,52. Le spectre de réflexion (courbe bleue de la figure B.2) montre un creux avec une
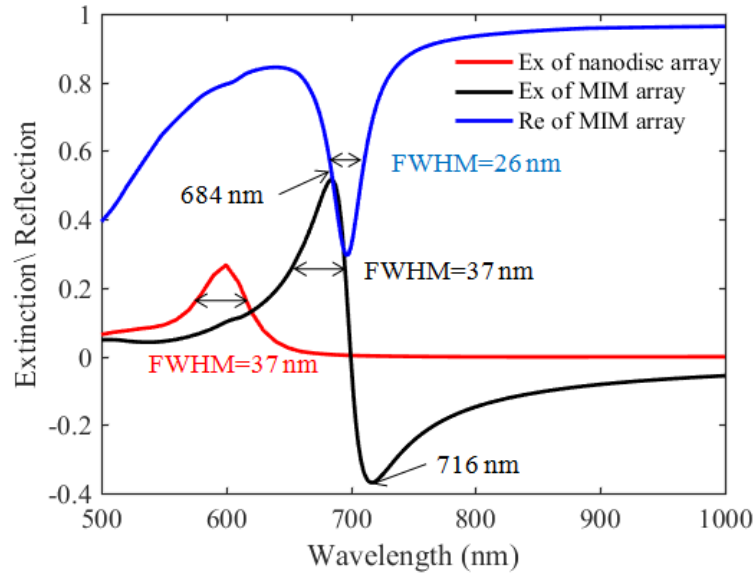
Figure B.2: Spectres d'extinction et de réflexion simulés pour des matrices de nanodisques Au sur substrat de verre et sur film d'or, séparés par un disque isolant SiO_2, le rayon du disque est de 40 nm dans les deux cas

FWHM de 26 nm et une perte de réflexion de 0,71. La résolution de détection IR sera améliorée à la fois par la largeur de raie plus étroite et par le rapport signal/bruit plus élevé obtenu dans la structure MIM par rapport aux nanostructures sur verre. En outre, au lieu d'une extinction en forme de raie de Lorentz dans l'ensemble de disques sur verre, le spectre d'extinction des structures MIM présente une forme de raie de Fano, avec une diminution abrupte entre 684 nm et 716 nm et une efficacité d'extinction variant de 0,52 à -0,39. Cette caractéristique de la forme de la raie de Fano peut être avantageuse pour la conception d'un capteur IR modulé en intensité extrêmement sensible en évaluant l'intensité à une certaine longueur d'onde [98].

Un autre avantage très important d'une structure MIM en tant qu'élément de détection IR est que ses modes plasmoniques peuvent toujours afficher des largeurs de raie très étroites, même pour les grands disques. La figure B.3 montre les spectres de réflexion diffuse (La réflexion diffuse est la réflexion de la lumière d'une surface qui est collectée sous plusieurs angles plutôt que sous un seul angle comme dans le cas de la réflexion spéculaire) simulés pour les matrices de disques sur verre (courbe rouge) et sur film mince Au (courbe bleue). Le diamètre du disque est de 320 nm dans les deux cas. Pour les matrices de Au disques sur verre, le mode dipolaire plasmonique est difficilement perceptible en raison d'excitations multi-modes et d'effets de retard, avec une FWHM de 227 nm. Dans la structure MIM, les modes plasmoniques se manifestent par des creux de réflexion. Dans les spectres de réflexion pour les structures MIM, une série de modes plasmoniques bien définis et distincts dans les cavités peut être trouvée à 640
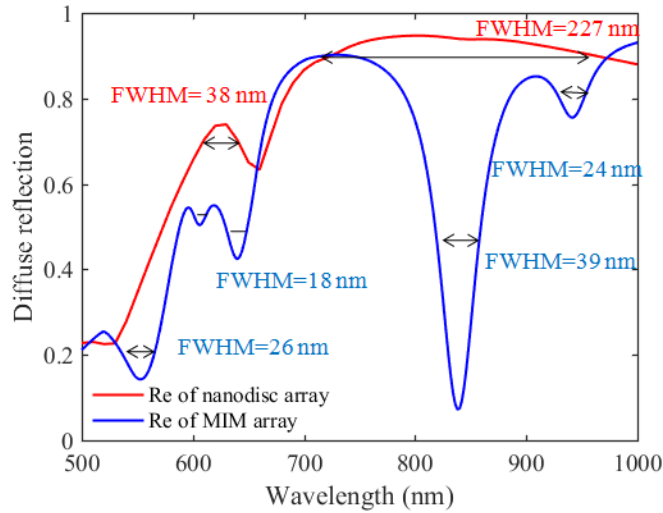
Figure B.3: Spectres de réflexion simulés pour des matrices Au nanodisc Au sur un substrat en verre et sur un film d'or séparés par un disque isolant SiO $_2$, les diamètres du disque sont de 320 nm dans les deux cas

nm, 838 nm et 940 nm, avec une largeur de raie de 18 nm, 39 nm et 24 nm, amélioration comparée à 227 nm dans les matrices de disques Au sur verre.

En conclusion, la structure MIM peut améliorer la capacité de détection IR de quatre manières:

- Sensibilité plus élevée basée sur un champ proche plus fort [93].

- Largeur de raie plus étroite pour une meilleure résolution de détection.

- Des pics d'extinction et des creux de réflexion plus prononcés permettent d'obtenir un rapport signal / bruit plus élevé pour une meilleure résolution de détection.

- Le profil de Fano montre un fort potentiel pour le capteur IR à modulation d'intensité .

B.1.4 Augmentation de l' EF du substrat SERS

Selon l'équation $EF \sim |E_{loc}|^4$, le facteur d'exaltation (EF) de SERS est proportionnel à la puissance quatre de l'intensité du champ proche local. Concevoir une configuration de nanostructures capable d'améliorer encore le champ local est le moyen le plus simple de fabriquer un substrat SERS avec un facteur EF élevé. Dans la figure B.4, les simulées champ E ($|E| = \sqrt{E_x^2 + E_y^2 + E_z^2}$) sont présentées pour différentes structures, excitées dans les mêmes conditions. Dans la figure B.4 (a), les dimensions des sous-parties correspondantes sont les mêmes. La hauteur des disques Au et des films Au est de 50
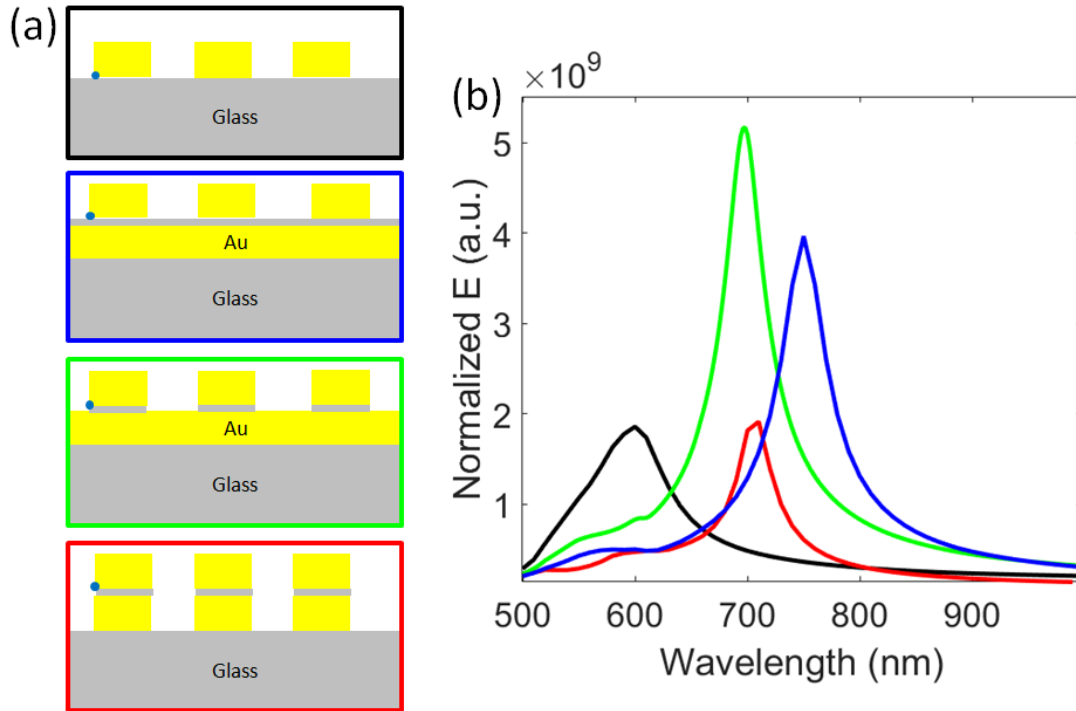
Figure B.4: Intensité de champ proche simulée pour différentes configurations de structure.

nm, la couche d'espacement est de 10 nm SiO$_2$. Les courbes de différentes couleurs dans la figure B.4 (b) représentent les de champ E de la structure dans un cadre de même couleur dans la figure B.4(a). Le champ E est évalué au bord inférieur des disques dorés dans chaque configuration, comme indiqué à la figure B.4(a) par les points bleus. Dans la figure B.4(b), il est clair que les champs locaux des structures MIM présentent une amélioration de champ supérieure à celle des réseaux de nanodisques sur verre. Dans le cas d'empilements de disques verticaux, la longueur d'onde de résonance plasmonique est décalée vers le rouge par rapport aux matrices de nanodisques, et seule une augmentation de champ local légèrement supérieure à la longueur d'onde de résonance est trouvée. Les nanoparticules sur Au film MIM montrent une amélioration plus forte que les nanoparticules sur verre. Dans le cas de nanodisques Au sur un film Au avec un disque intercalaire SiO$_2$, le champ proche amélioré est égal à 3 fois l'intensité de champ proche des nanodisques sur verre. Cependant, nous pouvons nous attendre à une meilleure capacité SERS des structures MIM que des nanodisques sur des substrats de verre. Des performances encore meilleures peuvent être attendues des structures MIM verticales lorsque le 'point chaud' dans l'isolant diélectrique est exposé à l'environnement de détection par gravure.

B.2 Fabrication de cavités MIM verticales

Des techniques sont demandées afin de fabriquer des structures ordonnées, par exemple, la technique EBL, fraisage faisceau d'ions focalisé (FIB). Pour les nanoparticules sur un film d'or pris en sandwich avec une couche isolante diélectrique, il est plus pratique de fabriquer avec la technique EBL. Les processus de fabrication des trois structures MIM verticales différentes que nous avons étudiées dans cette thèse sont plus ou moins similaires, l'EBL permettant d'obtenir les motifs souhaités en réserve puis de les transférer à la structure réelle par dépôt.
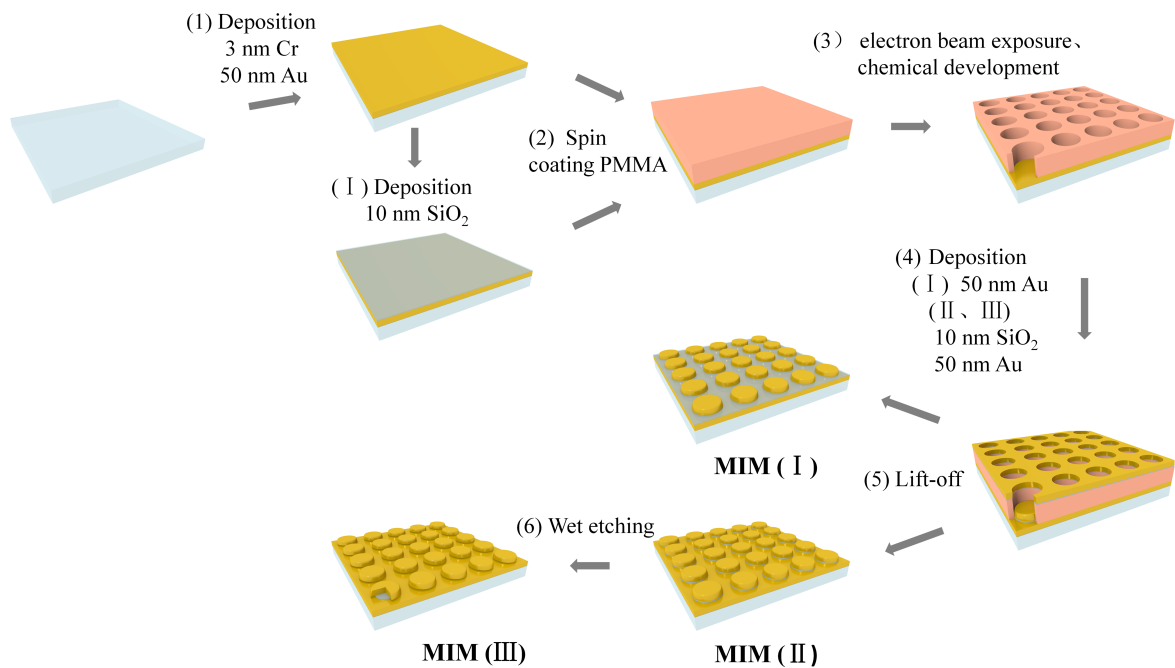
Figure B.5: Schéma de la fabrication des structures MIM verticales: avec une couche d'espacement de film SiO_2 (I), une isolant de disque SiO_2 où $R_{SiO_2} = R_{Au}$ (II), et disque SiO_2 où $R_{SiO_2} < R_{Au}$ (III).

Le processus de fabrication de matrices de cavités MIM, composées de disques d'or sur un film d'or séparés par un isolant diélectrique, est relativement simple. Comme le montre la figure B.5, le processus de fabrication commence par le nettoyage des substrats, le premier dépôt, le dépôt par centrifugation, la lithographie par faisceau d'électrons, puis le deuxième dépôt, suivi du soulèvement. Les détails de la fabrication d'un réseau de cavités MIM à disque avec SiO_2 film isolant, présentés dans la figure B.5 sous la forme MIM(I) sont les suivants:

* **Nettoyage des substrats:** Les substrats en verre ont d'abord été nettoyés dans une solution aqueuse d'hydroxyde de sodium dans un bain à ultrasons pendant 5 min, puis le même volume de peroxyde d'hydrogène à 35 % a été ajouté à

l'intérieur pour éliminer davantage les contaminants organiques présents sur le substrat. substrats, encore dans le bain à ultrasons pendant 5 min. Les substrats de verre ont ensuite été rincés à l'eau distillée et immergés dans de l'eau distillée propre et placés dans un bain à ultrasons pendant 5 min. Les substrats de verre nettoyés ont été séchés à l'aide d'un pistolet à azote.

* **Premier dépôt:** En raison de la faible adhérence de l'or évaporé thermiquement sur des substrats de verre, une couche d'adhérence entre le substrat et le film d'or est nécessaire. Certains utilisent des agents chimiques pour introduire des groupes actifs sur le substrat de verre, de manière à favoriser l'adhésion entre le film d'or et le substrat de verre. Une autre possibilité consiste à évaporer une fine couche de Cr, Ti ou TiO_x avant l'évaporation de l'or. Pour nos échantillons, nous avons évaporé 3 nm de Cr en tant que couche d'adhésion. Il existe deux types d'évaporation: l'évaporation thermique et l'évaporation par faisceau d'électrons, selon que le matériau cible soit chauffé par chauffage ohmique depuis un creuset ou par bombardement électronique d'un creuset. Dans nos expériences, le dépôt a été réalisé à l'aide de l'évaporateur PLASSYS MEB400. Dans cet évaporateur, il y a deux creusets pour l'évaporation thermique et six creusets pour l'évaporation par faisceau d'électrons avec contrôle automatique pour sélectionner le matériau de ciblage actif sans ouvrir la chambre d'évaporation. Habituellement, les métaux nobles sont évaporés par évaporation thermique, les matériaux diélectriques et les métaux à température de fusion élevée sont évaporés avec évaporation par faisceau d'électrons.

  La chambre d'évaporation a été pompée jusqu'à ce que la pression à l'intérieur de la chambre à vide soit de $\sim 4 \times 10^{-6}$ Torr . On a ensuite fait évaporer la couche de Cr à 3 nm par évaporation par faisceau électronique à une vitesse de 0,3 nm/s, puis par évaporation thermique du film de Au à 50 nm à une vitesse d'évaporation de 0,3 nm/s, puis par des couches isolantes prises en sandwich dans des cavités MIM. Les couches isolantes ont été obtenues en faisant évaporer 10 nm de SiO_2 en utilisant une évaporation par faisceau d'électrons à une vitesse de 0,03 nm/s.

* **Revêtement de spin:** Le polyméthacrylate de méthyle (PMMA) est le vernis EBL le plus couramment utilisé. La recette présentée ici est conçue pour obtenir une couche de PMMA d'une épaisseur d'environ 160 nm. 2.5 % PMMA dans MIBK (méthylisobutyle cétone) a été utilisée. Afin d'obtenir des couches minces de PMMA de haute qualité sur le substrat, un procédé de revêtement par centrifugation en deux étapes a été appliqué. Une faible vitesse de rotation de 2600 rps/min a été appliquée pendant 6 s pour étaler la résine sur tout le substrat et obtenir approximativement l'épaisseur de film conçue, puis une vitesse de rota-

tion élevée de 5000 rps/min pendant 60 s a été utilisée pour retirer les bourrelets d'angle et obtenir une couche de PMMA avec l'épaisseur désirée. Après le spin-coating de PMMA, les substrats sont postcuits à l'intérieur d' un four à 150 ° C pour évaporer le solvant restant et pour améliorer l'adhérence du PMMA sur le substrat.

* **Lithographie par faisceau d'électrons:** Les motifs à disques circulaires sont conçus avec des rayons différents et des distances d'espacement différentes. Au cours d'un processus EBL, un générateur de motifs et un dispositif de suppression de faisceau contrôlent les champs d'exposition et n'exposent que la zone structurée avec la dose d'exposition souhaitée. Il est essentiel de bien aligner le faisceau d'électrons avant de commencer l'exposition, afin d'obtenir les caractéristiques de structure souhaitées à l' échelle nanométrique. Lorsque le PMMA est soumis à une exposition aux électrons, les chaînes de PMMA se cassent et conduisent à une plus grande solubilité dans le MIBK. Après exposition au faisceau d'électrons, le substrat a ensuite été immergé dans un révélateur constitué de MIBK (méthylisobutyle cétone) / IPA (isopropanol) 1: 3, pendant 1 min 15 s, puis rincé à l'IPA et séché à l'aide d'un pistolet à azote. Les molécules de PMMA exposées se dissolvent dans le révélateur et sont éliminées par lavage. Par conséquent, l'étape de développement produira le motif conçu et un microscope à fond noir peut être utilisé pour vérifier facilement si la lithographie par faisceau d'électrons a été un succès en raison de l'effet de réseau des trous ordonnés dans le PMMA.

* **Deuxième dépôt:** Une deuxième évaporation est nécessaire pour obtenir la deuxième couche métallique afin de former la cavité MIM. Ainsi dans cette étape, 50 nm d'or ont été déposés par évaporation thermique à la vitesse de 0,3 nm/s.

* **Lift-off:** Après le second dépôt, le substrat a été immergé dans de l'acétone pendant 1 h. L'acétone attaque le PMMA et dissout la couche de PMMA avec le temps. En conséquence, la superstrat comprenant du PMMA non exposé et de l'or déposé par la deuxième évaporation pourrait être évacué doucement du substrat avec une pipette. Le processus de décollement donne la structure plasmonique constituée de cavités MIM ordonnées.

Dans la figure B.5, outre le disque MIM (I) avec un espaceur de film, les étapes de fabrication du disque MIM (II) et du disque MIM (III) sont également présentées. Le disque MIM (II) peut être obtenu en déplaçant simplement l'évaporation de 10 nm de SiO$_2$ de la première évaporation (appelée étape (1)) à la deuxième évaporation (appelée étape (4)). MIM (III) peut être fabriqué par gravure humide MIM (II) avec de l' acide

fluorhydrique dilué (HF). Ces trois structures ont été étudiées plus tard pour leurs différentes réponses plasmoniques et leurs performances en pour des applications de spectroscopie et de détection assistées par plasmon.

La géométrie et la dimension de l'échantillon fabriqué sont cruciales pour l'analyse numérique des modes plasmoniques et fournissent également des indications pour la cellule de simulation dans Comsol. Cependant, la résolution du microscope optique est limitée par la limite de diffraction optique, des nanostructures à l'échelle de quelques dizaines de nanomètres dépassant les capacités d'imagerie d'un microscope optique classique. La microscopie électronique à balayage (SEM) est beaucoup plus sophistiquée et constitue la méthode appropriée pour étudier la forme et les dimensions géométriques des nanostructures.
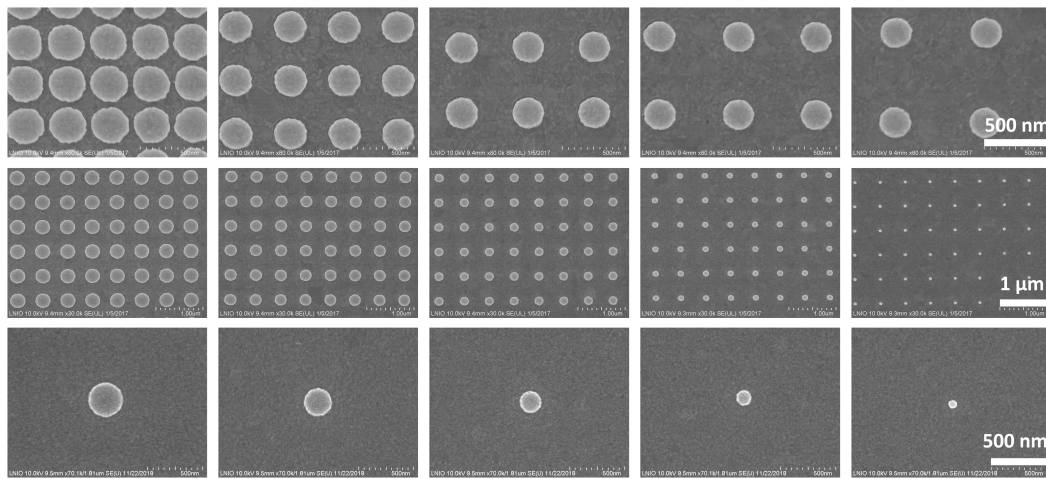
Figure B.6: Images SEM des cavités MIM du disque avec une entretoise de disque SiO_2. La première rangée présente des réseaux de cavités MIM ayant un rayon d'environ 260 nm et des périodes allant de 335 nm à 440 nm, 530 nm, 620 nm et 720 nm. La deuxième rangée présente des matrices de cavités MIM avec une période de 530 nm et leur rayon varie de 162 nm, 130 nm, 100 nm, 62 nm and 35 nm. Les cavités de monomère MIM avec des rayons de 169 nm, 132 nm, 103 nm, 70 nm, 35 nm sont représentées dans la troisième rangée. Les images de la même ligne partagent la même barre d'échelle que celle indiquée dans la dernière image de chaque ligne.

B.3   Géométrie des nanostructures

L'épaisseur de l'espaceur isolant pris en sandwich dans les cavités MIM était cruciale pour l'analyse numérique des réponses plasmoniques des structures MIM de la cavité, car le confinement du champ proche à l'intérieur de la cavité est associé à d^{-3}, où d est l'épaisseur de la couche isolante. L'ellipsométrie a également été utilisée pour

déterminer l'épaisseur de la couche d'espacement en film SiO$_2$. Cependant, les structures de cavité MIM sont trop compliquées avec trop de variables à déterminer: les épaisseurs du film d'or et de la couche de SiO$_2$, les constantes optiques de l'or évaporé et du SiO$_2$. D'autre part, une section transversale obtenue par usinage par faisceau d'ions focalisé constitue un moyen simple de vérifier l'épaisseur de la couche diélectrique mince, et les autres informations géométriques telles que l'angle d'inclinaison des parois latérales et les courbures des bords arrondis du disque en or peuvent également être obtenus à partir de la section transversale.

Un microscope à ions d'hélium (HIM) a été notre premier choix pour obtenir des sections transversales des cavités MIM en raison de sa résolution élevée, ce qui nous permet de découper chaque cavité MIM sélectionnée. Cependant, sans superstrat sacrificiel, la redéposition de l'or broyé entraîne une forte déformation de la structure usinée. Donc, dans cette thèse, nous avons finalement utilisé un microscope ionique de gallium focalisé (GIM) pour accomplir la section, même si la résolution ($\sim$ 50 nm) est beaucoup plus faible par rapport au HIM.
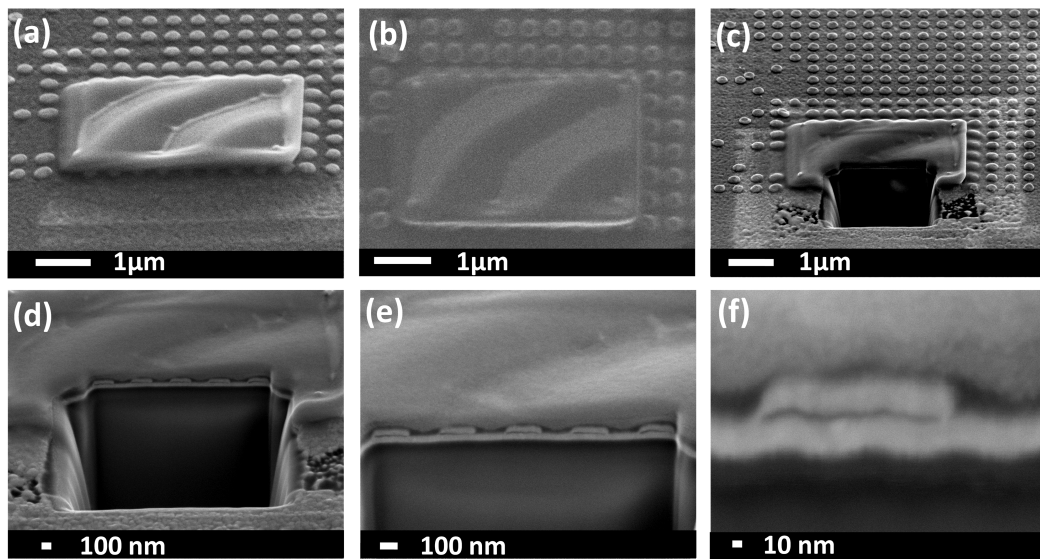
Figure B.7: Images SEM (a), (c-f) à un angle d'inclinaison de 52 ° et image FIB (b) de la vue de dessus du MIM des cavités après chaque étape afin de réaliser une section transversale par GIM. (a) $\sim$ 300 nm de platine sont déposées par faisceau d'électrons induite par un dépôt (BIDC) à une superficie de 4 µm × 4µm. (b) ont été déposés $\sim$ 800 nm de platine par FIB (-de faisceau d'ions) le dépôt induit dans le même secteur que dans (a). (c) Une coupe préliminaire de la coupe transversale de 3 µm × 2µm a été réalisée au bord de certaines cavités MIM. (d) Des coupes transversales avec des marches fines ont été réalisées afin d'obtenir une coupe transversale au centre des cavités MIM. (e) Une série de polis fins de la section transversale ont été réalisés afin d'obtenir une section transversale propre. (f) Une image en coupe transversale agrandie d'une cavité MIM. (Remerciement à Dr. Ronny Löffler pour son aimable collaboration)

La figure B.7 montre les images SEM du même réseau de cavités MIM après chaque

étape. Pour obtenir une coupe franche, les structures ont d'abord été recouvertes d'une couche sacrificielle de platine, puis découpées avec un faisceau d'ions gallium focalisé. Le dépôt de la couche de platine est crucial pour deux raisons: éliminer la déformation des structures MIM résultant de la redéposition et compenser la faible résolution de coupe pour obtenir une image en coupe nette au niveau de la région des cavités MIM. La figure B.7 (a), (c-f) a été obtenue par imagerie par faisceau d'électrons à un angle d'inclinaison de 52°, et la figure B.7 (b) a été obtenue avec une imagerie FIB de haut. De la vapeur de (méthylcyclopentadiényl) triméthyl platine a été introduite en tant que gaz précurseur pour déposer la couche de platine. Le dépôt induit par le FIB est beaucoup plus efficace que le dépôt induit par faisceau d'électrons (EBID) en raison de l'énergie beaucoup plus élevée du faisceau d'ions gallium. Toutefois, le faisceau d'ions risque de détruire les cavités en or du MIM lors du dépôt de platine. Nous avons donc appliqué la technique EBID pour réaliser tout d'abord une couche de platine de ~ 300 nm, comme le montre la figure B.7(a), pour protéger les cavités de MIM faisceau d'ions. Ensuite, le dépôt induit par FIB a été effectuée pour obtenir efficacement une couche de platine d' épaisseur de ~ 800 nm, comme dans la figure B.7 (b). Dans la figure B.7 (c), une coupe transversale préliminaire a été réalisée parallèlement aux bords des cavités MIM à une certaine rangée du réseau. Les cavités MIM situées en dehors de la couche de platine peuvent servir de référence. Cette opération est suivie d'une série de coupes transversales avec de petits pas pour se rapprocher du centre des cavités MIM sélectionnées, comme illustré à la figure B.7 (d). Dans la figure B.7 (e), les structures ont été inclinées de - 2 ° par rapport au faisceau d'ions focalisé, une série de polissages très fins de la section transversale ont été réalisés afin de nettoyer la croix section et se débarrasser des contaminants de la redéposition. La figure B.7 (f) montre une image agrandie d'une cavité MIM. La section transversale du film d'or, des disques et de l'espaceur est clairement visible dans la figure B.7(e-f). Les images en coupe obtenues par découpe FIB nous donneront des indications pour la conception de la cellule de simulation, afin d'avoir une meilleure correspondance entre la structure expérimentale et simulée.

B.4   Méthodes de simulation

Les structures plasmoniques couplées donnent des réponses plasmoniques très compliquées. Pour comprendre la physique qui se cache derrière la capacité de détection et d'amélioration du champ proche, il est important de mieux comprendre la nature des modes. D'autre part, si les simulations sont en bon accord avec les expériences, nous pouvons également utiliser la simulation comme moyen plus efficace d'optimiser la géométrie des cavités MIM en fonction de différentes situations. Dans cette thèse, des

simulations ont été effectuées à l'aide de Comsol Multiphysics, basée sur la méthode des éléments finis (FEM). La FEM est l'un des solveurs EM les plus populaires et il convient à l'analyse de la performance et de la géométrie d'antennes à une échelle plus petite que la longueur d'onde. Des simulations ont été effectuées pour des structures MIM de différentes géométries afin d'étudier leurs influences sur la distribution du champ et la longueur d'onde de résonance des modes plasmoniques. La figure B.8(a)
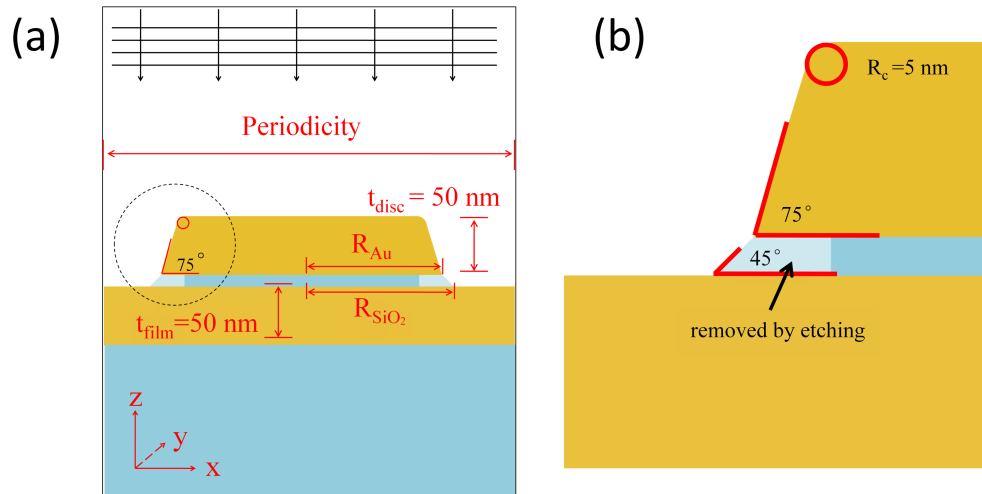

Figure B.8: Schéma de l'unité de simulation pour MIM(II) dans Comsol Multiphysics.

montre la cellule de simulation pour les matrices de MIM(II), pour un rayon de base du disque (R_{Au}) de 130 nm. Les paramètres géométriques ont été déterminés par les techniques de caractérisation afin d'avoir une bonne correspondance entre expériences et simulations. Dans ce chapitre, les méthodes et techniques utilisées dans cette thèse ont été présentées. Tout d'abord, les procédés de fabrication de différents systèmes MIM, allant du disque Au sur film aux cônes Au sur film, en passant par les dimères de disques optiques, ont été présentés. La technique EBL a été appliquée pour définir le motif, y compris le rayon du disque et les périodes, puis une méthode d'évaporation a été utilisée pour transférer le motif de la résistance aux structures MIM. Des écarts de distance de $\sim 10\ \mu$m peuvent facilement être réalisés avec des techniques d'évaporation bien établies avec une précision et une reproductibilité élevées. Différentes méthodes optiques ont été introduites pour étudier les propriétés plasmoniques des structures MIM fabriquées.

Les caractéristiques de champ lointain des modes plamoniques peuvent être étudiées par des méthodes d'extinction, de réflexion et de diffusion. Alors que ces méthodes de caractérisation en champ lointain peuvent montrer différentes caractéristiques des résonances plasmoniques en raison de différentes configurations d'excitation et de mesure, ces méthodes combinées permettent donc une étude plus systématique des modes plasmoniques dans les cavités MIM. La spectroscopie Raman est un outil d'analyse puissant

basé sur la caractéristique de champ proche des résonances plasmoniques. Grâce aux mesures en Raman, l'intensité du champ proche en fonction de MIM rayon de la cavité, différentes géométries d'isolant peuvent être démontrées sans SNOM.

B.5   Mode plasmon dans la cavité

Les modes plasmoniques des cavités MIM seront l'objet principal de l'étude. Les modes plasmoniques de la cavité dans les matrices de cavités MIM seront étudiés par différentes mesures optiques. Les résultats de la simulation FEM avec Comsol Multiphysics seront présentés afin de comprendre la physique fondamentale de ce système couplé et de fournir des directions pour la conception d'échantillons optimaux en fonction de différentes situations d'application. Pour simplifier, les modes plasmoniques de la cavité ont été étudiés dans un système à disque MIM (I) où les modes plasmoniques de la cavité se répartissent dans un isolant homogène (SiO_2 film continu), sauf indication contraire. Les modes plasmoniques de la cavité proviennent de l'interférence de SPP contre-propagatifs, qui sont réfléchis aux bords des cavités plasmoniques. La
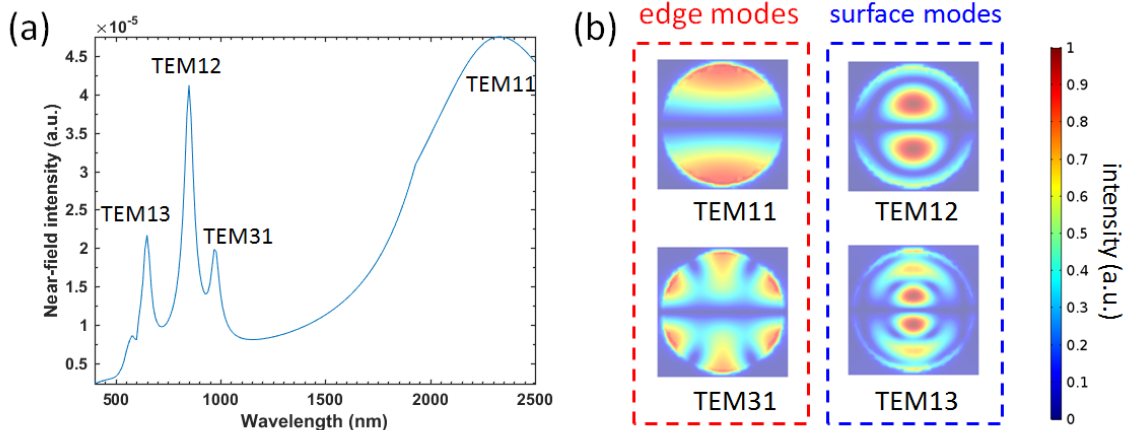
Figure B.9: (a) Spectres de résonance de champ proche simulés pour une structure MIM (I) avec un rayon de cavité de R_{Au}=160 nm, une hauteur de cavité de t_{SiO_2}=10 nm, une périodicité de P=350 nm. L'intensité du champ proche est intégrée à la surface inférieure du disque Au. Les modes plasmoniques de la cavité sont marqués dans les spectres, et les cartes de champ correspondantes aux longueurs d'onde de résonance sont représentées dans le panneau de droite (b). Deux ensembles de modes plasmoniques à cavité sont distingués: les modes bord et les modes surface.

figure B.9 montre le spectre de résonance en champ proche qui a été obtenu par simulation Comsol pour une structure de disque MIM (I) avec un rayon de cavité de R $_{Au}$ = 160 nm, une hauteur de cavité de t $_{SiO_2}$ = 10 nm, une périodicité de P = 350 nm. Le champ proche était intégré au bas des disques d'or. Les cartes de champ proche

à chaque longueur d'onde de résonance sont affichées dans le panneau de droite de la figure B.9. Les cartes de champ montrent des caractéristiques d'ondes stationnaires très claires et ressemblent à leurs homologues dans une cavité diélectrique Fabry-Pérot (FP). Dans la figure B.9 (a), deux ensembles de modes sont excités. D'une part, il existe des modes TEM_{m1} avec des lobes modaux le long des circonférences de la cavité circulaire, tels que les modes TEM11 et TEM31 comme dans la figure B.9 (b), appelés modes de bord de cavité. Par ailleurs, il existe les modes TEM_{1n} appelés modes cavité de surface, notamment les modes TEM12 et TEM13. Ces modes de cavité de surface possèdent des lobes modaux le long du diamètre de la cavité, la plus grande partie de l'énergie de champ proche résidant dans les lobes modaux centraux plutôt que dans les lobes périphériques. La condition de résonance des modes plasmons dans une cavité circulaire FP peut être décrite comme $k_{gsp}(R_{Au} + \Delta R) = \chi'_{mn}$, où k_{gsp} est le nombre d'ondes des modes de plasmons, ΔR est induit par le déphasage lors de la réflexion, $R_{Au} + \Delta R$ représente le rayon de résonance, χ'_{mn} est la racine n-ième de la première dérivée de la fonction de Bessel d'ordre m J'_m. Le mode TEMmn représente les modes plasmoniques de la cavité avec m nombre de maxima le long de la circonférence et n nombre de maxima le long du diamètre, respectivement.
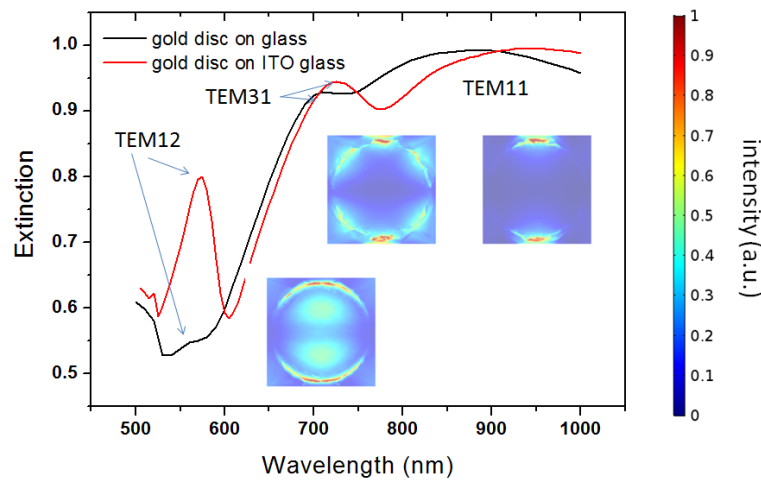
Figure B.10: Simulées spectres d'extinction de groupes de disques d'or avec un rayon de 160 nm sur de l'oxyde d'indium étain (ITO) (courbe rouge) et le substrat en verre standard (courbe noire). Le verre ITO est recouvert de 50 nm de film ITO. P=350 nm. Les cartes de champ proche sont affichées à côté de chaque résonance plasmonique.

La figure B.10 montre les spectres d'extinction d'un réseau de disques d'or avec un rayon de 160 nm et une périodicité de 350 nm sur substrat de verre (courbe noire) et du substrat en ITO (courbe rouge). L'épaisseur d'ITO est de 50 nm. Trois modes plasmoniques peuvent être identifiés par les maxima d'extinction: TEM11, TEM31 et TEM12. Les cartes de champ proche pour chaque résonance plasmonique sont

présentées sous chaque pic d'extinction, montrant les caractéristiques de l'onde stationnaire et un modèle modal similaire à ceux de la figure B.9. Pour un disque d'or de rayon 160 nm, la taille du disque est comparable à la longueur d'onde des modes SPP se propageant sur l'interface Au/SiO$_2$. Ainsi, une séquence d'ordres différents de modes stationnaires apparaît dans les spectres visible / IR proche, comme dans la figure B.9. La matrice de disques d'or sur un substrat de verre normal (courbe noire) présente le même profil que celle de l'ITO, mais avec des modes d'ordres supérieurs moins prononcés et des longueurs d'onde de résonance plus courtes en raison d'un indice de réfraction plus faible. Nos cartes de champ du mode TEMmn dans des matrices de disques d'or sont conformes aux cartes de champ obtenues en étudiant de grands nanodisques d'argent avec spectroscopie de perte d'énergie électronique (EELS) [162].

Nous concluons que une disque d' or fonctionne aussi en résonateur FP 2D circulaire comme une MIM cavité. Il existe deux raisons principales pour lesquelles les modes plasmoniques de la cavité dans les structures à disque d'or et les cavités MIM présentent des propriétés différentes. La plus importante est due à différents mécanismes d'amortissement plasmoniques. La forte atténuation des radiations des modes plasmoniques sur les structures de disque en or conduit à un élargissement des raies des modes. Pour les petits disques en or, seul le mode fondamental TEM11 apparaît dans la plage étudiée. Pour les gros disques d'or, les modes plasmoniques d'ordre supérieur sont excités. Cependant, en raison de la large largeur de raie de chaque mode plasmonique, leurs spectres de champ lointain se chevauchent, ce qui les rend difficiles à distinguer. En conséquence, aucun mode plasmonique distinct ne peut être identifié dans un spectre optique en champ lointain, comme le montre la figure B.10. Au contraire, les plasmons de surface gap dans les cavités MIM sont des plasmons lents avec un indice de réfraction effectif plus grand et ont une durée de vie beaucoup plus longue (la plus grande partie de l'énergie est confinée dans la cavité plutôt que de s'atténuer). Par conséquent, dans les cavités MIM, l'amortissement plasmonique provient principalement de désexitations non radiatives, ce qui conduit à une résonance avec une largeur de ligne étroite.. En conséquence, les modes plasmoniques de la cavité se présentent sous la forme de raie distinctes à bande passante étroite dans les spectres de champ lointain. La différence dans l'origine de l'amortissement conduit à une largeur de bande différente de chaque mode plasmonique dans le champ lointain. C'est la raison pour laquelle les modes TEMmn montrent toujours des creux de réflexion et des pics d'extinction bien définis dans le cas de la cavité MIM avec un grand R$_{Au}$, alors qu'aucun pic prononcé ne peut être identifié pour un grand disque d'or sur un substrat de verre.

La figure B.11(a) présente l'intensité de champ intégrée au fond du disque d'or dans le disque MIM (I) et les matrices de disques d'or pour les mêmes tailles et périodicités de disque. L'intensité de champ pour les modes TEM12 et TEM11 dans la cavité MIM
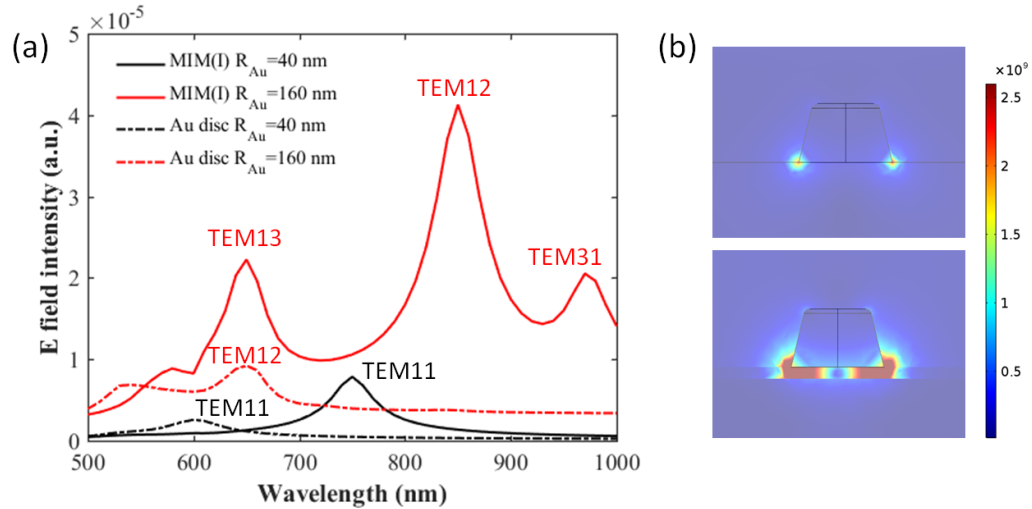
Figure B.11: (a) Forces du champ E simulé intégrée au fond du disque en or pour la cavité du disque MIM (I) (courbes pleines) et les matrices de disques en or (courbes en pointillés). La périodicité P=350 nm et la hauteur de la cavité t_{SiO_2}=10 nm. Le rayon du disque d'or R_{Au}=40 nm (courbes noires), R_{Au}=160 nm (courbes rouges). (B) Distribution du champ du mode de cavité TEM11 dans la section de cavité Mode TEM11 dans le disque d'or et la cavité MIM, R_{Au}=40 nm

(I) est 4,5 et 3 fois supérieure à celle du disque, lorsque R_{Au} = 160 nm et R_{Au} = 40 nm, respectivement. Dans la figure B.11(b), les cartes de champ en coupe transversale pour les modes de cavité TEM11 étaient représentées pour le disque en or et la cavité MIM. Dans le cas du disque en or, le mode LSPR est confiné sur environ dizaines de nanomètres. L'amélioration du confinement dans la direction perpendiculaire dans la cavité MIM est évidente car la distance entre les extrémmités du disque est beaucoup plus petite que la longueur de désintégration des plasmons de surface. Dans le sens radial, nous savons que le rayon de la cavité de résonance est égal à $R_{Au} + \Delta R$, comme le montre l'équation $k_{gsp}(R_{Au} + \Delta R) = \chi'_{mn}$, où ΔR est introduit par le déphasage lors de la réflexion au bord du disque. La profondeur de pénétration ΔR est analogue à la profondeur de pénétration au niveau des réflecteurs de Bragg dans un résonateur acoustique à fibre optique, où la profondeur de pénétration ΔR est proportionnelle à r^{-1} (r représente le reflet coefficacité) [165]. L'indice effectif plus élevé du mode TEMmn dans la cavité MIM, entraîne un coefficient de réfraction plus élevé dans le cas MIM, entraînant une réduction de la valeur de ΔR. Par conséquent, la cavité MIM offre également un meilleur confinement dans la direction radiale, par rapport aux disques en or, comme on peut le constater à la figure B.11(b).

Ainsi, dans les cavités MIM, l'étendue spatiale de l'énergie des plasmons est réduite perpendiculairement par les gaines en or et confinée radialement par les bords de la cavité circulaire hautement réfléchissants. L'énergie plasmonique est confinée à l'intérieur d'une cavité à très faible volume, jusqu'à $\lambda^3/1000$ dans une cavité MIM à disque, d'où

une intensité de champ plus élevée des modes TEMmn.

Lorsque la taille du disque est comparable à la longueur d'onde des polaritons plasmoniques (polaritons de plasmons de surface dans le disque d'or et plasmons de surface gap (PSG) dans la structure MIM), l'optique classique est toujours applicable dans ces cavités de PF. Cependant, la courte durée de vie des plasmons de surface dans l'interface métal unique/diélectrique conduit à une large largeur de raie de résonance dans les spectres de champ lointain. En conséquence, une séquence de différents ordres de modes de cavité n'a pas été repérée dans les expériences optiques. Les modes plasmoniques dans les grands disques métalliques sont toutefois distincts dans les spectres obtenus par EELS où la largeur de raie dépend principalement de l'amortissement non radiatif des plasmons de surface [162].

La présence d'un film d'or déplace les modes de cavité dans les échantillons de disque d'or vers une longueur d'onde plus longue. Plus important encore, l'amortissement des radiations au bord du disque de cavité est considérablement réduite en améliorant le coefficient de réflexion. Le facteur de qualité de la cavité FP circulaire est amélioré, et donc la durée de vie des modes TEMmn dans la cavité MIM est plus longue que dans le disque d'or. La durée de vie plus longue du PSG conduit à un faible amortissement du rayonnement et à une largeur de raie plus étroite du mode TEMmn dans les spectres en champ lointain. En conséquence, contrairement aux disques en or, les modes plasmoniques dans les cavités MIM peuvent être facilement distingués dans les spectres de champ lointain. Dans les cavités MIM, la lumière est confinée perpendiculairement dans le film diélectrique d'une épaisseur de quelques nanomètres sous la forme de polaritons de plasmon.

B.6   La dépendance sur la périodicité

Dans la figure B.12(a), des spectres de champ proche simulés intégrés au bas du disque dans le MIM(I) avec une périodicité différente P = 350 nm (courbe noire), P = 450 nm (courbe bleue), P = 550 nm (courbe verte), P = 650 nm (courbe rouge) sont présentés, respectivement. Hormis la périodicité, tous les autres paramètres sont fixes: $R_{Au} = $ 160 nm, $t_{SiO_2} = 10$ nm.

La position de résonance des modes plamoniques en fonction de la périodicité variable est présentée à la figure B.12(b). Le mode TEM11 dépend fortement des constantes de réseau et passe de 2330 nm à 2130 nm à 2090 nm, puis à 2080 nm pour P = 350 nm, 450 nm, 550 nm et 650 nm, respectivement. En revanche, les longueurs d'onde de résonance des modes de cavité TEM31, TEM12 et TEM13 ne sont guère modifiées
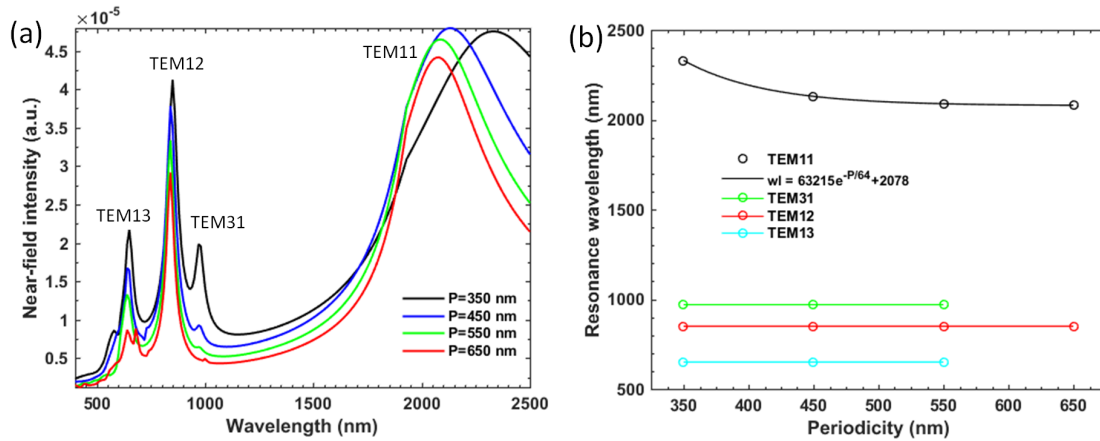
Figure B.12: (a) Spectres de résonance en champ proche simulés du disque MIM (I) avec R_{Au} = 160 nm et hauteur de la cavité t_{SiO_2} = 10 nm, et constantes de réseau variables de P = 350 nm (courbe noire), P = 450 nm (courbe bleue), P = 550 nm (courbe verte), P = 650 nm (courbe rouge); (b) Les longueurs d'onde de résonance de différents ordres de cavités en fonction de la périodicité.

par la périodicité variable apparaissant à 970 nm, 850 nm et 650 nm, respectivement. Le mode TEM11 est notamment influencé dans la petite plage de périodicité P = 350 nm. Cependant, comme le montre la courbe noire de la figure B.12(b), le mode TEM11 devient moins sensible à la variation de périodicité à mesure que la périodicité augmente, en raison du découplage des champs des modes TEM11 de disques voisins. Dans le cas des modes de cavité TEM31, TEM12 et TEM13, la longueur d'onde de PSG λ_{gsp} est plus courte que le mode TEM11. En outre, les indices de réfraction effectifs n_{gsp} sont supérieurs à TEM11, ce qui permet un meilleur confinement pour les modes TEMmn d'ordre supérieur. En conséquence, les champs proches de TEM31, TEM12 et TEM13 de deux cavités voisines sont découplés lorsque P $\geqslant$ 350 nm. Ceci explique pourquoi les modes de cavité d'ordre supérieur ne présentent aucune variation en fonction de la périodicité de la figure B.12(b). Nous pouvons en conclure qu'en général, les modes de cavité dans les cavités MIM sont très insensibles à la périodicité par rapport à ceux des matrices de disques d'or.

B.7   Comportement anti-croisement

Le comportement de séparation de Rabi a été largement étudié dans des nanosystèmes métalliques hybrides avec des points quantiques (QD), des colorants et des fluorophores, en mettant l'accent sur la modification de l'émission par couplage fort des émetteurs avec les modes plasmoniques. Un phénomène similaire se produit dans les cavités MIM consistant également en des matrices de disques d'or sur un système à film d'or. Le fort couplage entre les modes SPP et cavité entraîne des comportements d'anti-croisement

des modes plasmoniques, ce qui est la signature classique de la separation de Rabi.
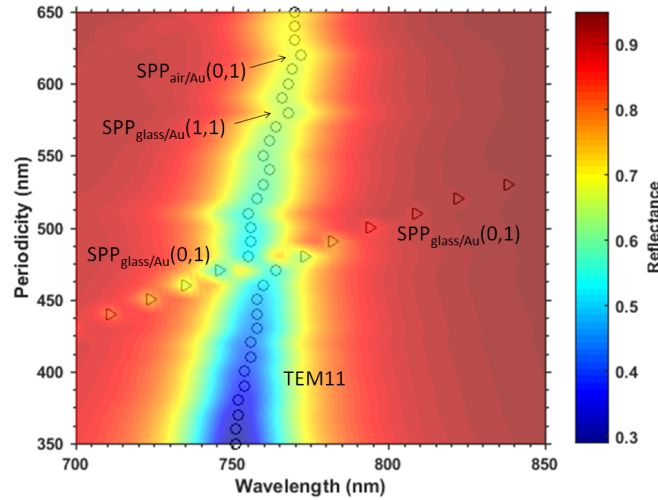

Figure B.13: Graphique du contour de la réflectance simulée en fonction de la périodicité et de la longueur d'onde pour les cavités MIM constituées de matrices de disques sur un film d'or. Les marqueurs circulaires et les marqueurs triangulaires indiquent la position de résonance du mode TEM11 et de SPP$_{verre/Au}$ (0,1), respectivement. Le rayon de la cavité R$_{Au}$ = 40 nm et la hauteur de la cavité t$_{SiO_2}$ = 10 nm.

La figure B.13 montre la variation simulée de la réflectance en fonction de la longueur d'onde et de la périodicité dans MIM(I) avec R$_{Au}$ = 40 nm, t$_{SiO_2}$ = 10 nm. Les positions de résonance de SPP$_{verre/Au}$(0,1) et du mode TEM11 se manifestent dans les spectres de réflexion par les minima d'intensité et sont désignées par des triangles et des cercles, respectivement. D'une part, le mode SPP dépend fortement de la périodicité: la longueur d'onde de résonance $\lambda_{verre/Au}$ (0,1) passe de 711 nm à 836 nm lorsque la périodicité varie de 440 nm à 530 nm. En revanche, le mode de cavité n'est guère influencé par la périodicité dans la plupart des cas. Cependant, à la périodicité P = 480 nm, le mode SPP$_{verre/Au}$ (0,1) ($\lambda_{verre/Au}$(0,1) = 762 nm initialement) et le mode TEM11 ($\sim$760 nm) coïncident. Un comportement d'anti-croisement peut être observé, impliquant un fort couplage entre les modes plasmoniques de la cavité et le mode SPP. Le couplage forme deux modes hybrides: l'un avec une longueur d'onde de résonance plus courte et l'autre avec une longueur d'onde de résonance plus longue que 760 nm. Les petites perturbations à la périodicité P = 620 nm sont dues à des modes SPP$_{air/Au}$(0,1).

Les spectres de réflexion simulés correspondants de la figure B.14(b) ont été obtenus avec une incidence normale de lumière collimatée et une ouverture numérique égale à 1. Un bon accord de la position de résonance des modes plasmoniques de la cavité peut être trouvé entre les expériences et les simulations pour différents R$_{Au}$. Sur la
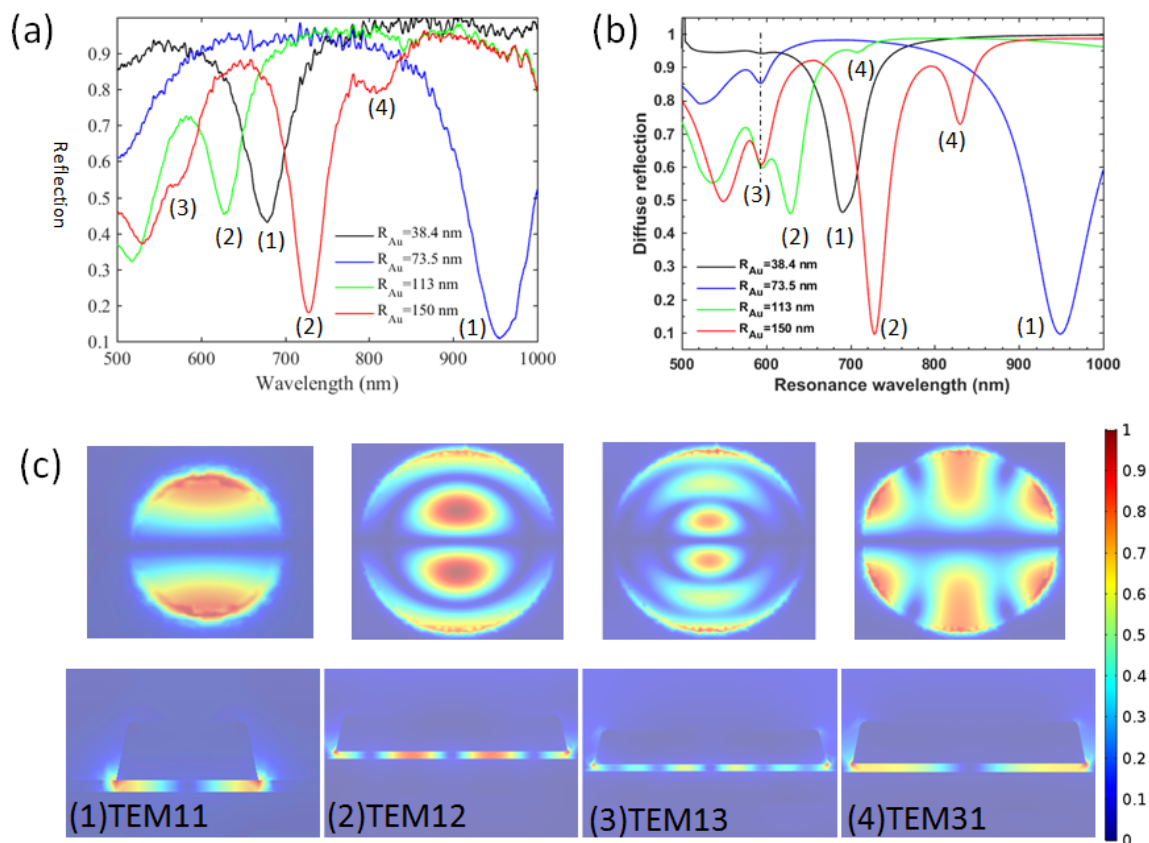
Figure B.14: Caractéristiques de résonance mesurées et simulées des modes plas-moniques dans les matrices de disques MIM. (a) Spectres de réflexion mesurés pour des matrices de disques avec la même périodicité de réseau P = 335 nm, hauteur de la cavité t_{SiO_2} = 12 nm et rayon de la cavité variable: 38 nm (courbe noire), 74 nm (courbe bleue), 113 nm (courbe verte) et 150 nm (courbe rouge); (b) spectres de réflexion simulés correspondant aux réseaux de cavités de disques de (a); (c) Cartes de terrain pour différents ordres de modes plasmoniques dans la cavité.

figure B.14(a), les modes TEM11, appelés mode (1), apparaissent à 670 nm et à 955 nm pour des nanocavités de rayons de 38 et 74 nm, respectivement. Les cartes de champ sont illustrées à la figure B.14 (c). Pour les plus grandes cavités, le mode TEM11 est décalé hors de la plage concernée. Un mode d'ordre supérieur, TEM12 qui est étiqueté comme mode (2), apparait pour les plus grandes cavités et passe de 630 nm à 728 nm lorsque le rayon augmente de 113 nm à 150 nm. En outre, pour les cavités de rayon 150 nm, deux autres modes d'ordre supérieur, les modes TEM31 et TEM13, apparaissent respectivement à 807 nm et à 570 nm, et sont désignés par les modes (4) et (3). En conclusion, la position de résonance d'un certain ordre de modes plasmoniques dans la cavité se déplace en fonction du rayon croissant, tandis que les modes plasmoniques dans la cavité d'ordre supérieur apparaissent dans la plage spectrale concernée.

B.8   Champ EM amélioré accessible
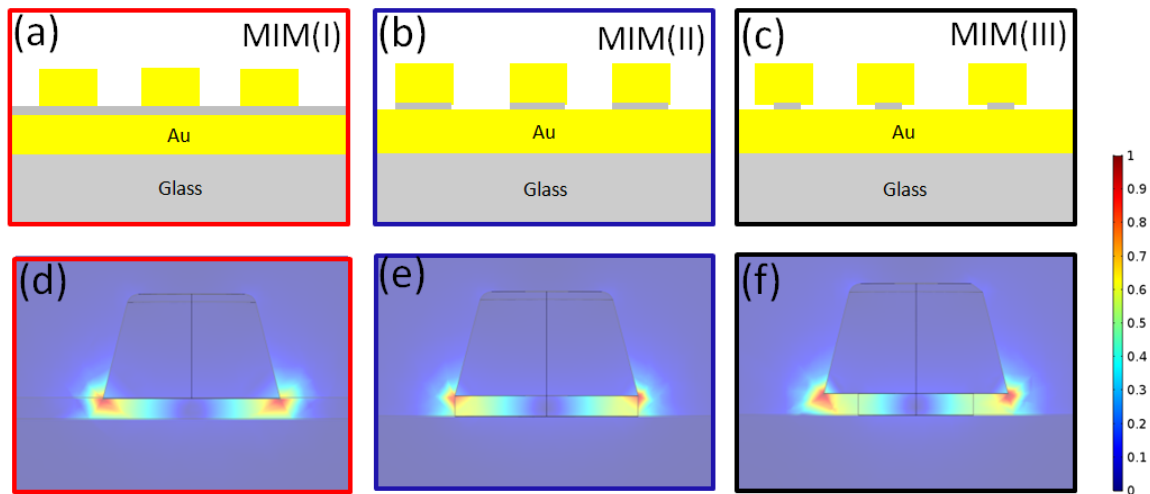
Figure B.15: Simulations de carte de champ pour différentes structures de cavité MIM.(a)-(c)schémas de structures MIM similaires avec des entretoises diamétrales différentes: le diamètre du disque en or est de 80 nm et le réseau constant de 350 nm. (a) intercalaire de film diélectrique; (b) un espaceur de disque diélectrique de rayon 40 nm; (c) espaceur diélectrique de diamètre 25 nm. (d) - (f) cartes de terrain des mêmes modes plasmoniques dans la cavité dans des simulations pour la configuration (a)-(c).

Dans la figure B.15, des cavités MIM avec un rayon de disque d'or de 40 nm et une constante de réseau de 350 nm ont été étudiées. La couche d'espacement varie d'un film de silice continu (a) à des espaceurs de disque de silice ayant le même diamètre $R_{SiO_2} = R_{Au} = 40nm$ (b) et plus petit que celui du disque d'or, $R_{SiO_2} = 25nm$ (c). La figure B.15(a)-(c) montre les schémas des trois différentes configurations de cavité MIM étudiées. Les cartes de champ correspondantes pour le mode de cavité fondamentale TEM11 pour chaque configuration sont illustrées sur la figure B.15(d)-(f).

Les distributions de champ de ce mode de cavité ne sont que légèrement modifiées lorsque la géométrie de l'espaceur est modifiée, tandis que les maxima de champ restent à leurs positions sous les bords du disque d'or. L'interprétation sera donnée dans la section suivante. Ici, il est important de noter que dans la configuration de cavité MIM(III), les 'points chauds' des modes de la cavité plasmonique sont exposés à l'environnement. Cela revêt une grande importance pour les amplifications des champs électromagnétiques où l'accessibilité à ces champs électromagnétiques fortement amplifiés est cruciale.

B.9 Décalage de résonance induit par sous-gravure

En conclusion, dans une cavité MIM ouverte, les distributions de champ des modes plasmoniques de la cavité sont insensibles au changement de la couche d'espacement. Les 'points chauds' des modes de la cavité plamonique peuvent être exposés à l'environnement en créant une dépression dans la cavité MIM. Alors que la distribution de champ ne
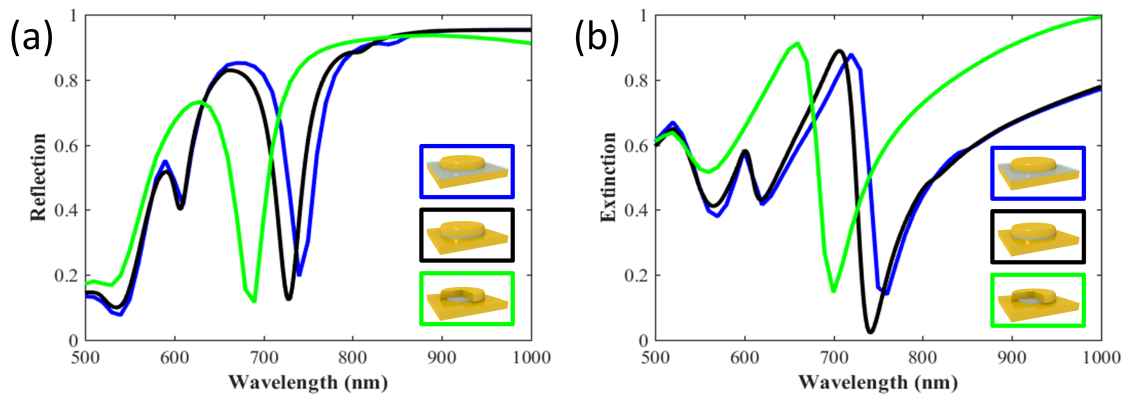
Figure B.16: Simulation des spectres de réflexion (a) et d'extinction (b) pour des cavités MIM avec différentes géométries d'espaceur isolant. Courbe bleue: SiO$_2$ film spacer (MIM (I)), courbe noire: SiO$_2$ disc spacer (MIM (II)), courbe verte: gravée SiO$_2$ disc spacer R$_{SiO_2}$ = R$_{Au}$/2 (MIM (III)). L'épaisseur de l'entretoise, le rayon du disque d'or et la constante du réseau sont respectivement de 10 nm, 130 nm et 350 nm.

présente qu'une perturbation mineure de la variation de taille de l'espaceur isolant, la position de la longueur d'onde de résonance de la cavité est nettement décalée du bleu de la configuration (a) à (c), comme le montre la figure B.16. Les spectres d'extinction des matrices de cavités MIM ont été enregistrés en prenant comme référence la transmission à travers un film d'or de 50 nm, avant et après que les matrices de structure MIM aient été gravées pendant 50 s. Une illumination collimatée a été utilisée et l'ouverture numérique de l'objectif de collecte est de 0,4.

La figure B.17 montre l'évolution des spectres d'extinction pour les cavités MIM de
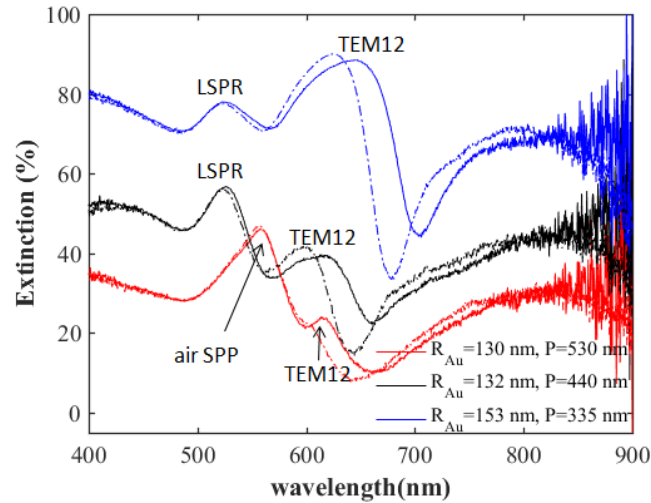
Figure B.17: Spectres d'extinction pour les réseaux de cavités MIM de diamètre environ 260 nm, avant (courbes pleines) et après (courbes en pointillés) l'étape de gravure humide, respectivement. Des réseaux de cavités MIM avec différentes constantes de réseau ont été étudiés: 335 nm (bleu), 440 nm (noir), 530 nm (rouge).

rayon environ 130 nm et de constantes de réseau variables, avant et après le processus de gravure. Les dimensions des cavités sont indiquées dans la légende avec R_{Au} et P indiquant le rayon et la période, respectivement. Le processus de gravure n'influence pas les positions de résonance des modes LSPR avec des 'points chauds' sur le bord supérieur des disques d'or (étudiés dans notre précédent ouvrage [91]), lorsque les constantes du réseau sont 335 nm et 440 nm. Dans le cas où la constante de réseau est de 530 nm, le mode montrant un pic d'extinction à 559 nm est un mode hybridé d'un mode LSPR et d'un mode SPP excité à l'interface *air/or*.De plus, ce mode hybride est également insensible au processus de gravure. Ceci peut être facilement compris par la condition de résonance du mode LSPR et du mode SPP. Les modes LSPR sont très sensibles au changement d'indice de réfraction à l'intérieur de ses 'points chauds', qui se situent à 50 nm environ de la variation de l'indice de réfraction dans l'isolant. D'autre part, les modes SPP induits par le réseau dépendent des constantes du réseau, de l'angle d'incidence et du changement de l'indice de réfraction à l'intérieur de leur champ proche. Par conséquent, les modes LSPR et SPP sont insensibles au changement d'indice de réfraction dans la couche isolante. En conséquence, ces modes restent à la même position avant et après la gravure, comme on peut le voir sur la figure B.17. Par ailleurs, les modes TEM12, comme indiqué dans la figure B.17, se décalent en bleu notamment après le processus de gravure, et correspondent bien aux simulations de la figure B.16. Les maxima d'extinction du mode TEM12 est passé de 647 nm à 626 nm, de 619 nm à 598 nm et de 616 nm à 600 nm, respectivement.

B.10 Détection de variation d'indice de réfraction

Dans cette section, nous présentons les résultats expérimentaux de détection du IR. Nous fabriquons des cavités MIM (II) de différents diamètres et périodes, et effectuons une détection IR en configuration d'immersion en masse. La solution IR standard est préparée avec une solution aqueuse de glycérine à différentes concentrations: 7%, 22% et 37%. L'indice de réfraction est ensuite confirmé par un réfractomètre: 1,34, 1,36 et 1,38 pour ces trois mélanges, respectivement. Les expériences de détection sont effectuées sur la base de mesures d'extinction et la configuration de mesure est illustrée à la figureB.18.
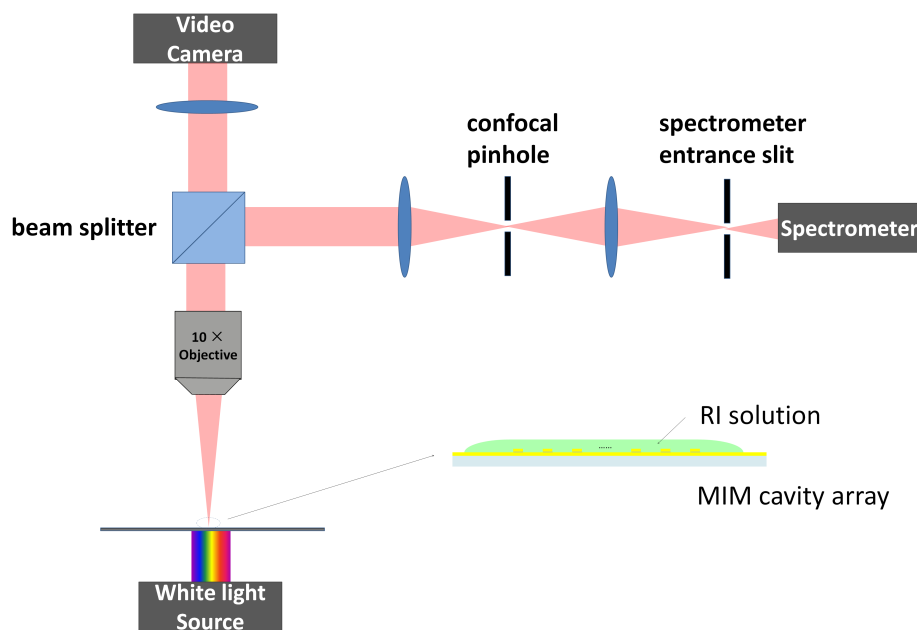
Figure B.18: La configuration de détection IR. La détection basée sur l'extinction est réalisée sur un microscope confocal. La source de lumière est illuminée à partir du bas des structures MIM verticales et la transmission est collectée selon un objectif de 10× avec un NA de 0,3. Le signal collecté est ensuite divisé en deux parties: une partie du signal passe dans la caméra pour une imagerie des structures et une partie du signal passe à travers un trou confocal et une fente d'entrée est insérée avant le spectromètre. La zone de détection est agrandie à mesure que l'image d'insertion, la matrice de cavités MIM est immergée par la solution de détection IR.

La configuration pour la détection IR basée sur l'extinction est illustrée à la figure B.18. La lumière incidente provient d'une lampe halogène, elle est éclairée par le bas de réseaux de cavités MIM verticales. La transmission à travers le substrat est ensuite collectée par un objectif de 10×. Un diviseur de faisceau divise ensuite la lumière transmise en deux parties, une partie étant envoyée vers une caméra pour la prise de vue en temps réel. L'autre partie traverse un trou confocal et une fente d'entrée du spectromètre pour éviter la lumière parasite avant qu'elle ne pénètre dans

le spectromètre. La zone de détection est montrée dans l'image d'insertion de la figure
B.18, le réseau de cavités MIM est immergé dans 20 μL de solution aqueuse de glycérine.
Nous avons enregistré la transmission à travers le substrat MIM pour 5 indices de
réfraction, dans l'ordre: n = 1 (air), n = 1,33 (eau), n = 1,34 (7% glycérine/eau), n
= 1,36 (22% glycérine/eau), n = 1,38 (37% glycérine/eau). Dans la figure B.19, les
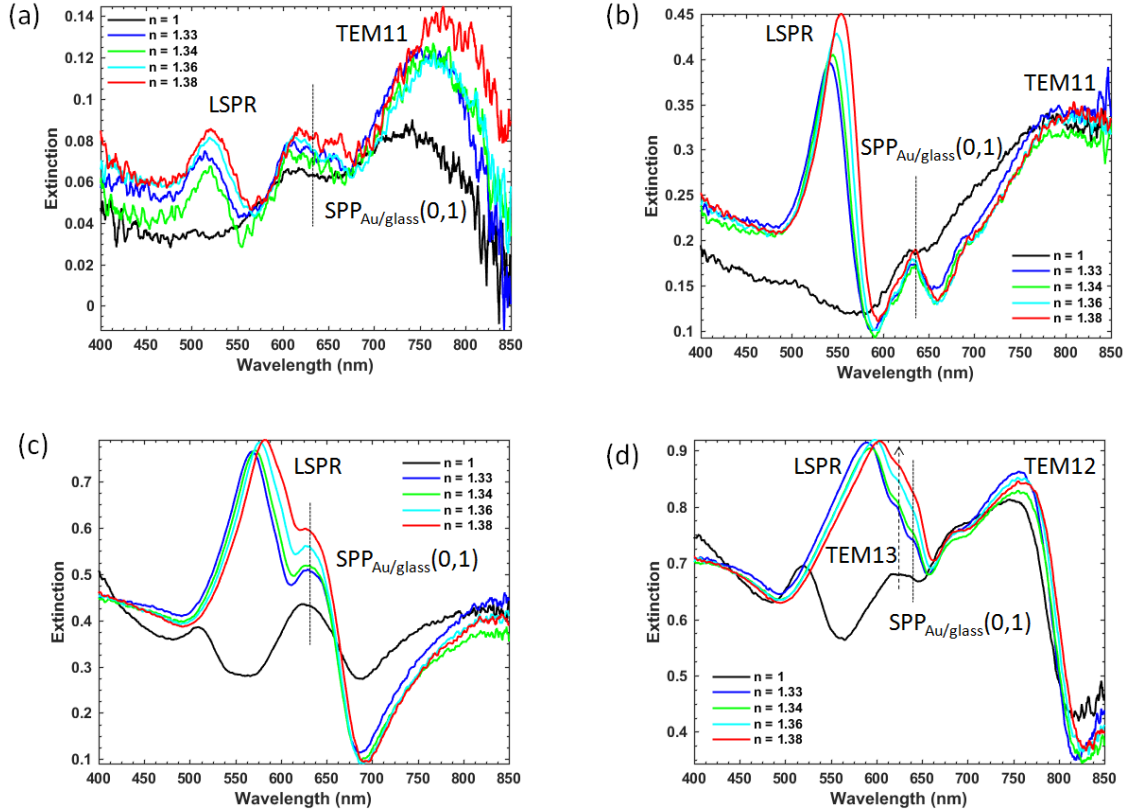
Figure B.19: Performances de détection du mode LSPR. Spectre d'extinction mesuré
à travers le réseau de cavités MIM (II) avec une périodicité P = 335 nm, (a) R_{Au} = 35
nm, (b) R_{Au} = 68 nm, (c) R_{Au} = 92 nm, (d) R_{Au} = 131 nm, pour différents indices
de réfraction d'immersion: 1 (courbe noire), 1,33 (courbe bleue), 1,34 (courbe verte),
1,36 (courbe cyan), 1,38 (courbe rouge). Les modes plasmoniques sont étiquetés en
conséquence.

spectres de détection de cavités MIM avec différents R_{Au}: (a) 35 nm, (b) 68 nm, (c)
92 nm et (d) 131 nm, en immersion dans différentes IR sont présentés. Les réseaux de
cavités ont la même hauteur de cavité que t_{SiO_2} = 12 nm et une périodicité de P = 335
nm. L'indice de réfraction varie de 1 à 1,38. Les modes plasmoniques sont étiquetés
en conséquence. L'efficacité d'extinction et la largeur de raie, ainsi que la sensibilité,
augmentent avec la taille du disque. La sensibilité augmente de 232 nm/RIU et 248
nm/RIU, 310 nm/RIU pour R_{Au} = 35 nm, 68 nm et 92 nm, respectivement. Ensuite,
la sensibilité diminue à 245 nm/RIU pour R_{Au} = 131 nm en raison du couplage avec
un mode insensible TEM13, comme le montre la figure B.19(d). Un FoM beaucoup
plus élevé (6,53) est obtenu à partir de MIM(II) par rapport à travaux réalisés au

laboratoire précédents avec MIM(I) (3,76).

B.11   Expériences SERS
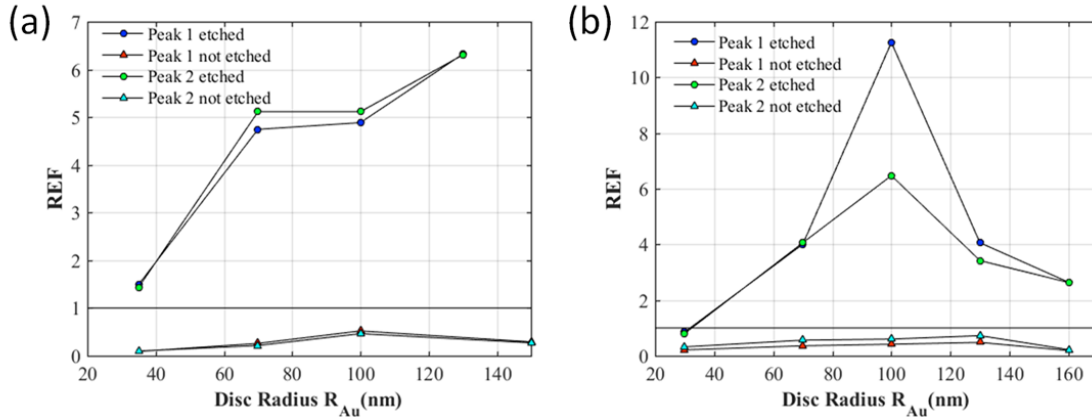
Figure B.20: Les facteurs relative d'amélioration des structures MIM en ce qui concerne le signal des films d'îles de 5 nm avant et après la gravure humide pour différents rayons de rayon Au disque et constantes de réseau (a) P = 335 nm et (b) P = 440 nm. les pics 1 et pics 2 représentent les bandes Raman à 1072 cm$_{-1}$ et 1587 cm$_{-1}$, respectivement

La figure B.20 présente les REF des structures MIM avant et après la gravure humide pour différents rayons et différentes constantes de réseau. Il est tout à fait clair que les structures MIM après gravure présentent une meilleure capacité SERS que les films d'îlots (Film d'or 5 nm) (REF>1, sauf R_{Au} <40 nm). Tandis que leurs homologues non gravés présentent un signal SERS plus faible que le film d'îlots, avec une REF inférieure à 1.

B.12   Conclusion

Nous avons étudié les performances des structures verticales métal-isolant-métal (MIM) en tant que capteurs d'indice de réfraction (RI) et substrats SERS. Les structures en disques sur films avec différents paramètres géométriques et différentes configurations d'espaceurs ont été étudiées de manière systématique par des expériences et des simulations. Les modèles circulaires de cavité FP (Fabry-Pérot) ont été appliqués pour décrire les modes de plasmon dans les cavités MIM. Les modes de plasmon de la cavité ont été divisés en modes de cavité de bord et modes de cavité de surface, ce qui montre différentes variations avec la gravure humide, les performances de détection RI et SERS. La dépendance des modes de plasmon de la cavité en fonction de la périodicité, du rayon de la cavité et de sa hauteur a été étudiée. L'origine des différentes raies

présentes dans les spectres optiques en champ lointain a été révélée. L'influence de différents espaceurs sur la localisation des 'points chauds' et des longueurs d'onde de résonance a été systématiquement étudiée. Les 'points chauds' des modes de plasmon dans la cavité ont été révélés par gravure humide. Les sensibilités RI des structures MIM ont été minutieusement étudiées. Des EF (facteur d'amélioration) SERS notables ont été atteints en sous-gravant. Des pics EF attribuables à différents ordres de modes de plasmon dans la cavité ont été observés à la fois dans les expériences et les simulations. Une comparaison de performance SERS a été faite entre le dimère de disque sur film et les dimères de disque verticaux.

Bibliography

[1] Stefan Alexander Maier. *Plasmonics: fundamentals and applications.* Springer Science & Business Media, 2007.

[2] Sergey V Gaponenko. *Introduction to nanophotonics.* Cambridge University Press, 2010.

[3] Heinz Raether. *Surface Plasmons on Smooth and Rough Surfaces and on Gratings*, volume 111. Springer, 2006.

[4] Eric Le Ru and Pablo Etchegoin. *Principles of Surface-Enhanced Raman Spectroscopy: and related plasmonic effects.* Elsevier, 2008.

[5] Jiří Homola. Surface plasmon resonance sensors for detection of chemical and biological species. *Chemical reviews*, 108(2):462–493, 2008.

[6] Jacqueline Jatschka, André Dathe, Andrea Csáki, Wolfgang Fritzsche, and Ondrej Stranik. Propagating and localized surface plasmon resonance sensing—a critical comparison based on measurements and theory. *Sensing and bio-sensing research*, 7:62–70, 2016.

[7] Prashant K Jain, Xiaohua Huang, Ivan H El-Sayed, and Mostafa A El-Sayed. Review of some interesting surface plasmon resonance-enhanced properties of noble metal nanoparticles and their applications to biosystems. *Plasmonics*, 2(3):107–118, 2007.

[8] Katherine A Willets and Richard P Van Duyne. Localized surface plasmon resonance spectroscopy and sensing. *Annu. Rev. Phys. Chem.*, 58:267–297, 2007.

[9] Ming Li, Scott K Cushing, and Nianqiang Wu. Plasmon-enhanced optical sensors: a review. *Analyst*, 140(2):386–406, 2015.

[10] Jiří Homola, Sinclair S Yee, and Günter Gauglitz. Surface plasmon resonance sensors. *Sensors and Actuators B: Chemical*, 54(1-2):3–15, 1999.

[11] Kathryn M Mayer and Jason H Hafner. Localized surface plasmon resonance sensors. *Chemical reviews*, 111(6):3828–3857, 2011.

[12] Bo Liedberg, Claes Nylander, and Ingemar Lunström. Surface plasmon resonance for gas detection and biosensing. *Sensors and actuators*, 4:299–304, 1983.

[13] http://www.reichertspr.com.

[14] https://www.gelifesciences.com/en/fr/shop/protein-analysis/spr-label-free-analysis/systems/biacore-8k-p 05540.

[15] Sookyoung Roh, Taerin Chung, and Byoungho Lee. Overview of the characteristics of micro-and nano-structured surface plasmon resonance sensors. *Sensors*, 11(2):1565–1588, 2011.

[16] B Sepúlveda, A Calle, Laura M Lechuga, and G Armelles. Highly sensitive detection of biomolecules with the magneto-optic surface-plasmon-resonance sensor. *Optics letters*, 31(8):1085–1087, 2006.

[17] Marek Piliarik, Hana Vaisocherová, and Jiří Homola. Towards parallelized surface plasmon resonance sensor platform for sensitive detection of oligonucleotides. *Sensors and Actuators B: Chemical*, 121(1):187–193, 2007.

[18] Henrik C Pedersen and Carsten Thirstrup. Design of near-field holographic optical elements by grating matching. *Applied optics*, 43(6):1209–1215, 2004.

[19] Garet G Nenninger, Marek Piliarik, and Jirí Homola. Data analysis for optical sensors based on spectroscopy of surface plasmons. *Measurement Science and Technology*, 13(12):2038, 2002.

[20] SY Wu, HP Ho, WC Law, Chinlon Lin, and SK Kong. Highly sensitive differential phase-sensitive surface plasmon resonance biosensor based on the Mach–Zehnder configuration. *Optics Letters*, 29(20):2378–2380, 2004.

[21] Gaige Zheng, Yunyun Chen, Linhua Xu, and Min Lai. Optical characteristics of subwavelength metallic grating coupled porous film surface plasmon resonance sensor with high sensitivity. *Optik-International Journal for Light and Electron Optics*, 124(21):4725–4728, 2013.

[22] Raman Kashyap and Galina Nemova. Surface plasmon resonance-based fiber and planar waveguide sensors. *Journal of Sensors*, 2009, 2009.

[23] Sookyoung Roh, Hwi Kim, and Byoungho Lee. A comparative analysis of surface plasmon resonance fiber sensor with symmetric and asymmetric metal coating

by three-dimensional ray-tracing. In *Photonic Fiber and Crystal Devices: Advances in Materials and Innovations in Device Applications IV*, volume 7781, page 778111. International Society for Optics and Photonics, 2010.

[24] Judith Langer, Sergey M Novikov, and Luis M Liz-Marzán. Sensing using plasmonic nanostructures and nanoparticles. *Nanotechnology*, 26(32):322001, 2015.

[25] K Lance Kelly, Eduardo Coronado, LinLin Zhao, and George C Schatz. The optical properties of metal nanoparticles: The influence of size, shape, and dielectric environment. *The Journal of Physical Chemistry B*, 107(3):668–677, 2003.

[26] Xiaoyu Zhang, Matthew A Young, Olga Lyandres, and Richard P Van Duyne. Rapid detection of an anthrax biomarker by surface-enhanced Raman spectroscopy. *Journal of the American Chemical Society*, 127(12):4484–4489, 2005.

[27] Taerin Chung, Seung-Yeol Lee, Eui Young Song, Honggu Chun, and Byoungho Lee. Plasmonic nanostructures for nano-scale bio-sensing. *Sensors*, 11(11):10907–10929, 2011.

[28] Jack J Mock, David R Smith, and Sheldon Schultz. Local refractive index dependence of plasmon resonance spectra from individual nanoparticles. *Nano letters*, 3(4):485–491, 2003.

[29] A Horrer, J Haas, K Freudenberger, G Gauglitz, DP Kern, and M Fleischer. Compact plasmonic optical biosensors based on nanostructured gradient index lenses integrated into microfluidic cells. *Nanoscale*, 9(44):17378–17386, 2017.

[30] Yongbin Lin, Yang Zou, Yuanyao Mo, Junpeng Guo, and Robert G Lindquist. E-beam patterned gold nanodot arrays on optical fiber tips for localized surface plasmon resonance biochemical sensing. *Sensors*, 10(10):9397–9406, 2010.

[31] Alexandre G Brolo, Reuven Gordon, Brian Leathem, and Karen L Kavanagh. Surface plasmon sensor based on the enhanced light transmission through arrays of nanoholes in gold films. *Langmuir*, 20(12):4813–4815, 2004.

[32] Peng Zheng, Scott K Cushing, Savan Suri, and Nianqiang Wu. Tailoring plasmonic properties of gold nanohole arrays for surface-enhanced Raman scattering. *Physical Chemistry Chemical Physics*, 17(33):21211–21219, 2015.

[33] Borja Sepúlveda, Paula C Angelomé, Laura M Lechuga, and Luis M Liz-Marzán. LSPR-based nanobiosensors. *nano today*, 4(3):244–251, 2009.

[34] Seung-Woo Lee, Kyeong-Seok Lee, Junhyoung Ahn, Jae-Jong Lee, Min-Gon Kim, and Yong-Beom Shin. Highly sensitive biosensing using arrays of plasmonic au nanodisks realized by nanoimprint lithography. *ACS nano*, 5(2):897–904, 2011.

[35] Sabine Szunerits and Rabah Boukherroub. Sensing using localised surface plasmon resonance sensors. *Chemical Communications*, 48(72):8999–9010, 2012.

[36] Kimani C Toussaint Jr, Brian J Roxworthy, Sarah Michaud, Hao Chen, Abdul M Bhuiya, and Qing Ding. Plasmonic nanoantennas: from nanotweezers to plasmonic photography. *Optics and Photonics News*, 26(6):24–31, 2015.

[37] Feifei Liu, Xinping Zhang, and Xiaohui Fang. Plasmonic plano-semi-cylindrical nanocavities with high-efficiency local-field confinement. *Scientific reports*, 7:40071, 2017.

[38] Na Liu, Ming L Tang, Mario Hentschel, Harald Giessen, and A Paul Alivisatos. Nanoantenna-enhanced gas sensing in a single tailored nanofocus. *Nature materials*, 10(8):631, 2011.

[39] Jianpeng Liu, Yaqi Ma, Jinhai Shao, Sichao Zhang, and Yifang Chen. Ultra-tall sub-wavelength gold nano pillars for high sensitive LSPR sensors. *Microelectronic Engineering*, 196:7–12, 2018.

[40] Guangyuan Si, Xiaoxiao Jiang, Jiangtao Lv, Qiongchan Gu, and Fengwen Wang. Fabrication and characterization of well-aligned plasmonic nanopillars with ultrasmall separations. *Nanoscale research letters*, 9(1):299, 2014.

[41] Federico Latorre, Stephan Kupfer, Thomas Bocklitz, Daniel Kinzel, Steffen Trautmann, Stefanie Gräfe, and Volker Deckert. Spatial resolution of tip-enhanced Raman spectroscopy–DFT assessment of the chemical effect. *Nanoscale*, 8(19):10229–10239, 2016.

[42] Yohan Lee, Sun-Je Kim, Hyeonsoo Park, and Byoungho Lee. Metamaterials and metasurfaces for sensor applications. *Sensors*, 17(8):1726, 2017.

[43] EC Le Ru, E Blackie, Matthias Meyer, and Pablo G Etchegoin. Surface enhanced Raman scattering enhancement factors: a comprehensive study. *The Journal of Physical Chemistry C*, 111(37):13794–13803, 2007.

[44] Geetha K Geen, K Durairaj, S Sreenath, and S Kumaran. Raman Fingerprints in Detection of Breast Cancer. *J of Biosens Biomark Diagn*, 1(1):1–11, 2016.

[45] Yuko S Yamamoto, Yukihiro Ozaki, and Tamitake Itoh. Recent progress and frontiers in the electromagnetic mechanism of surface-enhanced Raman scattering. *Journal of Photochemistry and Photobiology C: Photochemistry Reviews*, 21:81–104, 2014.

[46] Ricardo Aroca. *Surface-enhanced vibrational spectroscopy*. John Wiley & Sons, 2006.

[47] Martin Moskovits. Surface-enhanced spectroscopy. *Reviews of modern physics*, 57(3):783, 1985.

[48] Jon A Dieringer, Robert B Lettan, Karl A Scheidt, and Richard P Van Duyne. A frequency domain existence proof of single-molecule surface-enhanced Raman spectroscopy. *Journal of the American Chemical Society*, 129(51):16249–16256, 2007.

[49] Gang L Liu, Yu Lu, Jaeyoun Kim, Joseph C Doll, and Luke P Lee. Magnetic nanocrescents as controllable surface-enhanced Raman scattering nanoprobes for biomolecular imaging. *Advanced Materials*, 17(22):2683–2688, 2005.

[50] Paul L Stiles, Jon A Dieringer, Nilam C Shah, and Richard P Van Duyne. Surface-enhanced Raman spectroscopy. *Annu. Rev. Anal. Chem.*, 1:601–626, 2008.

[51] X-M Qian and SM Nie. Single-molecule and single-nanoparticle SERS: from fundamental mechanisms to biomedical applications. *Chemical Society Reviews*, 37(5):912–920, 2008.

[52] Dana Cialla, Anne März, René Böhme, Frank Theil, Karina Weber, Michael Schmitt, and Jürgen Popp. Surface-enhanced Raman spectroscopy (SERS): progress and trends. *Analytical and bioanalytical chemistry*, 403(1):27–54, 2012.

[53] Zhipeng Li and Hongxing Xu. Nanoantenna effect of surface-enhanced Raman scattering: managing light with plasmons at the nanometer scale. *Advances in Physics: X*, 1(3):492–521, 2016.

[54] Shahin Bagheri, Ksenia Weber, Timo Gissibl, Thomas Weiss, Frank Neubrech, and Harald Giessen. Fabrication of square-centimeter plasmonic nanoantenna arrays by femtosecond direct laser writing lithography: effects of collective excitations on SEIRA enhancement. *ACS Photonics*, 2(6):779–786, 2015.

[55] Frank Neubrech, Annemarie Pucci, Thomas Walter Cornelius, Shafqat Karim, Aitzol García-Etxarri, and Javier Aizpurua. Resonant plasmonic and vibrational coupling in a tailored nanoantenna for infrared detection. *Physical review letters*, 101(15):157403, 2008.

[56] Jungseok Chae, Basudev Lahiri, and Andrea Centrone. Engineering near-field SEIRA enhancements in plasmonic resonators. *Acs Photonics*, 3(1):87–95, 2015.

[57] Felicia Tam, Glenn P Goodrich, Bruce R Johnson, and Naomi J Halas. Plasmonic enhancement of molecular fluorescence. *Nano letters*, 7(2):496–501, 2007.

[58] Emmanuel Fort and Samuel Grésillon. Surface enhanced fluorescence. *Journal of Physics D: Applied Physics*, 41(1):013001, 2007.

[59] Weihua Zhang, Xudong Cui, Boon-Siang Yeo, Thomas Schmid, Christian Hafner, and Renato Zenobi. Nanoscale roughness on metal surfaces can increase tip-enhanced Raman scattering by an order of magnitude. *Nano letters*, 7(5):1401–1405, 2007.

[60] Jian Feng Li, Yi Fan Huang, Yong Ding, Zhi Lin Yang, Song Bo Li, Xiao Shun Zhou, Feng Ru Fan, Wei Zhang, Zhi You Zhou, Bin Ren, et al. Shell-isolated nanoparticle-enhanced Raman spectroscopy. *nature*, 464(7287):392, 2010.

[61] Dong-Kwon Lim, Ki-Seok Jeon, Hyung Min Kim, Jwa-Min Nam, and Yung Doug Suh. Nanogap-engineerable Raman-active nanodumbbells for single-molecule detection. *Nature materials*, 9(1):60, 2010.

[62] Dong-Kwon Lim, Ki-Seok Jeon, Jae-Ho Hwang, Hyoki Kim, Sunghoon Kwon, Yung Doug Suh, and Jwa-Min Nam. Highly uniform and reproducible surface-enhanced Raman scattering from DNA-tailorable nanoparticles with 1-nm interior gap. *Nature nanotechnology*, 6(7):452, 2011.

[63] Kristin L Wustholz, Christa L Brosseau, Francesca Casadio, and Richard P Van Duyne. Surface-enhanced Raman spectroscopy of dyes: from single molecules to the artists' canvas. *Physical Chemistry Chemical Physics*, 11(34):7350–7359, 2009.

[64] Katrin Kneipp, Yang Wang, Harald Kneipp, Lev T Perelman, Irving Itzkan, Ramachandra R Dasari, and Michael S Feld. Single molecule detection using surface-enhanced Raman scattering (SERS). *Physical review letters*, 78(9):1667, 1997.

[65] RP Van Duyne, JC Hulteen, and DA Treichel. Atomic force microscopy and surface-enhanced Raman spectroscopy. I. Ag island films and Ag film over polymer nanosphere surfaces supported on glass. *The Journal of chemical physics*, 99(3):2101–2115, 1993.

[66] P Corio, SDM Brown, A Marucci, MA Pimenta, K Kneipp, G Dresselhaus, and MS Dresselhaus. Surface-enhanced resonant Raman spectroscopy of single-wall carbon nanotubes adsorbed on silver and gold surfaces. *Physical Review B*, 61(19):13202, 2000.

[67] F Brouers, S Blacher, AN Lagarkov, Andrey K Sarychev, Patrice Gadenne, and Vladimir M Shalaev. Theory of giant Raman scattering from semicontinuous metal films. *Physical Review B*, 55(19):13234, 1997.

[68] F Brouers, S Blacher, and Andrey K Sarychev. Giant field fluctuations and anomalous light scattering from semicontinuous metal films. *Physical Review B*, 58(23):15897, 1998.

[69] Kadir Aslan, Zoya Leonenko, Joseph R Lakowicz, and Chris D Geddes. Annealed silver-island films for applications in metal-enhanced fluorescence: interpretation in terms of radiating plasmons. *Journal of fluorescence*, 15(5):643, 2005.

[70] Sudheer, Puspen Mondal, VN Rai, and AK Srivastava. A study of growth and thermal dewetting behavior of ultra-thin gold films using transmission electron microscopy. *AIP Advances*, 7(7):075303, 2017.

[71] David J Semin and Kathy L Rowlen. Influence of vapor deposition parameters on SERS active Ag film morphology and optical properties. *Analytical Chemistry*, 66(23):4324–4331, 1994.

[72] Prashant Nagpal, Nathan C Lindquist, Sang-Hyun Oh, and David J Norris. Ultrasmooth patterned metals for plasmonics and metamaterials. *Science*, 325(5940):594–597, 2009.

[73] Qiuming Yu, Phillip Guan, Dong Qin, Greg Golden, and Paul M Wallace. Inverted size-dependence of surface-enhanced Raman scattering on gold nanohole and nanodisk arrays. *Nano letters*, 8(7):1923–1928, 2008.

[74] Thomas H Reilly, Jordan D Corbman, and Kathy L Rowlen. Vapor deposition method for sensitivity studies on engineered surface-enhanced Raman scattering-active substrates. *Analytical chemistry*, 79(13):5078–5081, 2007.

[75] Alexandre G Brolo, Erin Arctander, Reuven Gordon, Brian Leathem, and Karen L Kavanagh. Nanohole-enhanced Raman scattering. *Nano Letters*, 4(10):2015–2018, 2004.

[76] Lisa A Dick, Adam D McFarland, Christy L Haynes, and Richard P Van Duyne. Metal film over nanosphere (MFON) electrodes for surface-enhanced Raman spectroscopy (SERS): Improvements in surface nanostructure stability and suppression of irreversible loss. *The Journal of Physical Chemistry B*, 106(4):853–860, 2002.

[77] Wen-Chi Lin, Lu-Shing Liao, Yi-Hui Chen, Hung-Chun Chang, Din Ping Tsai, and Hai-Pang Chiang. Size dependence of nanoparticle-SERS enhancement from silver film over nanosphere (AgFON) substrate. *Plasmonics*, 6(2):201–206, 2011.

[78] Dmitry N Chigrin, Christian Kremers, and Sergei V Zhukovsky. Plasmonic nanoparticle monomers and dimers: from nanoantennas to chiral metamaterials. *Applied Physics B*, 105(1):81, 2011.

[79] Renilkumar Mudachathi and Takuo Tanaka. Up scalable full colour plasmonic pixels with controllable hue, brightness and saturation. *Scientific Reports*, 7(1):1199, 2017.

[80] Jiaorong Fan, Zhongyuan Li, Zhuojie Chen, and Wengang Wu. Standing-wave resonances in plasmonic nanoumbrella cavities for color generation and colorimetric refractive index sensor. *Applied Surface Science*, 384:534–538, 2016.

[81] JR Fan, WG Wu, ZJ Chen, J Zhu, and J Li. Three-dimensional cavity nanoantennas with resonant-enhanced surface plasmons as dynamic color-tuning reflectors. *Nanoscale*, 9(10):3416–3423, 2017.

[82] Yu Liu, Wen Huang, Tianxun Gong, Yue Su, Hua Zhang, Yiwen He, Zhiwei Liu, and Bin Yu. Ultra-sensitive near-infrared graphene photodetectors with nanopillar antennas. *Nanoscale*, 9(44):17459–17464, 2017.

[83] Rehan Kapadia, Zhiyong Fan, Kuniharu Takei, and Ali Javey. Nanopillar photovoltaics: materials, processes, and devices. *Nano Energy*, 1(1):132–144, 2012.

[84] Bo Hua, Qingfeng Lin, Qianpeng Zhang, and Zhiyong Fan. Efficient photon management with nanostructures for photovoltaics. *Nanoscale*, 5(15):6627–6640, 2013.

[85] Yinghong Gu, Fei Qin, Joel KW Yang, Swee Ping Yeo, and Cheng-Wei Qiu. Direct excitation of dark plasmonic resonances under visible light at normal incidence. *Nanoscale*, 6(4):2106–2111, 2014.

[86] Kandammathe Valiyaveedu Sreekanth, Koduru Hari Krishna, Antonio De Luca, and Giuseppe Strangi. Large spontaneous emission rate enhancement in grating coupled hyperbolic metamaterials. *Scientific reports*, 4:6340, 2014.

[87] Johannes Srajer, Andreas Schwaighofer, Georg Ramer, Stefan Rotter, Bilal Guenay, Albert Kriegner, Wolfgang Knoll, Bernhard Lendl, and Christoph Nowak. Double-layered nanoparticle stacks for surface enhanced infrared absorption spectroscopy. *Nanoscale*, 6(1):127–131, 2014.

[88] Guozhen Li, Yang Shen, Guohui Xiao, and Chongjun Jin. Double-layered metal grating for high-performance refractive index sensing. *Optics express*, 23(7):8995–9003, 2015.

[89] Kandammathe Valiyaveedu Sreekanth, Koduru Hari Krishna, Antonio De Luca, and Giuseppe Strangi. Large spontaneous emission rate enhancement in grating coupled hyperbolic metamaterials. *Scientific reports*, 4:6340, 2014.

[90] Andreas Horrer, Katrin Krieg, Kathrin Freudenberger, Sabrina Rau, Lothar Leidner, Günter Gauglitz, Dieter P Kern, and Monika Fleischer. Plasmonic vertical dimer arrays as elements for biosensing. *Analytical and bioanalytical chemistry*, 407(27):8225–8231, 2015.

[91] Rana Nicolas, Gaëtan Lévêque, Joseph Marae-Djouda, Guillame Montay, Yazid Madi, Jérôme Plain, Ziad Herro, Michel Kazan, Pierre-Michel Adam, and Thomas Maurer. Plasmonic mode interferences and Fano resonances in metal-insulator-metal nanostructured interface. *Scientific reports*, 5:14419, 2015.

[92] Ahmad B Ayoub and Mohamed A Swillam. High performance optical systems using mim based plasmonic structures. *Journal of Physics Communications*, 1(3):035007, 2017.

[93] Manoj Manjare, Feng Wang, Sergio G Rodrigo, and Hayk Harutyunyan. Exposing optical near fields of plasmonic patch nanoantennas. *Applied Physics Letters*, 111(22):221106, 2017.

[94] Yizhuo Chu, Mohamad G Banaee, and Kenneth B Crozier. Double-resonance plasmon substrates for surface-enhanced Raman scattering with enhancement at excitation and stokes frequencies. *ACS nano*, 4(5):2804–2810, 2010.

[95] Yan-Qiang Cao, Kang Qin, Lin Zhu, Xu Qian, Xue-Jin Zhang, Di Wu, and Ai-Dong Li. Atomic-Layer-Deposition Assisted Formation of Wafer-Scale Double-Layer Metal Nanoparticles with Tunable Nanogap for Surface-Enhanced Raman Scattering. *Scientific Reports*, 7(1):5161, 2017.

[96] Markku Leskelä and Mikko Ritala. Atomic layer deposition chemistry: recent developments and future challenges. *Angewandte Chemie International Edition*, 42(45):5548–5554, 2003.

[97] Steven M George. Atomic layer deposition: an overview. *Chemical reviews*, 110(1):111–131, 2009.

[98] Yan Deng, Guangtao Cao, Hui Yang, Guanhai Li, Xiaoshuang Chen, and Wei Lu. Tunable and high-sensitivity sensing based on Fano resonance with coupled plasmonic cavities. *Scientific Reports*, 7(1):10639, 2017.

[99] Peter B Johnson and R-W Christy. Optical constants of the noble metals. *Physical review B*, 6(12):4370, 1972.

[100] Maxime Couture, Sandy Shuo Zhao, and Jean-Francois Masson. Modern surface plasmon resonance for bioanalytics and biophysics. *Physical Chemistry Chemical Physics*, 15(27):11190–11216, 2013.

[101] B Lamprecht, Gerburg Schider, RT Lechner, Harald Ditlbacher, Joachim R Krenn, Alfred Leitner, and Franz R Aussenegg. Metal nanoparticle gratings: influence of dipolar particle interaction on the plasmon resonance. *Physical review letters*, 84(20):4721, 2000.

[102] BS Simpkins, JP Long, OJ Glembocki, J Guo, JD Caldwell, and JC Owrutsky. Pitch-dependent resonances and near-field coupling in infrared nanoantenna arrays. *Optics express*, 20(25):27725–27739, 2012.

[103] Benjamin Gallinet and Olivier JF Martin. Relation between near–field and far–field properties of plasmonic Fano resonances. *Optics express*, 19(22):22167–22175, 2011.

[104] Richard Taubert, Ralf Ameling, Thomas Weiss, André Christ, and Harald Giessen. From near-field to far-field coupling in the third dimension: retarded interaction of particle plasmons. *Nano letters*, 11(10):4421–4424, 2011.

[105] Xiaoli Wang, Philippe Gogol, Edmond Cambril, and Bruno Palpant. Near-and far-field effects on the plasmon coupling in gold nanoparticle arrays. *The Journal of Physical Chemistry C*, 116(46):24741–24747, 2012.

[106] Nordin Félidj, Jean Aubard, Georges Lévi, Joachim R Krenn, Marco Salerno, Gerburg Schider, B Lamprecht, A Leitner, and FR Aussenegg. Controlling the optical response of regular arrays of gold particles for surface-enhanced Raman scattering. *Physical Review B*, 65(7):075419, 2002.

[107] M Meier, A Wokaun, and Paul F Liao. Enhanced fields on rough surfaces: dipolar interactions among particles of sizes exceeding the Rayleigh limit. *JOSA B*, 2(6):931–949, 1985.

[108] LinLin Zhao, K Lance Kelly, and George C Schatz. The extinction spectra of silver nanoparticle arrays: influence of array structure on plasmon resonance wavelength and width. *The Journal of Physical Chemistry B*, 107(30):7343–7350, 2003.

[109] Aziz Genç, Javier Patarroyo, Jordi Sancho-Parramon, Neus G Bastús, Victor Puntes, and Jordi Arbiol. Hollow metal nanostructures for enhanced plasmonics: synthesis, local plasmonic properties and applications. *Nanophotonics*, 6(1):193–213, 2017.

[110] Shangjr Gwo, Hung-Ying Chen, Meng-Hsien Lin, Liuyang Sun, and Xiaoqin Li. Nanomanipulation and controlled self-assembly of metal nanoparticles and nanocrystals for plasmonics. *Chemical Society Reviews*, 45(20):5672–5716, 2016.

[111] Viktor Myroshnychenko, Jessica Rodríguez-Fernández, Isabel Pastoriza-Santos, Alison M Funston, Carolina Novo, Paul Mulvaney, Luis M Liz-Marzan, and F Javier García de Abajo. Modelling the optical response of gold nanoparticles. *Chemical Society Reviews*, 37(9):1792–1805, 2008.

[112] Yumin Wang, Ziwei Li, Ke Zhao, Ali Sobhani, Xing Zhu, Zheyu Fang, and Naomi J Halas. Substrate-mediated charge transfer plasmons in simple and complex nanoparticle clusters. *Nanoscale*, 5(20):9897–9901, 2013.

[113] Srdjan S Acimovic, Mark P Kreuzer, María U González, and Romain Quidant. Plasmon near-field coupling in metal dimers as a step toward single-molecule sensing. *ACS nano*, 3(5):1231–1237, 2009.

[114] Nir Zohar, Lev Chuntonov, and Gilad Haran. The simplest plasmonic molecules: Metal nanoparticle dimers and trimers. *Journal of Photochemistry and Photobiology C: Photochemistry Reviews*, 21:26–39, 2014.

[115] Zhaosheng Hu, Tingli Ma, and Shuzi Hayase. Interparticle coupling effect of silver-gold heterodimer to enhance light harvesting in ultrathin perovskite solar cell. *Journal of Photonics for Energy*, 8(1):015502, 2018.

[116] Joachim R Krenn, Alain Dereux, Jean-Claude Weeber, E Bourillot, Y Lacroute, Jean-Pierre Goudonnet, Gerburg Schider, W Gotschy, Alfred Leitner, Franz R Aussenegg, et al. Squeezing the optical near-field zone by plasmon coupling of metallic nanoparticles. *Physical Review Letters*, 82(12):2590, 1999.

[117] B Prade, JY Vinet, and A Mysyrowicz. Guided optical waves in planar heterostructures with negative dielectric constant. *Physical Review B*, 44(24):13556, 1991.

[118] Dror Sarid. Long-range surface-plasma waves on very thin metal films. *Physical Review Letters*, 47(26):1927, 1981.

[119] Mohammad H Tahersima, M Danang Birowosuto, Zhizhen Ma, William C Coley, Michael D Valentin, Sahar Naghibi Alvillar, I-Hsi Lu, Yao Zhou, Ibrahim Sarpkaya, Aimee Martinez, et al. Testbeds for transition metal dichalcogenide photonics: Efficacy of light emission enhancement in monomer vs dimer nanoscale antennae. *ACS Photonics*, 4(7):1713–1721, 2017.

[120] Shih-Hui Gilbert Chang and Chia-Yi Sun. Avoided resonance crossing and non-reciprocal nearly perfect absorption in plasmonic nanodisks with near-field and far-field couplings. *Optics express*, 24(15):16822–16834, 2016.

[121] WD Heiss. Repulsion of resonance states and exceptional points. *Physical Review E*, 61(1):929, 2000.

[122] Yizhuo Chu and Kenneth B Crozier. Experimental study of the interaction between localized and propagating surface plasmons. *Optics letters*, 34(3):244–246, 2009.

[123] Binxing Yu, Jill I Tracey, Zhongkai Cheng, Martin Vacha, and Deirdre M O'Carroll. Plasmonic sphere-on-plane systems with semiconducting polymer spacer layers. *Physical Chemistry Chemical Physics*, 20(17):11749–11757, 2018.

[124] Felix Benz, Bart de Nijs, Christos Tserkezis, Rohit Chikkaraddy, Daniel O Sigle, Laurynas Pukenas, Stephen D Evans, Javier Aizpurua, and Jeremy J Baumberg. Generalized circuit model for coupled plasmonic systems. *Optics Express*, 23(26):33255–33269, 2015.

[125] Ghazal Hajisalem, Aftab Ahmed, Yuanjie Pang, and Reuven Gordon. Plasmon hybridization for enhanced nonlinear optical response. *Optics express*, 20(28):29923–29930, 2012.

[126] Alexandre Aubry, Dang Yuan Lei, Stefan A Maier, and John B Pendry. Plasmonic hybridization between nanowires and a metallic surface: a transformation optics approach. *ACS nano*, 5(4):3293–3308, 2011.

[127] Jack J Mock, Ryan T Hill, Aloyse Degiron, Stefan Zauscher, Ashutosh Chilkoti, and David R Smith. Distance-dependent plasmon resonant coupling between a gold nanoparticle and gold film. *Nano letters*, 8(8):2245–2252, 2008.

[128] Ming Xia, Pei Zhang, Kuan Qiao, Yu Bai, and Ya-Hong Xie. Coupling SPP with LSPR for enhanced field confinement: A simulation study. *The Journal of Physical Chemistry C*, 120(1):527–533, 2015.

[129] Pei Ding, Erjun Liang, Genwang Cai, Weiqin Hu, Chunzhen Fan, and Qianzhong Xue. Dual-band perfect absorption and field enhancement by interaction between localized and propagating surface plasmons in optical metamaterials. *Journal of Optics*, 13(7):075005, 2011.

[130] Robert Filter, Jing Qi, Carsten Rockstuhl, Falk Lederer, et al. Circular optical nanoantennas: an analytical theory. *Physical Review B*, 85(12):125429, 2012.

[131] Bhuwan P Joshi and Qi-Huo Wei. Cavity resonances of metal-dielectric-metal nanoantennas. *Optics Express*, 16(14):10315–10322, 2008.

[132] Feng Wang, Ayan Chakrabarty, Fred Minkowski, Kai Sun, and Qi-Huo Wei. Polarization conversion with elliptical patch nanoantennas. *Applied Physics Letters*, 101(2):023101, 2012.

[133] Fred Minkowski, Feng Wang, Ayan Chakrabarty, and Qi-Huo Wei. Resonant cavity modes of circular plasmonic patch nanoantennas. *Applied Physics Letters*, 104(2):021111, 2014.

[134] Ayan Chakrabarty, Feng Wang, Fred Minkowski, Kai Sun, and Qi-Huo Wei. Cavity modes and their excitations in elliptical plasmonic patch nanoantennas. *Optics express*, 20(11):11615–11624, 2012.

[135] Yinghong Gu, Lei Zhang, Joel KW Yang, Swee Ping Yeo, and Cheng-Wei Qiu. Color generation via subwavelength plasmonic nanostructures. *Nanoscale*, 7(15):6409–6419, 2015.

[136] Christina Manolatou and Farhan Rana. Subwavelength nanopatch cavities for semiconductor plasmon lasers. *IEEE Journal of quantum electronics*, 44(5):435–447, 2008.

[137] Kyoungsik Yu, Amit Lakhani, and Ming C Wu. Subwavelength metal-optic semiconductor nanopatch lasers. *Optics express*, 18(9):8790–8799, 2010.

[138] Michael G Nielsen, Anders Pors, Ole Albrektsen, and Sergey I Bozhevolnyi. Efficient absorption of visible radiation by gap plasmon resonators. *Optics express*, 20(12):13311–13319, 2012.

[139] Thomas Søndergaard, Jonas Beermann, Alexandra Boltasseva, and Sergey I Bozhevolnyi. Slow-plasmon resonant-nanostrip antennas: analysis and demonstration. *Physical Review B*, 77(11):115420, 2008.

[140] Thomas Søndergaard and Sergey Bozhevolnyi. Slow-plasmon resonant nanostructures: Scattering and field enhancements. *Physical Review B*, 75(7):073402, 2007.

[141] Rémi Faggiani. *Resonant nanophotonics: structural slow light and slow plasmons*. PhD thesis, Bordeaux, 2016.

[142] Jens Dorfmüller, Ralf Vogelgesang, R Thomas Weitz, Carsten Rockstuhl, Christoph Etrich, Thomas Pertsch, Falk Lederer, and Klaus Kern. Fabry-Pérot resonances in one-dimensional plasmonic nanostructures. *Nano letters*, 9(6):2372–2377, 2009.

[143] Tim H Taminiau, Fernando D Stefani, and Niek F van Hulst. Optical nanorod antennas modeled as cavities for dipolar emitters: evolution of sub-and superradiant modes. *Nano letters*, 11(3):1020–1024, 2011.

[144] Sergey I Bozhevolnyi and Thomas Søndergaard. General properties of slow-plasmon resonant nanostructures: nano-antennas and resonators. *Optics express*, 15(17):10869–10877, 2007.

[145] Gerburg Schider, Joachim R Krenn, Andreas Hohenau, Harald Ditlbacher, Alfred Leitner, Franz R Aussenegg, William L Schaich, Irina Puscasu, Brian Monacelli, and G Boreman. Plasmon dispersion relation of Au and Ag nanowires. *Physical Review B*, 68(15):155427, 2003.

[146] Eyal Feigenbaum and Meir Orenstein. Optical 3d cavity modes below the diffraction-limit using slow-wave surface-plasmon-polaritons. *Optics express*, 15(5):2607–2612, 2007.

[147] Guixin Li, Jensen Li, HL Tam, Che Ting Chan, and KW Cheah. Near field imaging with resonant cavity lens. *Optics Express*, 18(3):2325–2331, 2010.

[148] GX Li, HL Tam, FY Wang, and KW Cheah. Half-cylindrical far field superlens with coupled Fabry-Pérot cavities, 2008.

[149] Seymour B Cohn. Microwave bandpass filters containing high-Q dielectric resonators. *IEEE Transactions on Microwave Theory and Techniques*, 16(4):218–227, 1968.

[150] Aldo Petosa. *Dielectric resonator antenna handbook*. Artech House Publishers, 2007.

[151] Hideki T Miyazaki and Yoichi Kurokawa. Squeezing visible light waves into a 3-nm-thick and 55-nm-long plasmon cavity. *Physical review letters*, 96(9):097401, 2006.

[152] Michael G Nielsen, Dmitri K Gramotnev, Anders Pors, Ole Albrektsen, and Sergey I Bozhevolnyi. Continuous layer gap plasmon resonators. *Optics express*, 19(20):19310–19322, 2011.

[153] Benjamin Gallinet, Thomas Siegfried, Hans Sigg, Peter Nordlander, and Olivier JF Martin. Plasmonic radiance: probing structure at the Ångström scale with visible light. *Nano letters*, 13(2):497–503, 2013.

[154] Jorge Zuloaga and Peter Nordlander. On the energy shift between near-field and far-field peak intensities in localized plasmon systems. *Nano letters*, 11(3):1280–1283, 2011.

[155] Pablo Alonso-González, Pablo Albella, Frank Neubrech, Christian Huck, Jianing Chen, Federico Golmar, Félix Casanova, Luis E Hueso, Annemarie Pucci, Javier Aizpurua, et al. Experimental verification of the spectral shift between near-and far-field peak intensities of plasmonic infrared nanoantennas. *Physical review letters*, 110(20):203902, 2013.

[156] Shunping Zhang, Kui Bao, Naomi J Halas, Hongxing Xu, and Peter Nordlander. Substrate-induced Fano resonances of a plasmonic nanocube: a route to increased-sensitivity localized surface plasmon resonance sensors revealed. *Nano letters*, 11(4):1657–1663, 2011.

[157] Vivek R Shrestha, Sang-Shin Lee, Eun-Soo Kim, and Duk-Yong Choi. Aluminum plasmonics based highly transmissive polarization-independent subtractive color filters exploiting a nanopatch array. *Nano letters*, 14(11):6672–6678, 2014.

[158] AA Maradudin, Ingve Simonsen, J Polanco, and RM Fitzgerald. Rayleigh and Wood anomalies in the diffraction of light from a perfectly conducting reflection grating. *Journal of Optics*, 18(2):024004, 2016.

[159] Darko Kajfez and Pierre Guillon. *Dielectric resonators*. Norwood, MA, Artech House, Inc., 1986.

[160] Weng Cho Chew. Lectures on theory of microwave and optical waveguides. *University of Illinois Lecture*, 2012.

[161] EN Economou. Surface plasmons in thin films. *Physical review*, 182(2):539, 1969.

[162] Franz-Philipp Schmidt, Harald Ditlbacher, Ulrich Hohenester, Andreas Hohenau, Ferdinand Hofer, and Joachim R Krenn. Dark plasmonic breathing modes in silver nanodisks. *Nano letters*, 12(11):5780–5783, 2012.

[163] Yu Huang, Lingwei Ma, Mengjing Hou, Jianghao Li, Zheng Xie, and Zhengjun Zhang. Hybridized plasmon modes and near-field enhancement of metallic nanoparticle-dimer on a mirror. *Scientific reports*, 6:30011, 2016.

[164] J Seidel, FI Baida, L Bischoff, B Guizal, S Grafström, D Van Labeke, and LM Eng. Coupling between surface plasmon modes on metal films. *Physical Review B*, 69(12):121405, 2004.

[165] David Morgan. *Surface acoustic wave filters: With applications to electronic communications and signal processing.* Academic Press, 2010.

[166] K-H Su, Q-H Wei, X Zhang, JJ Mock, David R Smith, and S Schultz. Interparticle coupling effects on plasmon resonances of nanogold particles. *Nano letters*, 3(8):1087–1090, 2003.

[167] P Törmä and William L Barnes. Strong coupling between surface plasmon polaritons and emitters: a review. *Reports on Progress in Physics*, 78(1):013901, 2014.

[168] A Christ, SG Tikhodeev, NA Gippius, J Kuhl, and H Giessen. Waveguide-plasmon polaritons: strong coupling of photonic and electronic resonances in a metallic photonic crystal slab. *Physical review letters*, 91(18):183901, 2003.

[169] Ralf Ameling and Harald Giessen. Microcavity plasmonics: strong coupling of photonic cavities and plasmons. *Laser & Photonics Reviews*, 7(2):141–169, 2013.

[170] Zhiguang Liu, Jiafang Li, Zhe Liu, Wuxia Li, Junjie Li, Changzhi Gu, and Zhi-Yuan Li. Fano resonance Rabi splitting of surface plasmons. *Scientific reports*, 7(1):8010, 2017.

[171] Shumei Chen, Guixin Li, Dangyuan Lei, and Kok Wai Cheah. Efficient energy exchange between plasmon and cavity modes via Rabi-analogue splitting in a hybrid plasmonic nanocavity. *Nanoscale*, 5(19):9129–9133, 2013.

[172] DS Dovzhenko, SV Ryabchuk, Yu P Rakovich, and IR Nabiev. Light–matter interaction in the strong coupling regime: configurations, conditions, and applications. *Nanoscale*, 10(8):3589–3605, 2018.

[173] Gülis Zengin, Martin Wersäll, Sara Nilsson, Tomasz J Antosiewicz, Mikael Käll, and Timur Shegai. Realizing strong light-matter interactions between single-nanoparticle plasmons and molecular excitons at ambient conditions. *Physical Review Letters*, 114(15):157401, 2015.

[174] Lukas Novotny. Strong coupling, energy splitting, and level crossings: A classical perspective. *American Journal of Physics*, 78(11):1199–1202, 2010.

[175] Galina Khitrova, HM Gibbs, M Kira, Stephan W Koch, and Axel Scherer. Vacuum Rabi splitting in semiconductors. *Nature physics*, 2(2):81, 2006.

[176] Kotni Santhosh, Ora Bitton, Lev Chuntonov, and Gilad Haran. Vacuum Rabi splitting in a plasmonic cavity at the single quantum emitter limit. *Nature communications*, 7:ncomms11823, 2016.

[177] Fatemeh Hosseini Alast, Guixin Li, and KW Cheah. Rabi-like splitting from large area plasmonic microcavity. *AIP Advances*, 7(8):085201, 2017.

[178] Benjamin Gallinet and Olivier JF Martin. Ab initio theory of Fano resonances in plasmonic nanostructures and metamaterials. *Physical Review B*, 83(23):235427, 2011.

[179] Hideki T Miyazaki and Yoichi Kurokawa. Controlled plasmon resonance in closed metal/insulator/metal nanocavities. *Applied physics letters*, 89(21):211126, 2006.

[180] Srdjan S Aćimović, Hana Šípová, Gustav Emilsson, Andreas B Dahlin, Tomasz J Antosiewicz, and Mikael Käll. Superior LSPR substrates based on electromagnetic decoupling for on-a-chip high-throughput label-free biosensing. *Light: Science & Applications*, 6(8):e17042, 2017.

[181] Jan Becker, Andreas Trügler, Arpad Jakab, Ulrich Hohenester, and Carsten Sönnichsen. The optimal aspect ratio of gold nanorods for plasmonic bio-sensing. *Plasmonics*, 5(2):161–167, 2010.

[182] Bhavya Sharma, Renee R Frontiera, Anne-Isabelle Henry, Emilie Ringe, and Richard P Van Duyne. SERS: Materials, applications, and the future. *Materials today*, 15(1-2):16–25, 2012.

[183] Ilanit Doron-Mor, Zahava Barkay, Neta Filip-Granit, Alexander Vaskevich, and Israel Rubinstein. Ultrathin gold island films on silanized glass. morphology and optical properties. *Chemistry of Materials*, 16(18):3476–3483, 2004.

[184] John R Ferraro. *Introductory Raman spectroscopy.* Elsevier, 2003.

[185] Dominik Enders, Tadaaki Nagao, Annemarie Pucci, Tomonobu Nakayama, and Masakazu Aono. Surface-enhanced ATR-IR spectroscopy with interface-grown plasmonic gold-island films near the percolation threshold. *Physical Chemistry Chemical Physics*, 13(11):4935–4941, 2011.

[186] Jiwon Lee, Qianpeng Zhang, Seungyoung Park, Ayoung Choe, Zhiyong Fan, and Hyunhyub Ko. Particle–film plasmons on periodic silver film over nanosphere (AgFON): a hybrid plasmonic nanoarchitecture for surface-enhanced Raman spectroscopy. *ACS applied materials & interfaces*, 8(1):634–642, 2015.

[187] Bo-Kai Chao, Yi Xu, Hsin-Chia Ho, Pakman Yiu, Yi-Chen Lai, Chan-Hung Shek, and Chun-Hway Hsueh. Gold-rich ligament nanostructure by dealloying Au-based metallic glass ribbon for surface-enhanced Raman scattering. *Scientific reports*, 7(1):7485, 2017.

[188] Jonathan RI Lee, Trevor M Willey, Joakim Nilsson, Louis J Terminello, James J De Yoreo, and Tony van Buuren. Effect of ring substitution position on the structural conformation of mercaptobenzoic acid self-assembled monolayers on Au (111). *Langmuir*, 22(26):11134–11141, 2006.

[189] Shuang Lin, Xiang Lin, Xiu-Tao Lou, Fang Yang, Dian-Yang Lin, Zhi-Wei Lu, et al. Rapid fabrication of self-assembled interfacial film decorated filter paper as

an excellent surface-enhanced Raman scattering substrate. *Analytical Methods*, 6(24):9547–9553, 2014.

[190] Li Jiang, Tingting You, Penggang Yin, Yang Shang, Dongfeng Zhang, Lin Guo, and Shihe Yang. Surface-enhanced Raman scattering spectra of adsorbates on Cu_2O nanospheres: charge-transfer and electromagnetic enhancement. *Nanoscale*, 5(7):2784–2789, 2013.

[191] Weichun Ye, Yang Chen, Feng Zhou, Chunming Wang, and Yumin Li. Fluoride-assisted galvanic replacement synthesis of Ag and Au dendrites on aluminum foil with enhanced SERS and catalytic activities. *Journal of Materials Chemistry*, 22(35):18327–18334, 2012.

[192] Lijuan Wei, Bo Jin, and Sheng Dai. Polymer microbead-based surface enhanced Raman scattering immunoassays. *The Journal of Physical Chemistry C*, 116(32):17174–17181, 2012.

[193] S Murph. Metallic and hybrid nanostructures: fundamentals and applications. Technical report, SRS, 2012.

[194] Fu Wan, Haiyang Shi, Weigen Chen, Zhaoliang Gu, Lingling Du, Pinyi Wang, Jianxin Wang, and Yingzhou Huang. Charge transfer effect on Raman and surface enhanced Raman spectroscopy of furfural molecules. *Nanomaterials*, 7(8):210, 2017.

[195] Mahmood Toofan and Jahansooz Toofan. A brief review of the cleaning process for electronic device fabrication. In *Developments in Surface Contamination and Cleaning*, pages 185–212. Elsevier, 2015.

[196] Nordin Félidj, Jean Aubard, Georges Lévi, Joachim R Krenn, Andreas Hohenau, Gerburg Schider, Alfred Leitner, and Franz R Aussenegg. Optimized surface-enhanced Raman scattering on gold nanoparticle arrays. *Applied Physics Letters*, 82(18):3095–3097, 2003.

[197] Zhiping Zhuang, Xiumin Shi, Yufeng Chen, and Minghui Zuo. Surface-enhanced Raman scattering of trans-1, 2-bis (4-pyridyl)-ethylene on silver by theory calculations. *Spectrochimica Acta Part A: Molecular and Biomolecular Spectroscopy*, 79(5):1593–1599, 2011.

[198] Andreas Horrer, Christian Schäfer, Katharina Broch, Dominik A Gollmer, Jan Rogalski, Julia Fulmes, Dai Zhang, Alfred J Meixner, Frank Schreiber, Dieter P Kern, et al. Parallel fabrication of plasmonic nanocone sensing arrays. *small*, 9(23):3987–3992, 2013.